

Magazine of Civil Engineering

125th

ISSN
2712-8172



17(1), 2024



Magazine of Civil Engineering

ISSN 2712-8172

Online peer-reviewed open-access scientific journal in the field of Civil and Construction Engineering

Founder and Publisher: Peter the Great St. Petersburg Polytechnic University

This journal is registered by the Federal Service for Supervision of Communications, Information Technology, and Mass Media (ROSKOMNADZOR) in 2020. Certificate EI No. FS77-77906 issued February 19, 2020.

Periodicity: 8 issues per year

Publication in the journal is open and free for all authors and readers.

Indexing: Scopus, Web of Science (ESCI, RSCI), DOAJ, Compendex, Google Academia, Index Copernicus, ProQuest, Ulrich's Serials Analysis System, CNKI

Corresponding address: 29 Polytechnicheskaya st., Saint Petersburg, 195251, Russia

Chief science editor: associate member of RAS, D.S. in Engineering, Vitaly V. Sergeev

Deputy chief science editors:

D.S. in Engineering, Galina L. Kozinetc

D.S. in Engineering, Sergey V. Korniyenko

Executive editor: Ekaterina A. Linnik

Translator, editor: Darya Yu. Alekseeva

DT publishing specialist:

Anastasiya A. Kononova

Contacts:

E-mail: mce@spbstu.ru

Web: <http://www.engstroy.spbstu.ru>

Date of issue: 12.02.2024

© Peter the Great St. Petersburg Polytechnic University. All rights reserved.

© Coverpicture – Ilya Smagin

Editorial board:

T. Awwad, PhD, professor, Damascus University, Syrian Arab Republic

M.I. Balzannikov, D.Sc., professor, Samara State University of Economics, Russia

A.I. Belostotsky, D.Sc., professor, StaDyO Research & Engineering Centre, Russia

A.I. Borovkov, PhD, professor, Peter the Great St. Petersburg Polytechnic University, Russia

A. Borodinecs, Dr.Sc.Ing., professor, Riga Technical University, Latvia

M. Veljkovic, PhD, professor, Delft University of Technology, The Netherlands

R.D. Garg, PhD, professor, Indian Institute of Technology Roorkee (IIT Roorkee), India

M. Garifullin, PhD, postdoctoral researcher, Tampere University, Finland

T. Gries, Dr.-Ing., professor, RWTH Aachen University, Germany

T.A. Datsyuk, D.Sc., professor, Saint-Petersburg State University of Architecture and Civil Engineering, Russia

V.V. Elistratov, D.Sc., professor, Peter the Great St. Petersburg Polytechnic University, Russia

T. Kärki, Dr.-Ing., professor, Lappeenranta University of Technology, Russia

G.L. Kozinetc, D.Sc., professor, Peter the Great St. Petersburg Polytechnic University, Russia

D.V. Kozlov, D.Sc., professor, National Research Moscow State Civil Engineering University, Russia

S.V. Korniyenko, D.Sc., professor, Volgograd State Technical University, Russia

Yu.G. Lazarev, D.Sc., professor, Peter the Great St. Petersburg Polytechnic University, Russia

M.M. Muhammadiev, D.Sc., professor, Tashkent State Technical University, Republic of Uzbekistan

H. Pasternak, Dr.-Ing.habil., professor, Brandenburgische Technische Universität, Germany

F. Rögner, Dr.-Ing., professor, Technology Arts Science TH Köln, Germany

V.V. Sergeev, D.Sc., professor, Peter the Great St. Petersburg Polytechnic University, Russia

T.Z. Sultanov, D.Sc., professor, Tashkent Institute of Irrigation and Agricultural Mechanization Engineers, Republic of Uzbekistan

M.G. Tyagunov, D.Sc., professor, National Research University "Moscow Power Engineering Institute", Russia

M.P. Fedorov, D.Sc., professor, Peter the Great St. Petersburg Polytechnic University, Russia

D. Heck, Dr.-Ing., professor, Graz University of Technology, Austria

A.G. Shashkin, D.Sc., PI Georekonstruktsiya, LLC, Russia

V.B. Shtilman, D.Sc., JSC B.E. Vedeneev VNIIG, Russia

Contents

| | |
|--|-------|
| Bedov, A.I., Shaposhnikova, Yu.A. Bearing capacity of steel-reinforced concrete floor elements before the operation period | 12501 |
| Maltseva, T.V., Nabokov, A.V., Vatin, N. Consolidation of water-saturated viscoelastic subgrade | 12502 |
| Nguyen, D.P., Hoang, N.B., Thiep, H.T., Indra, P., Pham, B.T. Impact of roughness elements on reducing flow velocity at outlets of box culverts | 12503 |
| Al-Kinani, A.M., Thajeel, J.K., Al-Umar, M.H., Fattah, M.Y. Utilizing seismic techniques and dynamic field tests for soil dynamic response prediction in clay soils | 12504 |
| Baimukhametov, G., Gayfutdinov, R., Khafizov, E. Calculation of the influence of various compaction on the wear resistance of asphalt concrete using material loss calculation approach | 12505 |
| Hamrouni, F., Jamei, M., Alassaf, Y. Numerical analysis of rainfall-induced slope instability using a reduced-scale model | 12506 |
| Matveeva, O.I., Baishev, N.K., Makarov, A.I., Popov, A.L., Pavlyukova, I.R., Grigoriev, N.A. Enhancing lightweight concrete strength through modified zeolite-alkaline porous aggregate: composition optimization and structural application | 12507 |
| Burtseva, O.A., Evtushenko, S.I., Kokhanenko, V.N. Determining parameters of high-velocity open water flow | 12508 |
| Suprun, V.A., Ustinova, V.V. Pilot installation of a biosorption facility on a rice irrigation system | 12509 |
| Utkin, V.S., Kosheleva, Zh.V., Yarygina, O.V. Buckling analysis of piles in solid frozen soils | 12510 |





Research article

UDC 624.016

DOI: 10.34910/MCE.125.1



Bearing capacity of steel-reinforced concrete floor elements before the operation period

A.I. Bedov , Yu.A. Shaposhnikova 

Moscow State University of Civil Engineering (National Research University), Moscow, Russian Federation

 yuliatalyzova@yandex.ru

Keywords: combined action, condition survey, steel-reinforced concrete structures, structural assessment, stud connector, trapezoidal steel profiled sheeting, “Hoesch Additiv Decke®” technology

Abstract. The paper reflects the results of a survey and assessment of the technical condition of steel-reinforced concrete floor slabs using the “Hoesch Additiv Decke®” technology. Poor execution of concreting and reinforcing, lack of combined action between the elements of the slab, various deviations from the project significantly affect the stress-strain state of the steel-reinforced concrete floor. The aim of the work is to study the influence of various factors on the stress-strain state of steel-reinforced concrete floor slabs using the “Hoesch Additiv Decke®” technology before their operation. The main objectives of this study are: assessment of the technical condition of the steel-reinforced concrete floor slab, detection of defects and damage in the elements of the slab; check calculations of strength, deformability and fluctuation of individual elements, taking into account the identified defects and damage; search for the main decisive parameters in the production of construction and installation works, which significantly affect the strength, deformability and durability of the structure. The object of the study is the elements of the combined steel-reinforced concrete floor. The paper considers the influence of various factors on the stress-strain state of a combined steel-reinforced concrete floor before the start of operation. The authors apply the calculation-analytical method of research. The strength of the slab elements is checked using the “Scad Office” program. The verification of the deformability and fluctuation of the overlap is carried out by manual calculation in accordance with current regulations. Results. The authors performed check calculations of the slab elements, taking into account the identified defects and damages, the actual reinforcement and the thickness of the slab. Deficiencies in the construction and installation works and design errors led to a large number of defects in the floor, such as overloading of the slab, the appearance of force cracks in the slab above the beams, excessive deflections of structures, defects in reinforcement and in concreting. It is required to carry out comprehensive measures to strengthen the floor slabs according to a specially developed construction project developed by a specialized organization. Conclusions. The authors give recommendations on ensuring the operational characteristics of the examined bearing elements based on the results of assessing the technical state of the structures. The results of the research can be used in practical work by engineers in the design and construction of steel-reinforced concrete floor slabs, as well as in the examination and assessment of their technical state.

Citation: Bedov, A.I., Shaposhnikova, Yu.A. Bearing capacity of steel-reinforced concrete floor elements before the operation period. Magazine of Civil Engineering. 2024. 17(1). Article no. 12501 DOI: 10.34910/MCE.125.1

1. Introduction

The paper reflects the results of a survey and assessment of the technical condition of steel-reinforced concrete floor slabs made using the “Hoesch Additiv Decke®” technology (developed by ThyssenKrupp Bausysteme) for a three-story public building.

Technology “Hoesch Additiv Decke®” or “Hoesch Additive Floor®” is a system of lightweight pre-fabricated steel-reinforced concrete floors, made in Germany [1–3]. The system consists of metal rolled *I*-beams with a possible pitch of up to 5.9 m, a ribbed reinforced concrete plate and trapezoidal steel profiled sheeting used as a permanent formwork. The flooring type TRP 200 is used with a trapezoidal profile, 200 mm high or more. The profiled flooring is made in accordance with DIN EN 10346-2015 “Continuously hot-dip coated steel flat products for cold forming – Technical delivery conditions”. A distinctive feature of this technology is a patented method of supporting reinforced concrete slabs along profiled flooring on massive steel support elements. Supports are made of profiled steel of square section, which minimizes the construction height of the slab and maintains the useful height of the storey [1–3].

A typical design of a steel-reinforced concrete floor slab using the “Hoesch Additiv Decke®” technology is shown in Fig. 1 [4].

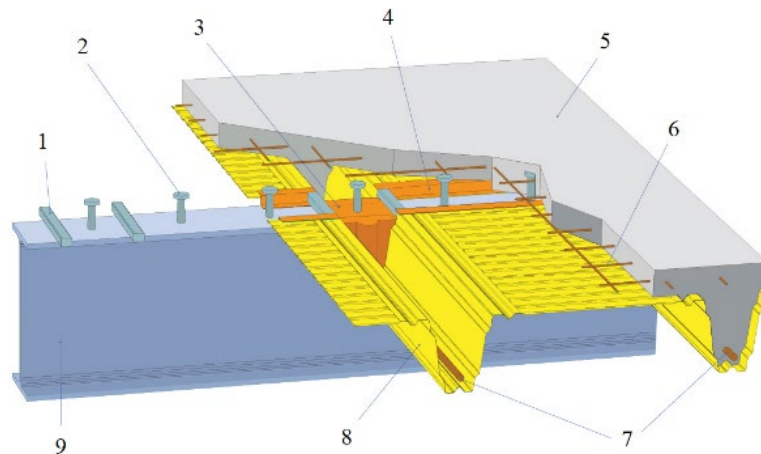


Figure 1. Steel-reinforced concrete floor slab using “Hoesch Additiv Decke®” technology: (1) steel support element, (2) stud connector, (3) plastic seal cover, (4) zigzag traverse, (5) ribbed reinforced concrete plate, (6) welded wire reinforcing mesh, (7) longitudinal ceiling reinforcement, (8) trapezoidal steel profiled sheeting, (9) composite steel beam.

In Europe, this technology is widespread and is used for multi-storey car parks and two-level parking areas. In the Russian Federation, this structural system was used in individual buildings in the cities of Moscow, St. Petersburg, Sochi and in some others, mainly for the construction of parking lots and shopping centers.

Steel-reinforced concrete floors have long been widely used both in the Russian Federation and abroad for buildings for various purposes [5–8]. The effectiveness of the use of such structures of floor slabs, their advantages and disadvantages are considered in [9–10]. Steel-reinforced concrete floors differ in design solutions, types and installation technology [11–12]. Traditional combined profiles have a height of no more than 70 mm and are installed on the upper shelf of a rolling *I*-beam. This significantly increases the building volume without increasing the useful height of the spaces.

The development of the construction industry contributes to the continuous improvement of existing and the introduction of new types of load-bearing structures, including steel-reinforced concrete floors. The use of modern load-bearing systems of buildings, which allow increasing the useful height without increasing financial costs, is especially relevant at the present time. The study of the operation of such floors, as well as the influence of various factors on the stress-strain state during construction and operation is of scientific and practical interest.

At the first stages of the development of steel-reinforced concrete structures, such domestic scientists as N.N. Streletsky, E.M. Gitman, E.E. Gibshman and others were engaged in the issues of their calculation and design. They were mainly engaged in large-span bridge structures or steel-concrete trusses. The possibilities of using steel-reinforced concrete in civil engineering were not considered at that time.

Many Russian and foreign scientists have studied the work of complex monolithic ceilings supported by metal beams. For example, E.S. Karapetov, C.T.T. Hsu, B. Jurkiewicz and others studied the problems and methods of including individual components of the steel-reinforced concrete floor in the joint work [13–15]. P. Colajanni, D. Kanchana, J. Qureshi and others dealt with the issues of shear resistance of an embedded joint between a reinforced concrete slab and a steel beam [16–18]. Researchers A. Albarram, J. Qureshi and A. Abbas studied the effect of rib geometry on the performance of composite beams [19]. F.S. Zamaliev, A.S.H. Suwaed and others considered the issues of joining the slab with metal beams

[20–21]. G.P. Tonkih, M. Konrad, S.W. Pathirana studied the joint work of a slab and metal beams by connecting with stud connectors and various anchor fasteners [22–24]. A.G. Tamrazyan, F.S. Zamaliev, S.N. Arutyunyan, E.G. Bikinin studied the features of the stress-strain state of a steel-reinforced concrete slab during construction [25–26]. Features of the calculation of such floors are presented in the works of such researchers as D.A. Urgalkina, M.L. Porter, V.S. Kuznetsov and others [27–29]. In the works of Yu.L. Rutman, V.E. Tarasikova, L.R. Gimranov, K.A. Nazarova the issues of the influence of various factors on the deformability of steel-reinforced concrete floors were studied [30–33]. Numerical modeling of reinforced concrete composite beams with reinforcement is presented in the works of M. Ramezani, F. Alsharari, J.L.P. Tamayo and others [34–36]. L.H. Reginato, A.N. Mironov, D.V. Bely, V.M. Anishchenkov paid attention to the effect of creep and cracking on the stress-strain state of such floors [37–39].

Initially, in the Russian Federation and abroad, the calculation of the strength of steel-reinforced concrete floors was carried out in accordance with the distribution of forces, in proportion to the stiffness of the floor elements [40]. In Russia, since 1984, the calculation of steel-reinforced concrete structures has been carried out in accordance with SNiP 35.13330.2011 “Bridges and culverts” and its subsequent versions. And in 2017, a new regulatory document SP (Russian Construction Rules) 266.1325800.2016 “Composite steel and concrete structures. Design rules”, which provides more detailed and precise recommendations for the calculation of such floors. In Europe, the calculation and design of steel-reinforced concrete structures is currently carried out on the basis of “Eurocode 4: Design of composite steel and concrete structures”, as well as in accordance with design guides [41–42].

Such scientists as S.B. Krylov, A.G. Tamrazyan, V.O. Almazov, S.N. Arutyunyan and many others were engaged in comparing the methods of calculation and design of steel-reinforced concrete slabs with profiled flooring according to Russian and European standards [43–45].

The stress-strain state of individual elements and steel-reinforced concrete floors as a whole before the start of operation is influenced by many different factors. Among the main factors that require a detailed analysis are the following [26]:

- the property of steel-reinforced concrete structures to change their stress-strain state after laying the concrete mix and in the process of concrete hardening;
- the effect of creep and concrete contraction on the redistribution of stresses, as well as on the increase in deflections before the start of operation;
- the influence of the development of elastic-plastic deformations of concrete on the formation of additional stresses in steel elements (the effect of additional loading);
- the effect of compliance of the contact joint between a steel beam and a reinforced concrete slab on the operation of the system due to the close location of the seam to the neutral zone of the composite beam section;
- the influence of the development of elastic-plastic deformations of concrete on the formation of additional stresses in steel elements (the effect of additional loading);
- influence of compliance of the contact line between a steel beam and a reinforced concrete slab on the work on the system due to the close location of the contact line to the neutral zone of the composite beam section;
- influence of heat transfer processes due to cement hydration processes on the stress-strain state of steel elements.

Unsatisfactory performance of concrete work (overflow of concrete mix, poor-quality concrete mix, its overdrying during the hardening process), poor performance of reinforcing work, lack of joint work between the elements of the slab, lack of adhesion of the profiled sheet to reinforced concrete, solutions that do not meet the requirements of construction documents, etc., can significantly affect the stress-strain state of the steel-reinforced concrete floor structure.

The defects and damages identified during the building survey in the elements of the steel-reinforced concrete floor before the start of the operation indicate the need for a detailed consideration of the influence of these factors on the work of the floors. The study of the features of the stress-strain state of steel-reinforced concrete slabs before the start of operation to prevent the development of various negative phenomena in structures is of particular interest to project designers and engineers. Identification of the main decisive parameters and important technological features in the production of construction and installation works for steel-reinforced concrete slabs using the “Hoesch Additiv Decke®” technology is of practical interest to modern civil engineers and erection supervisors.

The purpose of this work is to study the influence of various factors before the start of operation on the stress-strain state of steel-reinforced concrete floor slabs made using the “Hoesch Additiv Decke®” technology.

The main objectives of this study were:

- assessment of the technical condition of the steel-reinforced concrete floor slab, detection of defects and damage in the elements of the slab;
- verification calculations of strength, deformability and fluctuation of individual elements of a steel-reinforced concrete slab, taking into account the identified defects and damages;
- search for the main decisive parameters of construction and installation works, which significantly affect the strength, deformability and durability of the steel-reinforced concrete floor structure.

2. Methods

The paper reflects the results of a survey and assessment of the technical condition of steel-reinforced concrete floor slabs made using the “Hoesch Additiv Decke®” technology for a three-story public building [1–3]. The survey was carried out in accordance with GOST (Russian Government Standard) 31937-2011 “Buildings and constructions. Rules of inspection and monitoring of the technical condition” and SP (Russian Construction Rules) 13-102-2003 “Rules of inspection of bearing structures of buildings and facilities”.

The surveyed building is a detached 3-storey, single-span, rectangular in plan, floor height of 3.6 m. The structural scheme of the building is frame-and-link system, consisting of steel columns, welded steel and rolled beams, steel-reinforced concrete floors, portal brace between columns, half-timbered vertical and horizontal guides. Joints of beams with columns and columns with foundations are hinged. The load-bearing steel frame is a single-span three-story frame with a span of 15 m and a step of 5.2 m. Fig. 2 shows a bottom view of the second floor ceiling.



Figure 2. Bottom view of the floor slab of the second floor: significant deflections of the ribs of the profiled steel sheet.

The spatial rigidity of the building is sufficient, provided by the presence of a metal frame, united by monolithic steel-reinforced concrete floors along profiled steel flooring, as well as vertical portal brace and half-timbered vertical and horizontal guides from a square profile of 100×100×5 mm.

The ceiling is a monolithic steel-reinforced concrete slab. A monolithic slab on a profiled steel deck type TRP 200, with a total project thickness of 295 mm (flange thickness 90 mm), is laid on steel welded prestressed beams with reverse camber (650 mm high with a flange width of 180 mm). Joint work of beams and slabs is provided by stud connector welded to steel beams with a certain pitch. Profiled decking TRP 200–750 is used as a fixed formwork for reinforced concrete floors and rests through steel rectangular bars, 35 mm high, on the top flange of steel prestressed beams.

Steel-reinforced concrete beams are pivotally supported through a supporting steel plate using bolts on steel columns from an *I*-section 25K1 according to STO ASCHM (Russian Industry Standard of Association of Ferrous Metallurgy) 20-93 “Rolled steel sections. *I*-beams with parallel edges of flanges. Specifications”. The metal of the beams corresponds to the declared design class C355 according to the results of physical-chemical analysis. There are no suspended ceilings at the time of the survey.

Multiple defects and damage to the main load-bearing above-ground structures were found as a result of the survey.

The concrete class of the floor slabs corresponds to class *B20* according to the results of a series of strength tests in accordance with GOST (Russian Government Standard) 26633-2015 “Heavy-weight and sand concretes. Specifications”, which is lower than the *B25* class declared in the project.

The slab uses a profiled sheet TRP 200-750 with a thickness of $t \approx 0.9$ mm, which is less than the minimum thickness recommended by the “Hoesch Additiv Decke®” technology of 1 mm, and less than the $t = 1.25$ mm declared in the project. The metal of the profiled deck has a tensile strength of 343.77 MPa according to the results of a series of strength tests. The connection between the reinforced concrete floor slab and the profiled flooring using notches or anchors is not provided for by the project.

According to the results of the geodetic survey, deflections of rolled I -beams up to 18 mm were recorded, which is $l/833$, where the span of the beams between the columns is $l = 15$ m. The reverse bend provided by the project, up to 36 mm, is fixed only in some beams, which is up to $l/417$, where the span of the beams between the columns is $l = 15$ m.

The deflections of the profiled steel sheet ribs in the longitudinal direction reach up to 29 mm, which is $l/179$, where the span between the beams is $l = 5.2$ m. Deflection of the profiled steel sheet shelf in the longitudinal direction reaches a value of 75 mm, which is $l/69$, where the span between the beams is $l = 5.2$ m. The deflections of the corrugated board shelf in the transverse direction reach a value of 87 mm, which is $l/7$, where the span between the supports-ribs of the profiled sheet is $l = 0.58$ m.

The thickness of the cement-sand screed on the floor slabs was up to 60 mm. This is much more than the 30 mm declared in the project and leads to an excess of the constant load. There are no floor loads and operating loads at the time of the survey.

The deflections of the floor slab along the profiled steel sheet between the metal beams already exceeded the maximum allowable deflection $l/150$ at the time of the survey. Deflections of the profiled steel sheet in the transverse direction reached critical values up to $l/7$. These defects clearly indicate a significant overflow of the concrete mix of the floor slab over the profiled flooring. Inadmissible deformations indicate an insufficient design thickness of the profiled steel deck $t \approx 0.9$ mm, which is unable to support the weight of the concrete mix without significant deformations. The actual thickness of the floor slab flange reached 130 mm in some areas (up to 120 mm on average) due to the insufficient design thickness of the profiled sheet and the absence of its additional supports when concreting the floor slab. A significant overflow of the concrete mix and an almost 2-fold increase in the thickness of the cement-sand screed led to the fact that the actual load on the floor increased significantly. Overloading the floor slab with a constant load has a negative impact on the stress-strain state of the steel-reinforced concrete floor.

The joint work of the reinforced concrete slab and profiled deck is practically absent due to the excessive deflection of the profiled deck, as well as the lack of adhesion (for example, with the help of notches) of the concrete of the slab and the corrugated sheet.

Power cracks were fixed in reinforced concrete slabs above steel beams. Single or paired cracks are located in the direction along the steel beams for the entire width of the building, with an opening width of up to 1.5 mm for the entire thickness of the slab. The formation of such cracks indicates that the limiting tensile strains in the concrete of the slab are maximum. In the cross section of a steel-reinforced concrete slab above a metal support beam, only reinforcing bars work in tension. That is, in fact, the formation of a plastic hinge occurred in reinforced concrete floors in the supporting sections above the beams. Due to the occurrence of the described defects, the design scheme was changed from a multi-span reinforced concrete beam slab with design spans of 5.2 m to single-span hinged-supported slabs with a design span of 5.02 m for each (Fig. 3).

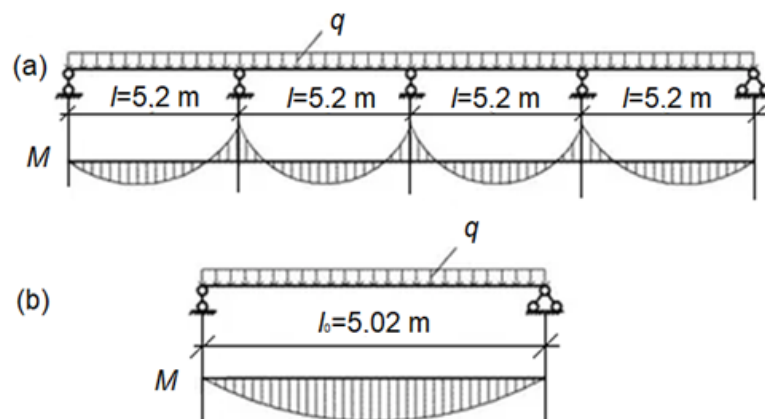


Figure 3. Calculation scheme of a reinforced concrete slab along a profiled deck:
(a) initial multi-span, (b) single-span with hinged support.

The protective layer was exposed in several areas to reveal the actual reinforcement of the floor slab. As an example, the results of opening a protective layer in a section above a steel beam in the middle of its span are presented (Fig. 4). The geometric dimensions of the steel-reinforced concrete floor elements based on the results of opening the protective layer and measurements are shown in Fig. 4. The actual thickness of the concrete protective layer and the reinforcement of the slab were established based on the results of the examination of the openings.

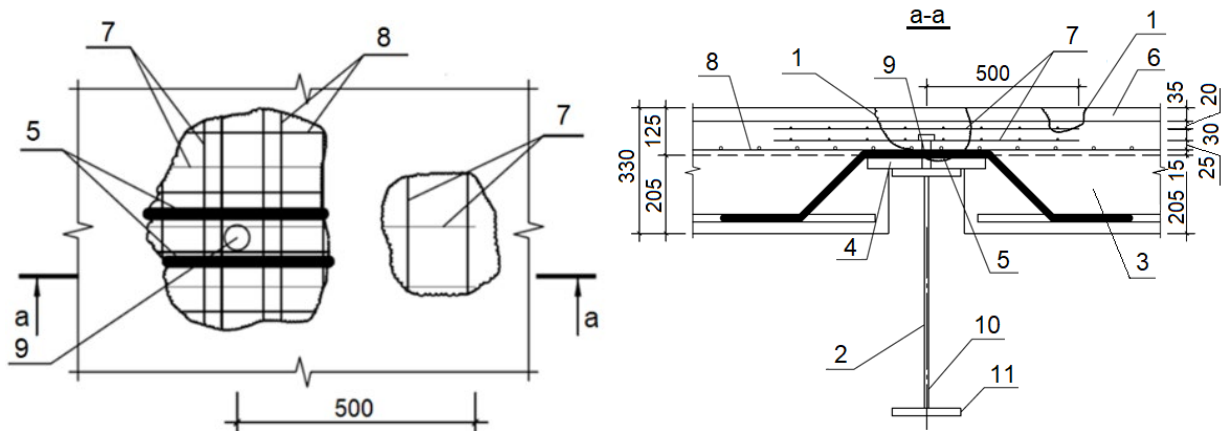


Figure 4. Section of the opening of the protective layer in the section above the steel beam: (1) opening area, (2) welded *I*-beam $h = 650$ mm, (3) monolithic reinforced concrete ribbed plate along the profiled deck, (4) steel support element, (5) bent reinforcing bars $2\phi 14$ A500S, (6) cement-sand screed, (7) reinforcing mesh 4B500-100, (8) reinforcing mesh 8A500S-100, (9) stud connector $\phi 22$, (10) *I*-beam web 12×600 mm, (11) bottom flange *I*-beam 25×180 mm.

According to the results of openings and measurements, it was revealed that the slab is reinforced with non-tensioned reinforcement:

- over the entire area of the floor slab, a reinforcing mesh $\phi 8$ A500S was laid, with a step of 100 mm in both directions, the thickness of the protective layer $a_z \approx 50 - 75$ mm from the upper surface of the concrete;
- in each rib of the reinforced concrete floor, along the profiled deck, a reinforcing bar $\phi 18$ A500S is laid, the thickness of the protective layer is $a_z \approx 40 - 60$ mm from the bottom surface of the concrete rib;
- bent reinforcing bars $2\phi 14$ A500S are laid in the reinforced concrete floor when supported through a steel beam, the thickness of the protective layer is $a_z \approx 10 - 15$ mm from the lower surface of the concrete of the slab shelf;
- in the upper zone above the metal beams, two reinforcing meshes $\phi 4$ B500 are laid with a step of 100 mm in both directions, the thickness of the protective layers is $a_z \approx 20 - 40$ mm and $a_z \approx 50 - 55$ mm from the upper surface of the concrete.

Reinforcement in the upper zone above the steel beams (two reinforcing mesh $\phi 4$ B500 with a step of 100 mm in both directions) does not correspond to the one declared in the project (two reinforcing mesh $\phi 5$ B500). The thickness of the protective layers of the floor reinforcement exceeds the design ones by 5–25 mm.

In accordance with Eurocode 4 and SP (Russian Construction Rules) 266.1325800.2016, the calculation of a steel-reinforced concrete floor slab traditionally includes two stages:

- the calculation of the profiled steel deck for the weight of the concrete mix during concrete placement;
- the calculation of the reinforced concrete slab with shear studs (stud connectors) on the support beams, where the profiled deck is additional external working slab reinforcement.

For a reinforced concrete slab in operation, designers carry out strength checks along normal and inclined sections, check the maximum deflection of the slab under the design load, check the adhesion strength of the profiled flooring to concrete, and evaluate the compliance of shear studs (stud connectors).

In the presented study, in order to assess the actual bearing capacity of the slab structure along the profiled decking, as well as the combined floor beam, verification calculations were performed taking into

account the actual reinforcement, the identified thicknesses of the protective layers of the reinforcement, the actual thickness of the slab, and taking into account the indicated defects and damage. Taking into account that the connection of the floor slab and the profiled flooring by means of notches or connectors is not provided for by the project, the operation of the profiled steel flooring as external working reinforcement was not taken into account in the calculation of the slab. Loads were assigned in accordance with SP (Russian Construction Rules) 20.13330.2016 “Loads and actions”.

Calculations of the reinforced concrete slab for strength and deformability were performed in accordance with SP (Russian Construction Rules) 63.13330.2018 “Concrete and reinforced concrete structures. General provisions” for three sections:

- cross-section on the support, checking for transverse force (only the rectangular part of the cross-section of the floor slab on the profiled deck works);
- cross-section at a distance x from the support, where the T -section is fully included in the work on the action of the transverse force (taking into account the most unfavorable option – the size of the section according to the project, without pouring the concrete mix, and the maximum value of the transverse force on the support);
- cross-section in the span-zone of the slab with its actual thickness (taking into account the overflow of the concrete mix) to the action of the bending moment.

Verification calculations for strength, deformability and unsteadiness for a steel-reinforced concrete combined beam were performed in accordance with SP (Russian Construction Rules) 266.1325800.2016 “Composite steel and concrete structures. Design rules”.

3. Results and Discussion

The results of verification calculations for various elements of the steel-reinforced concrete floor are presented below. The strength of the normal sections of the slab along the profiled flooring was tested taking into account the deformation model, which is based on the principle of dividing the section into many sections [27]. The shear strength of composite floor slabs depends on many factors [9]. In view of the peculiarities of the operation of the floor using the “Hoesch Additiv Decke®” technology, as well as the identified defects in the design of the slab, the most dangerous sections of the slab are considered below.

3.1. Checking the strength of the rectangular section of the slab along the profiled deck for the action of the shear force Q on the support

Only the rectangular part of the T -section of the reinforced concrete floor slab works on the support. The following initial data for the calculation were accepted: general partial factor $\gamma_n = 1.0$; effective length $l_0 = 5.02$ m. The actual section of the floor slab adopted for the calculation: $b = 750$ mm, $h = 90$ mm, $a_1 = 13$ mm, $a_2 = 44$ mm. Concrete of class B20 is accepted. Reinforcement was taken for calculation: bottom $2\phi 14$ A500S (bended rods in the lower zone of the slab flange), upper – $6\phi 10$ A500S, which corresponds to the actual reinforcement of the upper zone of the slab (Fig. 4). There is no cross reinforcement according to the project. The work of a profiled deck as a cross reinforcement is not taken into account due to the lack of its adhesion to the concrete of the floor slab.

The design section of the floor slab is shown in Fig. 5.

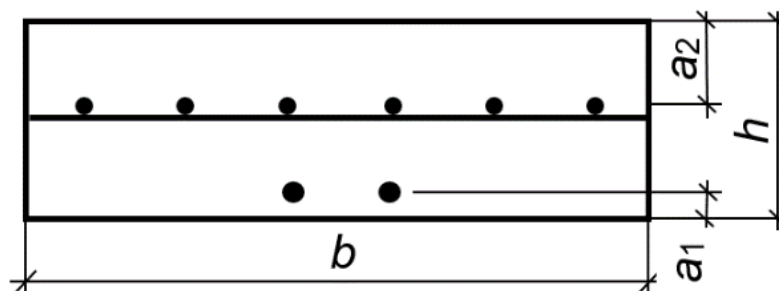


Figure 5. Design rectangular section of the floor slab.

Verification calculation was performed using the “Scad Office” program. The calculation results are presented in Table 1.

Table 1. Results of calculating the section of a floor slab on a support for the action of a transverse force.

| Verification | Utilization ratio |
|--|-------------------|
| Strength of a concrete strip between oblique sections | 0.183 |
| Strength of oblique sections without cross reinforcement | 1.4 |

The reinforced concrete slab on the profiled deck does not meet the requirements of the standards for the strength of oblique sections in a rectangular section near the support.

3.2. Checking the strength of the T -section of the slab along the profiled deck near the support for the action of the shear force Q .

The check is carried out at a distance x from the support, where the T -section is included in the work on the shear force. The most unfavorable option is taken into account – the size of the section according to the project (without overflowing the concrete mix) and the maximum value of the shear force on the support. The following initial data for the calculation were accepted: general partial factor $\gamma_n = 1.0$; effective length $l_0 = 5.02$ m. The actual section of the floor slab adopted for the calculation: $b = 125$ mm, $h = 295$ mm, $b_1 = 750$ mm, $h_1 = 90$ mm, $a_1 = 40$ mm, $a_2 = 44$ mm. Concrete of class B20 is accepted. Reinforcement was taken for calculation: bottom $2\phi 18$ A500S (in the ribs of the floor slab), upper – $6\phi 10$ A500S, which corresponds to the actual reinforcement of the upper zone of the slab flange (Fig. 4). There is no cross reinforcement according to the project. The work of a profiled deck as a cross reinforcement is not taken into account due to the lack of its adhesion to the concrete of the floor slab.

The design section of the floor slab is shown in Fig. 6.

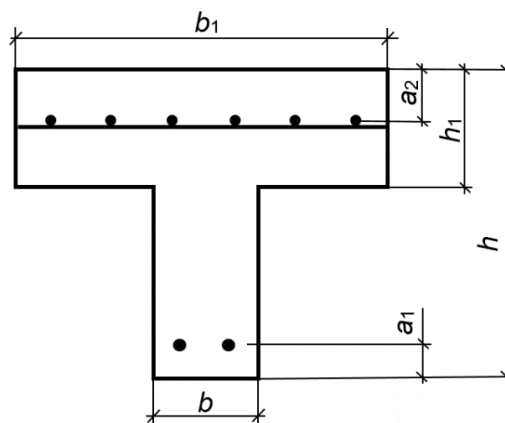


Figure 6. Design T -section of the floor slab near the support.

Verification calculation was performed using the “Scad Office” program. The calculation results are presented in Table 2.

Table 2. The results of the calculation of the floor slab on the support for the action of the shear force.

| Verification | Utilization ratio |
|--|-------------------|
| Strength of a concrete strip between oblique sections | 0.183 |
| Strength of oblique sections without cross reinforcement | 1.4 |

The reinforced concrete slab on the profiled deck **does not meet** the requirements of the standards for the strength of oblique sections in a rectangular section near the support.

3.3. Checking the strength of the tee section of the slab along the profiled deck in the span, taking into account the overflow of concrete

The following initial data for the calculation were accepted: general partial factor $\gamma_n = 1.0$; effective length $l_0 = 5.02$ m. The actual section of the floor slab adopted for the calculation: $b = 125$ mm, $h = 325$ mm, $b_1 = 750$ mm, $h_1 = 120$ mm, $a_1 = 60$ mm, $a_2 = 53$ mm. Concrete of class B20 is

accepted. Reinforcement was taken for calculation: bottom $1\phi 18$ A500S, upper – $5\phi 10$ A500S, which corresponds to the actual reinforcement of the upper zone of the slab flange (Fig. 4). There is no cross reinforcement according to the project. The work of a profiled deck as a cross reinforcement is not taken into account due to the lack of its adhesion to the concrete of the floor slab.

The calculated section of the floor slab is shown in Fig. 7.

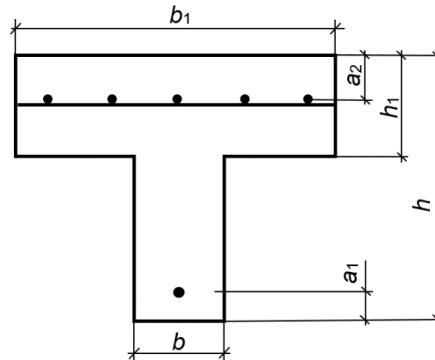


Figure 7. Design T-section of the floor slab in the span.

Verification calculation was performed using the “Scad Office” program. The calculation results are presented in Table 3.

Table 3. The results of the calculation of the floor slab in the span.

| Verification | Utilization ratio |
|--|-------------------|
| Strength at the ultimate moment of the section | 0.794 |
| Deformations in compressed concrete | 0.208 |
| Deformations in tension reinforcement | 0.116 |
| Crack width (short-term) | 1.17 |
| Crack width (long term) | 1.396 |

According to the results of the verification calculation, the reinforced concrete slab on the profiled deck does not meet the requirements of the standards for the width of the target crack width. The maximum calculated deflection of the floor slab along the profiled deck, taking into account operational loads, does not go beyond the normative values and is 17.37 mm, which is less than the maximum allowable $l/167 = 30$ mm.

3.4. Verification calculation of a composite steel-reinforced concrete

The following initial data for calculation are accepted.

Steel welded beam made of C355 steel, design tensile strength of steel $R_y = 305$ MPa; reinforcement modulus of elasticity $E_s = 2.05 \cdot 10^5$ MPa. Beam span $l = 15$ m, beam spacing $B = 5.2$ m. Composite beam section dimensions: flange width 180 mm; flange thickness 25 mm; web thickness 12 mm; the total height of the steel beam is 650 mm.

A monolithic reinforced concrete slab with a thickness of 90 mm is laid on metal welded T-section beams. Haunch height is 35 mm (Fig. 8). The design width of the reinforced concrete slab is 180 mm. Class of concrete is B20, design resistance of concrete to compression $R_b = 11.5$ MPa, concrete modulus of elasticity $E_b = 27.5 \cdot 10^3$ MPa. Class of reinforcement is A500S, design tensile strength of reinforcing steel $R_s = 435$ MPa, reinforcement modulus of elasticity $E_s = 2.05 \cdot 10^5$ MPa (Fig. 3–5). The main geometric characteristics of the section are shown in Fig. 8.

Geometric characteristics of the section: $A_{f1,st} = 45$ cm² is cross-sectional area of the lower flange of the beam; $A_{f2,st} = 45$ cm² is cross-sectional area of the upper flange of the beam; $A_{w,st} = 72$ cm² is cross-sectional area of the beam web; $A_s = 1.0$ cm² is cross-sectional area of bar tension reinforcement;

$A_b = 225 \text{ cm}^2$ is total cross-sectional area of a reinforced concrete slab with haunch; $A_{b,pl} = 162.0 \text{ cm}^2$ is cross-sectional area of a reinforced concrete slab; $A_{b,h} = 63.0 \text{ cm}^2$ is cross-sectional area of the reinforced concrete haunch of the slab; $A_{red} = 17.06 \text{ cm}^2$ is area of the transformed section; $Z_{f1,st} = 32.5 \text{ cm}$ is distance from the center of gravity of the section of the steel beam C_{st} to the lower edge of its section; $Z_{f2,st} = 32.5 \text{ cm}$ is distance from the center of gravity of the section of the steel beam C_{st} to the upper edge of its section; $Z_{b,st} = 38.75 \text{ cm}$ is distance from C_{st} to the center of gravity of reinforced concrete section C_b ; $Z_{st,red} = 2.27 \text{ cm}$ is distance from C_{st} to the center of gravity of the transformed section C_{red} ; $Z_{b,red} = 36.48 \text{ cm}$ is distance from C_{red} to C_b .

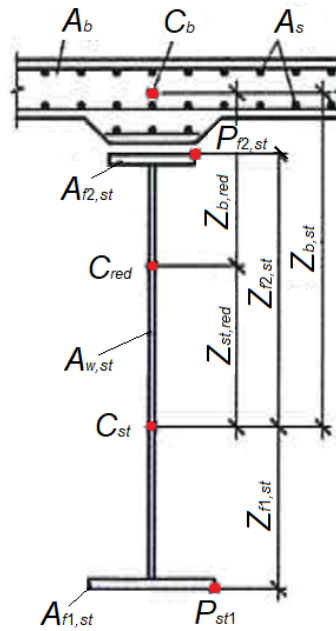


Figure 8. Geometric characteristics of the steel-reinforced concrete beam section:
 C_b is center of gravity of reinforced concrete section, C_{st} is center of gravity of steel beam section, C_{red} is center of gravity of the transformed section.

The dead weight of the steel beam is $P_1 = 0.134 \text{ t/r.m.}$

The first stage of loading (on a steel beam from a monolithic reinforced concrete floor slab and profiled deck) is 0.493 tf/m^2 .

The second load stage (only on the combined beam) is 0.661 tf/m^2 .

Load on steel beam $g_1 = 5.2 \cdot 0.493 + 0.12 = 2.697 \text{ t/r.m.}$

Load on steel-reinforced concrete beam $g_2 = 5.2 \cdot 0.661 = 3.437 \text{ t/r.m.}$

Full load on the steel-reinforced concrete beam $g = g_1 + g_2 = 6.134 \text{ t/r.m.}$

Maximum bending moment in span (from full loads) $M = g \cdot l_0^2 / 8 = 172.53 \text{ tf}\cdot\text{m}$, where $l_0 = 15 \text{ m}$ – is the calculated span of the steel-reinforced concrete beam.

Bending moment of the first stage of work $M_1 = g_1 \cdot l_0^2 / 8 = 75.86 \text{ tf}\cdot\text{m}$.

Bending moment of the second stage of work $M_2 = g_2 \cdot l_0^2 / 8 = 96.67 \text{ tf}\cdot\text{m}$.

Maximum shear force on supports (from full loads) $Q = g \cdot l_0 / 2 = 46.01 \text{ tf}$.

Verification of stresses in concrete in accordance with SP (Russian Construction Rules) 266.1325800.2016 is carried out according to the formula (1)

$$\sigma_b = \frac{M_2}{\alpha_b W_{b,red}} - \sigma_{bi} \geq \gamma_{bi} R_b, \quad (1)$$

where M_2 is the bending moment of the second stage of work; $\alpha_b = 22.36$ is reduction coefficient of concrete; $W_{b,red} = 3395.78 \text{ cm}^3$ is moment of resistance of the transformed concrete section; σ_{bi} is stresses in concrete; γ_{bi} is reliability factor for concrete; $R_b = 11.5 \text{ MPa}$ is design resistance of concrete to compression.

$$127.3 > 103.5 \text{ kg/cm}^2$$

The required strength condition for concrete is not met.

Checking the stresses in the reinforcement in accordance with SP (Russian Construction Rules) 266.1325800.2016 is carried out according to the formula (2)

$$\sigma_s = \frac{M_2}{\alpha_s W_{b,red}} - \sigma_{si} \geq \gamma_{si} R_s, \quad (2)$$

where M_2 is the bending moment of the second stage of work; $\alpha_s = 1$ is reduction coefficient of steel; $W_{b,red} = 3395.78 \text{ cm}^3$ is moment of resistance of the transformed concrete section; σ_{si} is stresses in reinforcement; γ_{si} is reliability factor for reinforcement; $R_s = 435 \text{ MPa}$ is design tensile strength of reinforcement.

$$2846.8 < 4350 \text{ kg/cm}^2$$

The required strength condition for reinforcement **is met**.

Checking the stresses in the upper flange of the steel beam in accordance with SP (Russian Construction Rules) 266.1325800.2016 is carried out according to the formula (3)

$$\frac{M - z_{b,st} N_{bR,sR}}{W_{f2,st}} - \frac{N_{bR,sR}}{A_{st}} < \gamma_s R_y, \quad (3)$$

where M is bending moment; $Z_{b,st} = 38.75 \text{ cm}$ is distance from the center of gravity of the steel beam to the center of gravity of the reinforced concrete slab; $N_{bR,sR}$ is compressive force of the upper part of the combined section; $W_{f2,st} = 3370.38 \text{ cm}^3$ is moment of resistance of section to the upper flange of the steel beam; γ_s is reliability factor for reinforcement; $R_y = 305 \text{ MPa}$ is design tensile strength of C355 steel.

$$4584.9 > 3050 \text{ kg/cm}^2$$

The required strength condition for the upper flange of the steel beam **is not met**.

Checking the stresses in the bottom flange of the steel beam in accordance with SP (Russian Construction Rules) 266.1325800.2016 is carried out according to the formula (4)

$$\frac{M - z_{b,st} N_{bR,sR}}{W_{f1,st}} - \frac{N_{bR,sR}}{A_{st}} < \gamma_s R_y, \quad (4)$$

where M is bending moment; $Z_{b,st} = 38.75 \text{ cm}$ is distance from the center of gravity of the steel beam to the center of gravity of the reinforced concrete slab; $N_{bR,sR}$ is compressive force of the upper part of the combined section; $W_{f1,st} = 3370.38 \text{ cm}^3$ is moment of resistance of section to the bottom flange of the steel beam; γ_s is reliability factor for reinforcement; $R_y = 305 \text{ MPa}$ is design tensile strength of C355 steel.

$$4966 > 3050 \text{ kg/cm}^2$$

The required strength condition for the bottom flange of the steel beam **is not met**.

The vertical total deflection of the steel-reinforced concrete floor should be calculated taking into account the pre-operational deformed state [6, 24, 25]. However, due to the many defects and damages found in the combined beam, it is not possible to determine the completeness of the joint work of steel beams and steel-reinforced concrete floor slabs. It is required to carry out additional studies of the joint operation of the floor elements and additional verification calculations. In view of the above, the steel beam deflection is checked separately from the reinforced concrete floor according to the well-known formula (5)

$$f = \frac{5g^n l^4}{384E_s I_{red}} = 134.5 \text{ mm}, \quad (5)$$

where $l = 15$ m is design span of the combined beam, g^n is total design load on the beam; $E_s = 2.05 \cdot 10^5$ MPa is modulus of elasticity for steel class C355; $I_{red} = 123892.3$ cm⁴ is inertia couple of the transformed section of the combined beam.

Taking into account the camber 50 mm, the deflection is $134.5 - 50 = 84.5$ mm.

$84.5 < l / 150 = 100$ mm is the required condition for deformations **is met**.

From the results of the performed strength calculations, taking into account the actual reinforcement and the actual class of concrete of the slab, as well as taking into account the identified defects and damage, it follows that the combined floor beams do not meet the requirements of standards for strength.

3.5. Verification calculation of a combined beam for fluctuation

Limit deflections of floor elements of residential and public buildings, based on physiological requirements, are determined in accordance with SP (Russian Construction Rules) 20.13330.2016 "Loads and impacts" according to the formula (6)

$$f_u = \frac{g(p + p_1 + q)}{30n^2(bp + p_1 + q)}, \quad (6)$$

where $g = 9.8$ m·s⁻² is acceleration of free fall; $p = 50$ kg/r.m. is the standard value of the load from people that excite vibrations; $p_1 = 70$ kg/r.m. is reduced standard value of the load on floors; $q = 772.5$ kg/r.m. is the standard value of the load from the weight of the calculated element and structures based on it; $n = 1.5$ is the frequency of application of the load when a person walks; b is the coefficient taken according to Table D.2 of SP (Russian Construction Rules) 20.13330.2016 "Loads and actions".

According to the results of the sway analysis for the combined beam, the maximum allowable deflection is $f_u = 74.4$ mm. Calculated deflection of the combined beam is

$$f = 84.5 > 74.4 \text{ mm.}$$

The fluctuation condition for the combined beam **is not met**.

According to the results of the calculation for fluctuation for a slab on a profiled deck, the maximum allowable deflection is $f_u = 26.3$ mm. Calculated slab deflection is

$$f = 17.37 < 26.3 \text{ mm.}$$

The fluctuation condition for the floor slab along the profiled deck is met.

4. Conclusions

- According to the results of the performed verification calculations:
 - steel-reinforced concrete slab on profiled deck does not meet the requirements of standards for strength from the impact of shear force and crack opening width;
 - combined floor beams do not meet the requirements of normative documentation for strength, deformability and fluctuation.

2. Violations in the course of construction and installation works and design errors led to the occurrence of a large number of defects in the installation of the floor slab: overloading of the slab, force cracks in the slab above the beams, excessive deflections of structures, deficiencies in reinforcement and concrete work.
3. The technical state of the floors is unacceptable. It is required to carry out complex measures to strengthen the floor slabs according to a specially developed project, carried out by a specialized organization.
4. When assessing the stress-strain state of steel-reinforced concrete structures, it is necessary to take into account the actual geometric characteristics of the section and the initial geometry of the deflection of the slab due to the possible overflow of the concrete mix.
5. During the construction of steel-reinforced concrete floor slabs, including the "Hoesch Additiv Decke®" technology, it is necessary:
 - apply design solutions, taking into account the recommendations of manufacturers and in accordance with all the necessary requirements of the applied technology;
 - strictly follow the design requirements for reinforcement and concrete work, check the class of concrete mix supplied to the construction site;
 - ensure collaboration between the elements of the steel-reinforced concrete slab by following the correct design decisions;
 - ensure the adhesion of profiled sheets to reinforced concrete with the help of notches or special anchors;
 - perform internal quality control, and if necessary, external quality control at all stages of design and construction and installation works.
6. As a result of the defects and damages identified during the inspection, it is currently not possible to accurately determine the completeness of the joint work of steel beams and a steel-reinforced concrete floor slab. It is necessary to study the influence of the identified defects and damages on the operation of the contact line, arranged by means of stud bolts, between the slab and the rolled beam. Additional verification calculations are required to evaluate the joint operation of the floor elements. This direction is a separate voluminous topic for analysis. The solution of the issues of the influence of various factors on the mating of the plate elements will be considered in future studies.
7. The results of the research can be used in practical work by engineers in the design and construction of steel-reinforced concrete floor slabs, as well as in the examination and assessment of their technical condition.

References

1. Jurisch, F. Hoesch Additive Floor® - The success story of an innovation. 2006.
2. Dujmovic, D., Androić, B., Lukačević, I. Hoesch Additive Floor. Composite Structures According to Eurocode 4. 2015. DOI: 10.1002/9783433604908.ch22
3. Dujmovic, D., Androić, B., Lukačević, I. Calculation of Simply Supported Composite Beam According to the Plastic Resistance of the Cross-Section. Composite Structures According to Eurocode 4. 2015. DOI: 10.1002/9783433604908.ch8
4. Sholts Y., Arutyunyan S.N. Profnastil i ankernyye upory v stalezhelezobetonnykh perekrytiyakh – bolshe chem konstruktiv! [Corrugated sheeting and anchor supports in steel-reinforced concrete floors are more than constructive!]. URL: proflist.ru/techinfo/ARSS201703.pdf (date of application: 15.03.2023). (rus)
5. Babalich, V.S., Androsov, E.N. Stalezhelezobetonnye konstrukcii i perspektiva ih primeneniya v stroitel'noy praktike Rossii [Steel-reinforced concrete structures and the prospect of their application in the construction practice of Russia]. Uspehi sovremennoy nauki. 2017. 4. Pp. 205–208. (rus)
6. Egorov, P.I., Korolev, S.A. The composite slabs. Far East: the problems of the development of the architectural and construction complex. 2015. 1. Pp. 310–313.
7. Zamaliev, F.S., Tamrazyan, A.G. To calculation of steel-reinforced concrete ribbed plates for refurbished floors. Building and Reconstruction. 2021. 5 (97). Pp. 3–15. DOI: 10.33979/2073-7416-2021-97-5-3-15
8. Kinzhitaeva, A. Primenenie i raschet stalezhelezobetonnykh konstrukcij v rossijskoj i zarubezhnoj praktike (obzor) [Application and calculation of steel-reinforced concrete structures in Russian and foreign practice (review)]. Innovatsii. Nauka. Obrazovaniye. 2021. 45. Pp. 157–166. (rus)
9. Ahmed, I.M., Tsavdaridis, K.D. The evolution of composite flooring systems: applications, testing, modelling and Eurocode design approaches. Journal of Constructional Steel Research. 2019. 155. Pp. 286–300. DOI: 10.1016/j.jcsr.2019.01.007
10. Tamrazyan, A.G., Arutyunyan, S.N. To the assessment of the reliability of steel slabs of slabs with profiled floorings. Bulletin of Civil Engineers. 2015. 6 (53). Pp. 52–57.
11. Vasdravellis, G., Uy, B., Tan, E.L., Kirkland, B. Behaviour and design of composite beams subjected to sagging bending and axial compression Original Research. Journal of Constructional Steel Research. 2015. 110. Pp. 29–39. DOI: 10.1016/j.jcsr.2015.03.010
12. Zamaliev, F.S., Zakirov, M.A. Some results of numerical studies of steel-concrete composite slabs. News of the Kazan State University of Architecture and Engineering. 2015. 3 (33). Pp. 56–63.

13. Hsu, C.T.T., Punurai, S., Punurai, W., Majdi, Y. New composite beams having cold-formed steel joists and concrete slab. *Engineering Structures*. 2014. 71. Pp. 187–200. DOI: 10.1016/j.engstruct.2014.04.011
14. Jurkiewicz, B., Braymand, S. Experimental study of a pre-cracked steel-concrete composite beam. *Journal of Constructional Steel Research*. 2007. 63(1). Pp. 135–144. DOI: 10.1016/j.jcsr.2006.03.013
15. Karapetov, E.S., Atanov A.A. Analysis of existing methods of incorporation of steel and reinforced concrete in combined action. *Proceedings of Petersburg Transport University*. 2018. 15(4). Pp. 592–604.
16. Kanchana Devi, A., Ramanjaneyulu, K., Gandhi, P. Shear resistance of embedded connection of composite girder with corrugated steel web. *Journal of Constructional Steel Research*. 2021. 187(2). 106994. DOI: 10.1016/j.jcsr.2021.106994
17. Colajanni, P., Mendola, L.L., Monaco, A. Review of push-out and shear response of hybrid steel-trussed concrete beams. *Buildings*. 2018. 8(10). P. 134. DOI: 10.3390/buildings8100134
18. Qureshi, J., Lamb, D., Yea, J. Effect of shear connector spacing and layout on the shear connector capacity in composite beams. *Journal of Constructional Steel Research*. 2011. 67. Pp. 706–719. DOI: 10.1016/j.jcsr.2010.11.009
19. Albarram, A., Qureshi, J., Abbas, A. Effect of rib geometry in steel-concrete composite beams with deep profiled sheeting. *International Journal of Steel Structures*. 2020. 20 (3). Pp. 931–953. DOI: 10.1007/s13296-020-00333-5
20. Zamaliev, F.S., Ismagilov, B.T. Numerical and full-scale studies of anchor links of steel reinforced structures. *News of the Kazan State University of Architecture and Engineering*. 2018. 3 (45). Pp. 121–128.
21. Suwaed, A.S.H., Karavasilis, T.L. Demountable steel-concrete composite beam with full-interaction and low degree of shear connection. *Journal of Constructional Steel Research*. 2020. 171. Pp. 106–152. DOI: 10.1016/j.jcsr.2020.106152
22. Pathirana, S.W., Uy, B., Mirza, O., Zhu, X. Bolted and welded connectors for the rehabilitation of composite beams. *Journal of Constructional Steel Research*. 2016. 125. Pp. 61–73. DOI: 10.1016/j.jcsr.2016.06.003
23. Tonkih, G.P., Chesnokov, D.A. Shear resistance of nailed connectors in composite beams with steel decking. *Industrial and civil engineering*. 2022. 7. Pp. 17–23.
24. Konrad, M. Headed studs used in trapezoidal steel sheeting according to Eurocode 4. *Structural Engineering International*. 2009. 19 (4). Pp. 420–426. DOI: 10.2749/101686609789847118
25. Tamrazyan, A.G., Arutyunyan, S.N. Issledovanie nachal'nyh naprjazhenij i progibov profnastila, vznikajushhih pri vozvedenii stalezhelezobetonnyh plit perekrytij [Investigation of initial stresses and deflections of profiled deck arising during the construction of composite floor slabs]. *Bezopasnost' stroitel'nogo fonda Rossii. Problemy i reshenija* [The Safety of the construction Fund of Russia. Problems and solutions]. 2017. Pp. 139–146. (rus)
26. Zamaliev, F.S., Bikinin, E.G. The main factors influencing the initial stress-strain state of steel-concrete composite structures. *News of the Kazan State University of Architecture and Engineering*. 2015. 4(34). Pp. 161–165.
27. Porter, M.L., Eckberg, C.E. *Design Recommendations for Steel Deck Floor Slabs*. ASCE Journal of the Structural Division. New York. 1976. 11 (102).
28. Urgalkina, D.A. Application of deformation model to calculation of reinforced concrete lines on steel profile sheet. *World Science*. 2019. 6 (27). Pp. 527–531.
29. Kuznetsov, V., Shaposhnikova, Yu. Features of calculation and design of complex concrete monolithic slabs. *MATEC Web of Conferences*. 2018. 251. DOI: 10.1051/mateconf/201825102027
30. Tarasikova, V.E. Vlijanie stad-boltov na deformativnost' stalezhelezobetonnoj plity perekrytija po stal'nomu profilirovannomu nastilu [Influence of stud bolts on the deformability of a steel-reinforced concrete floor slab over a steel profiled deck]. *Mezhdunarodnaja nauchno-tehnicheskaja konferencija molodyh uchenyh BGTU Im. V.G. Shuhova* [International scientific and technical conference of young scientists of BSTU named after V.G. Shukhov]. Belgorod State Technological University. V.G. Shukhov. Belgorod, 2021. Pp. 1655–1658. (rus)
31. Gimranov, L.R., Fattakhova, A.E. Flexible stop's force determining method in a combined plate using profiled flooring. *Monthly Journal on Construction and Architecture*. 2021. 16(8). Pp. 997–1005. DOI: 10.22227/1997-0935.2021.8.997-1005
32. Nazarova, K.A. *Naturnye jeksperimental'nye issledovanija stalezhelezobetonnogo perekrytija* [Full-scale experimental studies of steel-reinforced concrete floors.]. *Aktual'nye problemy sovremennogo stroitel'stva* [Actual problems of modern construction]. *Materialy LXXIV Vserossijskoj nauchno-prakticheskoi konferencii studentov, aspirantov i molodyh uchenyh* [Materials of the LXXIV All-Russian Scientific and Practical Conference of Students, Postgraduates and Young Scientists]. In 2 parts. Part 1. Saint Petersburg: Saint Petersburg State University of Architecture and Civil Engineering, 2021. Pp. 136–149. (rus)
33. Rutman, Yu.L., Chepilko, S.O. Stress and strain state of the steel-concrete composite beam. *Bulletin of Civil Engineers*. 2018. 4(69). Pp. 53–63. DOI: 10.23968/1999-5571-2018-15-4-53-63
34. Ramezani, M. Performance of composite connections strengthened with CFRP laminate. *Magazine of Civil Engineering*. 2021. 6(106). Pp. 10614. DOI: 10.34910/MCE.106.14
35. Alsharari, F., El-Zohairy, A., Salim, H., El-Sisi, A.E. Numerical investigation of the monotonic behavior of strengthened Steel-Concrete composite girders. *Engineering Structures*. 2021. 246(3)ю 113081. DOI: 10.1016/j.engstruct.2021.113081
36. Tamayo, J.L.P., Franco, M.I., Morsch, I.B., Désir, J.M., Wayar, A.M.M. Some aspects of numerical modeling of steel-concrete composite beams with prestressed tendons. *Latin American Journal of Solids and Structures*. 2019. 16(7). 1. DOI: 10.1590/1679-78255599
37. Mironov, A.N., Belyj, D.V., Anishhenkov, V.M. Investigation of the actual operation of steel-reinforced concrete slab structures using profiled flooring. *Metal Constructions*. 2020. 26(3). Pp. 117–129.
38. Mironov, A.N., Belyj, D.V., Anishhenkov, V.M., Volchkov, A.N. Creep of concrete in steel-reinforced concrete slab structures using profiled flooring. *Metal Constructions*. 2021. 27(1). Pp. 17–28.
39. Reginato, L.H., Tamayo, J.L.P., Morsch, I.B. Finite element study of effective width in steel-concrete composite beams under long-term service loads. *Latin American Journal of Solids and Structures*. 2018. 15(8). DOI: 10.1590/1679-78254599
40. Umansky, A.A. *Spravochnik proektirovshhika promyshlennyh, zhilyh i obshhestvennyh zdaniy i sooruzhenij. Raschetno-teoreticheskij* [Directory of the designer of industrial, residential and public buildings and structures. Calculated-theoretical]. 2nd edn. Moscow: Stroyizdat, 1972. 609 p. (rus)
41. *Design Manual for Composite Slabs*. ECCS – Technical Committee 7 – Cold Formed Thin-Walled Sheet Steel Technical Working Group 7.6 – Composite Slabs. First Edition. 1995.

42. European Committee for Standardization (CEN): EN 1994-1-1: 2004, Eurocode 4: Design of composite steel and concrete structures – Part 1-1: General rules and rules for buildings. Brussels. December. 2004.
43. Krylov, S.B., Semenov, V.A., Konin, D.V., Krylov, A.S., Rozhkova, L.S. On the New "Manual on Design of Composite Steel and Concrete Structures (in Elaboration of Formulary SP 266.13330.2016 "Composite Steel and Concrete Structures. Design Rules)". ACADEMIA. Architecture and Construction. 2019. 1. Pp. 99–106. DOI: 10.22337/2077-9038-2019-1-99-106
44. Almazov, V.O., Arutjunjan, S.N. Design of composite reinforced concrete slabs according to Eurocode 4 and Russian recommendations. Monthly Journal on Construction and Architecture. 2015. 8. Pp. 51–65.
45. Kobylina, M.A., Zolotozubov, D.G. Comparison of calculation methods for composite reinforced concrete slabs according russian recommendations and Eurocode 4. Moderne technologien im bauwesen. Theorie und Praxis. 2020. 2. Pp. 15–20.

Information about authors:

Anatoly Bedov, PhD in Technical Sciences

ORCID: <https://orcid.org/0000-0002-7003-3022>

E-mail: bedovai@mgsu.ru

Yulia Shaposhnikova, PhD in Technical Sciences

ORCID: <https://orcid.org/0000-0001-7740-9400>

E-mail: yuliatalyzova@yandex.ru

Received 21.06.2023. Approved after reviewing 08.12.2023. Accepted 27.12.2023.



Research article

UDC 624.1

DOI: 10.34910/MCE.125.2



Consolidation of water-saturated viscoelastic subgrade

T.V. Maltseva¹ , A.V. Nabokov¹, N. Vatin² 

¹ Industrial University of Tyumen, Tyumen, Russian Federation

² Peter the Great St. Petersburg Polytechnic University, St. Petersburg, Russian Federation

✉ maltsevatv@tyuiu.ru

Keywords: weak soils, water-saturated foundation, stresses and deformations, soil viscoelasticity, consolidation

Abstract. The stress-strain state of the foundations of buildings and structures made of weak viscoelastic soils is considered. The mechanical characteristics of a viscoelastic water-saturated soil base were determined experimentally. A macro sample of soil in a pipe about 1 m high had a water lock on top to create excess pore pressure in the sample. Excessive pore pressure simulated the depth of the sample from the surface. From the experiment, the universal parameter of the kinematic model was determined, and the foundation was calculated. Theoretical data obtained within the framework of a kinematic model considering the viscoelastic properties of the soil are compared with the known Flamant solution and experimental data for a stabilized state of the soil. The deviation of vertical displacements from experimental data is no more than 4 % (one-dimensional case). The deviation of the theoretical solution of the flat Flamant-type problem (considering residual pore pressures) from the known solution of the Flamant problem is 16 %. The proposed calculation method makes it possible to predict the deformation of foundations made of water-saturated viscoelastic soils more accurately than the solution for elastic and elastoplastic soils without the influence of pore pressure. The technique is novel because it allows one to simultaneously consider the soil's residual pore pressures and the soil's viscoelasticity.

Funding: This research was supported by a grant from the Russian Science Foundation No. 23-29-00118, <https://rscf.ru/project/23-29-00118/>

Citation: Maltseva, T.V., Nabokov, A.V., Vatin, N. Consolidation of water-saturated viscoelastic subgrade. Magazine of Civil Engineering. 2024. 17(1). Article no. 12502. DOI: 10.34910/MCE.125.2

1. Introduction

To improve methods for calculating soil foundations under construction projects, it is necessary to experimentally and theoretically study the process of consolidating foundations from water-saturated soils. Many factors influence the consolidation process: the presence of pore water in the soil and the soil skeleton's creep [1] since the soil is a viscoelastic material. For weak water-saturated soils (water saturation coefficient of more than 80 %), the work [2] proposed nonlinear patterns (stress-strain relationship) for the deformability of an elastoplastic soil model. In soil mechanics, time-dependent soil reactions have long been considered the result of the compaction process of elastic and single-phase soil [3]. Later, models of two-phase soils (soil skeleton and pore fluid) appeared. It was assumed that soil compaction would cease when the pore fluid pressure had completely dissipated. However, this assumption contradicts the results of laboratory [4] and field [5] experiments. It is proposed in [6] to consider soft soils (for example, clay and

loams) as a viscoelastic or viscoplastic material with rheological properties without considering the influence of pore fluid.

The manifestation of viscoelasticity properties in calculation models is considered through physical laws. The mechanical characteristics of the material included in the physical laws are determined from the experiment. Experimenting is another urgent task in studying the consolidation process [8].

In [10], the time-dependent behavior of soil is associated with primary consolidation (filtration consolidation) and with the viscoelastic properties of soils. On the one hand, the primary compaction of soils, caused by the dissipation of pore pressure, affects the stresses and deformations of bases and foundations. On the other hand, the soil is a viscoelastic medium; A. Mishra [11] used a three-parameter viscoelastic soil model. The viscoelasticity problem was converted into an elasticity problem using the Laplace transform. However, the soil is considered a solid body with viscoelastic properties, and the influence of residual pore pressure is not considered.

To predict changes in the stress-strain state of soil over time, the work [12] developed an elasto-visco-plastic soil model that considers the change in soil shape simultaneously with consolidation (without considering filtration consolidation). This model includes a linear relationship between the rate of development of shear strains and the effective stresses. The soil is single-phase, and the mechanics of a deformable solid body are applied to its modeling [13, 14].

Article [15] examines the influence of groundwater levels on the mechanical properties of soil. A two-layer soil model is proposed, which includes an unsaturated layer of water-saturated soil and a layer of non-water-saturated soil. The viscoelastic properties of the soil were not considered.

The creep of a weak two-phase soil considering excess pore water pressure was studied in [16] using the undrained triaxial unloading creep tests during the unloading of the sample. It was shown that soft soil's unloading creep behaviors are related to deviatoric stress and time. If the deviatoric stress is lower than the yield stress, then the deviatoric stress-strain curve exhibits linear viscoelastic properties. If the deviatoric stress is higher than the yield stress, then it exhibits strong nonlinear viscoplastic properties.

Previous studies have generally reduced soil consolidation to either compaction of saturated soil or compaction of unsaturated viscoelastic soil. The proposed soil models are not applicable for the analysis of real soil settlement since experiments show the presence of residual pore pressure in the soil after the completion of the filtration consolidation process. The soil is both water-saturated and viscoelastic. This article is devoted to partially eliminating these gaps. That is, it is proposed to model the process of soil consolidation considering water saturation and viscoelasticity. For this purpose, a kinematic soil model was chosen [7], into which physical laws for the soil skeleton and pore fluid were additionally introduced in the form of integral Boltzmann relations. Using the methods of operational calculus, the integral Boltzmann relations in the images coincided, up to notation, with the physical laws of the theory of elasticity. The viscoelastic problem solution is reduced to solving the problem in two stages. In the first stage, the elastic sample was calculated without considering time. In the second stage, a solution to the viscoelastic problem considering time was obtained. The authors have not found any other publications with this idea.

The kinematic model quantitatively describes the contribution of residual pore pressures to the stressed and deformed state of the two-phase foundation after the end of the filtration consolidation process. The soil is considered water-saturated. The water saturation is confirmed by numerous field experiments lasting up to 5 years, according to which the residual pore pressure at a depth of three to four meters can be up to 50 % of the total [5].

The kinematic model is based on two hypotheses [7]:

1. The difference in pore pressure does not cause the speed of water movement but causes small relative movements of particles of the soil skeleton and pore water.
2. The connection between solid and liquid soil particles is represented through relative movements (volume changes in the three-dimensional case).

It is necessary to conduct tests with water-saturated soil to consider the viscoelastic properties of the soil in the kinematic model (determining the model parameters). Creep tests mainly include macroscopic and microscopic aspects. Many researchers have proposed experiments at the macro level in an odometer [17] and at the micro level using a microscope to study the microstructure of the soil [18] or combine both aspects at once [8]. Testing samples of standard sizes (from 4 to 8 cm) cannot characterize the soil as two-phase. Firstly, all these experiments were carried out with samples of low height, up to 10 cm, and did not

capture the influence of pore water in the soil sample. Secondly, the purpose of these experiments was to exclude pore water from consideration; as described above, there were no mathematical models that considered the influence of residual pore pressure after the end of the filtration consolidation process. There was no need to conduct experiments with a soil sample that would remain saturated at the end of the filtration consolidation process. When using a kinematic model, the available experimental data is insufficient, and a new experiment with a large-sized soil sample is proposed to determine the model parameters.

The purpose of the study was to study the process of consolidation of water-saturated soil foundations, considering the viscoelastic properties of the soil. To achieve the goal, experimental and analytical-numerical solution methods were used.

The object of study is a foundation made of weak soils such as loam and clay. The subject of the study is the prediction of the stress-strain state of the foundation. In this article, to determine the parameters of the kinematic model, it is enough to experiment with a large sample (1 m or more in height) because the model is based on the physical equations of the state of a continuous medium. The novelty of the experiment is described below in the Methods section.

2. Methods

The article uses two research methods: experimental and theoretical.

2.1 Experimental studies

A laboratory experiment was carried out to determine the mechanical characteristics (parameters of the kinematic model). The description of the experimental stand and experimental conditions is given in [19]. Fig. 1 shows the setup in which the experiment was carried out.

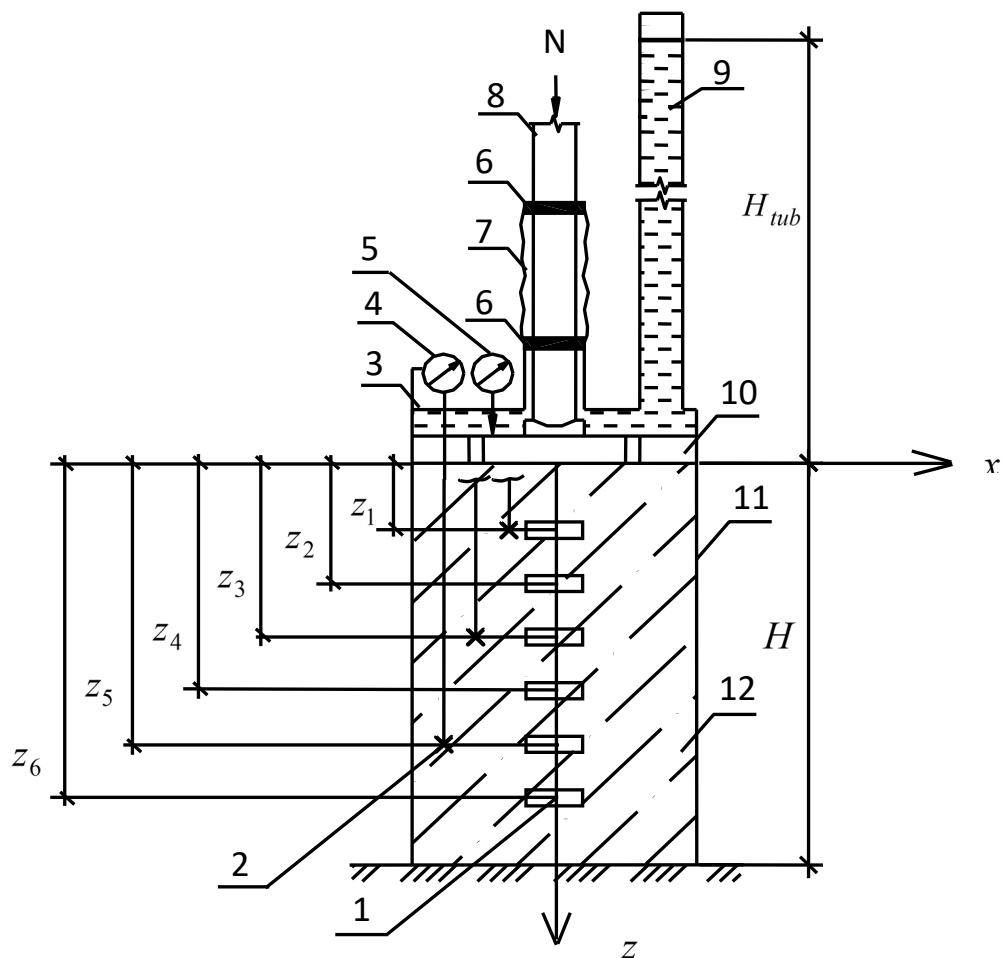


Figure 1 Test setup: 1 – sensor for determining total and pore pressure (mass dose); 2 – sensor for determining the movement of soil skeleton particles (brand); 3 – plug; 4 – deflection meter; 5 – dial indicator; 6 – clamp; 7 – rubber cuff; 8 – loading rod; 9 – water column tube; 10 – perforated stamp; 11 – pipe section; 12 – soil sample.

A two-phase soil sample had a diameter of $d = 0.311$ m and a height $H = 0.8$ m. The water column had a height of $H_{lub} = 2.2$ m above the sample. The sample was placed in a section of pipe with watertight walls and bottom. A polyethylene film was glued to the inner wall of the pipe using lithol, then a second layer of film was glued using technical petroleum jelly to eliminate friction of the sample against the pipe walls. The friction of one layer of film against another is so small that the tangential stresses that arise between the layers of the film can be neglected.

The water column simulated the distance from the daytime surface of the soil base to the soil sample, located at a depth of more than one meter. A working pressure of $\sigma_0 = 0.1$ MPa was applied to the perforated stamp with holes. Inside the sample, spaced apart in height, three membrane-type pressure sensors (BEC-A, manufactured by KYOWA, Japan) are installed to determine the total and pore pressure and sensors to determine the movements of soil skeleton particles (ICH-50, LLC NPP "Chelyabinsk Instrumental Plant", Chelyabinsk, Russia). The marks are installed at the same level as the messages. Fig. 1 shows the arrangement of messages and brands.

Dial indicators with a division value of 0.01 mm were installed on the stand to determine the movement of the stamp and stamps. The stamp was made of steel with dimensions: a height of 0.01 m and a diameter of 0.310 m. The stamp has 335 holes with a diameter of 0.004 m. Two layers of filter mesh and two layers of filter paper were laid at the stamp's base to prevent the stamp's holes

The experiment lasted 95 days. The maximum value of pore pressure, measured by the mass dose at the base of the sample, was 55 % of the applied pressure. Fig. 2. shows the experimental pore pressure curve in the horizontal section $z = 0.69$ m.

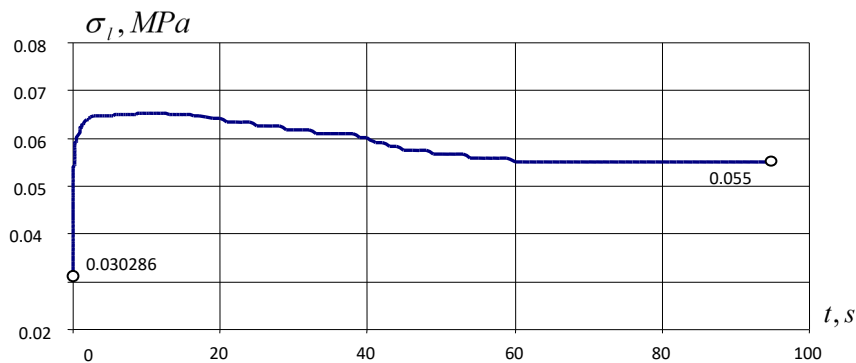


Figure 2. Pore pressure.

The novelty of the experiment was as follows: 1) the experiment was carried out with a large-sized sample; 2) water was additionally used over the sample, forming a water lock; 3) the waterlock increased the influence of pore water on the soil skeleton compared to the test without the waterlock.

2.2 Theoretical studies

Classical (viscoelastic) and generalized (structural viscoplastic) rheological models of soil are known. In [20], a generalized Voigt model was considered to simulate the viscoelastic properties of clay. The fractional calculus theory was first introduced in [21] with the dashpot element in a Kelvin-Voigt-type body to describe the compaction of viscoelastic saturated soils. In this theory, the soil's time-dependent stress-strain relationship is interconnected through the damage factor to a fractional degree. The model of viscoelastic plastic creep with a fractional derivative for frozen viscoelastic soils is considered in [22].

In contrast, in this article, the differential dependences of strains on stresses obtained in various viscoelastic models were not used. Still, the integral form of the dependence of strains on stresses was considered. The integral form is because the universal parameter of the kinematic model is determined from the experiment, so the structure of the material (soil) model is not interesting. The physical law of deformation from stress is specified using Boltzmann integrals based on experimentally found influence functions (creep). The experimental data were processed within the framework of the model of the linear hereditary theory of viscoelasticity proposed by A.A. Ilyushin [23]. The solution to the viscoelastic problem was obtained in two stages. In the first stage, the elastic sample was calculated without considering time. The resulting solution based on the Volterra principle (redesignation system) is written in Laplace-Carson images. In the second stage, for a fixed point in space, an approximate transition from the known image to

the original was made using the method of broken lines by L.E. Maltsev [24]. The original is also represented by a special broken line (spline) recorded in the images. Several numerical values of the image parameter are assigned, that is, a set of points p_i , $i = 1, \dots, n$, and the condition for the coincidence of the image of the broken line with the known image of the solution to the problem on the set of points is written. As a result, a system of linear algebraic equations is obtained, the order of which coincides with the number of links of the broken line.

Methodology of Ilyushin A.A. (splitting the problem's solution into two stages) for a Boussinesq-type problem about loading a viscoelastic water-saturated soil foundation with standard loads was applied earlier in [25, 26]. This article uses a two-stage technique to obtain a solution to the Flamant-type problem of loading a viscoelastic water-saturated soil foundation with a strip load.

3. Results and Discussion

3.1. Obtaining mechanical characteristics based on experimental data

The experimental graph $\sigma_l(t)$ (Fig. 2) was presented using polyline links and the Heaviside function:

$$\sigma_l(t) = \sigma(0) \cdot \left[1 - \sum_{i=0}^6 (b_i - b_{i+1}) \cdot (t - t_i) \cdot h(t - t_i) \right], \quad t = \frac{\bar{t}}{1s}. \quad (1)$$

The parameters of the function were as follows: $t_0 = b_0 = b_7 = 0$, $\sigma(0) = 0.030286$ MPa; $t_1 = 0.45$; $t_2 = 3.95$; $t_3 = 11.45$; $t_4 = 38$; $t_5 = 60$; $t_6 = 95$; $b_1 = 2.14973$; $b_2 = 0.04857$; $b_3 = 0.00279$; $b_4 = -0.00553$; $b_5 = -0.00889$; $b_6 = 0$.

Here $\sigma(0)$ is the voltage value at the initial moment of dimensionless time.

Using the retardation theorem, the Laplace-Carson image of the stress function with known parameters $\sigma_0, b_1, \dots, b_5$ is determined:

$$\left[\sigma_l(t) \right]^* = \sigma_l^*(p) = \sigma(0) \cdot \left[1 + \sum_{i=1}^6 b_i \cdot \frac{1}{p} \cdot \left(e^{-p \cdot t_{i-1}} - e^{-p \cdot t_i} \right) \right]. \quad (2)$$

The formula for the kinematic model parameter in images (the square means that the parameter always has a positive value) was [19]:

$$\left[a^2(t) \right]^* = \left[a^2 \right]^*(p) = -\frac{1}{z} \cdot \ln \left[1 - \frac{\left[\sigma_l^{\text{exp}}(t) \right]^*}{\sigma_0} \right], \quad (3)$$

where σ_0 is the load on the stamp, $z = 0.69$ m is the depth of the mass dose.

The broken line method [24] was used to find the original from a known image. The function $a^2(t)$ was represented by a polyline with five links:

$$\bar{a}^2(t) = a(0) \cdot \left[1 - \sum_{i=0}^5 (d_i - d_{i+1}) \cdot (t - t_i) \cdot h(t - t_i) \right]. \quad (4)$$

The image of the polyline, according to Laplace-Carson, is as follows:

$$\left[\bar{a}^2(t) \right]^* = a(0) \cdot \left[1 + \sum_{i=1}^5 d_i \cdot \frac{1}{p} \cdot \left(e^{-p \cdot t_{i-1}} - e^{-p \cdot t_i} \right) \right]. \quad (5)$$

Here $a(0)$ and d_i are the required parameters, determined from the condition of coincidence of functions in the images $\left[a^{-2} \right]^*(p_j) = \left[a^2 \right]^*(p_j)$. The points of coincidence of functions were assigned according to the formulas [7] as:

$$p_j = \frac{\ln T_j - \ln T_{j-1}}{T_j - T_{j-1}}, \quad j=1, \dots, 5, \quad T_j = 0.1T_{j+1}.$$

The obtained system of linear algebraic equations for points $p_j, j=1, \dots, 5$ of the fifth order was:

$$\begin{cases} \sum_{i=1}^5 d_i \left(e^{-p_1 T_{i-1}} - e^{-p_1 T_i} \right) = \left[\frac{\left[a^2 \right]^*(p_1)}{a(0)} - 1 \right] \cdot p_1 \\ \dots \\ \sum_{i=1}^5 d_i \left(e^{-p_{n-1} T_{i-1}} - e^{-p_{n-1} T_i} \right) = \left[\frac{\left[a^2 \right]^*(p_{n-1})}{a(0)} - 1 \right] \cdot p_{n-1} \\ \sum_{i=1}^5 d_i (T_i - T_{i-1}) = \frac{\left[a^2 \right]^*(p=0)}{a(0)} - 1 \end{cases} \quad (6)$$

The last equation of the system of equations (6) was written for the point $p_5 = 0$:

$$\sum_{i=1}^5 d_i (T_i - T_{i-1}) = \frac{\left[a^2 \right]^*(p=0)}{a(0)} - 1.$$

The parameter $a(0) = 0.522854$ for the point $p_0 = \infty$ was determined from the last equation of the system of equations (6).

The coefficient matrix of the system of equations (6) is weakly defined. The accuracy of solving the system of equations depended on the choice of coincidence points (collocations) p_j . Next, the collocation points were refined from the solution of the transcendental equation [25]:

$$m \left(e^{-p_j T_{i-1}} - e^{-p_j T_i} \right) = \left(e^{-p_j T_i} - e^{-p_j T_{i+1}} \right), \quad m = 0.8.$$

The supradiagonal elements of the matrix are 0.8 of the diagonal elements. This method led to improved conditionality of the matrix. The method was justified in [25].

As a result of solving the system of linear algebraic equations (6), the spline (broken line) parameters of the mechanical characteristics of water-saturated viscoelastic soil $a^2(t)$ were obtained: $T_0 = 0$; $T_1 = 0.1$; $T_2 = 1$; $T_3 = 5$; $T_4 = 25$; $T_5 = 60$; $p_0 = \infty$; $p_1 = 1.618$; $p_2 = 0.2275$; $p_3 = 0.03876$; $p_4 = 0.01713$; $p_5 = 0$; $d_1 = 2.8277$; $d_2 = 0.14067$; $d_3 = 0.00074$; $d_4 = -0.02296$; $d_5 = -0.0034$.

The graph of function $a^2(t)$ is shown in Fig. 3.

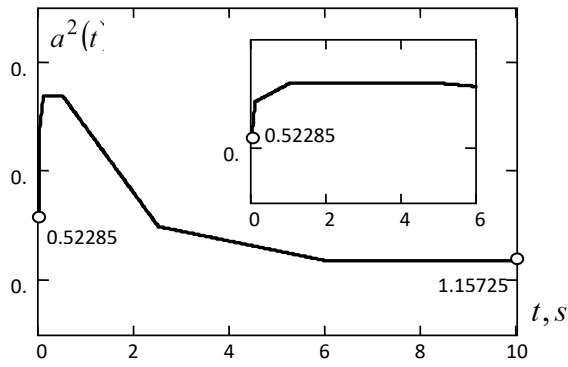


Figure 3. Model parameter $a^2(t)$.

3.2. Solution of the Flamant-type problem

A Flamant-type problem was solved within the framework of a kinematic model to describe the consolidation process of water-saturated viscoelastic soil under load.

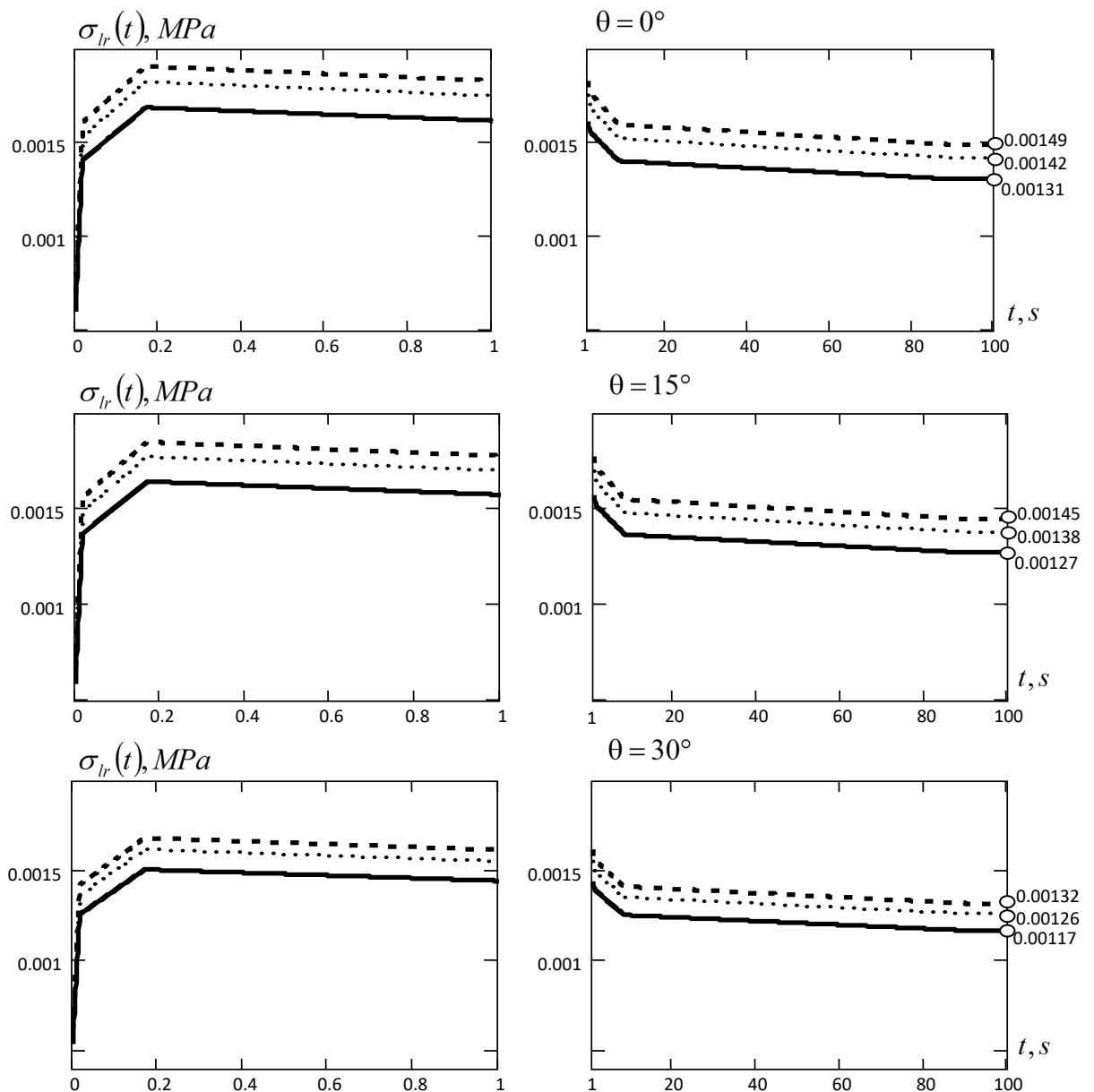


Figure 4. Pore pressure in different sections: $\theta = 0^\circ$: (—) $r_1 = 0.5$ m, ($\cdot \cdot \cdot$) $r_2 = 0.75$ m, (- - -) $r_3 = 1$ m; $\theta = 15^\circ$: (—) $r_1 = 0.52$ m, ($\cdot \cdot \cdot$) $r_2 = 0.76$ m, (- - -) $r_3 = 1.03$ m; $\theta = 30^\circ$: (—) $r_1 = 0.58$ m, ($\cdot \cdot \cdot$) $r_2 = 0.87$ m, (- - -) $r_3 = 1.16$ m.

The resulting universal parameter $a^2(t)$ of the kinematic model was used to calculate stresses and displacements in the problem of the action of a strip load on a two-phase viscoelastic half-space based on the analytical solution from [7]. The solution in Laplace-Carson images to the Flamant-type problem for a two-phase elastic half-space in polar coordinates is presented as:

$$[\sigma_{lr}(t)]^* = \frac{2F \cdot \cos \theta}{\pi} \cdot \lambda \cdot [a^2(t)]^* \cdot e^{-\lambda [a^2(t)]^* \cdot r} \cdot \int_{\rho}^r \frac{e^{\lambda [a^2(t)]^* \cdot r}}{r} dr, \quad (7)$$

where the strip load F , radius $\rho = 0.07$ m, and scale factor $\lambda = (H_{sam}/H_{tr})$.

For a fixed point in space (θ_i, r_i) , using the broken line method, we obtained the original pore pressure function $\sigma_{lr}(t)$ (Fig. 4), for which the initial time of nonmonotonic change was identified. The contribution of pore pressure increases with distance from the surface. Soil movements were determined using the polyline method.

The experiment conducted in a flume (Fig. 5, dimensions in mm) with the same soil as in a pipe (Fig. 1) was considered to compare the theoretical values obtained by solving a flat Flamant-type problem and the experimental values. The pore pressure curves and the function of the time of movement of the soil mass were obtained as a result of the experiment. Fig. 5 shows the sensor placement diagram. The values for a fixed time of the pore pressure function (stabilized state $t = 95$ days) are given in Table 1, and the displacement functions of soil skeleton particles are given in Table 2.

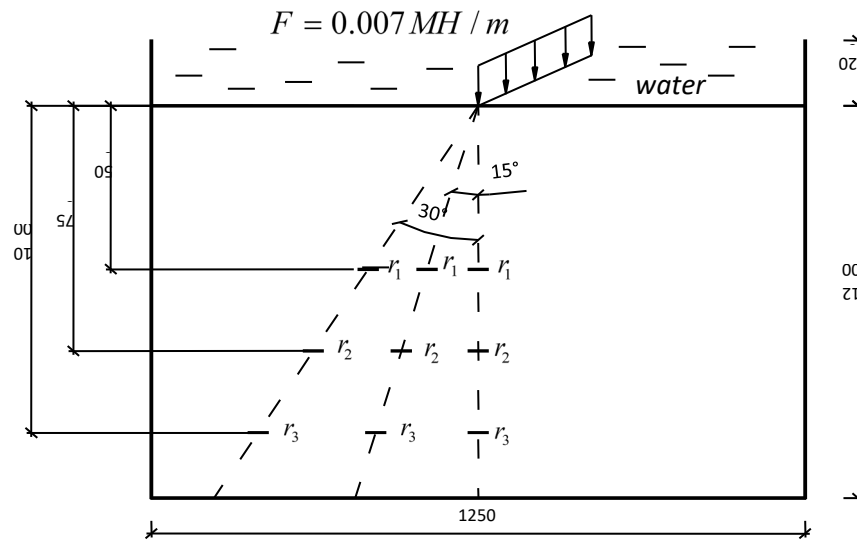


Figure 5. Tray with water-saturated clay and location of mass doses.

Table 1. Experimental and theoretical values of displacements.

| θ, deg | r, m | $\sigma_{lr}^{exp}(t = 95 \text{ days}), \text{MPa}$ | $\sigma_{lr}^{th}(t = 95 \text{ days}), \text{MPa}$ | $\delta, \%$ | $\sigma, \text{MPa},$ Flamant solution |
|----------------------|---------------|--|---|--------------|---|
| 0 | 0.5 | 0.0011 | 0.00131 | 16.0 | 0.008913 |
| | 0.75 | 0.0013 | 0.00142 | 8.5 | 0.00594 |
| | 1.0 | 0.0014 | 0.00149 | 6.0 | 0.004456 |
| 15 | 0.518 | 0.001 | 0.00127 | 21.3 | 0.00831 |
| | 0.776 | 0.00105 | 0.00138 | 20.3 | 0.005547 |
| | 1.035 | 0.0012 | 0.00145 | 17.2 | 0.00415 |
| 30 | 0.577 | 0.0009 | 0.00117 | 23.1 | 0.006686 |
| | 0.776 | 0.001 | 0.00126 | 20.6 | 0.004973 |
| | 1.155 | 0.0011 | 0.00132 | 16.7 | 0.003341 |

Table 2. Experimental and theoretical values of displacements for $\Theta = 0^\circ$.

| r, m | $w_s(r), m$ | $w_s(r), m$ | $\delta, \%$ | $w_s(r), m$ | $\delta, \%$ |
|--------|-------------|------------------|--------------|-------------|--------------|
| | experiment | Flamant solution | | theory | |
| 0.25 | 0.00079 | 0.00086 | 8.2 | 0.00081 | 3.7 |
| 0.50 | 0.00048 | 0.00052 | 7.8 | 0.00048 | 2.1 |
| 0.75 | 0.00027 | 0.00031 | 16.1 | 0.00027 | 3.7 |
| 1.0 | 0.00011 | 0.00017 | 35.2 | 0.00014 | 21.4 |

Tables 1 and 2 contain theoretical calculation data based on formula (7) for a fixed time $t = 95$ days. A comparison of experimental and theoretical values of vertical displacements showed good convergence except for the edge point $r = 1$ m. Here, the discrepancy was 21.4 %.

4. Conclusion

Based on an experiment with a large water-saturated sample using the proposed method, a mechanical characteristic of the soil (model parameter) was obtained. The viscoelastic mechanical characteristic was used to calculate the stress-strain state of the soil foundation. As a result of the calculation of a viscoelastic water-saturated foundation loaded with an external load, broken time functions of pore pressure and vertical displacements of the soil skeleton were obtained using the approximate method. A comparison was made with the experiment and the known Flamant solution, because of which it was established that:

1. The pore pressure changes nonmonotonically under constant external load. These nonmonotonic changes are a feature of two-phase soil. Pore pressure increased with increasing depth to 50 % of the total stress due to the unloading effect of pore water.
2. The maximum discrepancy between the movements of particles of the soil skeleton and the experimental data occurred at a depth of 1 m. It amounted to 35 % according to the well-known Flamant solution, and 21 % according to the solution proposed in the article. Still, this discrepancy is not indicative since the effect of a solid bottom of the tray is manifested. The actual discrepancies between theoretical and experimental values are within 1–4 %. The tests in the flume showed that pore water was actively involved in perceiving external load, starting from a depth of one meter from the surface. The total stresses in the pore fluid and soil skeleton coincided with the stresses obtained by Flamant. The highest calculated pore pressure was 39.5 % of the total at the point ($\theta = 30^\circ, r_3 = 1.155m$).

Studying the influence of the viscoelastic properties of the skeleton of water-saturated soil will significantly expand the field of geotechnical design using more accurate and efficient methods for calculating soil foundations.

References

- 1 Sharafutdinov, R.F. Clay soil stiffness under consolidated isotropic drained triaxial tests. Magazine of Civil Engineering. 2023. 121(5). Article no. 12106. DOI: 10.34910/MCE.121.6
- 2 Liu, E.L., Lai, Y.M., Wong, H., Feng, J.L. An elastoplastic model for saturated freezing soils based on thermo-poromechanics International Journal of Plasticity. 2018. 107. Pp. 246–285. DOI: 10.1016/j.ijplas.2018.04.007
- 3 Ai, Z.Y., Dai, Y.C., Cheng, Y.C. Time-dependent analysis of axially loaded piles in transversely isotropic saturated viscoelastic soils. Engineering Analysis with Boundary Elements. 2019. 101. Pp. 173–187. DOI: org/10.1016/j.enganabound.2019.01.004
- 4 Mesri, G., Choi, Y.K. Settlement analysis of embankments on soft clays. Journal of Geotechnical Engineering. 1985. 111(4). Pp. 441–464. DOI: 10.1061/(asce)0733-9410(1985)111:4(441)
- 5 Bugrov, A.K., Golli, A.V., Kagan, A.A., Kuraev, S.N., Pirogov, I.A., Shashkin, A.G. Naturnye issledovaniya napryazhenno-deformirovannogo sostoyaniya i konsolidacii osnovanij sooruzhenij kompleksa zashchity Sankt-Peterburga ot navodnenij [Field studies of the stress-strain state and consolidation of the foundations of the structures of the St. Petersburg flood protection complex]. Bases, foundations and soil mechanics. 1997. 1. Pp. 2–8. (rus)
- 6 Ai, Z.Y., Chu, Z.H., Cheng, Y.C. Time effect of vertically load ed piled rafts in layered cross-anisotropic viscoelastic saturated soils. Computers and Geotechnics. 2020. 119. 103384. DOI: 10.1016/j.compgeo.2019.103384
- 7 Maltseva, T.V. Matematicheskaya teoriya vodonasyshchennogo grunta [Mathematical theory of water-saturated soil]. Tyumen': Vektor Buk, 2012. 240 p. (rus)

- 8 Yuan, J., Gan, Y., Chen, J., Tan, S., Zhao, J. Experimental research on consolidation creep characteristics and microstructure evolution of soft soil. *Structural Materials*. 2023. 10. 1137324. DOI: 10.3389/fmats.2023.1137324
- 9 Ai, Z.Y., Wang, L.H., Hu, Y.D. Load transfer from an axially loaded pile to multilayered saturated media. *Applied Mathematical Modelling*. 2016. 40(13–14). Pp. 6509–6522. DOI: 10.1016/j.apm.2016.01.064
- 10 Wang L, Sun DA, Li P, Xie Y. Semi-analytical solution for one-dimensional consolidation of fractional derivative viscoelastic saturated soils. *Computers and Geotechnics*. 2017. 83. Pp. 30–39. DOI: 10.1016/j.compgeo.2016.10.020
- 11 Mishra, A., Patra, N.R. Analysis of creep settlement of pile groups in linear viscoelastic soil. *International Journal for Numerical and Analytical Methods in Geomechanics*. 2019. 43(14). Pp. 2288–2304. DOI: 10.1002/nag.2976
- 12 Sabri, M.M., Shashkin, K.G. Soil-structure interaction: theoretical research, in-situ observations, and practical applications. *Magazine of Civil Engineering*. 2023. 120(4). 12005. DOI: 10.34910/MCE.120.5
- 13 Qin, A., Sun, D., Zhang, J. Semi-analytical solution to one-dimensional consolidation for viscoelastic unsaturated soils. *Computers and Geotechnics*. 2014. 62. Pp.110–117. DOI: 10.1016/j.compgeo.2014.06.014
- 14 Shan, Z., Ling, D., Ding, H. Analytical solution for the 1D consolidation of unsaturated multi-layered soil. *Computers and Geotechnics*. 2014. 57. Pp. 17–23. DOI: 10.1016/j.compgeo.2013.11.009
- 15 Li, L., Qin, A., Jiang, L., Wang, L. One-dimensional consolidation of unsaturated–saturated soil system considering pervious or impervious drainage condition induced by time-dependent loading. *Computers and Geotechnics*. 2022. 152. 105053. DOI: 10.1016/j.compgeo.2022.105053
- 16 Huang, W., Wen, K., Li, D., Deng, X., Li, L., Jiang, H., Amini, F. Experiment study of lateral unloading stress path and excess pore water pressure on creep behavior of soft soil. *Advances in Civil Engineering*. 2019. 9898031. DOI: 10.1155/2019/9898031
- 17 Mataic, I., Wang, D., Korkiala-Tanttu, L. Effect of destructuration on the compressibility of perniö clay in incremental loading oedometer tests. *International Journal of Geomechanics*. 2016. 16(1). 04015016. DOI: 10.1061/(ASCE)GM.1943-5622.0000486
- 18 Li, Z., Wang, J., Yang, S., Liu, S., Li, Y. Characteristics of microstructural changes of malan loess in yan'an area during creep test. *Water*. 2022. 14(3). 438. DOI: 10.3390/w14030438
- 19 Bai, V.F., Nabokov, A.V., Maltseva, T.V. Mekhanicheskie harakteristiki dvuhfaznogo obrazca [Mechanical characteristics of a two-phase sample]. *News of universities. Oil and gas*. 2002. 1. Pp. 98–106.
- 20 Liu, J.C., Lei, G.H., Wang, X.D. One-dimensional consolidation of visco-elastic marine clay under depth-varying and time-dependent load. *Marine Georesour Geotechnol*. 2015. 33(4). Pp. 337–347. DOI: 10.1080/1064119X.2013.877109
- 21 Wang, L., Sun, D.A., Li, P., Xie, Y. Semi-analytical solution for one-dimensional consolidation of fractional derivative viscoelastic saturated soils. *Computers and geotechnics*. 2017. 83. Pp. 30–39. DOI: 10.1016/j.compgeo.2016.10.020
- 22 Liao, M., Lai, Y., Liu, E., Wan, X. A fractional order creep constitutive model of warm frozen silt. *Acta Geotechnica*. 2016. 12(2). Pp. 377–389. DOI: 10.1007/s11440-016-0466-4
- 23 Ilyushin, A.A., Pobedrya, B.E. Osnovy matematicheskoy teorii termovyazkoupругosti [Fundamentals of the mathematical theory of thermoviscoelasticity]. Moscow: Izd-vo Nauka, 1970. 280 p. (rus)
- 24 Maltsev, L.E., Karpenko, Yu.I. Teoriya vyazkoupругosti dlya inzhenerov – stroitelej [The theory of viscoelasticity for civil engineers]. Tyumen': Vektor Buk, 1999. 240 p.
- 25 Maltseva, T.V., Parfenova, T.V. Influence of collocation points on matrix conditionality. *News of Universities. Oil and Gas*. 2002. 4. Pp. 101–105.
- 26 Maltseva, T.V., Bai, V.F., Erenchinov, S.A., Esipov, A.V., Chumanova, N.A. Bearing capacity of frame-gantry pile foundations. *Magazine of Civil Engineering*. 2023. 122 (6). Article no. 12207. DOI: 10.34910/MCE.122.7

Information about authors:

Tatyana Maltseva, Doctor of Physics and Mathematics

ORCID: <https://orcid.org/0000-0002-0274-0673>

E-mail: maltsevatv@tyuiu.ru

Alexander Nabokov, PhD in Technical Sciences

E-mail: nabokovav@tyuiu.ru

Nikolai Vatin, Doctor of Technical Sciences

ORCID: <https://orcid.org/0000-0002-1196-8004>

E-mail: vatin@mail.ru

Received 09.10.2023. Approved after reviewing 05.12.2023. Accepted 05.12.2023.



Research article

UDC 621.22

DOI: 10.34910/MCE.125.3



Impact of roughness elements on reducing flow velocity at outlets of box culverts

D.P. Nguyen¹, N.B. Hoang¹, H.T. Tran¹, P. Indra², B.T. Pham³ ✉

¹ *University of Transport and Communications, Hanoi, Vietnam*

² *Geological Survey of India, Kolkata, India*

³ *University of Transport Technology, Hanoi, Vietnam*

✉ binhpt@utt.edu.vn

Keywords: flow velocity, roughness elements, box culverts, energy dissipaters

Abstract. For culverts on slopes greater than critical, rougher material causes greater depth of flow and less velocity in culverts of equal size. Velocity varies inversely with resistance thus roughness elements resistance is obviously an important factor in reducing velocity at the outlets of culverts on steep slopes to prevent scour in downstream of culverts on roads. The criteria for design directives of new energy dissipaters must provide for sufficient energy dissipation, characterized by simplicity of design, effectiveness of energy dissipation and low construction cost. In this study, two physical models were built with producing roughness elements at the end part of the culverts to evaluate the outlet velocities of high-energy culverts. The results showed that with a slope ranging from 5 % to 13 %, the proposed roughness elements reduce energy dissipation from 48.7 % to 52.9 % for roughness elements without gaps and from 51.6 % to 53.9 % for roughness elements with gaps. This result also indicated that the roughness elements in the sloping box culverts can be used to replace energy dissipater structures in the downstream of the box culverts in the Central region of Vietnam.

Citation: Nguyen, D.P., Hoang, N.B., Thiep, H.T., Indra, P., Pham, B.T. Impact of roughness elements on reducing flow velocity at outlets of box culverts. Magazine of Civil Engineering. 2024. 17(1). Article no. 12503. DOI: 10.34910/MCE.125.3

1. Introduction

Culverts are by far the most commonly used channel crossing structures on roads in mountainous or steep regions [1–3]. There is no backwater for very steep channels, but the problem is to avoid erosion from high velocity outfall. The outlet design should be effective in re-establishing tolerable non-erosive channel flow within the right-of-way or within a reasonably short distance below the culvert, and should resist undercutting and washout. Energy dissipaters should be simple, easy to build, economical and reasonably self-cleaning during periods of low flow.

Recently, reducing the flow energy in a channel with a relatively large slope ($S > S_c$) has drawn interest of many hydraulic scientists such as F. Yousefi et al. [4], J. George et al. [5], Y. Dilrooban et al. [6], P. Fošumpaur et al. [7], D.F. Peterson and P.K. Mohanty [8], H.M. Morris [9, 10], P.K. Mohanty [11], J.M. Wiggert and P.D. Erfle [12], S. Pagliara et al. [13]. A corrugated or rough bed has been shown to dissipate much more energy than a smooth bed, but the effect of the coarse bed does not increase once a certain level of crushed stone has been reached [14]. In 2013, the research showed that a drainage chute with staggered roughness elements of the two-dimensional bars of rectangular cross section throughout causes considerable reduction of exit velocity in the case of pipes on steep slopes under inlet control and

free exit, i.e., flowing partly full [15–18]. A.D. Arpan et al.. The exit Froude number can be reduced to nearly unity. A. Simon et al. [19] placed three circular rings (roughness elements) on the inside perimeter of the culvert near the outlet of model culverts as dissipaters to optimize the design of ring chambers that effectively reduce the outlet velocities of high-energy culverts by producing a hydraulic jump in the ring chamber. Experimental models showed model energy reduction up to 90 %. Thus, the ring chamber design that produces hydraulic jumps is most economical to construct and may be selected without limiting velocity-reducing capacity. R.H. Hotchkiss et al. [20] examined the jump geometry and effectiveness of each type of jump within the culvert barrel without the aid of tailwater for a horizontal apron with an end weir and a drop structure with an end weir to reduce the flow energy at the outlet. Experimental results showed that both simple alternatives are applicable to culverts with approach Froude number from 2.6 to 6.0 and are effective in reducing outlet velocity 0.21 to 2.59 m/s, and energy 6 % to 71 %. S. Song et al. [21] developed a theoretical model to quantify the effect of roughness on fully developed Stokes flow in the pipe. The investigated effects of periodically structured surface roughness upon flow field and pressure drop in a circular pipe show that the ratio of static flow resistivity and the ratio of the Darcy friction factor between rough and smooth pipes are expressed in four-order approximate formulations.

Even though energy dissipation in canals and culverts were studied over some past decades in several countries around the world; however, this topic is still limited in considering local characteristics of Vietnam. In this paper, thus, the main objective is to present the experimental results of the energy dissipation by producing staggered roughness elements of the two-dimensional bars of rectangular cross section at the end part of the box culverts. Box culverts with a relatively large slope ranging from 5 % to 13 % usually found in the midland and mountainous central regions of Vietnam were selected for the experiments and analysis.

2. Methods

The laboratory work consists of three main steps: setting up physical models, running different scenario models and calculating the hydraulic parameters.

2.1. Physical models setup

The first physical model was set up to determine the reasonable range of the roughness elements by placing a different number of roughness elements at the end part of the box culverts. The first physical model was carried out in a current flume 5.0 m long and 0.073 m wide of the Hydraulics – Hydrology Laboratory, University of Transport and Communications (UTC), Hanoi, Vietnam. The length from the flume end to the jack is 3.3 m. The flow meter is a Venturi tube mounted on the water supply pipe. The current flume system can change the slope as showed in Figure 1.

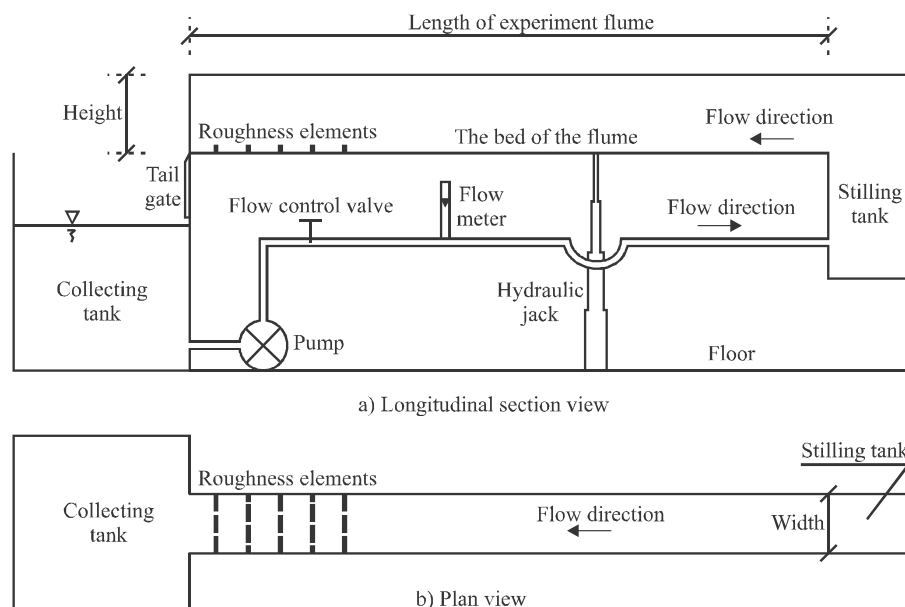


Figure 1. Schematic view of experimental setup of a flume with variable slope and jacking system (not in scale).

The second physical model was set up in order to determine the height of the roughness elements after choosing the arrangement of the first stage roughness elements. The second physical model was carried out in a current flume 7.5 m long and 0.28 m wide. Venturi tube mounted on the water supply pipe as shown in Figure 1. This current flume is located in Ho Chi Minh City Campus of UTC.

The main parameters of the experimental flume are shown in Table 1.

Table 1. Configuration details of the laboratory flume.

| Parameters | Symbols | Value | | Unit |
|---|------------|---------------|----------------|-------------------|
| | | Phase 1 (UTC) | Phase 2 (UTC2) | |
| Maximum flow rate | Q_{max} | 8 | 60 | m ³ /h |
| Hydraulic flume width | B | 73 | 275 | mm |
| Hydraulic flume length | L | 5000 | 7500 | mm |
| Maximum lifting height of hydraulic jack | h_{jack} | 120 | 350 | mm |
| Distance from hydraulic jack to tail gate | L_{jack} | 3300 | 6250 | mm |
| Flow rate observation | | Venturi meter | Venturi meter | |
| Water depth observation | | Pointer gauge | Pointer gauge | |

These models were constructed at a scale of 1:3.5 to 1:20.5 corresponding to the flow discharge per unit culvert width $q = 0.4 \div 2.8$ m³/s/m depending on the full-scale application.

In the first physical model, the experiments were conducted with and without roughness elements to examine the effect of roughness on reducing the flow kinetic energy. Two types of roughness element models were made.

- The first one consists of square shaped roughness elements with height and width of 10 mm with a space distance of 100 mm. These roughness elements are placed perpendicular to the flow (Figure 2).



Figure 2. Experimental image of first phase

- The second one consists of roughness elements with a gap as shown in detail in Figure 3, with a constant gap length of 0.5 mm; the length of rows of roughness elements with three gaps was 19 mm, while that for rows with two gaps was 21 mm.
- The number of roughness elements installed from the culvert end to upstream was 5, 10, 15, and 20 for both types of roughness elements.

The second physical model was conducted with two types of rectangular shaped roughness elements with and without gaps (Figure 3, Figure 4). The height of roughness elements was 15 mm, 20 mm, 25 mm, and 30 mm, respectively. The detailed structure of roughness elements with a gap is shown in

Table 3. The roughness elements were mounted on the rigid plate with a width of 0.275 m and a length of 2.4 m. The rigid plate slope can be changed by lifting one of its ends. There were five roughness elements installed in the downstream of the culvert.

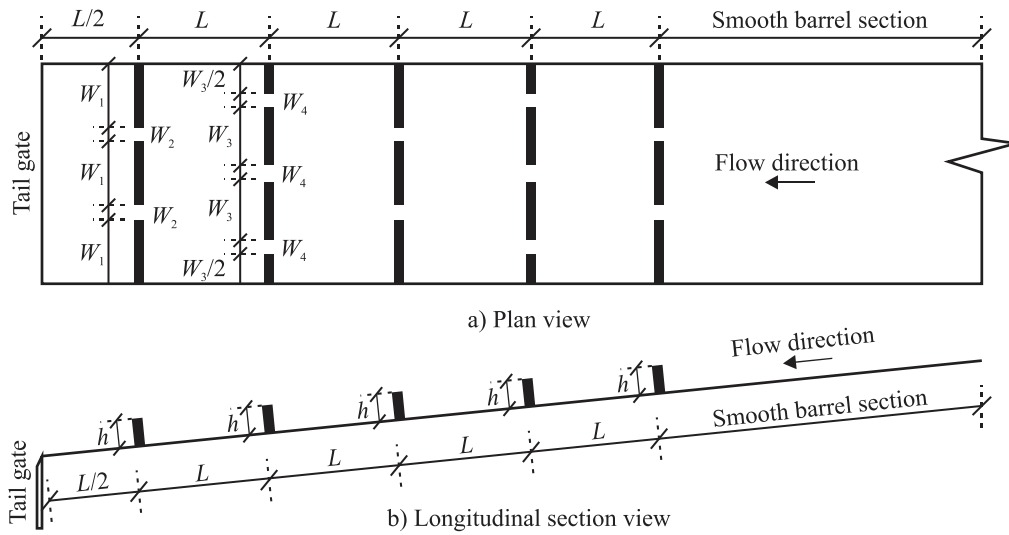


Figure 3. Staggered roughness elements used in the test (not in scale).

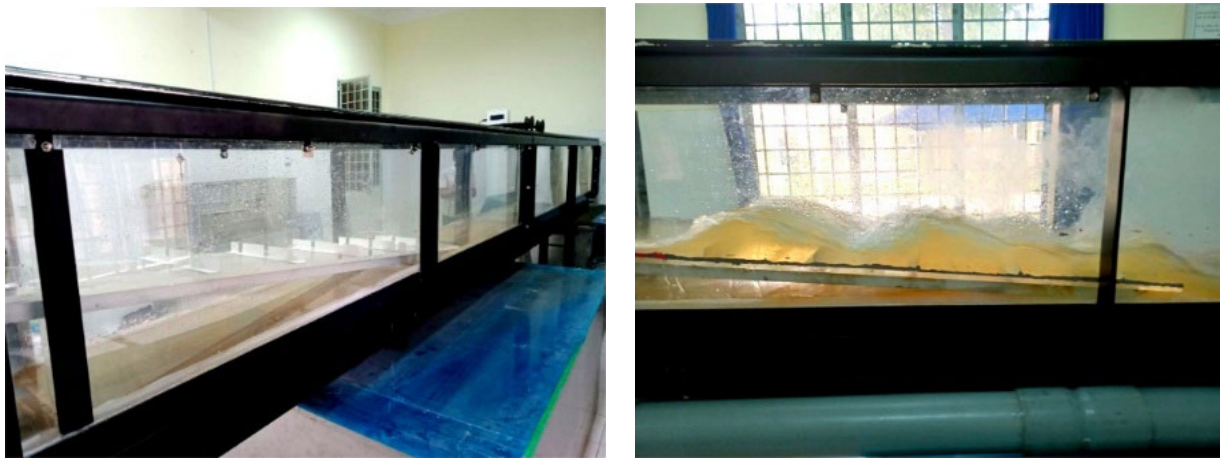


Figure 4. Experimental image of second phase.

Table 2. Dimensions of test roughness elements in phase 1.

| Parameter | Symbols | Unit | Value |
|-------------------------------------|---------|------|-------|
| Hydraulic flume width | B | mm | 73 |
| Roughness elements height | h | mm | 10 |
| Gap width | W_2 | mm | 5 |
| | W_1 | mm | 21 |
| Roughness elements width | W_3 | mm | 19 |
| | $W_3/2$ | mm | 9.5 |
| Distance between roughness elements | L | mm | 100 |

Table 3. Dimensions of test roughness elements in phase 2.

| Parameter | Symbols | Unit | Value | | | |
|--------------------------------|---------|------|---------|---------|---------|---------|
| Hydraulic flume width | B | mm | 275 | 275 | 275 | 275 |
| Roughness elements height | h | mm | 30 | 25 | 20 | 15 |
| Gap width | W_2 | mm | 15 | 12.5 | 10 | 7.5 |
| | W_1 | mm | 81.7 | 83.3 | 85.0 | 86.7 |
| Roughness elements width | W_3 | mm | 76.7 | 79.2 | 81.7 | 84.2 |
| | $W_3/2$ | mm | 38.3 | 39.6 | 40.8 | 42.1 |
| Distance of roughness elements | L | mm | 255÷300 | 213÷250 | 170÷200 | 128÷150 |

2.2. Experimental scenarios of the physical models

The first physical model was conducted with the constant maximum discharge of 6.83 m³/h (or 0.0019 m³/s) with four culvert slopes of 2 %, 3 %, 4 % and 5 %, and two types of roughness elements with and without gaps. The first physical model included 36 scenarios in total.

The second physical model were performed with the discharge of 59.65 m³/h (or 0.0166 m³/s), five culvert slopes of 5 %, 7 %, 9 %, 11 % and 13 %, and four types of roughness elements with and without gaps. The second physical model included 36 scenarios in total as well.

2.3. Calculation other hydraulic parameters

The Froude number was used in this study. It is known that the dominant forces in open channel problems are controlled by gravity, viscosity and other effects can be neglected, and the Froude's model law is applied. It means that the ratio of gravitational forces to inertial forces is the same in both physical models and prototypes to maintain dynamic similarity. The following hydraulic parameters are required to assess the effect of the roughness elements in box culverts:

- average observed flow depth (y) along the model was determined by N.D. Phong, H.T. Hai [22];
- the average velocity (V) is calculated from the continuity equation;
- the Froude number is a dimensionless parameter measuring the ratio of “ratio of the flow inertia to the external field” the inertial force divided by gravitational force. The Froude number can be expressed as:

$$Fr = V / (gy)^{0.5}, \quad (1)$$

where, Fr is the Froude number and V is average velocity (m/s).

- water column velocity is defined as follows:

$$h_v(m) = V^2 / (2g), \quad (2)$$

where, g is the gravity acceleration (m/s²).

- Specific energy

$$E_S(m) = y + h_v. \quad (3)$$

- Energy dissipation efficiency ΔE (%):

$$\Delta E = (E_{S1} - E_{S2}) / E_{S1} \cdot 100\%, \quad (4)$$

where, E_{S1} is the specific energy of a flow referred to the culvert bed without roughness elements; E_{S2} is the specific energy of a flow referred to the culvert bottom with roughness elements.

3. Results and Discussion

3.1. Hydraulic features

Based on the results of monitoring flow rate and flow depth at measurement points we calculated average flow rate, flow kinetic energy, the Froude number, velocity ratio, flow kinetic energy ratio with and without roughness elements. The experimental results and calculation of the average velocity, the Froude number, kinetic energy and flow energy at the outlet of the hydraulic flume are given in Table 4.

The results show that average depth reduced with the increasing of slope in all cases. In case of the presence of roughness elements with gaps the average depth reduced less than without gaps. The average velocity is proportional to slope and roughness elements with and without gap, and flow is supercritical ($Fr > 1$) at flow rate of 0.0019 m³/s with four flat bottom flume slopes ranging from 2 % to 5 %. The Froude number and velocity head increase in all cases of testing and are smaller in case of the roughness elements without gaps. The specific energy increase in case of no roughness elements and a decrease in cases of roughness elements the without gaps; there is a slight reduction in case of roughness elements with gaps.

Table 4. Experimental results and calculation of Froude number, kinetic energy and the flow

energy without roughness elements and with a different number of roughness elements.

| Slope (%) | No roughness elements | Number of roughness elements without gap | | | | Number of roughness elements with gap | | | |
|----------------------------|-----------------------|--|-------|-------|-------|---------------------------------------|-------|-------|-------|
| | | 20 | 15 | 10 | 5 | 20 | 15 | 10 | 5 |
| Average depth y (m) [20] | | | | | | | | | |
| 2 | 0.027 | 0.058 | 0.057 | 0.056 | 0.050 | 0.054 | 0.052 | 0.051 | 0.048 |
| 3 | 0.023 | 0.054 | 0.050 | 0.055 | 0.047 | 0.048 | 0.046 | 0.046 | 0.044 |
| 4 | 0.021 | 0.052 | 0.046 | 0.049 | 0.044 | 0.046 | 0.044 | 0.045 | 0.042 |
| 5 | 0.020 | 0.051 | 0.045 | 0.048 | 0.042 | 0.045 | 0.044 | 0.044 | 0.043 |
| Average velocity V (m/s) | | | | | | | | | |
| 2 | 0.975 | 0.452 | 0.458 | 0.467 | 0.523 | 0.484 | 0.499 | 0.506 | 0.545 |
| 3 | 1.118 | 0.481 | 0.525 | 0.476 | 0.559 | 0.540 | 0.563 | 0.564 | 0.594 |
| 4 | 1.219 | 0.498 | 0.563 | 0.529 | 0.598 | 0.563 | 0.592 | 0.580 | 0.619 |
| 5 | 1.300 | 0.510 | 0.578 | 0.542 | 0.619 | 0.578 | 0.591 | 0.591 | 0.605 |
| Froude number Fr | | | | | | | | | |
| 2 | 1.906 | 0.601 | 0.614 | 0.631 | 0.748 | 0.667 | 0.698 | 0.712 | 0.796 |
| 3 | 2.342 | 0.660 | 0.753 | 0.651 | 0.828 | 0.785 | 0.835 | 0.838 | 0.907 |
| 4 | 2.664 | 0.696 | 0.835 | 0.762 | 0.915 | 0.837 | 0.903 | 0.874 | 0.965 |
| 5 | 2.935 | 0.721 | 0.870 | 0.789 | 0.965 | 0.870 | 0.899 | 0.899 | 0.931 |
| Kinetic energy h_v (m) | | | | | | | | | |
| 2 | 0.048 | 0.010 | 0.011 | 0.011 | 0.014 | 0.012 | 0.013 | 0.013 | 0.015 |
| 3 | 0.064 | 0.012 | 0.014 | 0.012 | 0.016 | 0.015 | 0.016 | 0.016 | 0.018 |
| 4 | 0.076 | 0.013 | 0.016 | 0.014 | 0.018 | 0.016 | 0.018 | 0.017 | 0.020 |
| 5 | 0.086 | 0.013 | 0.017 | 0.015 | 0.020 | 0.017 | 0.018 | 0.018 | 0.019 |
| Specific energy E_S (m) | | | | | | | | | |
| 2 | 0.075 | 0.068 | 0.067 | 0.067 | 0.064 | 0.066 | 0.065 | 0.064 | 0.063 |
| 3 | 0.087 | 0.066 | 0.064 | 0.066 | 0.062 | 0.063 | 0.062 | 0.062 | 0.062 |
| 4 | 0.097 | 0.065 | 0.062 | 0.063 | 0.062 | 0.062 | 0.062 | 0.062 | 0.062 |
| 5 | 0.106 | 0.064 | 0.062 | 0.063 | 0.062 | 0.062 | 0.062 | 0.062 | 0.062 |

Calculation results of the reduction in flow energy with the presence of roughness elements are given in Table 5 and Figure 5, which show that the flow energy increases less with no gaps than with gaps and can be further reduced with more elements. The roughness elements with gaps show better energy reduction efficiency for slope culverts of 2 %, 3 %, however for the culverts on a larger slope of 4 %, 5 %, the energy reduction efficiency is almost the same.

Table 5. Flow energy reduction with different numbers of roughness elements.

| Slope (%) | Flow energy reduction ΔE (%) | | | | | | | |
|-----------|---|------|------|------|--|------|------|------|
| | Number of roughness elements without gaps (A) | | | | Number of roughness elements with gaps (B) | | | |
| | 20 | 15 | 10 | 5 | 20 | 15 | 10 | 5 |
| 2 | 9.6 | 10.2 | 11.1 | 15.2 | 12.6 | 13.7 | 14.2 | 16.3 |
| 3 | 24.3 | 26.9 | 24.0 | 28.2 | 27.6 | 28.3 | 28.4 | 29.0 |
| 4 | 33.2 | 35.8 | 34.7 | 36.4 | 35.8 | 36.3 | 36.1 | 36.6 |
| 5 | 39.5 | 41.6 | 40.7 | 42.0 | 41.6 | 41.8 | 41.8 | 41.9 |
| Mean | 26.6 | 28.6 | 27.6 | 30.5 | 29.4 | 30.1 | 30.1 | 31.0 |

Table 6. Velocity reduction with different numbers of roughness elements.

| Slope (%) | Percent velocity reduction (%) | | | | | | | |
|-----------|---|------|------|------|--|------|------|------|
| | Number of roughness elements without gaps (A) | | | | Number of roughness elements with gaps (B) | | | |
| | 20 | 15 | 10 | 5 | 20 | 15 | 10 | 5 |
| 2 | 53.7 | 53.0 | 52.1 | 46.4 | 50.4 | 48.8 | 48.1 | 44.2 |
| 3 | 57.0 | 53.1 | 57.4 | 50.0 | 51.7 | 49.7 | 49.6 | 46.9 |
| 4 | 59.1 | 53.8 | 56.6 | 51.0 | 53.8 | 51.4 | 52.4 | 49.2 |
| 5 | 60.8 | 55.6 | 58.3 | 52.4 | 55.6 | 54.5 | 54.5 | 53.5 |
| Mean | 57.6 | 53.9 | 56.1 | 49.9 | 52.9 | 51.1 | 51.2 | 48.4 |

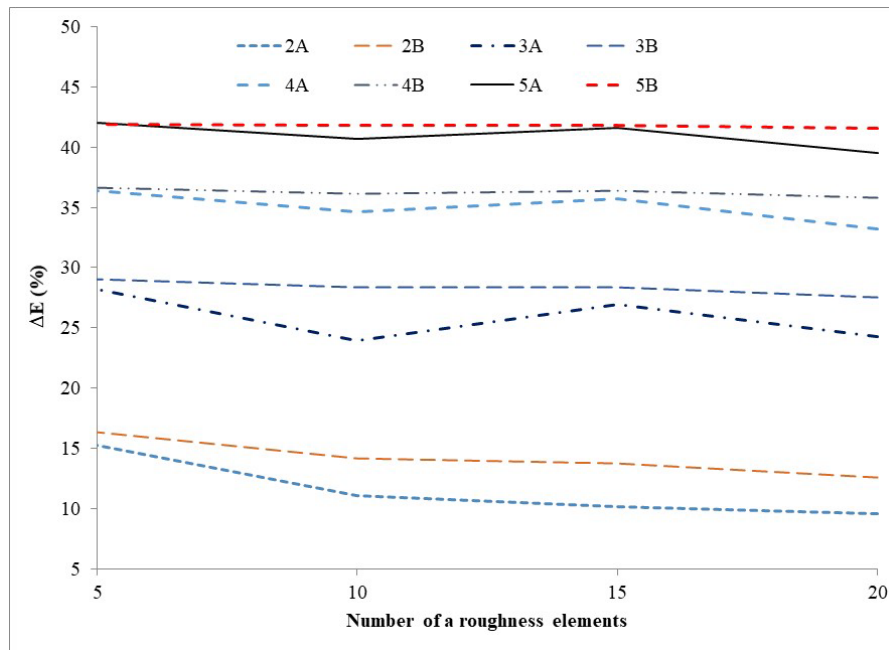


Figure 5. Effect of different roughness elements number on the decrease of specific energy 2, 3, 4, 5 – slopes of test flume (A – roughness elements without gaps and B – roughness elements with gaps).

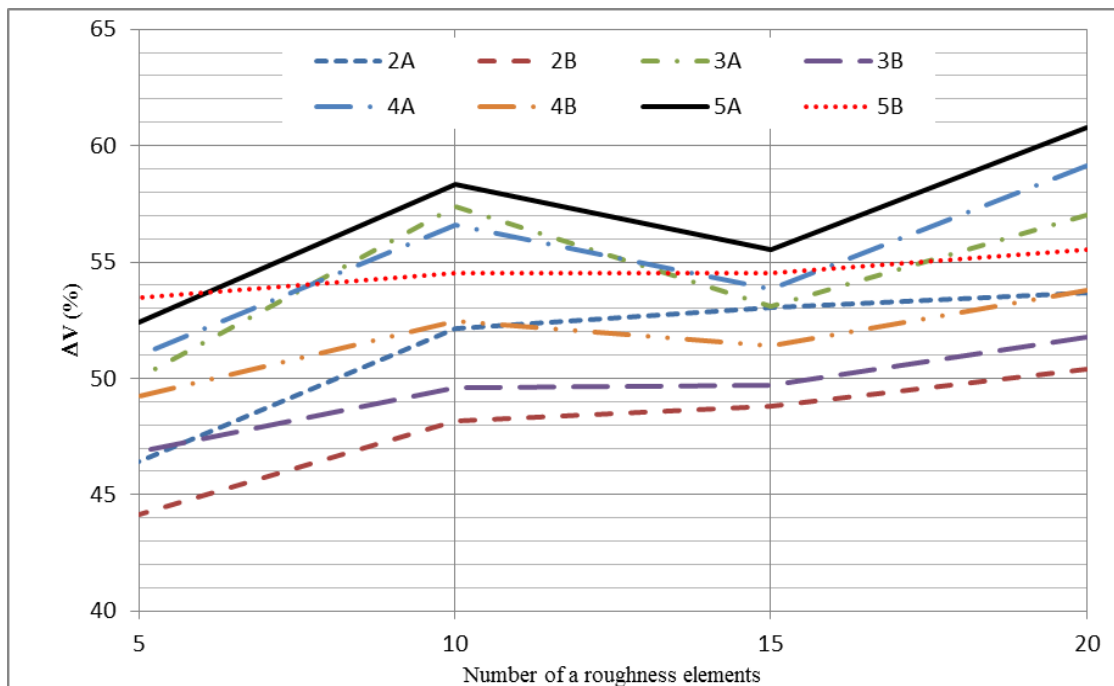


Figure 6. Effect of different roughness elements number on the decrease of velocity 2, 3, 4, 5 – slopes of test flume (A – roughness elements without gaps and B – roughness elements with gaps).

The flow energy in case of roughness elements present decreased compared to the case without a roughness element: the greater the slope, the greater the energy reduction. However, for the case of small slope (2 %), the energy reduction was not significant because of 16.3 % maximum reduction with five roughness elements with gaps. Thus, it can be seen that the roughness elements are suitable for slope culverts of 5 %; the energy reduction in this case is about 40 %.

In case of roughness elements without gaps, the velocity reduction decreased from 57.65 % to 39.93 % on average when the number of roughness elements decreased from 20 to 5, respectively. Similarly, in case of roughness elements with gaps, the velocity reduction decreased from 52.87 % to 48.43 % on average. These velocity reductions are larger than research results carried out by J. Wiggert, P. Erfle [23] (for the channel slope of 4.3 %, the average velocity reduction was 42.43 % and maximum 50.4 %).

The velocity reduction was proportional to the channel slope. For roughness elements with gaps, the velocity reduction increased from 44.14 % (for the number of roughness element of 5) to 55.56 % (for the number of roughness element of 20) on average when the channel slope rose from 2 % to 5 %, respectively. For roughness elements without gaps, the velocity reduction increased from 46.4 % (for the number of roughness element of 5) to 60.78 % (for the number of roughness element of 20) on average when the channel slope rose from 2% to 5 %.

In case of a larger number of roughness elements, the velocity decreased but the energy reduction efficiency almost remained the same and even decreases in some experiments. In general, it seemed that using more than five roughness elements at the end part of the culvert is disadvantageous as mentioned in P.L. Thompson, R.T. Kilgore [24].

From results of this research as well as previous researches on roughness elements, the row number of roughness elements arranged at the end of box culvert is recommended to be five. Five rows of roughness elements provide cyclical uniform flow pattern at the end of culvert, which maximizes the energy dissipation effect.

3.2. Affection of the roughness element heights

The average velocity, the Froude number, kinetic energy and flow energy at the outlet of the test flume are given in Table 7, based on the results of the second physical model and calculation. The average depth decreased in all experiments. The heights of the roughness elements with gaps resulted in a smaller average depth than without roughness elements, and it is also smaller than the case where the roughness element has no gap. The average velocity increased with the increasing of slope and without roughness elements. The average velocity, the Froude number, velocity head and specific energy increased with height of roughness elements higher than 30 mm and decreased in remaining heights.

Table 7. Experimental results and calculation of the Froude number, kinetic energy and flow energy in case of no roughness elements and with roughness elements of different heights

| Slope (%) | No roughness elements | Roughness elements height without gaps | | | | Roughness elements height with gaps | | | |
|----------------------------|-----------------------|--|-------|-------|-------|-------------------------------------|-------|-------|-------|
| | | 30 mm | 25 mm | 20 mm | 15 mm | 30 mm | 25 mm | 20 mm | 15 mm |
| Average depth y (m) | | | | | | | | | |
| 5 | 0.039 | 0.103 | 0.092 | 0.089 | 0.069 | 0.103 | 0.087 | 0.083 | 0.071 |
| 7 | 0.030 | 0.108 | 0.093 | 0.084 | 0.069 | 0.081 | 0.086 | 0.079 | 0.068 |
| 9 | 0.028 | 0.103 | 0.101 | 0.084 | 0.081 | 0.088 | 0.091 | 0.072 | 0.061 |
| 11 | 0.026 | 0.101 | 0.112 | 0.097 | 0.081 | 0.076 | 0.103 | 0.102 | 0.079 |
| 13 | 0.026 | 0.098 | 0.106 | 0.104 | 0.110 | 0.076 | 0.097 | 0.089 | 0.085 |
| Average velocity V (m/s) | | | | | | | | | |
| 5 | 1.532 | 0.572 | 0.643 | 0.665 | 0.864 | 0.577 | 0.677 | 0.713 | 0.829 |
| 7 | 2.006 | 0.548 | 0.638 | 0.707 | 0.858 | 0.731 | 0.686 | 0.751 | 0.865 |
| 9 | 2.086 | 0.575 | 0.584 | 0.707 | 0.728 | 0.671 | 0.652 | 0.826 | 0.970 |
| 11 | 2.309 | 0.586 | 0.527 | 0.608 | 0.728 | 0.781 | 0.575 | 0.580 | 0.745 |
| 13 | 2.276 | 0.605 | 0.561 | 0.568 | 0.538 | 0.783 | 0.612 | 0.663 | 0.693 |
| Froude number Fr | | | | | | | | | |
| 5 | 2.489 | 0.568 | 0.677 | 0.712 | 1.054 | 0.575 | 0.731 | 0.790 | 0.990 |
| 7 | 3.729 | 0.532 | 0.669 | 0.780 | 1.042 | 0.820 | 0.746 | 0.854 | 1.056 |
| 9 | 3.953 | 0.572 | 0.586 | 0.780 | 0.815 | 0.721 | 0.691 | 0.986 | 1.254 |
| 11 | 4.606 | 0.589 | 0.502 | 0.622 | 0.815 | 0.905 | 0.572 | 0.580 | 0.844 |

| Slope (%) | No roughness elements | Roughness elements height without gaps | | | | Roughness elements height with gaps | | | |
|---------------------------|-----------------------|--|-------|-------|-------|-------------------------------------|-------|-------|-------|
| | | 30 mm | 25 mm | 20 mm | 15 mm | 30 mm | 25 mm | 20 mm | 15 mm |
| 13 | 4.507 | 0.618 | 0.551 | 0.561 | 0.518 | 0.909 | 0.628 | 0.709 | 0.758 |
| Kinetic energy h_v (m) | | | | | | | | | |
| 5 | 0.120 | 0.017 | 0.021 | 0.023 | 0.038 | 0.017 | 0.023 | 0.026 | 0.035 |
| 7 | 0.205 | 0.015 | 0.021 | 0.025 | 0.037 | 0.027 | 0.024 | 0.029 | 0.038 |
| 9 | 0.222 | 0.017 | 0.017 | 0.025 | 0.027 | 0.023 | 0.022 | 0.035 | 0.048 |
| 11 | 0.272 | 0.017 | 0.014 | 0.019 | 0.027 | 0.031 | 0.017 | 0.017 | 0.028 |
| 13 | 0.264 | 0.019 | 0.016 | 0.016 | 0.015 | 0.031 | 0.019 | 0.022 | 0.025 |
| Specific energy E_s (m) | | | | | | | | | |
| 5 | 0.158 | 0.120 | 0.113 | 0.112 | 0.107 | 0.120 | 0.111 | 0.109 | 0.106 |
| 7 | 0.235 | 0.123 | 0.113 | 0.109 | 0.106 | 0.108 | 0.110 | 0.108 | 0.107 |
| 9 | 0.250 | 0.120 | 0.119 | 0.109 | 0.108 | 0.111 | 0.112 | 0.106 | 0.109 |
| 11 | 0.297 | 0.118 | 0.126 | 0.116 | 0.108 | 0.107 | 0.120 | 0.119 | 0.108 |
| 13 | 0.290 | 0.116 | 0.122 | 0.121 | 0.125 | 0.107 | 0.116 | 0.112 | 0.110 |

Calculation results of the reduction in flow energy due to roughness elements are given in Table 8 and Figure 7.

The experimental results showed that the flow was supercritical ($Fr > 1$) at the flow rate of $0.0166 \text{ m}^3/\text{s}$ with different flume slopes in this study. Some experimental results of the roughness elements showed an area of 15 mm high ($h/B = 15/275 = 0.055$) in supercritical flow ($Fr > 1$). With the small roughness elements height ($h/B \leq 0.055$), there seemed to be no advantage of energy dissipation efficiency, however, the effect of velocity reductions is relatively high.

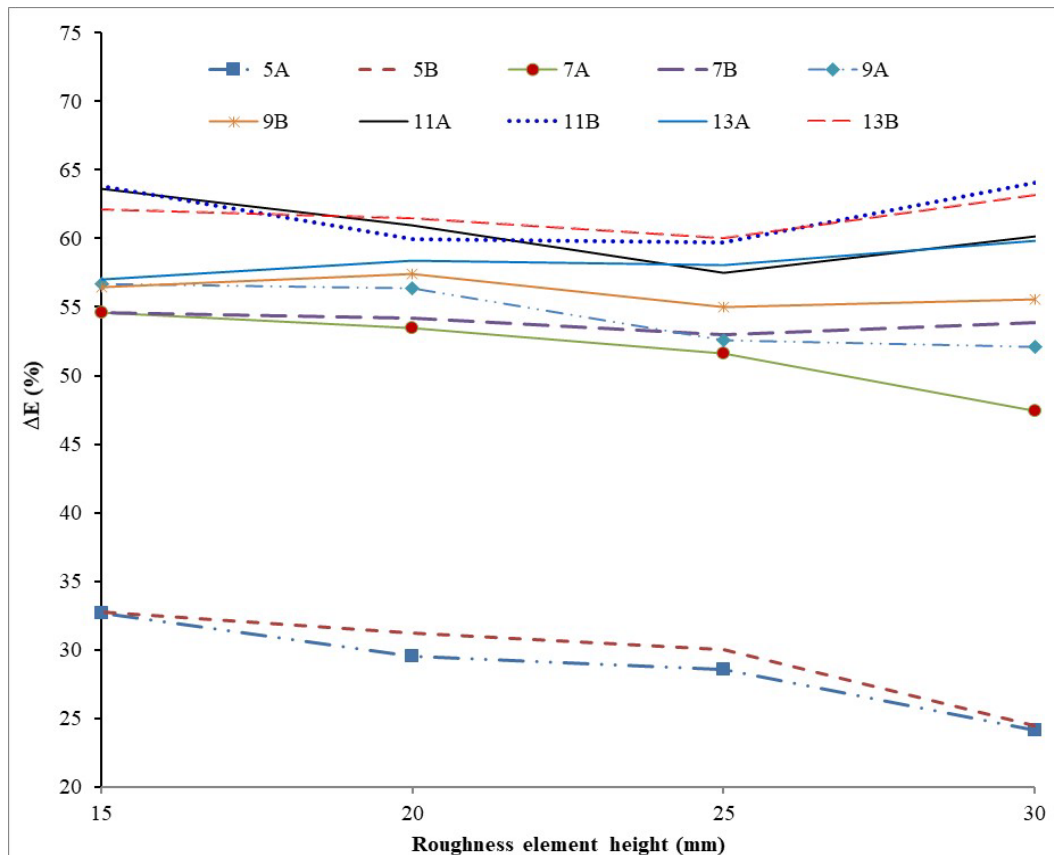


Figure 7. Effect of different roughness elements height on the variation of the percent of specific energy. 5, 7, 9, 11, 13 – slopes of test flume (A – roughness elements without gaps and B – roughness elements with gaps).

The energy dissipation efficiency was relatively small for a slope of 5 %, compared to the higher slopes (28.7 % with gapless roughness elements and 29.6 % with gap roughness elements). At the same time, there is a power dissipation efficiency of up to 50 % for slopes above 5 % (except dissipation efficiency of 47.4 % with the gapless roughness elements 30 mm high on a slope of 7 %). Similarly, the velocity reduction for the channel slope of 5 % is also relatively small compared to the case of steeper slopes.

The roughness elements with gaps gain a greater effective dissipation efficiency, averaging 58.4 % and 56.3 % compared with gapless abutments. The energy dissipation in models with roughness elements varied from $h/B = 20/275 = 0.073$ to $h/B = 30/275 = 0.109$ ($h/B \approx 0.1$). The energy dissipation efficiency is almost unchanged: for example, in case of roughness elements with gaps on a slope of 11 %, the average power dissipation efficiency is 61.2 % while the smallest efficiency is 59.7 % and the maximum energy dissipation efficiency is 64.1 %. The energy dissipation efficiency in this study is equivalent to the research results carried by Nghi, Yen [25]. According to Nghi, Yen [25] the energy reduction in chute flow using roughness elements was average of 60.75 %, and maximum of 64 %.

Similar to the energy dissipation efficiency, the velocity reduction did not change much (from 67.2 % to 71.2 % for roughness elements without gaps and from 64.4 % to 67.7 % for roughness elements with gaps) in case of roughness elements heights from $h/B = 20/275 = 0.073$ to $h/B = 30/275 = 0.109$ ($h/B \approx 0.1$). This velocity reduction is relatively consistent with the research on circular culverts using roughness elements carried by J.M. Wiggert and P.D. Erfle [12] (maximum velocity reduction of 68 % when $Fr = 7$).

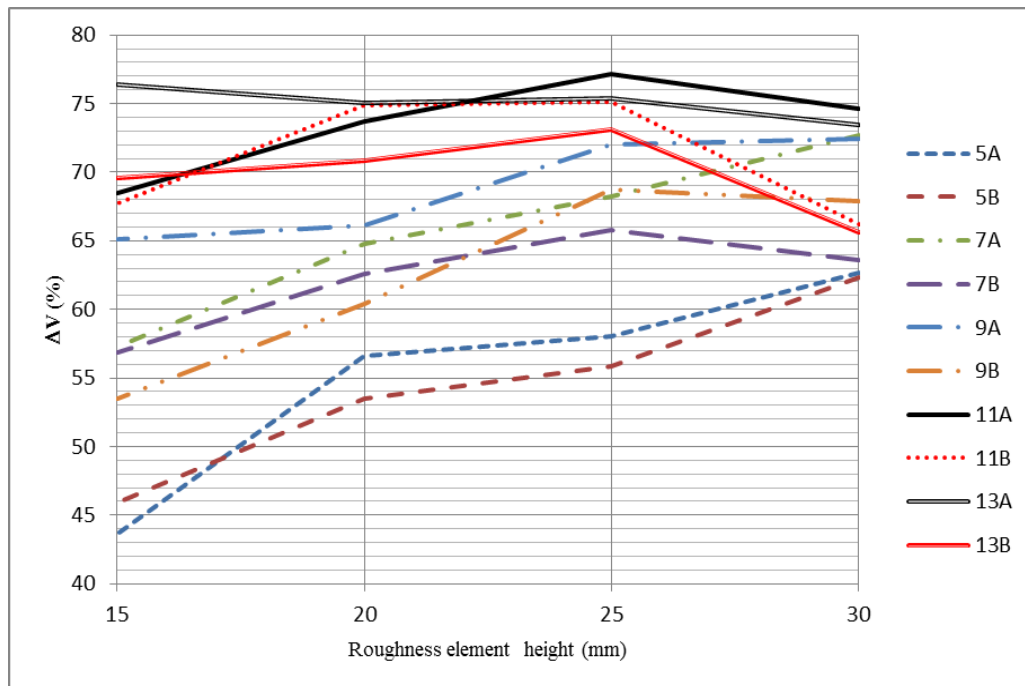


Figure 8. Effect of different roughness elements height on the variation of the percent of velocity. 5, 7, 9, 11, 13 – slopes of test flume (A – roughness elements without gaps and B – roughness elements with gaps).

Table 8. Percent of flow energy reduction with the different heights of roughness elements.

| Slope (%) | Reduction of specific energy (m) | | | | | | | |
|-----------|--|-------|-------|-------|---|-------|-------|-------|
| | Roughness elements height without gaps (A) | | | | Roughness elements height with gaps (B) | | | |
| | 30 mm | 25 mm | 20 mm | 15 mm | 30 mm | 25 mm | 20 mm | 15 mm |
| 5 | 24.1 | 28.5 | 29.5 | 32.7 | 24.5 | 30.0 | 31.2 | 32.8 |
| 7 | 47.4 | 51.6 | 53.5 | 54.6 | 53.9 | 53.0 | 54.2 | 54.6 |
| 9 | 52.1 | 52.5 | 56.3 | 56.7 | 55.5 | 55.0 | 57.4 | 56.4 |
| 11 | 60.2 | 57.5 | 60.9 | 63.6 | 64.1 | 59.7 | 59.9 | 63.8 |
| 13 | 59.8 | 58.1 | 58.4 | 57.0 | 63.2 | 60.1 | 61.5 | 62.1 |
| Mean | 48.7 | 49.7 | 51.7 | 52.9 | 52.2 | 51.6 | 52.8 | 53.9 |

Table 9. Percent of velocity reduction with the different heights of roughness elements.

| Slope (%) | Percent velocity reduction (%) | | | | | | | |
|-----------|---|------|------|------|--|------|------|------|
| | Roughness elements height without gap (A) | | | | Roughness elements height with gap (B) | | | |
| | 30 | 25 | 20 | 15 | 30 | 25 | 20 | 15 |
| 5 | 62.6 | 58.0 | 56.6 | 43.6 | 62.4 | 55.8 | 53.5 | 45.9 |
| 7 | 72.7 | 68.2 | 64.8 | 57.2 | 63.6 | 65.8 | 62.6 | 56.9 |
| 9 | 72.5 | 72.0 | 66.1 | 65.1 | 67.8 | 68.8 | 60.4 | 53.5 |
| 11 | 74.6 | 77.2 | 73.7 | 68.5 | 66.2 | 75.1 | 74.9 | 67.7 |
| 13 | 73.4 | 75.4 | 75.1 | 76.4 | 65.6 | 73.1 | 70.9 | 69.5 |
| Mean | 71.2 | 70.1 | 67.2 | 62.2 | 65.1 | 67.7 | 64.4 | 58.7 |

4. Conclusions

The impact of roughness elements on reducing flow velocity at outlets of box culverts considering the local characteristics of Vietnam was assessed in this study. Based on the experimental results, the following conclusions can be drawn:

1. The energy dissipation efficiency increases along with the increase in the number of roughness elements, but insignificantly. Therefore, five roughness elements are recommended to install at the end of the box culverts to ensure a relatively uniform cyclic flow pattern there.
2. Arrangement of roughness elements with staggered clearance at the end part of the sloping box culvert instead of gapless roughness elements provides greater energy dissipation efficiency; and at the same time, roughness elements with gaps contribute to passing of the sediment and reduce the deposition in drainage.
3. Roughness elements with gaps with a height of about 0.1 times the width of the culvert should be employed because with this height, the advantage of energy dissipation efficiency exceeds 50 %. If roughness elements height was small ($h/B < 0.055$), there seemed to be no advantage of energy efficiency; if the roughness elements height was great, the power dissipation efficiency increased insignificantly, which causes more difficulties in construction and maintenance.
4. The results of this study are most suitable for box culverts with slopes from 5 % to 13%. When the culvert slope is larger, the same structure can be considered.

References

1. Jungerius, P., Matundura, J., Van De Ancker, J. Road construction and gully erosion in West Pokot, Kenya. *Earth Surface Processes and Landforms*. 2002. 27(11). Pp. 1237–1247.
2. Galia, T., Šilhán, K., Škarpich, V. The geomorphic impacts of culverts at paved forest roads: Examples from Carpathian headwater channels, Czech Republic. 2017. *Catena*. 157. Pp. 424–435.
3. Johnson, P.A. Incorporating road crossings into stream and river restoration projects. *Ecological Restoration*. 2002. 20(4). Pp. 270–277.
4. Yousefi, F., Mozaffari, J., Movahed, S. Developing a hydraulic jump length model on horizontal rough beds. *Journal of the South African Institution Of Civil Engineering*. 2019. 61(3). Pp. 2–6.
5. George, J., Simone, A., Iaccarino, G., Jiménez, J. Modeling roughness effects in turbulent boundary layers by elliptic relaxation. *Proceedings of the Summer Program*. 2010. Pp. 119–128.
6. Dilrooban, Y., Pathirana, K., Sujana, K., Imasalan, K. Effect of bed roughness on submerged hydraulic jumps. *Engineer*. 2014. 27(04). Pp. 33–39.
7. Fošumpaur, P., Kašpar, T., Králík, M., Zúkal, M. Study of boundary conditions for design of new types of fibre concrete energy dissipators in hydraulic structures. *IOP Conference Series: Materials Science and Engineering*. 2019. 596(1). 012031. DOI: 10.1088/1757-899X/596/1/012031
8. Peterson, D.F., Mohanty, P.K. Flume Studies of Flow in Steep Rough Channels. *ASCE Hydraulics Journal*. 1960. DOI: 10.1061/jyceaj.0000543
9. Morris, H.M. Hydraulics of energy dissipation in steep, rough channels. 1968. Bull. no. 19. Research Division, Virginia Polytechnic Institute, Blacksburg, Virginia, USA. 108 p.
10. Morris, H.M. Design of Roughness Elements for Energy Dissipation in Highway Drainage Chutes. *Highway Research*. 1969. 261. Pp. 79–86.
11. Mohanty, P.K. The Dynamics of Turbulent Flow in Steep, Rough, Open Channels. Ph.D. Dissertation, Utah State University, Logan, Utah, 1959.
12. Wiggert, J.M., Erfle, P.D. Roughness Elements as Energy Dissipators of Free Surface Flow in Circular Pipes. *Highway Research Record*. 1971. 373. Pp. 64–73.
13. Pagliara, S., Roshni, T., Palermo, M. Energy dissipation over large-scale roughness for both transition and uniform flow conditions. *International Journal of Civil Engineering. Transaction A: Civil Engineering*. 2015. 13(3). Pp. 341–346.
14. Arpan, A.D., Naveen, S., Avinash, D.V., Aniruddha, D.G. Effect of roughness on sequent depth in hydraulic jumps over rough bed. *Journal of the Croatian Association of Civil Engineers*. 2019. 71(2). Pp. 105–111.

15. André, S., Boillat, J., Schleiss, A., Matos, J. Energy dissipation and hydrodynamic forces of aerated flow over macro-roughness linings for overtopped embankment dams. Proceedings of the Int. Conference on Hydraulics of Dams & River Structures. Balkema, Rotterdam, Netherlands, 2004. Pp. 189–196.
16. André, S., Boillat, J.-L., Schleiss, A. Efficient surface protection by macro-roughness linings for overtopped embankment dams. Dam Maintenance and Rehabilitation. 2002. 369. Pp. 407–416.
17. André, S., Schleiss, A. High velocity aerated flows on stepped chutes with macro-roughness elements. 2004.
18. Gonzalez, C.A., Chanson, H. Hydraulic design of stepped spillways and downstream energy dissipators for embankment dams. Dam Engineering. 2007. 17(4). Pp. 223–244.
19. Simon, A., Sarikelle, S., Korom, S. Internal Energy Dissipators for Culverts on Steep Slopes with Inlet Control. Transportation Research Record. 1987. 1151. Pp. 26–31.
20. Hotchkiss, R.H., Larson, E.A., Admiraal, D.M. Energy Dissipation in Culverts by Forced Hydraulic Jump Within a Barrel. 2005. Transportation Research Record, Transportation Research Board. 2005. 1904(1). Pp. 124–132. DOI: 10.1177/0361198105190400113
21. Song, S., Yang, X., Xin, F., Lu, T.J. Modeling of surface roughness effects on Stokes flow in circular pipes. Physics of Fluids. 2018. 30(2). 023604.
22. Phong, N.D., Hai, H.T. Research on the efficiency of energy reduction in box culverts on roads by roughness elements. XXII Science and Technology Conference, University of Transport and Communications, Hanoi, Vietnam, University of Transport and Communications, 2020.
23. Wiggert, J., Erfle, P. Culvert velocity reduction by internal energy dissipators. Concrete Pipe News. 1972. 24(5). Pp. 87–94.
24. Thompson, P.L., Kilgore, R.T. Hydraulic Design of Energy Dissipators for Culverts and Channels: Hydraulic Engineering Circular Number 14. 3rd edition. 2006. National Highway Institute (US), 2006. 287 p.
25. Nghi, L.V., Yên, Đ.T.M. Hiệu quả tiêu hao năng lượng dọc đường của giải pháp nhám gia cường trên dốc nước [Energy dissipation efficiency of roughness elements on chute flow]. Journal of Water Resources Science and Technology. 2013. 16(8). Pp. 17-24. (Vietnamese)

Information about authors:

Dang Phong Nguyen, PhD

E-mail: phongnd@utc.edu.vn

Nam Binh Hoang, PhD

E-mail: binhnhn@utc.edu.vn

Huy Thiep Tran,

E-mail: thiepth_ph@utc.edu.vn

Prakash Indra,

E-mail: indra52prakash@gmail.com

Binh Thai Pham,

E-mail: binhpt@utt.edu.vn

Received 31.10.2022. Approved after reviewing 18.12.2023. Accepted 01.01.2024.



Research article

UDC 624

DOI: 10.34910/MCE.125.4



Utilizing seismic techniques and dynamic field tests for soil dynamic response prediction in clay soils

A.M. Al-Kinani¹ ✉, J.K. Thajeel¹, M.H. Al-Umar¹, M.Y. Fattah²

¹ Department of Civil Engineering, University of Thi-Qar, Thi-Qar, Iraq

² Department of Civil Engineering, University of Technology-Baghdad, Iraq

✉ ali-majid@utq.edu.iq

Keywords: shear wave velocity, SPT N-value, geophysical measurement, GIS

Abstract. When evaluating the dynamic response of soil, shear modulus is an essential parameter to consider. In most cases, the shear modulus is estimated using the shear wave velocity (V_s) of the soil as observed in field geophysical testing. Consequently, shear modulus is the main parameter for geotechnical earthquake engineering problems, both quantitatively and qualitatively. Its measuring must be done meticulously. In many cases, however, the shear wave velocity may be predicted using field dynamic tests such as the Standard Penetration Test (SPT) N-value of soil when direct measurements of V_s are unavailable. There are various empirical formulae that associate soil type and SPT N-value to predict the shear wave velocity. On the other hand, all of these equations are based on several field observations related to specific places and geology. In this paper, different approaches for estimating the actual shear wave velocity measurements from SPT data were clarified and compared. The data of 59 boreholes in Al Nasiriya's soil investigation were used. The standard penetration test data computations were applied. The current study investigated and possessed shear wave velocity based on SPT N-values using the Excel application, then represented it in the Geographical Information System (GIS) and compared it with geophysical exploration. The SPT- V_s correlation generated for Al Nasiriya, Iraq, demonstrated a better degree of fitness for the dataset. There was also a suggestion for a site-specific SPT- V_s connection. On the other hand, most of the SPT- V_s expressions evaluations indicated a valuable predictive ability.

Citation: Al-Kinani, A.M., Thajeel, J.K., Al-Umar, M.H., Fattah, M.Y. Utilizing seismic techniques and dynamic field tests for soil dynamic response prediction in clay soils. Magazine of Civil Engineering. 2024. 17(1). Article no. 12504. DOI: 10.34910/MCE.125.4

Acknowledgment: The authors would like to express their sincere gratitude to the University of Thi-Qar/College of Engineering, Engineering Consulting Bureau for providing the data essential to conduct the results of the study and to the International Conference on Geotechnical Engineering and Energetic-Iraq.

1. Introduction

Native soil strongly affects the amplification of seismic waves produced by earthquakes. Many earthquakes have confirmed this reality throughout the last century. Ground response calculations that solely include upward propagating shear waves are commonly used to estimate the ground motion parameters at the surface. The shear wave velocity (V_s) is one of the most essential input factors in these assessments for representing the stiffness of native soil layers. In comparison to the other in situ approaches, measuring shear wave velocity in the field is preferable. However, due to space limitations and the high noise levels associated with these tests, it is frequently not economically feasible to conduct the shear wave velocity measurement in all circumstances, especially in civil areas. In geotechnical engineering, the standard penetration test (SPT) is connected to a number of soil design parameters. The shear wave (V_s) must therefore be determined indirectly, such as via the SPT test [1]. Theoretically, there

is no connection between destructive processes (such as SPT) and non-destructive ones (e.g., seismic methods). As a result, numerous studies have been conducted to assess the geotechnical characteristics of the soil and to discover empirical correlations between SPT N and Vs qualities. Numerous researchers have suggested an experimental relation between SPT N and Vs since 1970 even now. Hossain et al. [2], explained that the number of borehole data sets required to determine shear wave velocity is important. The regression curves would be more accurate if there were additional borehole datasets. Some coefficients were decreased due to a lack of data, the number of equations utilized, and other causes. The regression equation generated by calculating Vs from SPT blow count provides a viable alternative to real field data that may be utilized for preliminary seismic microzonation and seismic site response for the research region [2]. According to Hasan et al. [3], a new formulation of the equation between Vs and N has been presented, and it is able to accurately forecast the values of Vs. The proposed equation was put to the test again using a sizable dataset in Erbil city to see how well it predicts the future [3]. Additionally, various correlations were formed on the zones of a region and presented for specific ranges of Vs. A chronological overview of the numerical link between SPT N and shear waves was reported by Jafari et al. [4]. For all soil types, with the exception of gravel, Hasancebi and Ulusay [5] investigated similar numerical correlations and superior empirical relationships using 97 data sets obtained from a location in the north-western region of Turkey. The experience connection was defined as upper and lower boundaries rather than an average curve for computing seismic velocities and relative density by researchers in Turkey using 327 samples collected from various places. In order to estimate seismic velocities and relative density, Ulugergerli and Uyank [6] used 327 samples gathered from various regions of Turkey to study statistical correlations. They described the experience correlation as lower and upper bounds rather than a single average curve. According to Eq. (1), 200 data pairs of the shear wave velocity (Vs) and SPT N collected at 50 Chennai locations, largely made up of very soft to highly stiff clay and very loose to dense sand, showed a correlation between each other [7]:

$$V_s = 95.64 \cdot N^{0.301} \quad (1)$$

In-situ tests in Greece were used to estimate the shear wave velocity using empirical data. Soil type appears to play a significant role in these connections, as different patterns were detected for different soil groups. Clays and marls have Vs-values up to 25 per cent greater than sandy soils, while soft and loose soils (N_{60}) have Vs-values up to 30 per cent higher than sandy soils. Using a corrected final blow count ($(NI)_{60}$) may have caused the low R²-values, which may have overemphasized the overburden issue (CN) [8]. For the appropriate design, construction, and operation of all sorts of geotechnical projects, including foundations, earth dams, embankments, excavation, and seismic hazards, geotechnical subsurface knowledge is necessary. GIS-based maps and contour maps can be used to represent geotechnical subsurface information, such as soil N value, soil classification, and water table. For assessing geotechnical earthquake engineering challenges, including site-specific amplification factor and ground reaction analysis, SPT N-value and shear wave velocity are crucial input factors. The most popular method for obtaining shear wave velocity (Vs) data is borehole logging, but it is expensive and challenging to drill and log to the depths needed for seismic ground motion research [9]. Even though GIS-based maps have many limitations, foundation designers will find them helpful in both static and seismic circumstances during the early stage of site selection. Subsurface investigations are less common in low-cost home complexes, but they can be used in those as well [10]. A collection of Thematic Maps for the soil variation in Bearing Capacity was developed Using SPTs and MATLAB for the important Iraqi city of Al-Basrah. Drilling 135 boreholes down 10 meters below the surface of the ground as part of the soil survey. The first-order polynomial was the most effective among the other trials despite the fact that several-order interpolation polynomials were utilized to calculate the bearing capacity of the soil. The reason for this is that it is simple and has quick calculations [11]. The development of thematic maps illustrates how driven pile-bearing capacities vary over the whole Al-Basrah Governorate with respect to various depths. The outcomes of the statistical equations demonstrated that the results and those obtained from the SPT data are in good agreement [12].

Also, for each of the models that were tried, the Root Mean Squared Error (RMSE) was essentially the same.

The objective of this study is determination of the SPT N-values and Vs empirical correlations for Thi-Qar regime in Iraq. Cross-hole experiments were carried out at four places in Thi-Qar to generate the shear wave velocity profiles. Geotechnical boreholes were used to verify the data. The statistical analysis of the data was conducted. To take into account soil type, a set of empirical relationships for forecasting shear-wave velocity from SPT N were created.

2. Methods

2.1. Site Geology and Seismicity of The Studied Area

Specifically, this research focuses on the southern Iraqi city of Nasiriya, the administrative headquarters of Thi-Qar Province. Nasiriya is an oil city producing conventional oil. The Mesopotamian sediments that cover the city's foundation include flood plain deposits, fluvial deposits, marsh deposits, and Aeolian deposits, as seen in Fig. 1 [13].

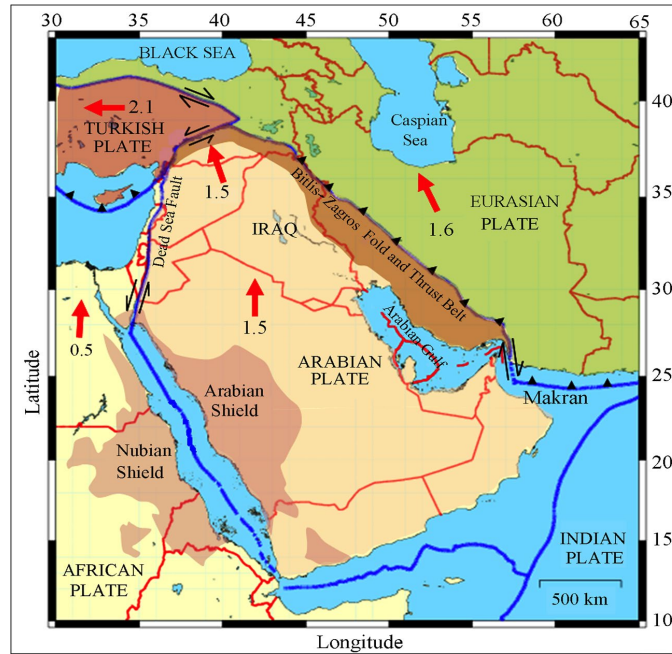


Figure 1. Tectonic setting of Iraq and environs [14].

The area of study represents selected 59 boreholes from Al-Nasiriyah metropolis dispensed on each side of the Euphrates River, as shown in Fig. 2.

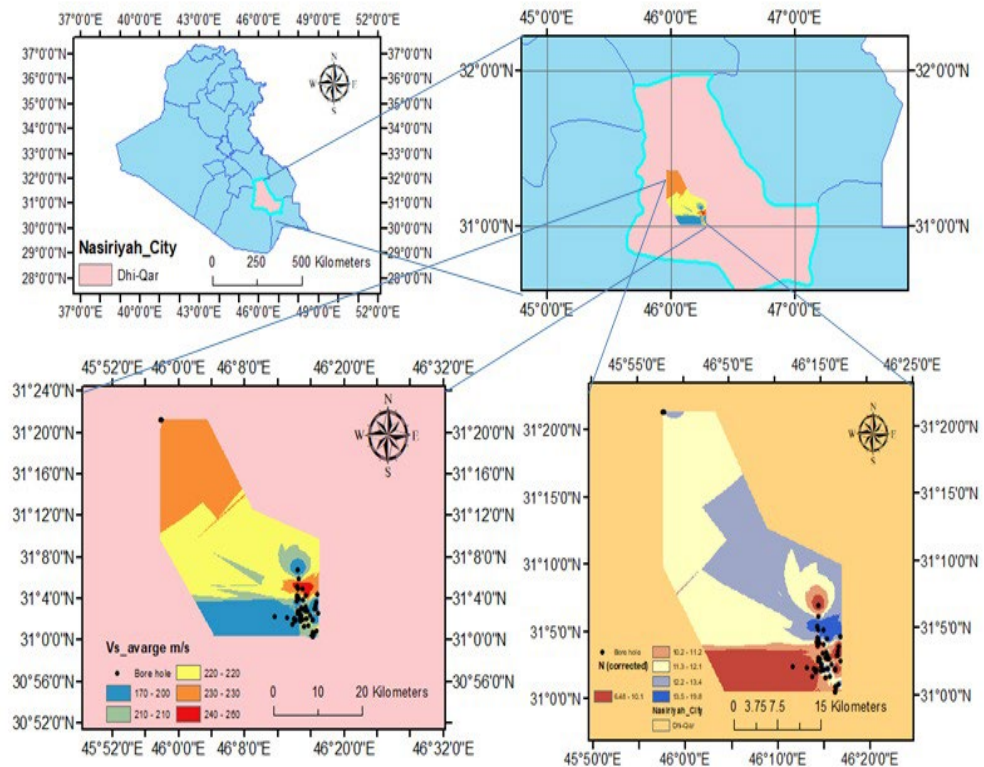


Figure 2. Location of geotechnical and seismic investigation in the study site.

The Arabian plate's northeastern border, where Iraq lies, is a seismically active location. It is clear from the country's seismic records that earthquakes occurred with greater frequency in Iraq's northern and northeastern regions and the country's southern and southwest regions, but these earthquakes were much less potent than those in Iraq's northern, northeastern regions, as shown in Fig. 3 [15, 16].

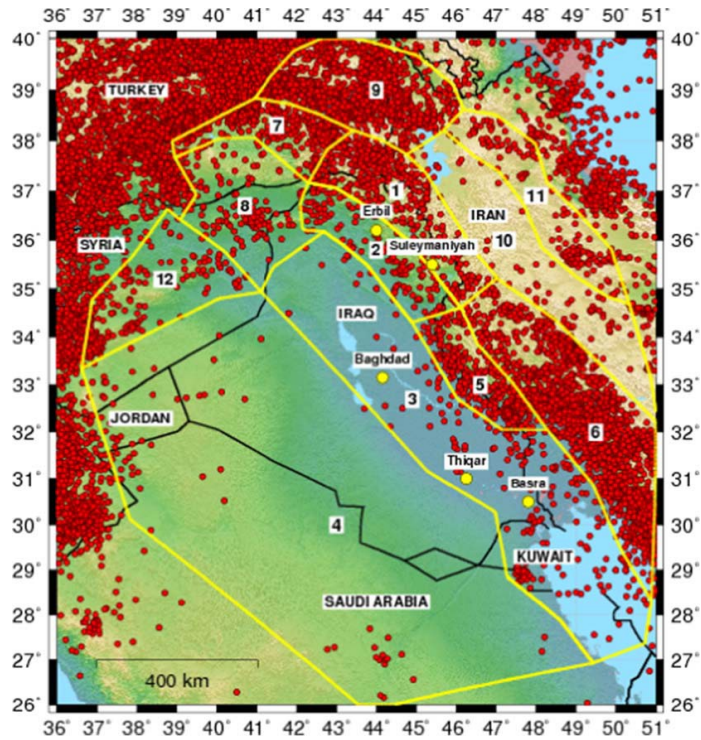


Figure 3. Delineation of seismic source zones in Iraq and adjacent areas [13].

As Jassim and Goff have argued, the Mesopotamian region of volatile shelves includes the city of Nasiriya, which sits within the Euphrates subzone of the Mesopotamian solid shelf. According to the seismic zoning chart, Al-Nasiriya is a no-destruction zone. Fig. 4 shows this clearly [14–20].

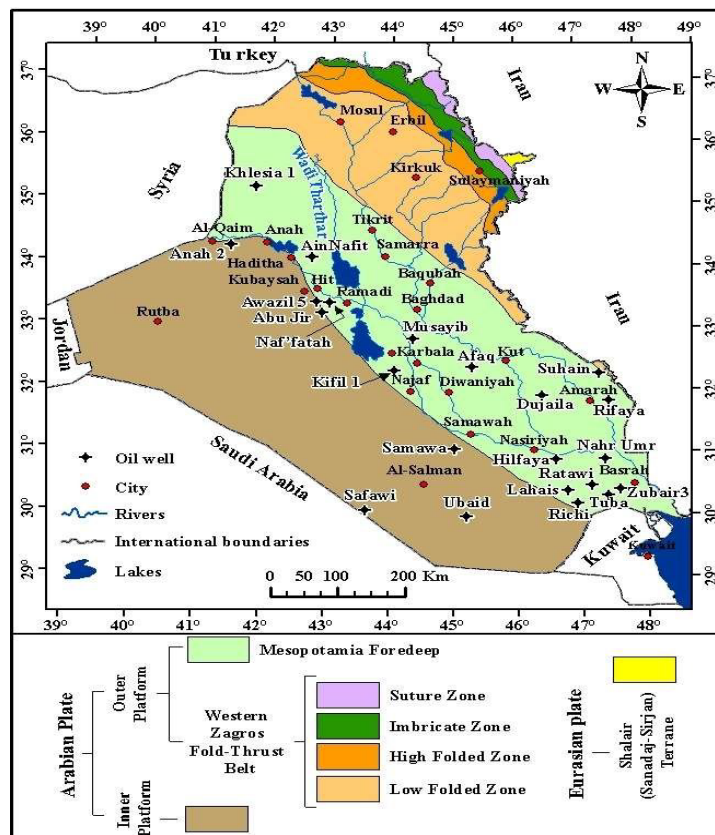


Figure 4. Tectonic divisions of Iraq [19].

2.2. Field dynamic test and geo-seismic investigations

The information from 59 borehole sources was used in this analysis to characterize the site completely. To ascertain the soil conditions and characteristics at the study site, a model drilling rig was used to drill holes with a depth range of 0.5 m to 25 m. SPT N-values for N_{60} were adjusted for field testing procedures at 60 % hammer efficiency and normalized at 1 % effective overburden pressure. The following steps were used to execute SPT in all boreholes. Split barrel samplers were used for this experiment. The sampler was driven into the ground at different depths by a 63.5 kg slide-hammer that fell freely from a height of 760 mm onto an anvil that was placed on surface of the drill rod. To advance the final 300 mm sampler, the number of blows required was mentioned. A good shear wave velocity profile is required to assess seismic site dependent parameters appropriately. Cross-hole and down-hole seismic methods are the most extensively employed for velocity logging nowadays. The dynamic properties of the underlying layers can also be determined via seismic refraction, which is widely employed.

The cross-hole and down/up-hole approaches both rely on monitoring body waves and yield reasonably accurate results. On the other hand, boreholes necessitate the drilling of one or more. Also in progress were down-hole seismic explorations at four locations. As seismic waves move through the surrounding rock and soil, the arrival times of compressional (P) and shear (S) waves will be recorded during borehole seismic surveys. To collect data for the down-hole test, a seismic source (hammer, wood, and steel plate) is set up on the surface near the hole, and the receiver is lowered into the hole and then raised with a 1-meter depth interval. The following is how the source is created:

A hammer striking a steel plate produces P-waves. There is a steel plate 1.25 meters from the borehole's centre. S-waves are created by hammering a piece of wood on both ends to create S-waves with polarity opposite each other. Fig. 5 shows that the wood is put 2.5 meters from the borehole's centre, as depicted. A 3D (xyz) pattern of three direction geophones makes up the receiver. S-wave and P-wave time arrivals are detected using two orthogonal horizontal geophones (x, y) and one vertical z. A clamping mechanism secures the tool to the borehole wall at each receiver level, ensuring good coupling between the wall and geophones and, as a result, reduced seismic noise. When conducting a down-hole survey, the raw data collected includes travel periods for P and S waves, distances from the source to the borehole, and receiver depths. The compression velocity of (V_p) and shear wave velocity (V_s) may be estimated using the measured time and measured distance. The Shear Modulus (G), Poisson's Ratio (ν), Mass Density (ρ) and Young's Modulus (E) could then be calculated using the Eq. (2, 3 and 4) below:

$$\text{Shear Modulus : } G = \rho V_s^2; \quad (2)$$

$$\text{Poisson's Ratio : } \nu = \left(V_p^2 - 2V_s^2 \right) / 2 \left(V_p^2 - V_s^2 \right); \quad (3)$$

$$\text{Young's Modulus : } E = 2G(1 + \nu). \quad (4)$$

The seismic wave velocity test was conducted for four (4) downhole tests the project site. The downhole locations are 1, 2, 3, and 4 at location coordinates. Summary of test results is shown in Table 1.

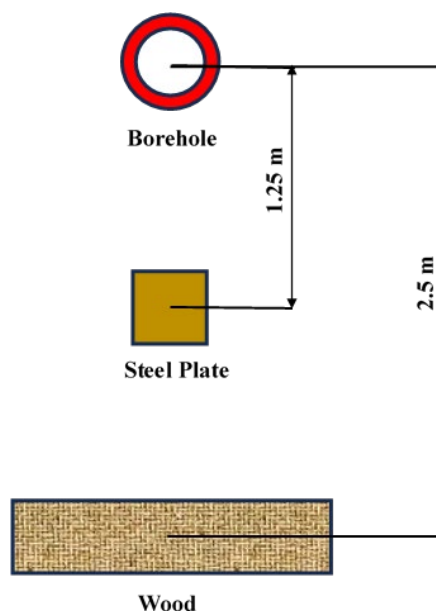


Figure 5. Express of Down-hole velocity test.

Table 1. Summary of results of Down-hole test.

| Site NO. | Location Coordinates | | L.L% average | P.I% average | N (average) | Undrained shear strength C_u (Average) kPa | Average Shear Wave Velocity (\bar{V}_s) |
|----------|----------------------|-----------|--------------|--------------|-------------|--|---|
| | E | N | | | | | |
| 1 | 45.964396 | 31.354063 | 45 | 24 | 10 | 72.9 | 224.7 |
| 2 | 45.964746 | 31.353724 | 45.5 | 20.9 | 10 | 200.2 | 225.3 |
| 3 | 45.965898 | 31.354026 | 50.4 | 29.6 | 8 | 50 | 224.1 |
| 4 | 45.966386 | 31.354499 | 45 | 26 | 20 | 34 | 238.1 |

3. Results and Discussion

3.1. Suggested correlation between SPT N and shear wave velocity

This investigation developed correlations between V_s and SPT-N using 59 data points from borehole pairings. The N-SPT has to be corrected according to the following correction [21].

$$\dot{N}_{cor} = \dot{N}_{field} \cdot C_N \cdot \eta_1 \cdot \eta_2 \cdot \eta_3 \cdot \eta_4.$$

where C_N adjustment for effective overburden correction computed as:

$$C_N = \left(\frac{95.76}{\dot{\sigma}_0} \right)^{0.5}$$

- \dot{N}_{cor} is numbers of bowls corrected,
- η_4 is correction for Bore hole diameter,
- η_3 is correction for length of drill rods,
- η_2 is correction for length depends on the length,
- η_1 is correction for energy.

Correlations were derived from the current database using a simple regression analysis SPT-N adjusted values, and the measured values of V_s are given in Figure 6 as a scatter plot of points. For each SPT-N value, a correlation was applied to predict V_s . We calculated the R-squared value (R^2) and the root mean square deviation for each correlation based on the actual and expected V_s values (RMSD). This study proposed new connections between V_s and the soil's corrected SPT-N levels. The correlations are also presented in Fig. 6. Table 2 below provides a summary of the current, pertinent SPT- V_s that were chosen for study.

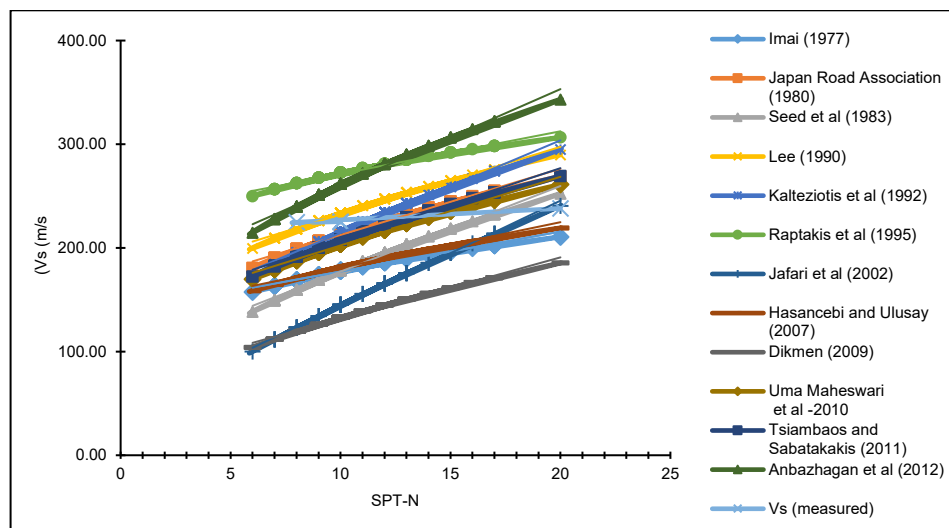


Figure 6. Correlation of VS and N-SPT for all locations.

Table 2. Summary of existing relevant SPT-Vs selected for evaluation.

| Item No. | Authors | Original Equations | Remarks |
|---------------------|---------------------------------------|-------------------------|--|
| SPT-Vs Correlations | | | |
| 1 | Imai (1977) [22] | $V_s = 102N^{0.242}$ | Developed for Cohesive-Soils based on geophysical tests for Vs |
| 2 | Japan Road Association (1980) [23] | $V_s = 100 N^{0.33}$ | Developed for Cohesive- Soils based on geophysical tests for Vs |
| 3 | Seed et al. (1983) [24] | $V_s = 56.4 N^{0.5}$ | Developed for Cohesionless Soils based on geophysical tests for Vs |
| 4 | Lee (1990) [25] | $V_s = 114.43 N^{0.31}$ | Developed for Cohesive Soils – Vs from seismic downhole tests |
| 5 | Kalteziotis et al. (1992) [26] | $V_s = 76.6 N^{0.45}$ | Developed for Cohesive-Soils using geophysical tests for Vs Soils |
| 6 | Raptakis et al. (1995) [27] | $V_s = 184.2 N^{0.17}$ | Developed for Cohesive Soils using geophysical tests for Vs |
| 7 | Jafari et al. (2002) [4] | $V_s = 27 N^{0.73}$ | Developed for Cohesive Soils – Vs from seismic refraction, downhole and SASW |
| 8 | Hasancebi and Ulusay (2007) [5] | $V_s = 97.89 N^{0.269}$ | Developed for Cohesive Soils – Vs found from field Geoseismic tests |
| 9 | Dikmen (2009) [28] | $V_s = 44 N^{0.48}$ | Developed for Cohesive-Soils – Vs determined from field Geoseismic tests |
| 10 | Uma Maheswari et al. (2010) [29] | $V_s = 89.31 N^{0.358}$ | Developed for Cohesive-Soils – Vs determined from MASW |
| 11 | Tsiambaos and Sabatakakis (2011) [30] | $V_s = 88.8N^{0.370}$ | Developed for Cohesive-Soils – Vs based on seismic cross hole tests |
| 12 | Anbazhagan et al. (2012) [31] | $V_s = 106.63 N^{0.39}$ | Developed for Cohesive-Soils – Modified previous correlations to suit indigenous setting |

3.2. Data Analysis

Most process modelling applications rely on graphical residual analysis, a statistical tool used for model validation. The appropriateness of different model parts can be assessed using several sorts of plots of residuals from a fitted model. The (R^2) statistics and other numerical model validation methods are also valuable, but they are rarely as effective as graphical methods. It is easy to visualize a wide range of complex relationships between the model and data using graphic tools. In this way, the validity of the regression model is examined further by doing residual analysis. The residual graphs for each model are shown in Fig. 7. The residuals are horizontal, evenly dispersed, and random, demonstrating a satisfactory fit to the data by the regression model with equal variance from the horizontal axis. For the most part, the regressed data is well-suited to all of the regression equations' values. The normalized consistency ratio can assess how well the equations for predicting Vs value are performing. It is expressed in Eq. (5) as Normalized Consistency Ratio (Cd).

$$Cd = (V_{SM} - V_{SC}) / N_{(SPT)}. \quad (5)$$

V_{SC} is derived using correlation shear wave velocity models, and SPT-N is the SPT blow count corresponding to V_{SC} , whereas V_{SM} is derived from down-hole test Vs measurements. Fig. 7 compares V_{SM} and V_{SC} to assess the predictive strength of the correlations. The proposed correlations, with the exception of SPT-N values, appear to perform well in the prediction of Vs according to the figure, therefore the Cd value is close to zero.

To assess how well the various formulae performed in foretelling the shear wave velocity of the collected data, the Root Mean Square Error (RMSE) values of the proposed correlation were compared to the other formulas. Eq. (6) gives the RMSE values, where V_{SM} is derived from the Down-hole Test and derived from correlation shear wave velocity models, whereas V_{SC} is derived from SPT-N blow counts that correlate to V_{SC} , and where n is the number of measurements. As demonstrated in Table 3, the average shear waves with RMSE of 21.23 (m/Sec) had a lower error value than all of those provided by researchers.

$$RMSE = \sqrt{\frac{\sum_i^n V_{SC} - V_{SM}}{n}} \quad (6)$$

Fig. 8 also shows comparisons between the measured Vs and the anticipated Vs from several models.

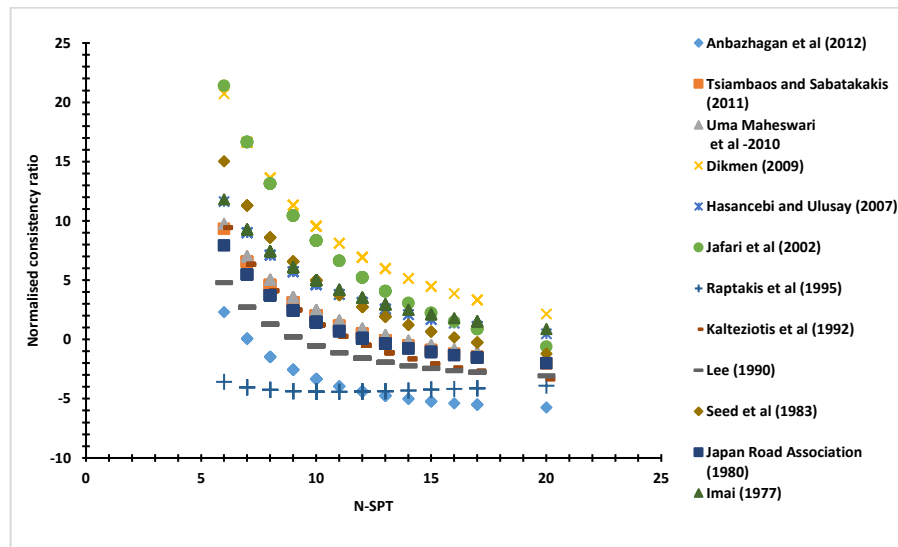


Figure 7. Normalized consistency ratio (Cd) calculated using corrected N values and correlation shear wave velocity Vs from different references.

Table 3. Comparison of the RMSE values of the studied correlations with measured average shear wave.

| Item No. | Authors | Original Equations | RMSE (m/sec) | R ² |
|----------|---------------------------------------|-------------------------|--------------|----------------|
| 1 | Imai (1977) [22] | $V_s = 102N^{0.242}$ | 48.11 | 0.9853 |
| 2 | Japan Road Association (1980) [23] | $V_s = 100 N^{0.33}$ | 21.23 | 0.9885 |
| 3 | Seed et al. (1983) [24] | $V_s = 56.4 N^{0.5}$ | 48.67 | 0.9936 |
| 4 | Lee (1990) [25] | $V_s = 114.43 N^{0.31}$ | 23.03 | 0.988 |
| 5 | Kalteziotis et al (1992) [26] | $V_s = 76.6 N^{0.45}$ | 27.44 | 0.9923 |
| 6 | Raptakis et al (1995) [27] | $V_s = 184.2 N^{0.17}$ | 49.49 | 0.9824 |
| 7 | Jafari et al (2002) [4] | $V_s = 27 N^{0.73}$ | 78.74 | 0.9981 |
| 8 | Hasancebi and Ulusay (2007) [5] | $V_s = 97.89 N^{0.269}$ | 44.40 | 0.9863 |
| 9 | Dikmen (2009) [28] | $V_s = 44 N^{0.48}$ | 91.32 | 0.9931 |
| 10 | Uma Maheswari et al. (2010) [7] | $V_s = 89.31 N^{0.358}$ | 27.25 | 0.9894 |
| 11 | Tsiambaos and Sabatakakis (2011) [30] | $V_s = 88.8N^{0.370}$ | 25.21 | 0.9898 |
| 12 | Anbazhagan et al. (2012) [32] | $V_s = 106.63 N^{0.39}$ | 51.04 | 0.9905 |

A specific correlation was created to account for the impact of the local SPT hammers utilized, workmanship, and geology. Statistical correlations between the two parameters were created using 63 data pairs between corrected SPT-N values and measured values of Vs. Because corrected SPT-N values have a significant impact on the estimation of Vs, they were used in the creation of this correlation. The models listed below were chosen to provide correlations between SPT-N and Vs for Eq. (7):

$$V_s = p \cdot N^q, \quad (7)$$

where N is corrected SPT-N and p, q are coefficients. The overburden effects and the SPT-N variance were taken into account by using this model. Fig. 8 makes it evident that the Vs changes practically linearly with N. Nonlinear regression was performed for the model using least squares analysis. The Equation 7 was developed as presented in Eq.(8):

$$V_s = 92.922 \cdot N^{0.3408}. \quad (8)$$

Table 4 provides an overview of the degree of fitness of various equations. Equation (8) produced the strongest correlation, with an R^2 of 0.9889 and an RMSD of 28.46, demonstrating the highest ability to forecast. It is suggested that this equation be used because of its high fitness level for the dataset.

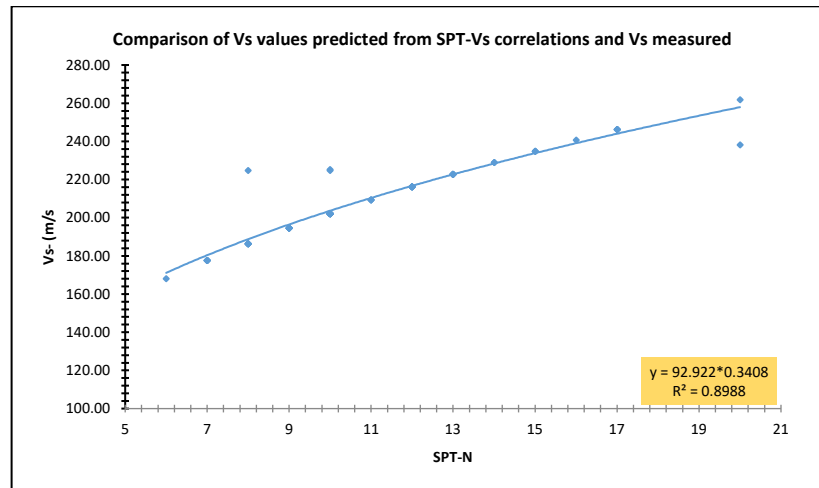


Figure 8. Comparisons between Proposed and measured Vs and SPT-N Correlations.

Table 4. The degree of fitness of various equations.

| Correlation for Vs (m/s) | RMSD | R^2 |
|---------------------------|-------|--------|
| $V_s = 92.922 N^{0.3408}$ | 28.46 | 0.9889 |

4. Conclusions

The study used the data from 59 borehole locations in the city of Al-Nasiriya where dynamic field SPT tests were carried out and used to complete the full field testing. After conducting necessary data analyses, SPT tests close to the down-hole test locations were chosen to create correlations between SPT-N and Vs. The required data were analyzed using linear models and correlation coefficients (R^2) were determined. R^2 and error values for the power model were high, indicating that this model provides the best fitting relationship between the Vs and SPT-N parameters. The following conclusions were obtained:

1. Regression analysis yielded correlations between the adjusted N-values and Vs for all equations (with a power model). The high correlation coefficient for all of the produced correlations reveals a strong association between these two soil parameters (SPT N and Vs), indicating that these proposed correlations can be used to estimate the Vs value of this location acceptably.
2. Compared to other equations, the proposed formula had a lower RMSE value of 21.23 and performed better at predicting Vs values. The dataset is best fit by the empirical correlations presented in this study.

Finally, GIS is an important tool for geotechnical engineering, including preliminary site investigations. On the GIS-based map that displays average shear wave velocity (Vs) and average value N in Al-Nasiriya city, the corrected average SPT-N values and average shear wave velocity (Vs) for all locations of the study area are readily visible. The GIS-based maps created in this study can be useful to foundation designers during the initial site selection and preliminary design of the project in both static and seismic conditions.

References

1. Karim, H.H., Fattah, M.Y., Hasan, A.M. Evaluation of some geotechnical properties and liquefaction potential from seismic parameters. *Iraqi Journal of Civil Engineering*. 2010. 6(3). Pp. 30–45.
2. Ashikuzzaman, Md, Ar Salan, Md S., Rahman, Md A., Hasan, Md M. Development of empirical correlations between shear wave velocity and standard penetration value: a case study of Rajshahi district, Bangladesh. *American Journal of Mechanical and Industrial Engineering*. 2021. 6(1). Pp. 1–6.
3. Hasan, A., Mawlood, Y., Ahmed, A., Ibrahim, H. Correlation of shear wave velocity with SPT-N for a tower- building site at Erbil city. *The Journal of the University of Duhok*. 2021. 23. Pp. 235–245. DOI: 10.26682/csjuod.2020.23.2.19.
4. Jafari, M.K., Shafiee, A., Razmkhah, A. Dynamic properties of fine grained soils in south of Tehran. *Journal of Seismology and Earthquake Engineering*. 2002. 4(1). Pp. 25–35.
5. Hasancebi, N., Ulusay, R. Empirical correlations between shear wave velocity and penetration resistance for ground shaking assessments. *Bulletin of Engineering Geology and the Environment*. 2007. 66(2). Pp. 203–213.
6. Ulugergerli, E.U., Uyanik, O. Statistical correlations between seismic wave velocities and SPT blow counts and the relative density of soils. *Journal of Testing and Evaluation*. 2007. 35(2). Pp. 187–191.

7. Uma Maheswari, R., Boominathan, A., Dodagoudar, G.R. Use of surface waves in statistical correlations of shear wave velocity and penetration resistance of Chennai soils. *Geotechnical and Geological Engineering*. 2010. 28(2). Pp. 119–137.
8. Tsiambaos, G., Sabatakakis, N. Empirical estimation of shear wave velocity from in situ tests on soil formations in Greece. *Bulletin of Engineering Geology and the Environment*. 2011. 70(2). Pp. 291–297.
9. Subba Rao, Ch. Estimation of shear wave velocity from soil indices. *Indian Geotechnical Journal*. 2013. 43(3). Pp. 267–273.
10. Sharma, B., Rahman, S.K. Use of GIS based maps for preliminary assessment of subsoil of Guwahati City. *Journal of Geoscience and Environment Protection*. 2016. 4. Pp. 106–116.
11. Muttashar, R.A., Mahmoud, W.R. Classification of Bearing Strata at Nasiriya City-Thi Qar Governorate/Southern of Iraq, and Study of some of their Geotechnical Properties. *University of Thi-Qar Journal*. 2012. 8(1). Pp. 1–15.
12. Onur, T., Gok, R., Abdunapby, W., Shakir, A., Mahdi, H., Numan, N., Al-Shukri, H., Chalib, H., Ameen, T., Abd, N. Probabilistic seismic hazard assessment for Iraq. Lawrence Livermore National Lab.(LLNL), Livermore, CA (United States), 2016.
13. Alsinawi, S. The prospects of seismological research in Iraq. *Proceedings of the First Scientific Conf. of National Research Foundation of Iraq*, 1972.
14. Buday, T. The regional geology of Iraq. Vol. 1. Stratigraphy and paleogeography. Dar Al-Kutub Publishing House, University of Mosul, Mosul, Iraq, 1980. 445 p.
15. Darweesh, H.A., Obed, A.Z.M., Albadran, B.N. Structural study of basins configuration in Mesopotamian area. *International Journal Of Engineering And Applied Sciences*. 2017. 4(9). Pp. 54–58.
16. Jassim, S.Z., Goff, J.C. (ed.). *Geology of Iraq*. DOLIN, sro, distributed by Geological Society of London, 2006.
17. Fouad, S.F.A. Tectonic and structural evolution of the Mesopotamia Foredeep, Iraq. *Iraqi Bulletin of Geology and Mining*. 2010. 6(2). Pp. 41–53.
18. Imai, T. P and S wave velocities of the ground in Japan. *Proc. 9th ICSMFE*, 1977. Pp. 257–260.
19. Thaker, T.P., Rao, K.S. Development of statistical correlations between shear wave velocity and penetration resistance using MASW technique. *Pan-Am CGS, geotechnical conference*, 2011.
20. Seed, H.B., Idriss, I.M. Evaluation of liquefaction potential sand deposits based on observation of performance in previous earthquakes. *ASCE National Convention (MO)*. 1981. Pp. 481–544.
21. Lee, Sh.H.-H. Regression models of shear wave velocities in Taipei basin. *Journal of the Chinese Institute of Engineers*. 1990. 13(5). Pp. 519–532.
22. Kalteziotis, N., Sabatakakis, N., Vassiliou, J. Evaluation of dynamic characteristics of Greek soil formations. *Second Hellenic Conference on Geotechnical Engineering*. 1992. Pp. 239–246.
23. Semblat, J.-F., Kham, A., Parara, E., Bard, P.-Y. Seismic wave amplification: Basin geometry vs soil layering. *Soil Dynamics and Earthquake Engineering*. 2005. 25(7-10). Pp. 529–538. DOI: 10.1016/j.soildyn.2004.11.003
24. Dikmen, Ü. Statistical correlations of shear wave velocity and penetration resistance for soils. *Journal of Geophysics and Engineering*. 2009. 6(1). Pp. 61–72. DOI: 10.1088/1742-2132/6/1/007
25. Uma Maheswari, R., Boominathan, A., Dodagoudar, G.R. Use of surface waves in statistical correlations of shear wave velocity and penetration resistance of Chennai soils. *Geotechnical and Geological Engineering*. 2010. 28(2). Pp. 119–137. DOI: 10.1007/s10706-009-9285-9
26. Tsiambaos, G., Sabatakakis, N. Empirical estimation of shear wave velocity from in situ tests on soil formations in Greece. *Bulletin of Engineering Geology and the Environment*. 2011. 70(2). Pp. 291–297. DOI: 10.1007/s10064-010-0324-9
27. Anbazhagan, P., Parihar, A., Rashmi, H.N. Review of correlations between SPT N and shear modulus: a new correlation applicable to any region. *Soil Dynamics and Earthquake Engineering*. 2012. 36. Pp. 52–69. DOI: 10.1016/j.soildyn.2012.01.005

Information about authors:

Ali Majid Al-Kinani,

E-mail: ali-majid@utq.edu.iq

Jawad K. Thajeel,

E-mail: jawad.thajeel@utq.edu.iq

Mohammad Hydar Al-Umar,

E-mail: mohammad.hydar@utq.edu.iq

Mohammed Y. Fattah,

E-mail: myf_1968@yahoo.com

Received 29.11.2022. Approved after reviewing 15.09.2023. Accepted 25.12.2023.



Research article

UDC 625.852

DOI: 10.34910/MCE.125.5



Calculation of the influence of various compaction on the wear resistance of asphalt concrete using material loss calculation approach

G. Baimukhametov¹ , R. Gayfutdinov¹ , E. Khafizov² 

¹ State public institution Glavtadortrans, Kazan, Russian Federation

² Kazan State University of Architecture and Engineering, Kazan, Russian Federation

✉ baimukhametovi@mail.ru

Keywords: air voids, asphalt, abrasive wear, asphalt compaction, wear model, asphalt pavements, experimental investigations, wear resistance

Abstract. Rutting is the most common and most dangerous defect of asphalt pavements. One of the problems of northern countries such as the Russian Federation is abrasive rut due to studded tire loading. Precise prediction of the asphalt concrete abrasion and wear resistance allows improving the durability and reliability of asphalt pavements. Several laboratory tests are used for the prediction of asphalt concrete abrasion resistance. An abrasive wear model of asphalt concrete is needed to predict wear resistance changes under different conditions. The aim of this article is to evaluate compaction quality effect and air voids value on the abrasion resistance of asphalt concrete. To estimate the influence of the percentage of connected voids on abrasive wear of asphalt concrete, an asphalt wear model was presented. This model is based on G.Y. Lee's approach. This approach divides the abrasive processes into normal abrasion and particle loss. Air voids lead to the aggregate loss and affect the abrasion resistance of the asphalt pavements. Calculation of these effects is possible using G.Y. Lee's approach. Calculations of the lost particles include the empirical coefficient X (1/mm) characterizing the influence of the pores on the lack of adhesion to the aggregate particle surface and the influence of the lack of adhesion on the fraction of lost particles. The Prall test was used for the abrasion resistance estimation. The saturation degree method was used for the estimation of compaction quality and air voids content. For the coefficient estimation, 63 samples of different mixes were tested. The mixes were used for the construction of the Republic of Tatarstan road network. The used asphalt concretes correspond to requirements of Russian standards GOST 9128-2013 and GOST 31015-2002. The experiments show good reliability of the presented model. This model predicts abrasion resistance of asphalt concretes under uncompaction and provides insight into the abrasive wear processes in the asphalt concretes. Furthermore, the study results allow us to improve the laboratory tests precision by 2.3 % by excluding the uncompaction effect during the comparison of the results.

Citation: Baimukhametov, G., Gayfutdinov, R., Khafizov, E. Calculation of the influence of various compaction on the wear resistance of asphalt concrete using material loss calculation approach. Magazine of Civil Engineering. 2024. 17(1). Article no. 12505. DOI: 10.34910/MCE.125.5

1. Introduction

Fast and safe roads between cities and regions is the most vital component of every country. The Russian Federation has more than 1.4 million km of roadways including 1 million km of roads with concrete pavement. Rutting is one of the most dangerous defects of pavements; it can result from permanent deformation or abrasion. Most roads of the Russian Federation are located in regions with cold climates,

which leads to damages to roads during the winter season. Abrasive ruts have become a commonplace with the increasing traffic and the emergence of studded tires. Many researches aimed to confirm the abrasion genesis of the ruts on heavy traffic roads [1]. Abrasion rutting is a common problem for the Nordic countries, the northern states of USA, et.al. [2].

This problem has been under study in different countries. In 1980s, the government of Japan began investigating complaints about increasing dust pollution and rut propagation in different cities. After public litigations pursued by civil society organizations it was decided to reduce the use and distribution of studded tires in Japan. These government limitations were accompanied by studless tire use education programs carried out in different cities. Studless tires have better performance than the studded tires in the case of dry and wet surface without snow. Tests in the ice crust conditions showed that accurate and effective using of studless tire can have the same performance as a studded tire [3]. As a result, the rut propagation and dust pollution reduction was achieved in Sapporo within the three years of the requirements enactment. Despite a small increase of the vehicle accident rate these measures were admitted as an expedient by the Japanese government and society [4]. In the Nordic countries this problem has become sever in the second half of the last century. Many researches were performed to estimate the effect of studded tires on the pavement. In Sweden, regular and lightweight studs damage on the pavement was compared by Swedish National Road and Transport Research Institute. Based on the above statistical data, it was calculated that the studded tire damage causes above 1.5–2 times more road maintenance costs, including the road wear and the environmental damage [5]. In the Baltic countries, similar calculations were performed by Vilnius Gediminas Technical University. It was concluded that the use of studded tires brings more than 38 million EUR losses. Despite the road accidents, it was concluded, that the Baltic countries have to prohibit studded tires use [6]. The researches performed in the United States show that the annual cost to repair the damage caused by studded tires in Alaska is approximately \$13.7 million and it has significant effect for the other northern states [7]. Thus, the performed researches emphasize the significance of abrasive wear resistance. Therefore, it is important to research the abrasive wear properties of asphalt concretes.



Figure 1. Wear rut investigation in Kazan: (a) rut propagation monitoring by Glavtadortrans; (b) transverse profile of rut by the KGASU [8].

SOI “Glavtadortrans” supervises all of the region roads of the Republic of Tatarstan and controls the quality of roads. Abrasive wear investigation was carried out in SOI “Glavtadortrans” due to rut propagation on the new roads (Fig. 1. a). Before it, in 2016 the Kazan State University of Architecture and Engineering did a research to confirm the wear nature of the ruts on the main streets of Kazan city (Fig. 1. b). The rutting became a common problem for the Russian Federation and the Republic of Tatarstan particularly. It affects both asphalt and rigid pavements. The investigations of these types of defects were performed in the Russian Federation by many researchers [9]. The relevance of the investigation in this direction is emphasized by the increasing number of cement concrete pavement roads. The president of the Republic of Tatarstan ordered to construct such pavements using local road construction materials. Abrasion resistance is a critical parameter for the cement concrete roads in contrast to the asphalt pavements with the bitumen binders, which have the ability to remove a fraction of microcracks in the asphalt concrete structure. The understanding of the processes between the pavement and studded tires is necessary for the safe and reliable road network construction in the future.

Several researches were performed to evaluate the properties of asphalt concrete, which affects the abrasion resistance. Field measurements collected in Alaska and analyzed by the National Academy of Sciences show that the best abrasion resistance of asphalt concrete can be achieved using a polymer modified binder with a hard aggregate in the asphalt pavement. Good binder quality can lead to higher

toughness of material and abrasion resistance of asphalt concrete, while hard aggregate improves the abrasion resistance of asphalt concrete [10]. Different properties of asphalt concrete were estimated several times in the Nordic countries. It was concluded that aggregate properties and a type of mix grading have the most influence on the asphalt pavement abrasion resistance. Increasing the maximum aggregate size and the amount of a coarse aggregate improve the abrasion resistance of asphalt concrete. However, it is impossible to unlimitedly increase the coarse aggregate size due to the huge noise pollution of such pavements [11, 12]. Increased abrasion resistance of aggregate can be used for the high abrasion resistance asphalt concrete production. Several researches were performed to estimate the effect of various types of an aggregate for the asphalt pavements abrasion resistance [2, 13]. The previous researches of the SOI "Glavtadortrans" show the influence of the aforementioned properties of asphalt concrete on the asphalt concrete abrasion resistance and note the air voids content effect [8].

The effect of air voids on the abrasion resistance of asphalt concrete was explored in several studies [14–17]. Air voids can reduce the asphalt concrete abrasion resistance due to different causes. One paper [15] studying the raveling resistance of the porous asphalt pavements affected by hydrocarbon spills noticed the air voids effect on the raveling resistance. The influence occurs both from the side of the decrease of asphalt concrete strength and the susceptibility to the erosion of the asphalt concrete by water and the other conditions. A few air voids can lead to severe rutting, similar to the case of low compaction [14]. However, the increasing of air voids leads to the reduction of asphalt strength. It leads to freeze damage of asphalt concrete and low fatigue life [18]. The importance of this parameter stipulates the requirements for pavements.

Asphalt concrete can be classified as a composite material. Nowadays several models for the different abrasion types exist. Existing models of composite wear are mostly related to the pin-on-disc type of abrasive wear due to the typical exploitation conditions of such composites. Existing models are based on the tribological properties of several particle and fiber reinforced composites [19, 20]. The G.Y. Lee's composites abrasion model includes the reinforcement particle removal (Fig. 2); this process is similar to the wear processes in asphalt concretes. G.Y. Lee's approach is based on the inverse rule of mixtures, and includes the composite microstructure. It can be used for the simplified modeling of the abrasive wear of asphalt concrete including the air voids and uncompacting effect [21].

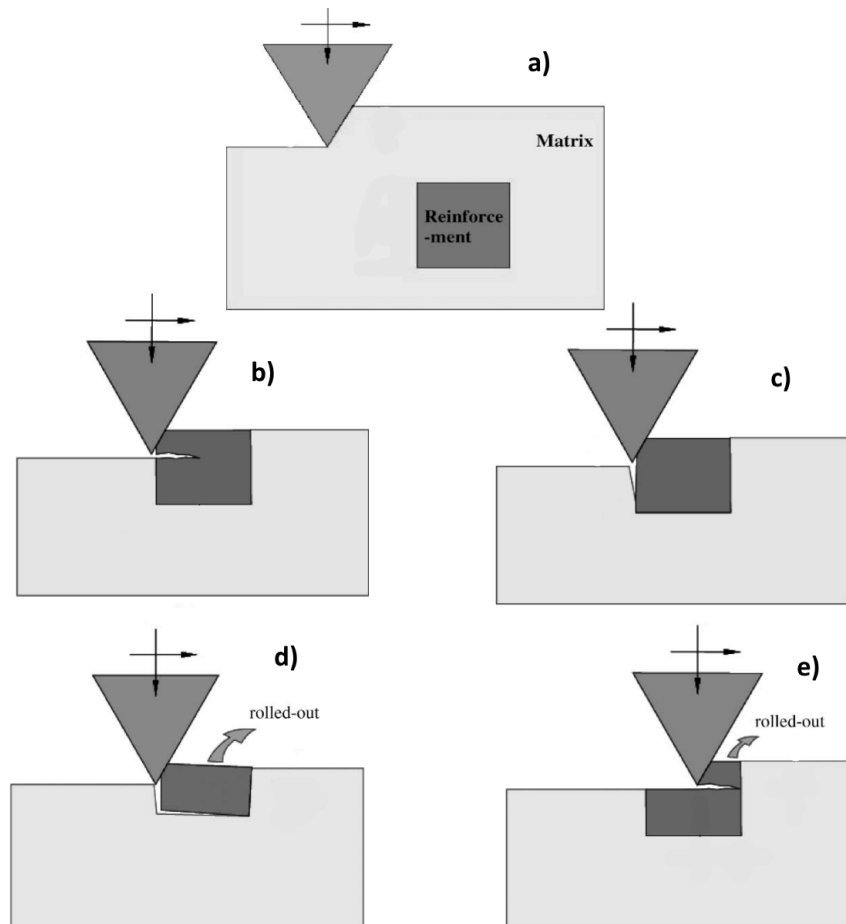


Figure 2. General schematic drawing of two-phase composite in abrasion with simplified sliding wear geometry: plowing mechanism (a); cracking at the matrix (b)/reinforcement (c); particle removal at the matrix (d)/reinforcement (e) [21].

Calculation of the air voids effects in asphalt concretes is important due to various compaction requirements for the asphalt concrete pavements. The existing testing methods and abrasion resistance requirements do not include uncompacting and air voids effect on the asphalt material. It can lead to the misunderstanding of pavement properties and reduction in durability of pavement in the northern countries with severe winter exploitation conditions. The existing models of composite abrasion resistance use and the empirical data can reduce the mix design errors and increase the reliability of abrasion resistance evaluation.

The aim of this study is to determine the compaction quality effect on abrasion resistance of asphalt pavement. This is necessary for accurate prediction of the development of pavement wear on highways and accurate selection of materials in the design of asphalt concrete mixes. The study includes the existing model of composite materials wear modification for the case of studded tire wear of asphalt concrete. For the empirical determination of the equation coefficient, various mixes were tested. The analysis of obtained data is needed for the coefficient determination.

2. Materials and Methods

2.1. Applied materials

The research includes testing of various grades of stone mastic asphalt and dense graded asphalt with different types of aggregate and binder. Tests and materials were made according to the Russian series of standards (GOST). GOST include dense graded and stone mastic hot mix asphalt with nominal maximum sizes of 5/10/15/20 mm regulation. The difference between the nominal dimensions of the aggregate from European and American ones is that the shape of the sieve hole is round according to Russian standards [22].

For this study, sixty-three asphalt samples of mixes were tested during 2018–2020. The mixes included different mix types: stone mastic asphalt concretes and dense graded asphalt concrete type A. In the Russian Federation, specifications on stone mastic asphalt concrete (SMA) are given in GOST 31015-2002 “Bituminous stone mastic mixtures and stone mastic asphalt. Specifications” and specifications on dense graded mix type “A” in GOST 9128-2013 “Asphaltic concrete and polymer asphaltic concrete mixtures, asphaltic concrete and polymer asphaltic concrete for roads and aerodromes. Specifications”. Grading of the tested mixes is shown in Fig. 3. Nominal sizes 2.5; 5; 10; 15; 20 mm in Russian standards corresponds to 2; 4; 8; 11,2; 16 mm in European and US standards due to round sieve opening shapes. Comparing of Russian mixes with international ones by the EN and other protocols is not necessary for this study.

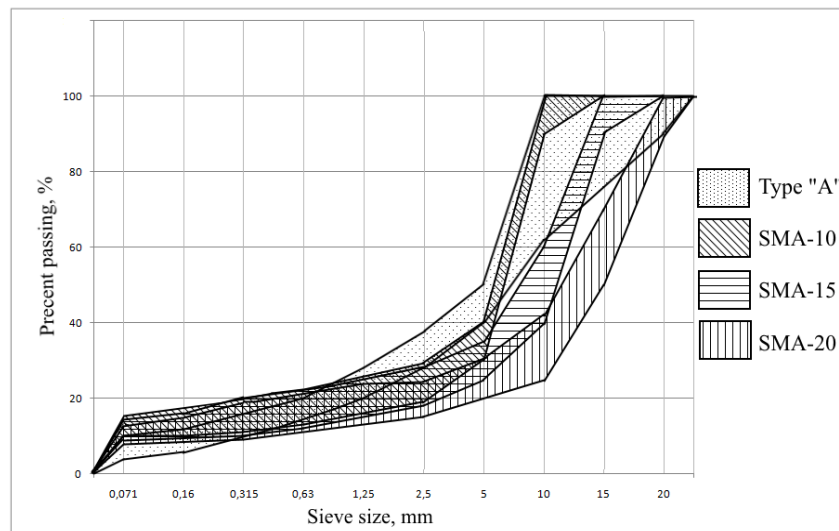


Figure 3. Tested mixes grading limits according to GOST 9128-2013 and GOST 31015-2002 [8].

Testing mixes fell into nineteen groups according to the mix type, type of binder and type of aggregate. Mix samples are shown in Table 2. Each mix was used in the real construction of the road network of the Republic of Tatarstan. Aggregates include stone from the different carriers of the Russian Federation as a “Sangalyck”, “Pervouralskiy”, “Sheleyka” et al. Binders include the polymer modified binders (styrene-butadiene-styrene) and non-modified binders.

2.2. Numerical methods

Asphalt concrete is defined as a particle composite material containing three parts: mastic or binder as a matrix, coarse and fine aggregate as a reinforcement and pores inclusion. Besides, the abrasive wear of asphalt concrete can be shown as a two-dimensional process with a wear surface, which can be represented as a line. In this case, wear surface is defined as a surface of asphalt concrete in contact with an abrasive medium such as a studded tire or a steel ball in laboratory experiment and loses the material due to abrasion (Fig. 4,a).

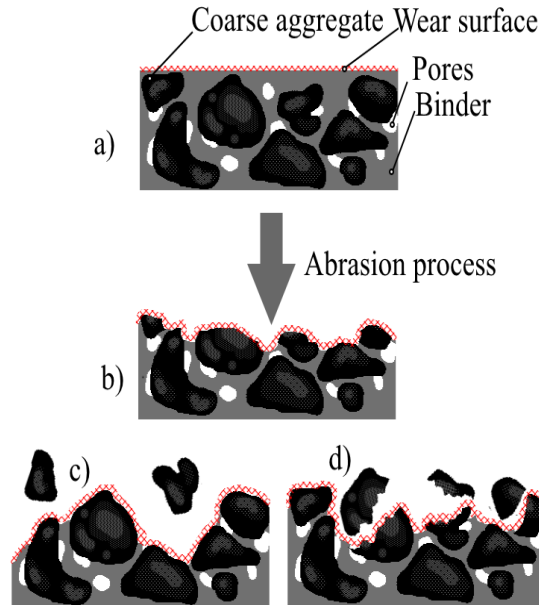


Figure 4. Asphalt concrete abrasive wear process: a) Original asphalt concrete before abrasion, b) regular abrasion process is plowing, c) particle removal, d) cracking [8].

G.Y. Lee reports that the mechanism of composites abrasive wear can occur in three general scenarios: plowing, cracking and particle removal [21]. In terms of asphalt concrete, it means the abrasion of aggregate with binder (Fig. 4 (b)), aggregate fragmentation due to removal (Fig. 4(c)) and cracking (Fig. 4(d)). Plowing is a simple process which can be modeled by several models [23]. Thus, the abrasion resistance of asphalt concrete depends on abrasion resistance of aggregate, binder and pores. However, the abrasion resistance of pores and binder is much less than the abrasion resistance of aggregate. The mutual influence of the various content can be described using two main approaches. The first is an inverse rule of mixtures introduced by Khrushchev and Babichev:

$$1/W_c = V_1/W_1 + V_2/W_2, \quad (1)$$

where W_c is the wear rate of the composite; W_i is the wear rate of the material, meaning wear of each material separately under an equal abrasion loading, the subscript means the number of components; V_i is the volume part of the materials, the subscript means the number of components.

In Eq. (1) $1/W_i$ means wear resistance of the component. Eq. (1) is based on the assumption that each component of the composite wears at the equal rate. The equal wear rate means straight wear surface and uniform wear of each component due to its fraction. For example, the wear rate of aggregate is less than the wear rate of binder and pores in the case of asphalt concrete and wear resistance primarily depends on the wear resistance of asphalt aggregate, which is perfectly observed in practice [10, 24].

The second approach is given by K.-H. Zum Gahr and is aimed to explain the experimental data. The governing assumption is an independent wear of each component of the composite, summary wear is an algebraic sum of each component wear multiplied to its volume fraction.

$$W_c = V_1 \cdot W_1 + V_2 \cdot W_2. \quad (2)$$

The geometrical representation of this approach is the lack of continuous wear surface and nonlinear process of wear. Despite the nonlinear wear process representation, according to practice, this approach is disadvantageous for the pores problem due to complexity of pores representation in equations and the nature of abrasive wear in case of flat pavements (Fig. 4 (b)). For our problem, both of these approaches

are required for different parts of abrasive wear evolution. The first approach in Eq. (1) needs to be modified due to the curved form of the wear surface (Fig. 5). However, the second approach in Eq. (2) can be used as is because of the continuous wear surface.

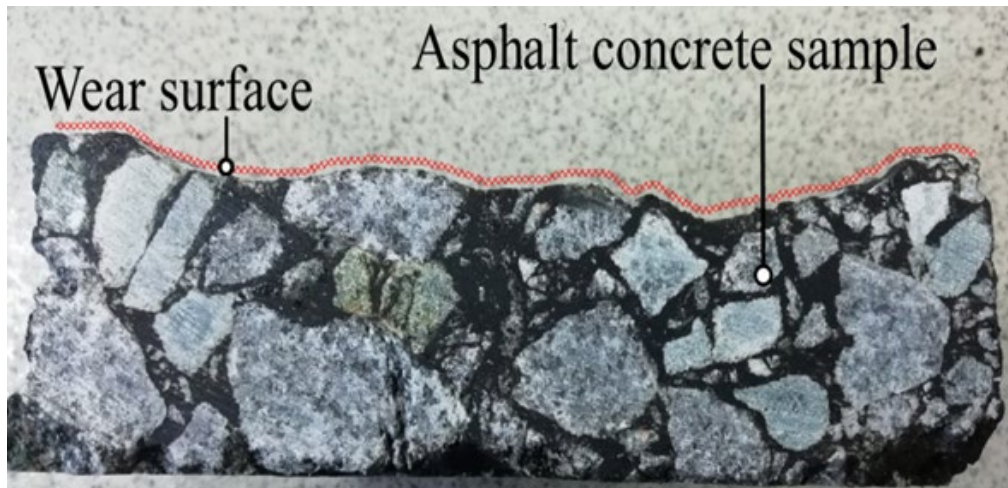


Figure 5. Asphalt concrete wear surface.

In any case, using both assumptions is complicated due to the impossibility of wear surface control during the test and modified Khrushchev and Babichev method is comprehensive with required for the test precision.

G. Y. Lee suggested a modified approach for the problem solving. This approach is based on the modified Eq. (1) with a coefficient of non-contributing portion (NCP). The governing equation based on the G.Y. Lee's approach is shown below [21].

$$1/W_c = C \cdot V_1/W_1 + V_2/W_2, \quad (3)$$

where C is the contribution coefficient of the reinforcement;

$$C = 1 - C', \quad (4)$$

where C' is the non-contributing portion.

The physical meaning of NCP is a fraction of material particles that are removed during the abrasion (Fig. 4 (c)). Because of the similar processes of cracking (Fig. 4 (d)) and removal (Fig. 4 (c)) of material during testing and the impact of pores on these processes, we assume that cracking particles in this problem can be replaced as removed particles. For the determination of the NCP removal model is needed. For the aggregate particles modeling we represent them in a form of spheres. Potential volume of pores can be represented as a space around the sphere thickness of dl . The dl variable does not characterize actual space thickness around the particle, it is a representation for the determination of the contact area between pores and particles. This space can be filled with the binder or other particles and in these cases this space represents a filled space. Pores can open the space on the fraction of L' . The opening of the space on the proportion of L' is a condition to lose the NCP with volume of X' fraction (Fig. 6).

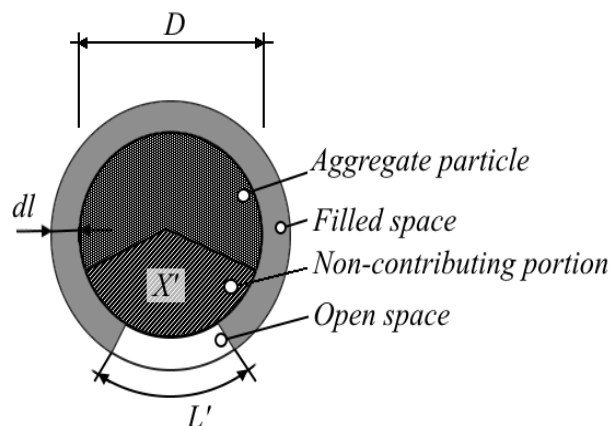


Figure 6. Non-contributing portion loss condition.

With the proportional increase of particle size, proportional increase of surface area occurs, which makes these conditions independent of the particle size. The volume of the space around the particle can be shown with the equation below.

$$CV_v = \pi \cdot D \cdot dl, \quad (5)$$

where CV_v is the volume of space around the particle; D is the size of a particle.

The volume of a single non-contributing portion can be represented as:

$$V' = X' \cdot \pi \cdot D^2 / 4, \quad (6)$$

where X' is the fraction of a single particle supposed to be a non-contributing portion.

The non-contributing portion can be represented as:

$$C' = V' \cdot CV / (L' \cdot CV_v), \quad (7)$$

where $CV / (L' \cdot CV_v)$ is the conventional number of non-contributing portions.

This assumption is conventional due to the lack of tangible representation of L' . In the practice this value is not a fraction of open space around the particle but characterizes the total number of deficiencies of adhesion. The tangible sense of equations above is a coefficient area of the particle in the contact of pore and lack of adhesion on the surface. Due to equations above, the final expression of C' is:

$$C' = D \cdot CV \cdot X' / (4 \cdot dl \cdot L') = D \cdot CV \cdot X / 4, \quad (8)$$

where X is the conventional empirical value characterizing the area of contact between pores and particles and the amount of lost material due to the lack of adhesion. This value includes all of the unknown constants of the Eq. (8). This coefficient is unique for every material and depends on the adhesion, quality of aggregate, roughness and the binder type. The aim of this study is finding average X coefficient for the group of materials conventionally used in the construction in the Russian Federation. The problem of this equation is determining the diameter of the particles D . Calculation of the fraction of NCP for each size of material is complicated. Therefore, the average diameter of particles can be represented as:

$$D = 4 \cdot \sum pV_i / \sum pS_i, \quad (9)$$

where pV_i is the volume of the particles of i size; pS_i is the surface area of the particles of i size.

The particles less than 1 mm are determined as a part of binder. The volume of particles of every size and mass is a proportional value due to the conventional constant of specific gravity of every size of particles. Thus, the volume of particles can be founded through the grading curve of mixes. The surface area of particles can be found by Eq. (10).

$$pS_i = 4 \cdot pV_i / D_i. \quad (10)$$

V_1 and V_2 variables of the Eq. (3) mean asphalt concrete without connected voids fraction and connected voids fraction respectively. It is obvious that wear resistance of the open voids V_2 / W_2 is equal to zero. So, the summary equation for this study is presented below:

$$W_1^{ab} = \frac{W_2^{ab} \cdot (1 - D \cdot CV_2 \cdot X / 4) \cdot (1 - CV_2)}{(1 - D \cdot CV_1 \cdot X / 4) \cdot (1 - CV_1)}, \quad (11)$$

where W_1^{ab} is the wear value or the Prall test value of an asphalt concrete with CV_1 connected void value or the degree of saturation; W_2^{ab} is the wear value or the Prall test value of an asphalt concrete with CV_2 connected void value or the degree of saturation.

2.3. Experimental methods

As a measure of the compaction quality, the saturation degree method can be used. This method is trivial for quality control of the asphalt concrete pavement in the Russian Federation. Moreover, it had been

the most common method of compaction quality control before the new asphalt concrete designing systems were introduced in 2020. The degree of saturation value is equivalent to the connected void under the vacuum conditions for the asphalt concrete saturation in the laboratory (2000 Pa/15 mm Hg, 1 hour). Usually this parameter shows more than 80 % of the total air voids in the asphalt concrete [25]. It depends on the quality of compaction, mix grade, percentage of binder and type of aggregate. The value of saturation test method according to GOST 12801-98 "Materials on the basis of organic binders for road and airfield construction. Test methods." was used to determine the compaction quality. The value of saturated water depends on a percentage of air voids [16]. This method is fast and acceptable for the case when the evaluation of maximum specific gravity is impossible. This method is acceptable for the determination of connected void value as a compaction quality.

For the evaluation of percentage of saturated water according to GOST 12801-98, clean and dry weighted samples of asphalt were saturated under (20 ± 2) °C water for the specific bulk volume evaluation for 30 min. After saturation, the samples were weighed in water and in the air. After the weighing, the samples were placed under water and saturated under 2000 Pa vacuum for 1 hour and with atmospheric pressure for 30 minutes. The degree of saturation was determined by the following formula:

$$CV = \frac{m_3 - m}{m_2 - m_1}, \quad (12)$$

where m is the mass of the dry sample in the air (g); m_1 is the mass of the sample under water (g); m_2 is the mass of the sample saturated for 30 minutes, in the air (g); m_3 is the mass of the vacuum-saturated sample in the air (g).

It is impossible to make evaluation for this research based on the field measurement of the rut propagation. Constant abrasion loading requires laboratory test equipment. The Glavtadortrans, SPI laboratory is equipped with a Prall testing machine to imitate the damage from the studded tires. The Prall test is commonly used in Northern Europe for the testing of asphalt specimens and has good precision to determine the abrasion resistance of asphalt concrete [26]. As an alternative, the following methods are most commonly used in the world practice: Cantabro test, VTI road simulator and various tests for the abrasion resistance of stone testing [27]. The Cantabro test was invented for the similar type of the asphalt concrete damage: raveling and adhesion loss. But it cannot be used for the abrasion modeling. At the same time, different testing methods for the abrasion resistance of stone cannot be used due to the polishing nature of abrasion loading (for example, EN14157 or ASTM C241 tests) [28]. One of the main drawbacks of these methods is temperature and moisture conditions. In the case of asphalt concrete it is obvious that the typical abrasion conditions are spring and fall weather with wet and cold surface of the road. Due to the prevalence of Prall test in Europe, it is more often applied for the researching and testing in the Russian Federation as well.

The Prall test method was used to determine the abrasion resistance. It is described in EN 12697-16 "Bituminous mixtures – Test methods – Part 16: Abrasion by studded tyres" in Europe and in GOST 58406.5 "Automobile roads of general use. Hot asphalt mixtures and asphalt. Method for determination of abrasion." in the Russian Federation. The Russian test method corresponds to the European one [8].

The test requires asphalt specimens with a height of 30 mm and diameter of 100 mm. The specimens can be prepared on Marshall or gyratory compactor or can be sampled from the pavement. Compacted specimens must be cut to the required size. Preparing for the test includes saturation with water at a temperature of 5 °C for 5 hours. Sample weight after saturation is m_4 . Prall apparatus included specimen holder (Fig. 7), abrasive loading, including 40 steel balls 12 mm in diameter, engine and cooler. During the test, the specimens were subjected to a loading impact with frequency of 950 strikes per minute with water cooled for 5 °C for 15 minutes. After the test, the samples were weighted (m_5).

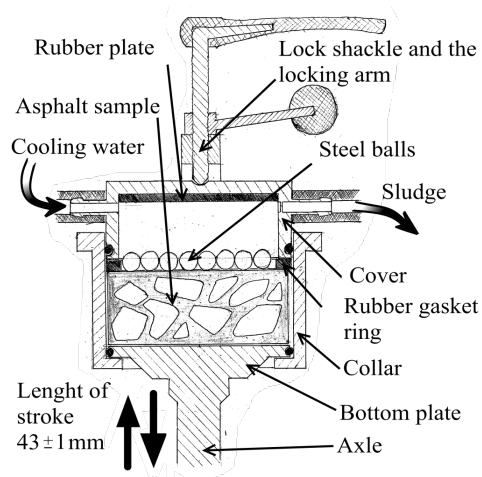


Figure 7. Prall test equipment.

Prall test wear value is determined by the following formula:

$$W^{ab} = \frac{m_4 - m_5}{G_{mb}}, \quad (13)$$

where W^{ab} is the Prall test abrasion value (cm^3); m_4 is the mass of the specimen before testing (g); m_5 is the mass of the specimen after testing (g) (Fig. 8); G_{mb} is the bulk gravity of the specimen (g/cm^3).



Figure 8. Asphalt sample with steel balls after testing.

The classification of the abrasion resistance of asphalt concrete in the Russian Federation is carried out in accordance with GOST R 58406.1 "Automobile roads of general use. Stone-mastic asphalt mixtures and asphalt concrete. Specifications" recommendations. The classification is shown in Table 1.

Table 1. Abrasion resistance classification of asphalt concrete according to the Russian Federation GOST R 58406.1 "Automobile roads of general use. Stone-mastic asphalt mixtures and asphalt concrete. Specifications".

| The abrasion resistance class | The Prall Test value, cm^3 |
|-------------------------------|-------------------------------------|
| 1 | Less than 25 |
| 2 | From 26 to 35 |
| 3 | From 36 to 45 |

For example, for the stone mastic asphalt it is recommended to use mixes with the 1st class of abrasion resistance. The contractor can decide on abrasion resistance for each road depending on the loading if necessary.

Considering all of the above, using these laboratory tests, it is possible to obtain all the necessary terms of Eq. (11).

3. Results and Discussion

To provide experimental verification of the proposed model abrasive wear test, we prepared and analyzed 63 samples. For the abrasive wear test, VTI Prall test machine was used (Fig. 7). The test results are presented below (Table 2).

Table 2. Mixes abrasion testing result with calculated average size (Eq. 9) of aggregate and estimated degree of saturation.

| The sample number | The mix number | Average size of aggregate, D (mm) | Mix type | The degree of saturation, CV (%) | Prall test value, W^{ab} (cm ³) |
|-------------------|----------------|-------------------------------------|----------|------------------------------------|---|
| 1 | 1 | 11.04 | SMA 20 | 4.19 | 18.00 |
| 2 | 1 | 11.04 | SMA 20 | 1.14 | 13.23 |
| 3 | 2 | 7.98 | SMA 15 | 2.18 | 20.26 |
| 4 | 2 | 7.98 | SMA 15 | 1.73 | 18.29 |
| 5 | 3 | 11.04 | SMA 20 | 3.38 | 22.40 |
| 6 | 3 | 11.04 | SMA 20 | 0.91 | 20.20 |
| 7 | 3 | 11.04 | SMA 20 | 0.96 | 20.80 |
| 8 | 4 | 7.98 | SMA 15 | 2.59 | 23.58 |
| 9 | 4 | 7.98 | SMA 15 | 2.26 | 23.95 |
| 10 | 5 | 11.04 | SMA 20 | 1.94 | 24.67 |
| 11 | 5 | 11.04 | SMA 20 | 1.86 | 25.05 |
| 12 | 6 | 11.04 | SMA 20 | 3.35 | 27.33 |
| 13 | 6 | 11.04 | SMA 20 | 3.77 | 20.68 |
| 14 | 6 | 11.04 | SMA 20 | 3.60 | 25.29 |
| 15 | 6 | 11.04 | SMA 20 | 2.29 | 23.32 |
| 16 | 6 | 11.04 | SMA 20 | 3.18 | 22.64 |
| 17 | 6 | 11.04 | SMA 20 | 3.80 | 25.64 |
| 18 | 6 | 11.04 | SMA 20 | 3.34 | 21.46 |
| 19 | 6 | 11.04 | SMA 20 | 2.73 | 20.94 |
| 20 | 6 | 11.04 | SMA 20 | 3.55 | 25.04 |
| 21 | 7 | 11.04 | SMA 20 | 3.68 | 17.45 |
| 22 | 7 | 11.04 | SMA 20 | 1.51 | 16.08 |
| 23 | 7 | 11.04 | SMA 20 | 2.16 | 18.38 |
| 24 | 7 | 11.04 | SMA 20 | 4.83 | 20.90 |
| 25 | 7 | 11.04 | SMA 20 | 3.31 | 18.58 |
| 26 | 7 | 11.04 | SMA 20 | 1.92 | 17.95 |
| 27 | 7 | 11.04 | SMA 20 | 2.69 | 22.33 |
| 28 | 7 | 11.04 | SMA 20 | 3.14 | 17.77 |
| 29 | 7 | 11.04 | SMA 20 | 3.94 | 29.60 |
| 30 | 8 | 4.70 | Type "A" | 3.87 | 28.54 |
| 31 | 8 | 4.70 | Type "A" | 4.03 | 25.22 |
| 32 | 8 | 4.70 | Type "A" | 3.07 | 21.60 |
| 33 | 8 | 4.70 | Type "A" | 3.67 | 23.58 |
| 34 | 8 | 4.70 | Type "A" | 3.67 | 22.74 |
| 35 | 9 | 6.10 | SMA 10 | 3.92 | 26.80 |
| 36 | 9 | 6.10 | SMA 10 | 0.61 | 22.92 |
| 37 | 9 | 6.10 | SMA 10 | 4.42 | 28.29 |
| 38 | 9 | 6.10 | SMA 10 | 3.12 | 28.67 |
| 39 | 10 | 7.98 | SMA 15 | 2.17 | 18.68 |
| 40 | 10 | 7.98 | SMA 15 | 1.08 | 19.71 |
| 41 | 11 | 11.04 | SMA 20 | 1.34 | 27.54 |
| 42 | 11 | 11.04 | SMA 20 | 0.59 | 26.34 |
| 43 | 12 | 7.98 | SMA 15 | 1.40 | 21.40 |

| The sample number | The mix number | Average size of aggregate, D (mm) | Mix type | The degree of saturation, CV (%) | Prall test value, W^{ab} (cm ³) |
|-------------------|----------------|-------------------------------------|----------|------------------------------------|---|
| 44 | 12 | 7.98 | SMA 15 | 2.60 | 23.37 |
| 45 | 12 | 7.98 | SMA 15 | 2.02 | 18.40 |
| 46 | 13 | 11.04 | SMA 20 | 1.97 | 21.31 |
| 47 | 13 | 11.04 | SMA 20 | 3.20 | 26.58 |
| 48 | 13 | 11.04 | SMA 20 | 3.03 | 23.35 |
| 49 | 13 | 11.04 | SMA 20 | 3.50 | 26.84 |
| 50 | 14 | 7.98 | SMA 15 | 3.65 | 29.53 |
| 51 | 14 | 7.98 | SMA 15 | 2.12 | 27.53 |
| 52 | 15 | 6.10 | SMA 10 | 3.04 | 33.70 |
| 53 | 15 | 6.10 | SMA 10 | 0.51 | 28.30 |
| 54 | 16 | 7.98 | SMA 15 | 2.63 | 28.40 |
| 55 | 16 | 7.98 | SMA 15 | 3.85 | 28.90 |
| 56 | 16 | 7.98 | SMA 15 | 0.67 | 26.30 |
| 57 | 16 | 7.98 | SMA 15 | 2.44 | 30.70 |
| 58 | 17 | 7.98 | SMA 15 | 0.70 | 23.47 |
| 59 | 17 | 7.98 | SMA 15 | 2.41 | 25.20 |
| 60 | 18 | 11.04 | SMA 20 | 0.83 | 19.59 |
| 61 | 18 | 11.04 | SMA 20 | 0.53 | 20.01 |
| 62 | 19 | 6.10 | SMA 10 | 3.28 | 22.98 |
| 63 | 19 | 6.10 | SMA 10 | 3.62 | 26.67 |

Statistical values of the tested mixes are shown in Table 3.

Table 3. Mean abrasion value, standard deviation and coefficient of variation of every mixes test with the average of the values.

| The mix number | Mean abrasion value (cm ³) | Standard deviation (cm ³) | Coefficient of variation |
|----------------|--|---------------------------------------|--------------------------|
| 1 | 15.615 | 3.373 | 0.216 |
| 2 | 19.275 | 1.393 | 0.072 |
| 3 | 21.133 | 1.137 | 0.054 |
| 4 | 23.765 | 0.262 | 0.011 |
| 5 | 24.860 | 0.269 | 0.011 |
| 6 | 23.593 | 2.350 | 0.100 |
| 7 | 19.893 | 4.092 | 0.206 |
| 8 | 24.336 | 2.695 | 0.111 |
| 9 | 26.670 | 2.627 | 0.099 |
| 10 | 19.195 | 0.728 | 0.038 |
| 11 | 26.940 | 0.849 | 0.031 |
| 12 | 21.057 | 2.503 | 0.119 |
| 13 | 24.520 | 2.665 | 0.109 |
| 14 | 28.530 | 1.414 | 0.050 |
| 15 | 31.000 | 3.818 | 0.123 |
| 16 | 28.575 | 1.810 | 0.063 |
| 17 | 24.335 | 1.223 | 0.050 |
| 18 | 19.800 | 0.297 | 0.015 |
| 19 | 24.825 | 2.609 | 0.105 |
| Average | 23.575 | 1.901 | 0.083 |

The data obtained were analyzed using Eq. (11). To verify the approach, for each of the 19 groups of materials, the Prall test value for the asphalt concrete with zero connected void was calculated. The

minimum of the average coefficient of variation was found by changing the X coefficient value. The empirical X coefficient was found equal to 1.974 (Fig. 9).

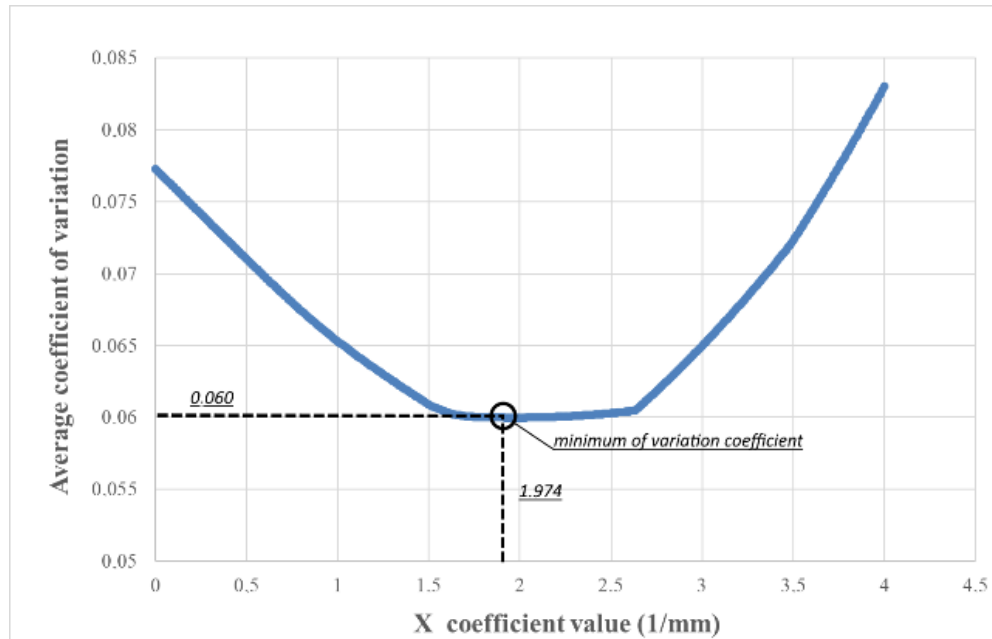


Figure 9. Average coefficient of variation depending on the X value.

The large minimum range of the graph and the presence of an obvious minimum indicates a good reliability of the approach and the obtained value of the coefficient X . The final value of abrasion loss for the asphalt concretes with zero value of connected voids is given in the table below (Table 4).

Table 4. Mean abrasion value, standard deviation and coefficient of variation of every mix obtained by Eq. 11 abrasion value.

| The mix number | Mean abrasion value (cm ³) | Standard deviation (cm ³) | Coefficient of variation |
|----------------|--|---------------------------------------|--------------------------|
| 1 | 12.787 | 0.736 | 0.058 |
| 2 | 17.433 | 0.967 | 0.055 |
| 3 | 18.734 | 0.966 | 0.052 |
| 4 | 20.975 | 0.494 | 0.024 |
| 5 | 21.863 | 0.324 | 0.015 |
| 6 | 18.712 | 1.788 | 0.096 |
| 7 | 16.013 | 2.778 | 0.174 |
| 8 | 21.436 | 2.185 | 0.102 |
| 9 | 23.420 | 1.248 | 0.053 |
| 10 | 17.690 | 1.382 | 0.078 |
| 11 | 25.265 | 0.110 | 0.004 |
| 12 | 18.987 | 2.087 | 0.110 |
| 13 | 19.939 | 1.352 | 0.068 |
| 14 | 24.529 | 0.237 | 0.010 |
| 15 | 28.704 | 1.387 | 0.048 |
| 16 | 25.217 | 1.458 | 0.058 |
| 17 | 22.461 | 0.286 | 0.013 |
| 18 | 18.939 | 0.552 | 0.029 |
| 19 | 21.467 | 2.031 | 0.095 |
| Average | 20.767 | 1.177 | 0.060 |

Using the particle loss model (Eq.11) reduces the variation coefficient of the test results from 0.083 to 0.060 and points to good reliability of the approach. In addition, the approach to evaluation of the

connected voids influence of asphalt concretes allows improving the laboratory abrasion tests precision due to ignoring the voids fraction influence in the comparison of the asphalt specimen's abrasion values.

Summary expression for the asphalt concretes with obtained X coefficient is shown below:

$$W_1^{ab} = \frac{W_2^{ab} \cdot (1 - D \cdot CV_2 \cdot 1.974/4) \cdot (1 - CV_2)}{(1 - D \cdot CV_1 \cdot 1.974/4) \cdot (1 - CV_1)} \quad (14)$$

Note that connected voids value in the expression is in fractions of a unit.

The obtained model and the expression does not contradict the existing model of the abrasive wear of composites, but complements it. A fast and reliable way to include the pores effect on the abrasive wear can effectively improve the precision of the abrasion resistance assessment.

This expression Eq. (14) allows us to calculate the degree of the connected voids influence on the abrasion resistance of the asphalt concrete. For the demonstration of the connected voids effect on the asphalt concrete, abrasion resistance evaluation of the relative abrasion resistance of asphalt concrete for the different connected voids values is presented in Fig. 10.

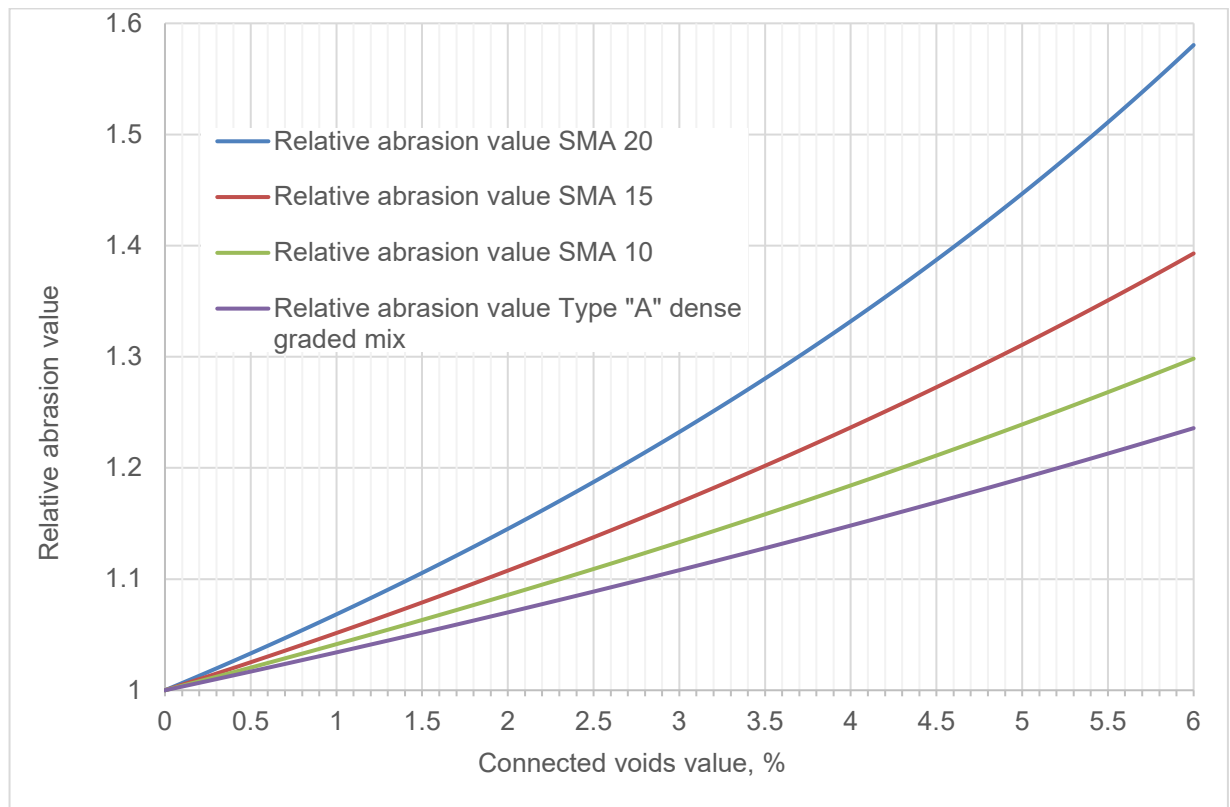


Figure 10. Calculated relative abrasion value for different mix types with different connected voids values.

The obtained dependence confirms the other studies results [8]. These results allow us to assess the abrasive wear resistance of asphalt concretes. For example, for SMA mixes to be reliable asphalt pavements, the Prall test value has to be less than 20 cm^3 to have the 1st class of the abrasion resistance in the case of uncompaction in the permissible limits by specifications (1 to 3.5 % of saturating water or the connected voids value). On the contrary, abrasion resistance can be reduced for the pavements with the stable compaction quality. This approach shows the vital role of compaction quality for the pavement life.

4. Conclusions

1. The existing models of composite abrasion have good accuracy for various types of composite and single materials but the asphalt concrete. Asphalt concrete is a unique composite structure, which consists of a hard reinforcement coarse aggregate, fine aggregate and binder presented by bitumen, mineral powder and various additives. Asphalt concrete in pavement as a material can contain pores and other inclusions which affect asphalt concrete. Various models obtaining asphalt properties were investigated, but the conventional model of asphalt concrete abrasive wear needs to be evaluated for the accurate prediction of the asphalt pavement behavior under loads.

2. The proposed model of asphalt concrete fragmentation under abrasive wear is based on two basic processes: normal abrasive wear of each component and particles loss (Fig. 4). Due to a large aggregate influence on the abrasive wear resistance, the latter has a big impact on abrasive wear. Normal abrasive wear of each component is a common task for the existing models of composites wear (Eq. (1–2)). However aggregate particles evaluation is a difficult problem. Based on the G.Y. Lee's approach, the presented model uses Khrushchev-Babichev wear model to estimate particles loss. The particles loss condition is based on the case when a part of particle surface lacks adhesion due to pores. The lack of adhesion and fraction loss calculations are a practical problem. It was solved with finding an empirical coefficient X (Eq.11). G.Y. Lee's approach can not be applied to the wear of asphalt concrete due to the complex loading conditions and difference of the aggregate size. The empirical coefficient calculation presented in this study allows us to modify the method for particle loss calculation.
3. The proposed model allows us to assess the abrasion resistance of the asphalt concrete and changes under various compaction conditions. An understanding of the particle loss process is necessary for the following research. The approach allows obtaining all the coefficients by laboratory tests for every type of material or an average coefficient for all types of the materials used.
4. The Prall test was used to verify the model. We tested 63 samples in 19 groups (Table 2). The mixes were sampled at the road construction works of the Republic of Tatarstan in 2018–2020. The saturation method was used to estimate pores volume fraction. In accordance with the mix grading (Fig. 3), the average particle size (Eq. (9)) was calculated. The standard deviation and the coefficient of variation were calculated for each mix (Table 3).
5. The experimental data show good reliability of the model. The average coefficient of variation was reduced from 8.3 % to a 6.00 % significantly improving the test accuracy. The empirical coefficient X was found equal to 1.974 (1/mm) for the mixes presented.
6. The obtained coefficient for materials used in the Russian Federation road construction and the modified G.Y. Lee's approach (Eq. (14)) allows assessing the connected voids and compaction effect on the abrasion resistance of materials and provides insight into the processes in asphalt concrete under hard winter loads.

References

1. Bajmukhametov, G. New methods of abrasion test in the road building. *Technique and Technology of Transport*. 2019. 11. Pp. 22.
2. Li, X., Zhang, K., Bahadori, A., Muhunthan, B. Modification of Asphalt Materials to Resist Studded-Tire Wear on Pavements. *Journal of Materials in Civil Engineering*. 2020. 32 (3). 04020023. DOI: 10.1061/(ASCE)MT.1943-5533.0003067
3. Horiuchi, K. Studless Tires Use in Japan. *SAE Transactions*. 1989. 98. Pp. 39–45.
4. KoNAGAI, N., Asano, M., Horita, N. Influence of Regulation of Studded Tire Use in Hokkaido, Japan. *Transportation Research Record*. 1993. 1387. Pp. 5.
5. Oberg, G. Socioeconomic Calculations for Winter Tires. *Transportation Research Board Conference Proceedings*. 1997. 16. Pp. 4.
6. Laurinavičius, A., Miškinis, D., Vaiškūnaitė, R., Laurinavičius, A. Analysis and Evaluation of The Effect of Studded Tyres on Road Pavement and Environment (III). *The Baltic Journal of Road and Bridge Engineering*. 2010. 5 (3). Pp. 169–176. DOI: 10.3846/bjrbe.2010.24
7. Zubeck, H., Aleshire, L., Harvey, S., Porhola, S., Larson, E. Socio-economic effects of studded tire use in alaska. *Alaska Department of Transportation and Public Facilities*, 2004.
8. Gayfutdinov, R., Bajmukhametov, G., Hafizov, E. Pavement wear process and abrasive wear resistance of asphalt concrete. *E3S Web of Conferences*. 2021. 274. 02008. DOI: 10.1051/e3sconf/202127402008
9. Ushakov, V., Jelagin, D., Dyakov, G., Dmitriev, S., Goryachev, M. Field evaluation of rutting in concrete pavements. *IOP Conference Series: Materials Science and Engineering*. 2020. 832 (1). 012033. DOI: 10.1088/1757-899X/832/1/012033
10. Abaza, O.A., Dahms, D. Performance Evaluation of Studded Tire Ruts for Asphalt Mix Designs in a Cold Region Environment. *Transportation Research Record: Journal of the Transportation Research Board*. 2021. 2675 (7). Pp. 32–44. DOI: 10.1177/0361198121994120
11. Snilsberg, B., Saba, R.G., Uthus, N. Asphalt pavement wear by studded tires – Effects of aggregate grading and amount of coarse aggregate. *Proceedings of 6th Eurasphalt & Eurobitume Congress*. 2016. DOI: 10.14311/EE.2016.072
12. Raitanen, N. Measuring of noise and wearing of quiet surfaces. *Espoo, Helsinki University of Technology* 2005, 2005.
13. Wen, H., Wu, S., Bhusal, S. Performance Evaluation of Asphalt Mixes Containing Steel Slag Aggregate as a Measure to Resist Studded Tire Wear. *Journal of Materials in Civil Engineering*. 2016. 28 (5). 04015191. DOI: 10.1061/(ASCE)MT.1943-5533.0001475
14. Zaltuom, A.M. A Review Study of The Effect of Air Voids on Asphalt Pavement Life. *Proceedings of First Conference for Engineering Sciences and Technology: Vol. 2*. 2018. Pp. 618–625. DOI: 10.21467/proceedings.4.29
15. Rodriguez-Hernandez, J., Andrés-Valeri, V., Calzada-Pérez, M., Vega-Zamanillo, Á., Castro-Fresno, D. Study of the Raveling Resistance of Porous Asphalt Pavements Used in Sustainable Drainage Systems Affected by Hydrocarbon Spills. *Sustainability*. 2015. 7(12). Pp. 16226–16236. DOI: 10.3390/su71215812

16. Badeli, S., Carter, A., Doré, G. The Importance of Asphalt Mixture Air Voids on the Damage Evolution During Freeze-Thaw Cycles. Proceedings of the Sixth-First Annual Conference of the Canadian Technical Asphalt Association (CTAA). 2016. Pp. 57–81.
17. Leon Raj, J., Chockalingam, T. Strength and abrasion characteristics of pervious concrete. Road Materials and Pavement Design. 2020. 21(8). Pp. 2180–2197. DOI: 10.1080/14680629.2019.1596828
18. Hassan, N.A., Mahmud, M.Z.H., Adi, N., Rahmat, N., Hainin, M.R., Jaya, R.P. Effects of air voids content on the performance of porous asphalt mixtures. ARPN Journal of Engineering and Applied Sciences. 2016. 11 (20). Pp. 5.
19. Şahin, Y., Şahin, H. Microstructure and Abrasive Wear of Particle-Filled Composites. Proceedings of the 8th International Conference on Fracture, Fatigue and Wear. Singapore, Springer Singapore, 2021. Pp. 623–634.
20. Prem Kumar, R., Girisha, L., Pravinprabu, T., Felix Sahayaraj, A., Santhosh Kumar, Sns., Subbiah, R. Analysis of abrasive wear resistance on scandium composite. Materials Today: Proceedings. 2021. Pp. S2214785321002923. DOI: 10.1016/j.matpr.2021.01.203
21. Lee, G.Y., Dharan, C.K.H., Ritchie, R.O. A physically-based abrasive wear model for composite materials. Wear. 2002. 252(3–4). Pp. 322–331. DOI: 10.1016/S0043-1648(01)00896-1
22. Korochkin, A.V. Influence of Type and Thickness of Cement-Concrete on the Calculation of Rigid Road Surfaces with Asphalt-Concrete Pavement. IOP Conference Series: Materials Science and Engineering. 2020. 753 (2). 022029. DOI: 10.1088/1757-899X/753/2/022029
23. Khanal, M., Morrison, R. Discrete element method study of abrasion. Minerals Engineering. 2008. 21 (11). Pp. 751–760. DOI: 10.1016/j.mineng.2008.06.008
24. Bahadori, A., Zhang, K., Xiaojun Li, Muhunthan, B. Development of Asphalt Materials to Mitigate Studded Tire Wear of Pavements. 2019. DOI: 10.13140/RG.2.2.23938.02243
25. Yi, J., Shen, S., Wang, D., Feng, D., Huang, Y. Effect of Testing Conditions on Laboratory Moisture Test for Asphalt Mixtures. Journal of Testing and Evaluation. 2016. 44 (2). Pp. 20150128. DOI: 10.1520/JTE20150128
26. Tuomala, A. Kiviaineksen laadun vaikutus asfalttipäällysteen nastarengaskulumiskestävyyyteen [The Effect of Aggregate's Quality on the Asphalt Pavement's Abrasion Resistance by Studded Tyres] Finnish Transport Infrastructure Agency. 2020. Pp. 162.
27. Mabui, D.S., Tjaronge, M.W., Adisasmita, S.A., Pasra, M. Resistance to cohesion loss in cantabro test on specimens of porous asphalt containing modified asbuton. IOP Conference Series: Earth and Environmental Science. 2020. 419 (1). 012100. DOI: 10.1088/1755-1315/419/1/012100
28. Strzałkowski, P., Kaźmierczak, U., Wolny, M. Assessment of the method for abrasion resistance determination of sandstones on Böhme abrasion test apparatus. Bulletin of Engineering Geology and the Environment. 2020. 79 (9). Pp. 4947–4956. DOI: 10.1007/s10064-020-01868-x

Information about authors:

Gadel Baimukhametov,

ORCID: <https://orcid.org/0000-0003-1892-006X>

E-mail: baimuhametovi@mail.ru

Rustem Gayfutdinov,

ORCID: <https://orcid.org/0000-0001-9927-6100>

E-mail: rustem_iben@list.ru

Edvard Khafizov, PhD in Technical Sciences

ORCID: <https://orcid.org/0000-0003-4227-1733>

E-mail: hafizov@kgasu.ru

Received 10.09.2021. Approved after reviewing 12.01.2024. Accepted 12.01.2024.



Research article

UDC 624.13

DOI: 10.34910/MCE.125.6



Numerical analysis of rainfall-induced slope instability using a reduced-scale model

F. Hamrouni¹ , M. Jamei²  , Y. Alassaf² 

¹ Tunis El Manar University, National Engineering School of Tunis, Civil Engineering Laboratory, Tunis, Tunisia

² Northern Border University, Arar, Saudi Arabia

 mehjamei@yahoo.fr

Keywords: climate changes, landslide, rainfall, finite element modeling, unsaturated soil, physical model

Abstract. The climatic changes induce now more and more serious environmental problems such as landslides, especially in arid and semi-arid countries where rainfalls happen with high and short duration intensity. This paper aims to study the influence of unsaturated mechanical properties on the slope instability. The research was conducted based on the combination of a physical model and numerical simulations with the aim to analyze rainfall-induced slope failure. The benefits of the proposed method are: 1) increase of monitoring efficiency by considering several parameters in large ranges of variation; 2) cost reduction by a combination of minimal laboratory physical model data and numerical modeling. In this study, the effect of rainfall intensity and duration as a hydraulic loading was investigated. The used model is an elastoplastic one based on effective stresses and a non-associative flow rule. A function of a reduction of mechanical parameters with suction was implemented in CODE_BRIGHT software. The results are presented in terms of: 1) displacement values; 2) evolution of pore water pressure (PWP); 3) plastic deviatoric strains and saturation zones.

Funding: The authors extend their appreciation to the Deanship of Scientific Research at Northern Border University, Arar, Saudi Arabia, for funding this research work through the project number “NBU-FFR-2024-2740-01”.

Citation: Hamrouni, F., Jamei, M., Alassaf, Y. Numerical analysis of rainfall-induced slope instability using a reduced-scale model. Magazine of Civil Engineering. 2024. 17(1). Article no. 12506. DOI: 10.34910/MCE.125.6

1. Introduction

Weathered shallow landslides have been observed in different regions in the world. In fact, climatic changes have led to many extreme weathering scenarios. Among them, the rainfalls which are more and more intensive and happen in a short duration, causing different environmental hazards such as landslides. Serious landslides have often occurred during or just after rainfall (a non-exhaustive example of disaster has occurred in the North West of Tunisia (Béja) [1, 2]). So, the objective of this study is to provide an expertise methodology, based on the consideration of the hydro-mechanical coupling for unsaturated soils. This expertise aims to: 1) provide a power modeling tool to reproduce some experimental results [1, 2]; 2) to evaluate the role of the main physical and hydraulic parameters (grain size distribution, density or porosity, saturated permeability) to explore how landslides occur and the shear band develops; 3) to inform about the influence of such numerical parameters as the mesh elements and the test of convergence.

Currently, to investigate the effects of the water pressure increase due to the rainfall water infiltration, various theoretical and numerical methods have been used. The limit analysis approach and the elastoplastic model using the so-called c-phi reduction method have been frequently used in the

engineering field. However, these approaches do not explicitly include the hydraulic-mechanical coupling stresses. Thus, in the last two decades, numerous studies have proposed several approaches considering hydraulic-mechanical coupling, which have provided a powerful tool for the prediction of the rainfall-induced landslide [2, 11]. Other researches have been also proposed to combine the modeling and field monitoring to evaluate the landslide risk [12].

In fact, some of the previously coupling approaches have considered the dependence of apparent cohesion, effective stress and friction angle with suction (and eventually the degree of saturation as function of void ratio), as well as the variation of permeability with the suction [2, 8, 9, 13]. Other approaches consider the suction or the degree of saturation as a state variable [8]. In addition, many rainfall-induced slope instability studies have focused on the role of the water retention properties under diverse rainfall scenarios on unsaturated slope stabilities [14, 17].

As noticed by experimental results, the increase of water table level is one of the most relevant conditions to landslide incidence [18–20]. The shear band, defined as a band where plastic shear strain is well developed in relation with the pore water pressure increase, which in the end, governs the failure mode. In order to deeply understand the mechanisms of such rainfall-induced failure, the study of coupling problems is now becoming an absolute need in the environmental engineering field. In this context, different reduced-scale slope models were developed to investigate the main conditions that cause slope failure and quantify the main factors that govern it under rainwater infiltration, particularly in extreme weather conditions, and under hydraulic and environmental cycles effects [20, 29].

Relevance of this study lies in the quantification, separately, of the unsaturated hydraulic parameters (unsaturated permeability and water retention function) and mechanical parameters leading to slope failure considering numerous types of soils. This study detailed the observations of the failure process, duration of soil moisture content development and pore-water pressure during the rainfall period. A pre-failure stage analysis was performed by plastic strain development. The CODE_BRIGHT program [30] was used, where the proposed model was implemented [18].

Indeed, the proposed model was based on the extension of effective stress concept to unsaturated soils, considering the cohesion reduction under humidification [8, 31, 33] (e.g., the reduction of the suction as an internal variable in the model).

The obtained numerical results show that for the long rainfall duration and for the well permeable soil, infiltration develops groundwater table from the bottom up, leading to matric suction loss in the transient unsaturated to saturated zone. Analysis of the strain evolution indicates that failure localization originates in the lower part and the shear zone develops through the superficial part to the upper part of the slope. The suction loss and the increase of the pore water pressure in the saturated zone, near the toe of the slope, are considered as the main factors leading to the slope failure.

2. Methods

2.1. The proposed hydro-mechanical model

As it is mentioned above, landslides may occur due to rapid reduction of suction under rainwater infiltration [3, 23, 34]. Obviously, experimental efforts are yet needed to link the mechanical parameters as stiffness, compressibility, cohesion and friction angle to the water content/degree of saturation and suction evolution and consider this issue in landslide analysis. For some authors, adding to the internal variables such the elastic and plastic deformation, the degree of saturation is considered as an internal variable [8]. This idea was firstly proposed by [31], and was open to debate based on experimental and theoretical evidence. At the first stage, various shear test results showed the influence of water content on friction and cohesion due to wetting-drying cycles [35, 36]. These tests highlighted the fact that the increase of water content (or saturation degree) has led to a decrease of the suction in the soil and consequently, the decrease of “apparent” cohesion and then the decrease of effective stresses. Obviously, the decrease of these mechanical parameters entailed a reduction in the soil shear strength.

In this paper, an elastoplastic model is proposed and formulated in an elastic and visco-plastic framework. A modified Mohr–Coulomb model based on effective stress (using an extended mathematical relation of [32]) has been proposed and implemented in the CODE_BRIGHT software. The algorithm of the resolution of the obtained iterative non-linear equations system was solved using a regularization method [18]. To find different previous forms of extended effective stresses formula, see, e.g. [33, 37, 39].

The suggested model defined the apparent cohesion as a nonlinear function of suction, thus leading to a non-linear shear strength-suction relationship [40].

We use here some results of triaxial drained tests conducted by [20], on the Kumano silty sand with initial relative densities (D_r , varied from 58 % to 86 %). The soil was used in a physical slope model. These tests showed a Young modulus dependency on suction, which varied in the range of 3–10 MPa.

The equations of the proposed model were implemented in the CODE_BRIGHT software. Table 1 and Table 2 summarize the mechanical and hydraulic equations (for more details about the implementation of hydro-mechanical model and the applied regularization method, see, e.g. [17, 18, 39]).

Table 1. Mechanical equations used in the model.

| Mechanical part of the model | | |
|---|---|--|
| Balance equations (the variable is the effective stress tensor of water pressure) | $Div(\sigma') = \gamma - Grad(u_w)$ | $Div(.)$ and $grad(.)$ are respectively the divergence and gradient operators. γ is the vertical volumetric force (vertical unit weight force) |
| The effective strain rate | $\dot{\varepsilon} = \frac{d\varepsilon}{dt} = \frac{d\varepsilon^e}{dt} + \frac{d\varepsilon^p}{dt}$ $\frac{d\varepsilon^e}{dt} = \underline{A} : \frac{d\sigma'}{dt}$ | ε^e and ε^p are respectively the elastic and plastic components of an effective strain tensor. Hooke's law was used to link the elastic tensor's components to the effective stress components. σ' is effective stress, \underline{A} is the behavior tensor with components depending on the stiffness E (function of suction) and Poisson's ratio ν (not dependent on the suction). |
| Plastic effective deformation (determined using a non-associative flow law) | $\frac{d\varepsilon^p}{dt} = \Gamma_0 \langle \Phi(F) \rangle \frac{\partial G}{\partial \sigma'}$ | Γ_0 (s^{-1}) is a fluidity parameter, F (MPa) is the yield function (Here is the Mohr–Coulomb function), G (MPa) is the plastic potential, Φ is a stress function. |
| The stress function | $\langle \Phi(F) \rangle = \begin{cases} 0 & \text{if } \Phi(F) < 0 \\ \Phi(F) = F^m & \text{if } \Phi(F) > 0 \end{cases}$ | m is a parameter which depends on the material. It is experimentally calibrated. For instance, m was calibrated by some primarily numerical tests and fixed at 3 (this calibration was convenient for the studied sandy soil which exhibited dilatancy). |
| The yield function (F) and the visco-plastic potential (G) | $F + c'\beta = q - \delta p'$ $G + c'\beta = q - \alpha \delta p'$ | α is a parameter to define non-associative plasticity rules. where $\delta = \frac{6\sin\phi'}{3 - \sin\phi'} \quad \text{and} \quad \beta = \frac{6\cos\phi'}{3 - \sin\phi'}$ |
| The first and second invariants p and q | $p = \frac{1}{3}(\sigma'_x + \sigma'_y + \sigma'_z)$ $q = \frac{1}{\sqrt{2}} \sqrt{(\sigma'_x - \sigma'_y)^2 + (\sigma'_y - \sigma'_z)^2 + (\sigma'_z - \sigma'_x)^2 + 6(\tau_{xy}^2 + \tau_{yz}^2 + \tau_{zx}^2)}$ c' is the effective cohesion and ϕ' is the effective friction angle. | |
| The effective stress | $\sigma'_{ij} = \sigma_{ij} - u_a \delta_{ij} + \chi(u_a - u_w) \delta_{ij}$ The general expression of the adapted cohesion is as follows $c = c' + (u_a - u_w) \tan\phi' \left(1 + \left(\frac{u_a - u_w}{P_0} \right)^{1-\lambda} \right)^{-\lambda}$ δ_{ij} is the Kroemer's symbol ($\delta_{ij} = 1$ if $i = j$; $\delta_{ij} = 0$ if $i \neq j$) | |

2.2. Hydraulic constitutive models

For numerical simulations, the needed hydraulic properties are the soil-water retention curve, the relative permeability variation with suction or degree of saturation and the variation of intrinsic permeability with porosity. The following table presents all the used functions (The relative permeability function [41], van Genuchten equation fitting the water retention curve [42] and the effective saturation S_e is defined by Mualem [43]).

Fig. 1 and 2 give respectively an example of experimental calibration of water retention function and intrinsic permeability.

Table 2. Hydraulic constitutive equations.

| | | |
|--|---|---|
| <p>The flow motion Richards equation</p> | $q_w = -\frac{k k_{rw}}{\mu_w} (\nabla u_w + \rho_w g \nabla z)$ | <p>q_w (m/s) is the flux of the water, and ∇u_w is the pressure gradient vector (Pa/m). K (m/s) represents the hydraulic conductivity, k (m²) the intrinsic permeability, ρ_w (kg/m³) the water density ($\rho_w = 10^3$ kg/m³), g (m/s²) the acceleration of gravity and μ_w (Pa.s) the dynamic viscosity of water ($\mu_w = 10^{-3}$ Pa.s). These parameters are fixed for a temperature $T = 20^\circ$.</p> |
| <p>The relative permeability function</p> | $k_{rw} = S_e^\xi$ | <p>S_e is the effective saturation. For numerical simulation $\xi = 3$.</p> |
| <p>And the intrinsic permeability</p> | $k = k_o \frac{n^3}{(1-n)^2} \frac{(1-n_o)^2}{n_o^3}$ | <p>n_o is the initial porosity and k_o is the saturated permeability corresponding to n_o. (For the calibrated experimental data, $k_o = 1.8 \cdot 10^{-11}$ m² and $n_o = 0.471$).</p> |
| <p>Van Genuchten equation fitting the water retention curve</p> | $S_e = \left(1 + \left(\frac{u_a - u_w}{P_0} \right)^{1-\lambda} \right)^{-\lambda}$ $S_e = \frac{S_r - S_{rmin}}{S_{rmax} - S_{rmin}}$ | <p>S_r is the saturation degree, S_{rmax} and S_{rmin} denotes respectively the maximum and the residual saturation degree, λ and P_0 are respectively the van Genuchten parameters (P_0 is a reference capillary pressure and λ is a shape's curve), (for the calibrated experimental data, $\lambda = 0.4$, $P_0 = 4 \cdot 10^{-4}$ MPa, $S_{rmax} = 1$ and $S_{rmin} = 0.22$).</p> |

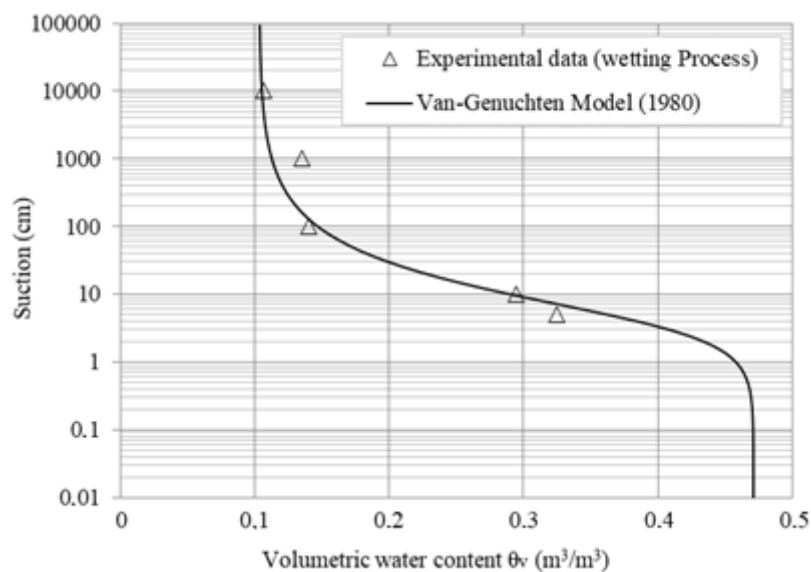


Figure 1. Fitting of water retention curve with experimental data [18].

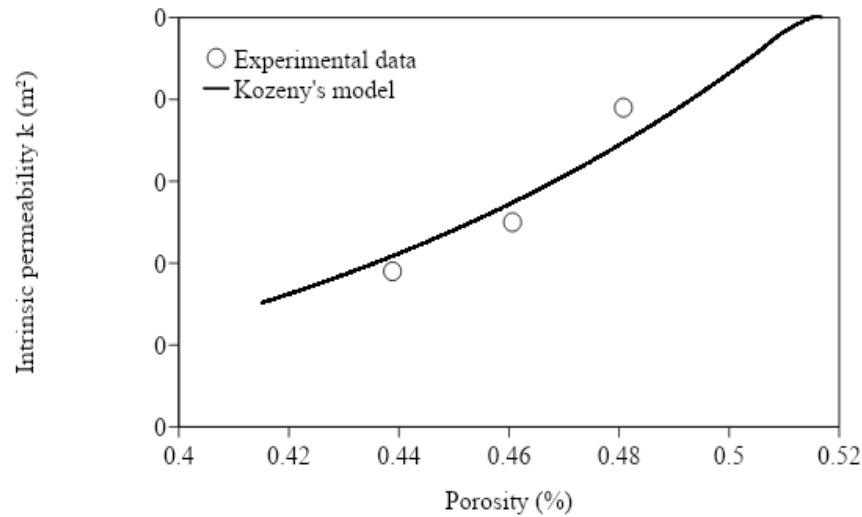


Figure 2. Saturated permeability as function of porosity for a silty sandy soil [18].

In the same context, Table 3 summarizes the modeling parameters values used in the simulations.

Table 3. Constitutive parameters.

| ELASTICITY | | |
|-----------------------------|-------------|--|
| Parameters | Value | Parameters definition |
| E (MPa) | 10 | Young's modulus |
| ν | 0.3 | Poisson's Ratio |
| VISCO-PLASTICITY PARAMETERS | | |
| Parameters | Value | Parameters' definition |
| m | 3 | Stress power |
| Γ_o (s^{-1}) | 1.10^6 | Viscosity coefficient (a high value is needed to approach the plastic behavior) |
| Q ($J\ mol^{-1}$) | 0.0 | Parameter for temperature dependency |
| c' | 0.0 | Total cohesion |
| $\tan \phi'$ | 0.4762 | |
| λ | 0.4 | $c = c' + (u_a - u_w) \tan \phi' \left[1 + \left(\frac{u_a - u_w}{P_0} \right)^{1-\lambda} \right]^{-\lambda}$ |
| P_0 | 4.10^{-4} | |
| α | 1.10^{-4} | Parameter to reduce dilatancy: a low value for the sandy soil case (which can exhibit dilatancy) |
| δ | 1.462 | $\delta = \frac{6 \sin \phi'}{3 - \sin \phi'}$ |

3. Results and Discussion

We employed the finite element code (CODE_BRIGHT) to build the geometry of the slope model, and used GiD pre- and post-processor [30, 44]. The slope's angle was 40 degrees. As indicated in Fig. 3 for the finite element mesh, the elements were of a four-node quadrilateral type. The numerical simulation was performed by taking into account the hydraulic and mechanical boundary conditions of the flow as shown in Fig. 3.

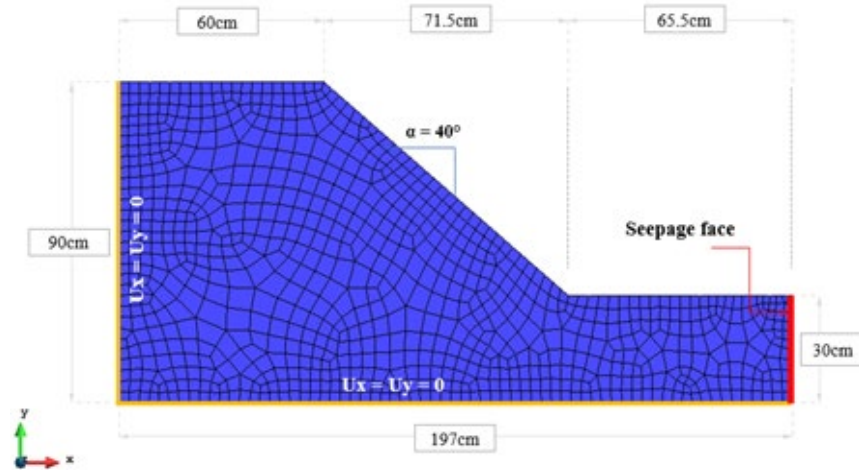


Figure 3. Geometry, hydraulic, and mechanical boundary conditions for the proposed numerical model.

Moreover, the simulations were performed in 2D with plane strain assumption. In order to study the effect of rainwater infiltration on slope stability, two numerical simulations were presented in this paper in Table 4.

Table 4. Reduced scale slope model characteristics, initial and boundary conditions.

| Model type | Type of Test | Initial and boundary conditions | Rainfall period |
|------------|--------------|---|-----------------|
| A | Rainfall | Slope angle $\alpha = 40\%$, porosity $n_0 = 0.471$, saturation degree $S_i = 30\%$, suction, $s = 12.85\text{kPa}$ and rainfall intensity $I = 50 \text{ mm/h}$ | 40000 sec |
| B | Rainfall | Slope angle $\alpha = 40\%$, porosity $n_0 = 0.415$, saturation degree $S_i = 30\%$, suction $s = 12.85\text{kPa}$ and rainfall intensity $I = 50 \text{ mm/h}$ | 20000 sec |

For the first test (Type A model as indicated in Table 4), the following figure shows the displacement and suction evolutions during the simulation and the obtained numerical results show that important displacements have occurred when the region near the toe of the slope becomes fully saturated. In addition, Fig. 4 confirms that important displacement (plastic deformation) occurred due the positive pore water pressure increase near the toe of the slope. Fig. 5 shows that the groundwater table begins to develop in the lower part of the slope and that the upper part remains unsaturated until the end of the simulation. On the other hand, Fig. 6 represents the positive pore water pressure isovalue at the end of the simulation. The obtained numerical results confirm that landslides occurred when the toe of the slope became saturated and positive pore water pressure developed. In our case, a superficial landslide occurred as shown in Fig. 7.

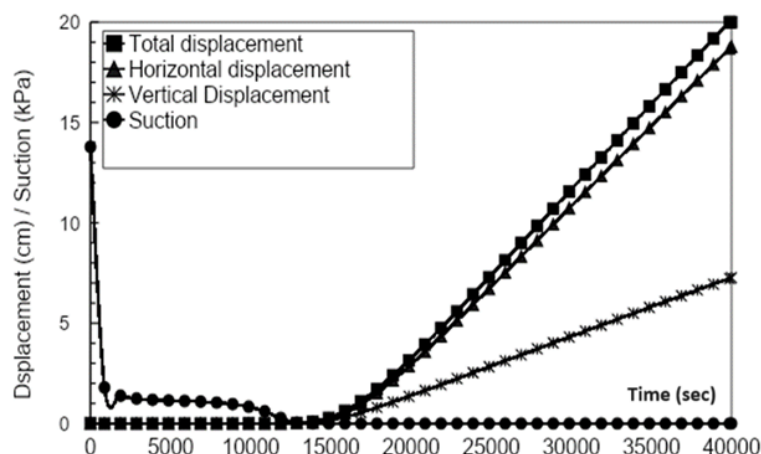


Figure 4. Displacement and suction against time for rainfall water infiltration.

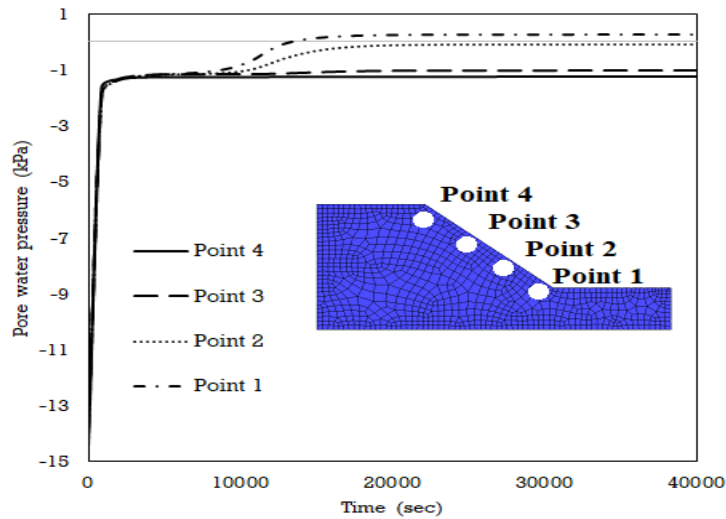


Figure 5. Pore water pressure in different points on the top layer of the slope.

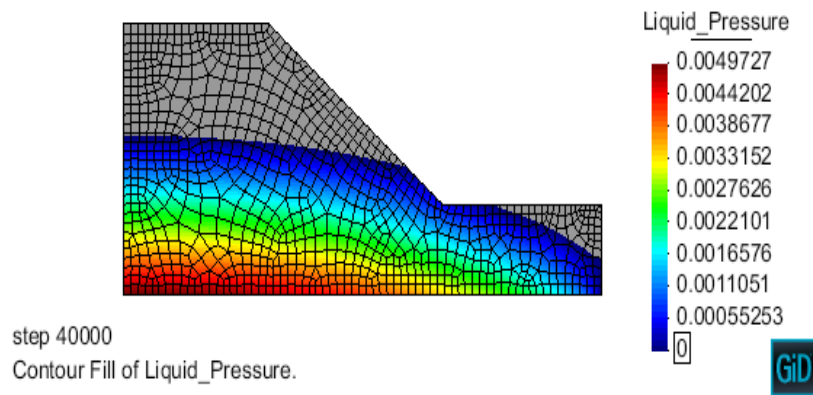


Figure 6. Positive pore water pressure isovalue at the end of infiltration period.

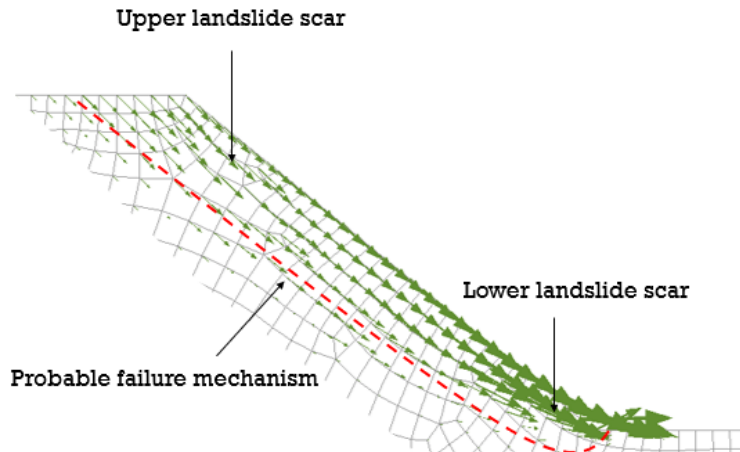


Figure 7. Vectors of incremental displacements at the end of rainwater infiltration.

In the second test, only the soil porosity and rainfall test duration were modified. Fig. 8 shows the numerical results of the vectors of incremental displacement and the contour of deviatoric plastic strain at the end of rainwater infiltration. The vectors of incremental displacements in Fig. 8 (a) delineate the most probable failure mechanism under current loading conditions. The consequences of rain infiltration on slope deformation are noticeable as the contours of accumulated deviatoric plastic strains ϵ_d^p in Fig. 8 (b) illustrate.

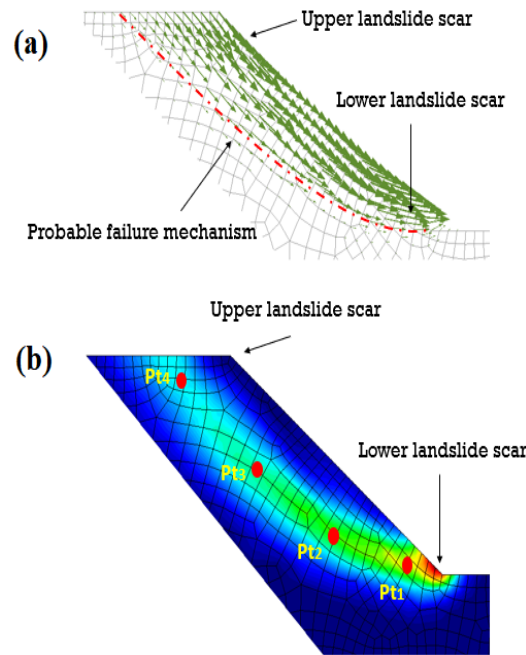


Figure 8. Vectors of incremental displacements and the contour of deviatoric plastic strains at the end of rainwater infiltration duration.

In this part of our simulation, an analysis of the temporal evolution of deviatoric plastic strains for different points located in the superficial layer of the slope allows identifying the most active shear zones during the water flow associated with the formation of a progressive failure mechanism (Fig. 9). Four different points, which are located in the shear zone identified in Fig. 8 (b), are selected for the analysis. At the beginning of rain infiltration, deviatoric plastic strain occurs in the shallow (Pt 1), lower part of the slope. Subsequently, plastic strain mobilized in the middle part (Pt 2) and finally in the upper part of the slope (Pts 3 and 4). As indicated, large irreversible shear strain occurred after 1200 sec of rainwater infiltration in the toe of the slope part. The most probable failure mechanism originates in the lower part of the slope, then the lower part is sheared and finally the shear zone spreads through the soil to the slope surface in the upper part.

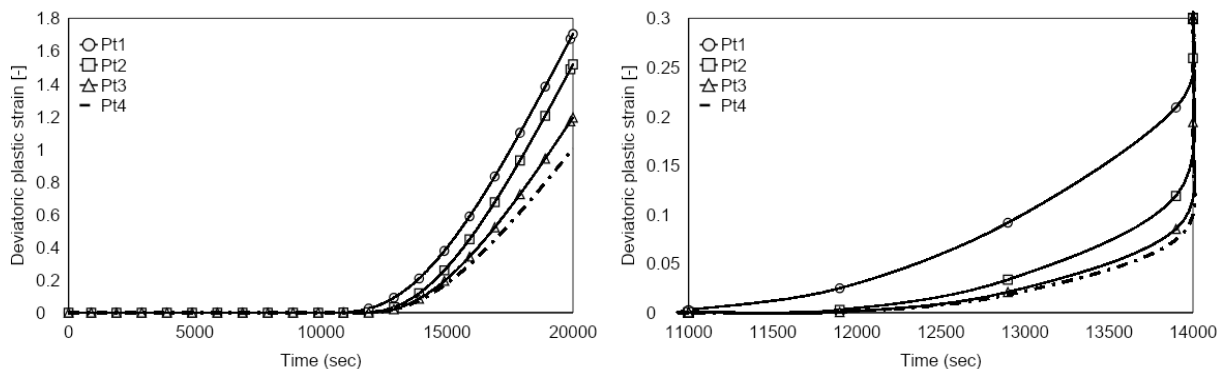


Figure 9. Evolution of deviatoric plastic strains in different superficial points.

4. Conclusions

Based on a current proposal of hydro-mechanical modeling, some conclusions can be given. Firstly, the introduced model modified Terzaghi's definition of the effective stresses by introducing parameter χ equal to the effective degree of saturation.

This means that the effective stresses change not only with water pressure, but also with the degree of saturation. The cohesion was formulated as a function of suction, and decreases along with suction. As a consequence, the soil shear strength decreases with the reduction in suction.

This model permitted the deformations calculation from the elastic state to plastic state until reaching the slope failure. This allowed us to analyze the progressive failure mechanism of one layer and multilayer slope.

In addition, we demonstrated that:

- The capillarity benefit was lost due to rainwater infiltration. Water infiltration led to an increase of pore water pressure (decrease of suction). The proposed numerical model also demonstrated its capability to correctly reproduce the pore water pressure distribution that triggers slope failure.
- The obtained numerical results show for the first time that rainwater infiltration leads to a loss in suction from the top slope layer. If the rainfall duration is long, the groundwater table level goes back up from the slope bottom. According to the analysis of plastic deformation in different parts of the slope, the failure mechanism originates in the lower part of the slope and the shear zone moves through the superficial part of the soil to the upper part of the slope. A large irreversible shear strain occurred, firstly in the toe of the slope due to the increase of pore water pressure and the decrease of the effective stress, and then a decrease in soil shear strength (which can be vanished in the extreme case) is considered as the main factor leading to the slope instability.
- The rainfall duration is a significant parameter for slope failure. The longer the duration is, the more rainwater infiltration happens. This induces local and shallow slope failure. If the duration is long, failure mass occurred more.
- The moved mass of soil is occurred according to a kinematic log-spiral line as it was proved for friction granular soils.
- Deviatoric plastic strain is a main parameter used for failure assessment. Large deviatoric strain was reached in the failure zone (20 %) and the plastic irreversible strain started from 2 % to localize the beginning of a failure zone.
- When suction tends to zero (saturated zone), total and horizontal displacements increase suddenly.
- Using unsaturated hydraulic permeability and water retention curve, effective cohesion and friction as main data, the model has the capability to introduce different initial hydraulic and environmental conditions (wetting-drying cycles) and hydro-mechanical boundary conditions (wetting by raining, drying by evaporation and the mechanical loading).

References

1. Olivella, S., Jamei, M., Guiras, H., Hamouda, K. Ben, Hatira, M., Olivella, S. A study of the slope stability in unsaturated marly clay soil. *Studia Geotechnica et Mechanica*. 2008. XXX (1-2).
2. Jamei, M., Guiras, H., Olivella, S. Analysis of slope movement initiation induced by rainfall using the Elastoplastic Barcelona Basic Model. *European Journal of Environmental and Civil Engineering*. 2015. 19(9). Pp. 1033–1058. DOI: 10.1080/19648189.2014.996670
3. Lee, K., Suk, J., Kim, H., Jeong, S. Modeling of rainfall-induced landslides using a full-scale flume test. *Landslides*. 2021. 18(3). Pp. 1153–1162. DOI: 10.1007/s10346-020-01563-8
4. Batali, L., Andreea, C. Slope Stability Analysis Using the Unsaturated Stress Analysis. Case Study. *Procedia Engineering*. 2016. 143. Pp. 284–291. DOI: 10.1016/j.proeng.2016.06.036
5. Borja, R.I., Liu, X., White, J.A. Multiphysics hillslope processes triggering landslides. *Acta Geotechnica*. 2012. 7(4). Pp. 261–269. DOI: 10.1007/s11440-012-0175-6
6. Kakogiannou, E., Sanavia, L., Nicot, F., Darve, F., Schrefler, B.A. A porous media finite element approach for soil instability including the second-order work criterion. *Acta Geotechnica*. 2016. 11(4). Pp. 805–825. DOI: 10.1007/s11440-016-0473-5
7. Klubertanz, G., Bouchelaghem, F., Laloui, L., Vulliet, L. Miscible and immiscible multiphase flow in deformable porous media. *Mathematical and Computer Modelling*. 2003. 37(5–6). Pp. 571–582. DOI: 10.1016/S0895-7177(03)00050-5
8. Khalili, N., Geiser, F., Blight, G.E. Effective Stress in Unsaturated Soils: Review with New Evidence. *International Journal of Geomechanics*. 2004. 4(2). Pp. 115–126. DOI: 10.1061/(asce)1532-3641(2004)4:2(115)
9. Qi, S., Vanapalli, S.K. Simulating Hydraulic and Mechanical Responses of Unsaturated Expansive Soil Slope to Rainfall: Case Study. *International Journal of Geomechanics*. 2018. 18(6). Pp. 1–17. DOI: 10.1061/(asce)gm.1943-5622.0001106
10. Rahimi, A., Rahardjo, H., Leong, E.C. Effect of hydraulic properties of soil on rainfall-induced slope failure. *Engineering Geology*. 2010. 114(3–4). Pp. 135–143. DOI: 10.1016/j.enggeo.2010.04.010
11. Sanavia, L. Numerical modelling of a slope stability test by means of porous media mechanics. *Engineering Computations (Swansea, Wales)*. 2009. 26(3). Pp. 245–266. DOI: 10.1108/02644400910943608
12. Chen, P., Lu, N., Formetta, G., Godt, J.W., Wayllace, A. Tropical Storm-Induced Landslide Potential Using Combined Field Monitoring and Numerical Modeling. *Journal of Geotechnical and Geoenvironmental Engineering*. 2018. 144(11). DOI: 10.1061/(asce)gt.1943-5606.0001969
13. Karube, D., Kawai, K. The role of pore water in the mechanical behavior of unsaturated soils. *Geotechnical and Geological Engineering*. 2001. 19(3–4). Pp. 211–241. DOI: 10.1023/A:1013188200053
14. Pham, K., Lee, H., Kim, D., Lee, I.M., Choi, H. Influence of hydraulic characteristics on stability of unsaturated slope under transient seepage conditions. *Landslides*. 2018. 15(9). Pp. 1787–1799. DOI: 10.1007/s10346-018-0989-x
15. Pham, K., Kim, D., Choi, H.J., Lee, I.M., Choi, H. A numerical framework for infinite slope stability analysis under transient unsaturated seepage conditions. *Engineering Geology*. 2018. 243. Pp. 36–49. DOI: 10.1016/j.enggeo.2018.05.021
16. Ran, Q., Hong, Y., Li, W., Gao, J. A modelling study of rainfall-induced shallow landslide mechanisms under different rainfall characteristics. *Journal of Hydrology*. 2018. 563. Pp. 790–801. DOI: 10.1016/j.jhydrol.2018.06.040.

17. Hamrouni, F., Trabelsi, H., Jamei, M. Numerical Analysis of the Drilled Horizontal Drains Efficiency in Physical Slope Model: The Role of the Soil Water Retention Property. *Geotechnical and Geological Engineering*. 2022. 40(1). Pp. 195–211. DOI: 10.1007/s10706-021-01894-w
18. Hamrouni, F., Trabelsi, H., Jamei, M., Olivella, S. Numerical analysis of landslides caused by rainfall in a reduced physical slope model. *European Journal of Environmental and Civil Engineering*. 2019. DOI: 10.1080/19648189.2019.1580223
19. Kim, J., Kim, Y., Jeong, S., Hong, M. Rainfall-induced landslides by deficit field matric suction in unsaturated soil slopes. *Environmental Earth Sciences*. 2017. 76(23). Pp. 1–17. DOI: 10.1007/s12665-017-7127-2
20. Orense, R.P., Shimoma, S., Maeda, K., Towhata, I. Instrumented Model Slope Failure due to Water Seepage. *Journal of Natural Disaster Science*. 2004. 26(1). Pp. 15–26. DOI: 10.2328/jnds.26.15
21. Chueasamat, A., Hori, T., Saito, H., Sato, T., Kohgo, Y. Experimental tests of slope failure due to rainfalls using 1g physical slope models. *Soils and Foundations*. 2018. 58(2). Pp. 290–305. DOI: 10.1016/j.sandf.2018.02.003
22. Orense, R.P. Slope Failures Triggered by Heavy Rainfall. *Philippine Engineering Journal Pej*. 2004. 25(2). Pp. 73–90.
23. Damiano, E., Olivares, L. The role of infiltration processes in steep slope stability of pyroclastic granular soils: Laboratory and numerical investigation. *Natural Hazards*. 2010. 52(2). Pp. 329–350. DOI: 10.1007/s11069-009-9374-3
24. Hakro, M.R., Harahap, I.S.H. Laboratory experiments on rainfall-induced flowslide from pore pressure and moisture content measurements. *Natural Hazards and Earth System Sciences Discussions*. 2015. 3(2). Pp. 1575–1613. DOI: 10.5194/nhessd-3-1575-2015
25. Yan, J. fan, Shi, B., Ansari, F., Zhu, H. hu, Song, Z. pu, Nazarian, E. Analysis of the strain process of soil slope model during infiltration using BOTDA. *Bulletin of Engineering Geology and the Environment*. 2017. 76(3). Pp. 947–959. DOI: 10.1007/s10064-016-0916-0
26. Ling, H., Ling, H.I. Centrifuge Model Simulations of Rainfall-Induced Slope Instability. *Journal of Geotechnical and Geoenvironmental Engineering*. 2012. 138(9). Pp. 1151–1157. DOI: 10.1061/(asce)gt.1943-5606.0000679
27. Montrasio, L., Valentino, R. A model for triggering mechanisms of shallow landslides. *Natural Hazards and Earth System Science*. 2008. 8(5). Pp. 1149–1159. DOI: 10.5194/nhess-8-1149-2008
28. Montrasio, L., Schilirò, L., Terrone, A. Physical and numerical modelling of shallow landslides. *Landslides*. 2016. 13(5). Pp. 873–883. DOI: 10.1007/s10346-015-0642-x
29. Sasahara, K., Sakai, N. Development of shear deformation due to the increase of pore pressure in a sandy model slope during rainfall. *Engineering Geology*. 2014. 170. Pp. 43–51. DOI: 10.1016/j.enggeo.2013.12.005.
30. Olivella, S., Gens, A., Carrera, J., Alonso, E.E. Numerical formulation for a simulator (CODE_BRIGHT) for the coupled analysis of saline media. *Engineering Computations (Swansea, Wales)*. 1996. 13(7). Pp. 87–112. DOI: 10.1108/02644409610151575
31. Laloui, L., Nuth, M. On the use of the generalised effective stress in the constitutive modelling of unsaturated soils. *Computers and Geotechnics*. 2009. 36(1–2). Pp. 20–23. DOI: 10.1016/j.compgeo.2008.03.002
32. Lu, N., Khalili, N., Nikooee, E., Hassanizadeh, S.M. Principle of Effective Stress in Variably Saturated Porous Media. *Vadose Zone Journal*. 2014. 13(5). Pp. vj2014.04.0038. DOI: 10.2136/vj2014.04.0038
33. Lu, N., Godt, J.W., Wu, D.T. A closed-form equation for effective stress in unsaturated soil. *Water Resources Research*. 2010. 46(5). Pp. 1–14. DOI: 10.1029/2009wr008646
34. Ali, T., Showkat, R., Babu, G.L.S. Hydro-Mechanical Simulations of Unsaturated Soil Slope. *Indian Geotechnical Journal*. 2021. 51(4). Pp. 861–869. DOI: 10.1007/s40098-021-00554-3
35. Fredlund, D.G., Vanapalli, S.K., Rahardjo, H. Use of linear and nonlinear shear strength versus matric suction relations in slope stability analyses. *Landslides; proceedings of the sixth international symposium*. 1992. 6 (January 2021). Pp. 531–537.
36. Fredlund, D.G., Vanapalli, S.K. Shear Strength of Unsaturated Soils. *Methods of Soil Analysis, Part 4: Physical Methods*. 2018. 321. Pp. 329–361. DOI: 10.2136/sssabookser5.4.c15
37. Lu, N., Likos, W.J. Suction Stress Characteristic Curve for Unsaturated Soil. *Journal of Geotechnical and Geoenvironmental Engineering*. 2006. 132(2). Pp. 131–142. DOI: 10.1061/(asce)1090-0241(2006)132:2(131)
38. Zhang, L.L., Fredlund, D.G., Fredlund, M.D., Ward Wilson, G. Modeling the unsaturated soil zone in slope stability analysis. *Canadian Geotechnical Journal*. 2013. 51(12). Pp. 1384–1398. DOI: 10.1139/cgj-2013-0394
39. Zeng, F., Li, Y., Labuz, J.F. Paul-Mohr-Coulomb Failure Criterion for Geomaterials. *Journal of Geotechnical and Geoenvironmental Engineering*. 2018. 144(2). Pp. 1–5. DOI: 10.1061/(asce)gt.1943-5606.0001829
40. Damiano, E., Olivares, L., Picarelli, L. Steep-slope monitoring in unsaturated pyroclastic soils. *Engineering Geology*. 2012. 137–138. Pp. 1–12. DOI: 10.1016/j.enggeo.2012.03.002
41. Mualem, Y. Hydraulic conductivity of unsaturated porous media: Generalized macroscopic approach. *Water Resources Research*. 1978. 14(2). Pp. 325–334. DOI: 10.1029/WR014i002p00325
42. Genuchten, V.M. A closed-form equation for predicting the hydraulic conductivity of unsaturated soils. *Soil Science Society of America Journal*. 1980. 44(5). Pp. 892–898.
43. Mualem, Y. A new model for predicting the hydraulic conduc. *Water Resources Research*. 1976. 12(3). Pp. 513–522.
44. Vaunat, J., Nord, C. Code _ Bright / Gid : a 3-D Program for Thermo-Hydro-Mechanical Analysis in. Pp. 3–6.

Information about authors:

Facker Hamrouni,

ORCID: <https://orcid.org/0000-0002-6165-2550>

E-mail: fakher.hamrouni@gmail.com

Mehrez Jamei, Doctor of Science

ORCID: <https://orcid.org/0000-0002-9430-3920>

E-mail: mehjamei@yahoo.fr

Yahya Alassaf, PhD

ORCID: <https://orcid.org/0000-0002-9430-3920>

E-mail: yahya.lassaf@nbu.edu.sa

Received 24.05.2022. Approved after reviewing 09.01.2023. Accepted 16.01.2023.



Research article

UDC 691.3

DOI: 10.34910/MCE.125.7



Enhancing lightweight concrete strength through modified zeolite-alkaline porous aggregate: composition optimization and structural application


O.I. Matveeva ¹, N.K. Baishev ², A.I. Makarov ² , A.L. Popov ^{2,3}  , I.R. Pavlyukova ⁴,
N.A. Grigoriev ²

¹ YakutPNIS-Commercial Center, Yakutsk, Russian Federation

² North-Eastern Federal University named after M. K. Ammosov, Yakutsk, Russian Federation

³ Institute of Problems of Oil and Gas of the Siberian Branch of the Russian Academy of Sciences, Yakutsk, Russian Federation

⁴ JSC Yakutsk State Design, Research Institute of Construction, Yakutsk, Russian Federation

 surrukin@gmail.com

Keywords: lightweight concrete, porous aggregate, modified zeolite, strength characteristics, structural application, composition optimization

Abstract. The work is aimed at research of technology of lightweight concrete with porous aggregate with improved strength characteristics to expand the field of its application in reinforced concrete structures. The lack of demand for lightweight concrete in structural construction is due to its low reliability in view of the increased ultimate deformation of compression and tension. However, as recent studies show, when taking into account the ultimate compressive strain of lightweight concrete, it is quite possible to ensure the reliability of such structures. In order to expand the scope of application of light concretes in bearing layers of multilayered enclosing and bearing reinforced concrete structures, our purpose was to determine the features of the lightweight concrete composition selection technique with improved characteristics using a porous aggregate of modified zeolite-alkaline charge. Empirical equations of dependence of lightweight concrete strength on concrete density and aggregate density as well as dependence of lightweight concrete strength on coarse aggregate volume concentration and aggregate strength were established to determine rational compositions of lightweight concrete. The possibility of producing structural lightweight concrete of strength classes B15 to B27.5, with the frost-resistance mark F_1 150 with the use of porous aggregate modified zeolite-alkaline batch is shown.

Citation: Matveeva, O.I., Baishev, N.K., Makarov, A.I., Popov, A.L., Pavlyukova, I.R., Grigoriev, N.A. Enhancing lightweight concrete strength through modified zeolite-alkaline porous aggregate: composition optimization and structural application. Magazine of Civil Engineering. 2024. 17(1). Article no. 12507. DOI: 10.34910/MCE.125.7

1. Introduction

Currently, a large volume of experimental and theoretical studies devoted to the study of physical-mechanical and thermal properties of lightweight concretes on glassy porous aggregates has been accumulated [1–3]. Analysis of the works indicates that researchers have developed effective aggregates for light concretes with increased content of glassy phase, which open up new possibilities of improving the whole complex of properties of light concretes and structures from them. Promising glassy aggregates with partially or completely amorphous grain structure include: granulated foam glass, granulated foam glass

ceramics and other similar aggregates with a closed cellular structure and bulk density of less than 250 kg/m³, on the basis of which it is possible to obtain light concrete with a density grade D600-D800 and with a strength class up to B2.5. [4, 5]. Major research is aimed at obtaining lightweight high-strength concrete with expanded areas of application using alternative aggregates, including waste glass sand (WGS), municipal solid waste incineration bottom ash (MSWI-BA), recycled coarse aggregates (RCA), fly ash (FA), waste rubber (WR), steel waste (SW), and waste plastic (WP), etc. [6–8].

We have made an attempt to develop compositions of light structural zeolite concretes for the manufacture of load-bearing layers of multilayer enclosing, load-bearing reinforced concrete structures (wall panels) and load-bearing reinforced concrete structures for low-rise construction (walls, lintels, floor slabs and overlaps) with specified properties: B15; D1600, F₁100. For this purpose, previous studies have produced pilot batch of foam-zeolite porous aggregate on the production base of LLC "Suntarzeolit" with bulk density of 680–740 kg/m³ (bulk density mark M700-800) and a strength of 2.45–2.63 MPa (grade of strength P100-P125).

However, when selecting the composition of concrete, we encountered low verification of the actual properties of concrete with the calculated ones. This fact is due to the fact that the existing methods of selection are suitable either for heavy concretes with a density of 2200–2800 kg/m³ [9, 10] or for light concretes with a density of less than 800 kg/m³ [11]. The inefficiency of concretes with a density of 1000–1800 kg/m³ is due to intermediate values of the properties of lightweight concrete, which does not allow their use in energy-efficient construction as a heat insulating material due to insufficiently low thermal conductivity and in structural engineering because of low reliability in view of the increased ultimate deformation of compression and tension. As one of the options for combining such concretes, scientists from Beirut Arab University considered the option of a reinforced concrete beam with lightweight concrete in the tension zone. However, the presence of lightweight aggregate in the tension zone tends to cause brittle failure of the beam [12]. To increase the relevance of the use of lightweight intermediate density concretes, researchers from the University of the West of England, Bristol, describe the ultimate compressive strain of lightweight concrete by a linear dependence on the ultimate compressive strain of heavyweight concrete, described by the coefficient η :

$$\eta = 0.4 + 0.6 \frac{P}{2200}. \quad (1)$$

If you take into account this figure it is possible to calculate a reinforced concrete beam of lightweight concrete with ultimate compressive strain of 2.18 % and a reduction in reinforcement to 47 % [13]. Also, scientists from Anhui Jianzhu University, China, who were able to simulate the fatigue life of lightweight concrete on porous aggregate using the Weibull distribution, are studying the reliability of lightweight concrete in reinforced concrete structures [14]. Increasing the durability of lightweight concrete on porous aggregates is related to water absorption and porosity of lightweight aggregates, and as the team of authors from Republic of Korea, Germany, Poland and Egypt emphasize, the aggregate used should either be artificially treated to close open pores or artificial porous aggregate with closed surface pores should be used [15]. Alternatively, cold granulation aggregates with closed porosity have been proposed, which uses cement as a binder and filler in the form of fly ash [16] or aggregates from industrial wastes such as POS [17].

Thus, the development of technology of lightweight concrete with porous aggregate with improved durability characteristics to expand its application in the load-bearing layers of multilayer enclosing, load-bearing reinforced concrete structures (wall panels) and load-bearing reinforced concrete structures for low-rise construction (walls, lintels, roof slabs and floor slabs) is relevant.

The aim of the study is to establish the technology and peculiarities of selecting the composition of lightweight concrete using porous aggregate from modified zeolite-alkaline charge that improves its properties. As the first step towards achieving this goal, the task was set to clarify the method for selecting the composition of lightweight concrete by deriving new dependencies for the influence of the quantitative and qualitative composition of components on the strength and density of concrete. The method was also tested.

2. Materials and Methods

When selecting the composition of lightweight concrete, the following components were used: as a binder, Portland cement grade CEM I 32,5B by Interstate Standard 31108-2016, produced by JSC PA Yakutement with the characteristics indicated in Table 1; river sand was used as a fine dense aggregate from the Lena River floodplain (Table 2); porous aggregate of the pilot batch manufactured by Suntarzeolite LLC is used as a coarse aggregate (Table 3); as the plasticizing additive used was an additive for concrete and mortars produced by JSC Polyplast (LLC Polyplast-UralSib) – Superplasticizer SP-1.

Table 1. Properties of used Portland cement.

| No. | Cement quality index | Unit. | Value |
|-----|--|-------|------------|
| 1 | Cement strength class | MPa | 32.5 |
| 2 | Flexural/compression strength at 2 days of age | MPa | 3.8 / 16.8 |
| 3 | Compressive strength after steaming | MPa | 27.1 |
| 4 | Uniformity of volume change | mm | 0.0 |
| 5 | Normal cement density | % | 26.5 |
| 6 | Mass fraction of sulfur oxide (VI) SO ₃ | % | 2.55 |
| 7 | Mass fraction of chloride ion | % | 0.026 |
| 8 | Initial setting time | min | 135 |
| | Information about clinker: | | |
| | - C ₃ S + C ₂ S | % | 76.55 |
| 9 | - CaO/SiO ₂ | - | 3.09 |
| | - MgO | - | 2.12 |
| 10 | Signs of a false setting | - | no |

Table 2. Grain composition of used sand.

| No. | Indicator name | Unit. | Requirements of Interstate Standard 8736-2014 | Actual value |
|-----|---|-------------------|---|--------------|
| 1 | 2 | 3 | 4 | 5 |
| 1. | Bulk density | kg/m ³ | not regulated | 1444 |
| 2. | Total residue on sieve with mesh No. 063, % by mass | % | up to 10 | 0.06 |
| 3. | The content of grains smaller than 0.16 mm | % | no more than 20 | 4.84 |
| 4. | Modulus of grain size | Mod. | from 1.0 to 1.5 for the "very fine" group | 1.09 |
| | The content of grains in coarseness, by mass: | | | |
| 5. | more than 10 mm. | % | not more than 0.5 | 0.10 |
| | more than 5 mm. | | not more than 10 | 0.00 |
| 6. | Content of dusty and clayey particles | % | not more than 5 for class II sand | 0.25 |
| 7. | Clay content in clumps | % | not more than 0.5 for class II sand | 0.00 |
| 8. | True density | g/cm ³ | 2.0 to 2.8 | 2.62 |
| 9. | The content of organic impurities | standard | lighter than the standard | lighter |
| 10. | Hollowness | % | not regulated | 44.89 |

Experimental studies of the initial materials (fine and coarse aggregates) were carried out in accordance with the following regulatory documents:

- Interstate Standard 9758-2012 "Non-organic porous aggregates for construction work. Test methods". Controllable characteristics of foam-zeolite.
- Interstate Standard 8735-88 "Sand for construction work. Testing methods". Controllable characteristics of dense sand.

Concrete mixtures and concretes were tested in accordance with the following standards:

- Interstate Standard 10181-2000 "Concrete mixtures. Methods of testing". Controllable characteristics of concrete mixtures;
- Interstate Standard 10180-2012 "Concretes. Methods for strength determination using reference specimens";
- Interstate Standard 12730.1-78 "Concretes. Methods of determination of density";
- Interstate Standard 12730.2-78 "Concretes. Method of determination of moisture content";
- Interstate Standard 10060-2012 "Concretes. Methods for determination of frost-resistance";

- Interstate Standard 7076-99 "Building materials and products. Method of determination of steady-state thermal conductivity and thermal resistance".

Table 3. Physical and mechanical properties of the experimental batch of foam-zeolite.

| No. | Name of indicators | Requirements of Interstate Standard 32496-2013 | Actual value |
|-----|--|--|--------------|
| 1 | 2 | 3 | 4 |
| | Bulk density, kg/m ³ | | |
| 1. | fr. 5 -10 (screening) | 600 to 700 for M700 | 696 |
| | fr. 10-20 | 700 to 800 for M800 | 733 |
| | Crushing strength of foam-zeolite in a cylinder, MPa | | |
| 2. | fr. 5 -10 (screening) | 2.0 to 2.5 for P100 | 2.31 |
| | fr. 10-20 | 2.5 to 3.3 for P125 | 2.53 |
| 3. | True density, g/cm ³ | | 2.40 |
| | Average density, g/cm ³ | | |
| 4. | fr. 5 -10 (screening) | Not rationed | 1.12 |
| | fr. 10-20 | | 1.25 |
| | Resistance against silicate decay, % | | |
| 5. | fr. 5 -10 (screening) | No more than 5 | 1.93 |
| | fr. 10-20 | | 1.77 |
| | Resistance to ferrous decay, % | | |
| 6. | fr. 5 -10 (screening) | No more than 5 | 1.56 |
| | fr. 10-20 | | 1.32 |
| 7. | Mass loss on ignition, % | No more than 3 | 1.20 |
| | Mass loss by boiling, % | | |
| 8. | fr. 5 -10 (screening) | No more than 5 | 2.87 |
| | fr. 10-20 | | 2.53 |
| | Softening coefficient | | |
| 9. | fr. 5 -10 (screening) | At least 0.75 | 0.77 |
| | fr. 10-20 | | 0.85 |
| | Grain shape coefficient | | |
| 10. | fr. 5 -10 (screening) | No more than 1.5 | 1.21 |
| | fr. 10-20 | | 1.37 |
| | Water absorption, % | | |
| 11. | fr. 5 -10 (screening) | No more than 20 | 15.04 |
| | fr. 10-20 | | 13.86 |
| | Frost resistance grade (weight loss after 3 cycles of testing in sodium sulfate solution, %) | | |
| 12. | fr. 5 -10 (screening) | F15 (No more than 8) | F15 (4.38) |
| | fr. 10-20 | | F15 (5.65) |

The calculation of the composition of lightweight concrete with porous aggregate is based on Interstate Standard 27006, reference book "Artificial porous aggregates and lightweight concrete on their basis" [18], normative and industrial edition "Recommendations on the selection of lightweight concrete compositions (for Interstate Standard 27006-86)" [11].

The average strength of the class when making selections is assigned equal to the strength of the concrete with a coefficient of variation $V_n = 13.5\%$. To do this, the specified concrete class is multiplied by the specified strength coefficient K_T equal to the specified coefficient of variation.

$$R = B \cdot K_T, \quad (2)$$

where B is the strength value corresponding to the adopted class of concrete, MPa; K_T is coefficient of specified strength.

According to the reference manual "Artificial porous aggregates and lightweight concretes based on them". [18], the ultimate strength of concrete can be achieved depending on the mass strength of the coarse aggregate and is calculated by the following formula:

$$R = 2R_{ag.} \frac{1-\varphi}{0.5}, \quad (3)$$

where $R_{ag.}$ is the grade strength of coarse aggregate; φ – volumetric concentration of coarse aggregate.

Immediately, you can calculate the consumption of coarse aggregate K :

$$K = 1000 \cdot \varphi \cdot \rho_{ag.}, \quad (4)$$

$\rho_{ag.}$ is average aggregate density, g/cm³.

The dependence of cement consumption on the density of concrete is described by the formula:

$$\rho_{con.} = 0.97\rho_{ag.} + C(1.15 - 0.4\rho_{ag.}), \quad (5)$$

where $\rho_{ag.}$ is the average density of the aggregate, g/cm³; $\rho_{con.}$ is average density of concrete, g/cm³.

Then the cement consumption (C) can be found according to the derived formula, g/cm³:

$$C = \frac{\rho_{con.} - 0.97\rho_{ag.}}{1.15 - 0.4\rho_{ag.}}. \quad (6)$$

Next, the amount of fine aggregate required is calculated by the formula:

$$V_P = (1000 - (C/\rho_{cs}) - \varphi \cdot 1000) \cdot \alpha, \quad (7)$$

where ρ_{cs} is the true density of cement stone, kg/l; α is coefficient of grain separation equal to 1.12.

The amount of fine aggregate (P) in the absolute volume of aggregates is calculated by the formula:

$$P = V_S \cdot \rho_b, \quad (8)$$

where ρ_b is the bulk density of the sand used, kg/l.

The water flow rate is calculated by the formula:

$$B = B_0 + B_1 + B_2, \quad (9)$$

where B_0 is the initial consumption of water, taken according to the methodological manual for the grade of workability P1 with the use of plasticizer equal to 165 liters per cubic meter.

B_1 and B_2 are correction for water consumption of fine and coarse aggregate, determined by the following formulas:

$$B_1 = 0.025 \frac{P}{\rho_P} (W_P - 7), \quad (10)$$

$$B_2 = \frac{0.75(B_0 + B_1)}{C} \cdot \frac{(W_K - 15)}{100} \times K. \quad (11)$$

The optimal amount of additives, if any, is determined by the manufacturer's recommendations.

According to the provisions of doctoral dissertation of A.N. Davidyuk for aggregates grade P15-50 an updated formula (12) is proposed for formula (3), calculated on the basis of experimental data [19, 20].

$$R = 1.1 \cdot R_{ag} \cdot e^{\left(1.8 \cdot \frac{1-\phi}{0.5}\right)} \quad (12)$$

This formula with exponential growth of the influence of the volumetric concentration of coarse aggregate is more correct. Further calculation of the composition of lightweight concrete continues by formulas 4–11.

In this work, our task was to derive experimental formulas for the ultimate strength of concrete depending on the strength of coarse aggregate, which will make it possible to predict the physical and mechanical properties of concrete on the basis of non-standard properties of foam-zeolite on the basis of modified charge from the experimental batch.

3. Results and Discussion

An analysis of empirical data from early studies and tests of lightweight concretes on porous aggregates has been carried out and equations with exponential growth of strength depending on concrete density and aggregate density have been derived (Table 4, Fig. 1). According to sources, the minimum voids content of materials of the same fraction varies from 33 % to 47.7 % depending on the topology [21, 22]. Then when grouping aggregate by density when using it in cement stone with a true density of 2.65 g/cm³, it is possible with a step that will be equal to the difference of the minimum hollowness multiplied by the true density of the cement stone, which is approximately 300 kg/m³.

If the task of selecting the composition of lightweight concrete satisfies the dependencies shown in the figure, you can carry out further calculations according to this methodology.

From the empirical data of earlier studies (Table 5), formula 12 is corrected for porous aggregates of different grades of strength with a grouped step of 2.2–2.5 MPa (formulas 13–15).

Table 4. Properties of lightweight concrete depending on the density of aggregates used

| Density grade of aggregate | Concrete density | | Concrete strength | |
|----------------------------|------------------|------|-------------------|------|
| From M150 to M450 | ---* | | | |
| | 1100 | 1600 | 5.9 | 25 |
| From M500 to M800 | 1185 | 1150 | 7.8 | 7 |
| | 1100 | 1150 | 6.5 | 8.3 |
| | 1500 | 1000 | 17 | 5 |
| | 1672 | 1916 | 19 | 26.4 |
| From M900 to M1200 | 1708 | 1919 | 17.8 | 33.2 |
| | 1975 | 1610 | 28.6 | 11.5 |
| | 1944 | 1637 | 25.9 | 11.9 |
| | 1958 | 1649 | 33 | 16.8 |
| | 1929 | | 35.6 | |

* For a given aggregate grade, the equation of dependence is taken according to the source [20].

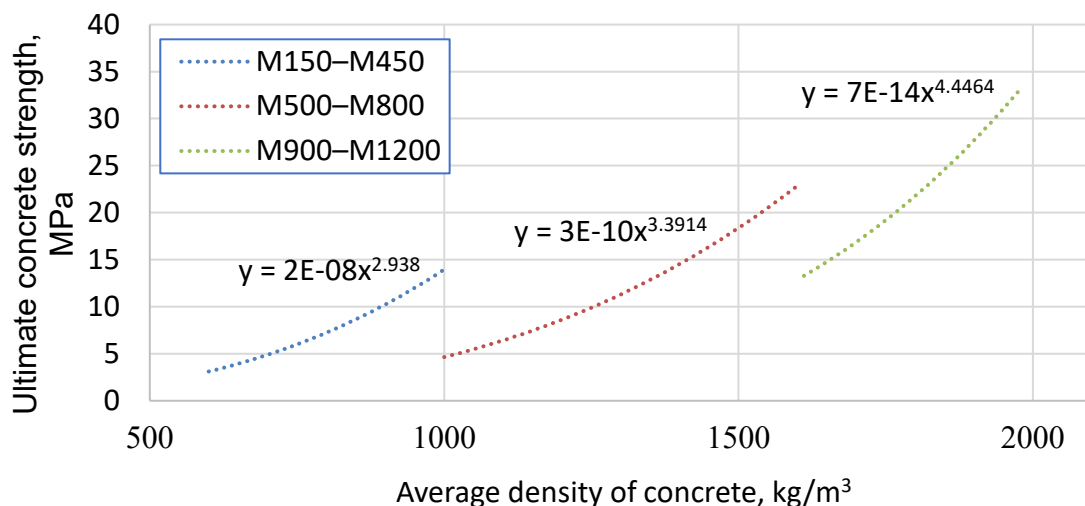


Figure 1. Experimental equations for the dependence of concrete strength on concrete density and aggregate density.

Table 5. Properties of lightweight concrete depending on the strength of the aggregates used.

| Strength grade of the aggregate | Volume concentration of coarse aggregate | Concrete strength |
|---------------------------------|--|-------------------|
| P15–50 ($R_{ag.} = 0.8$) | --- | --- |
| P75–125 ($R_{ag.} = 3.3$) | 0.4 | 13 |
| | 0.5 | 11 |
| | 0.6 | 9 |
| P150–250 ($R_{ag.} = 5.5$) | 0.4 | 19.5 |
| | 0.54 | 19.5 |
| | 0.57 | 25 |
| P300–400 ($R_{ag.} = 8$) | 0.4 | 28 |
| | 0.5 | 26 |
| | 0.6 | 23 |

* For a given aggregate grade, the equation of dependence is taken according to the source [20].

For aggregate grade P75-125:

$$R = 1.03 \cdot R_{ag.} \cdot e^{\left(1.14 \frac{1-\varphi}{0.5}\right)} \quad (13)$$

For aggregate grade P150–250:

$$R = -2.5 \cdot \left(\frac{1-\varphi}{0.5}\right)^2 + 18.5 \cdot \frac{1-\varphi}{0.5} + 0.98 \cdot R_{ag.} \quad (14)$$

For aggregate grade P300–400:

$$R = -5.3 \cdot \left(\frac{1-\varphi}{0.5}\right)^2 + 23.2 \cdot \frac{1-\varphi}{0.5} + 0.94 \cdot R_{ag.} \quad (15)$$

A graphical representation of the dependence of concrete strength on the volumetric concentration of coarse aggregate was also obtained (Fig. 2). The dependence for stronger aggregates is described by a quadratic function, and for less strong aggregates by an exponential function. As a confirmation in the work of the authors from Nanjing University of Aeronautics and Astronautics, China, the effect of coarse aggregate volume concentration with an aggregate strength of 10 MPa, is also described by a quadratic function. However, in their case, an increase in aggregate fraction greater than 0.61 is accompanied by an increase in concrete strength, which we cannot agree with [23].

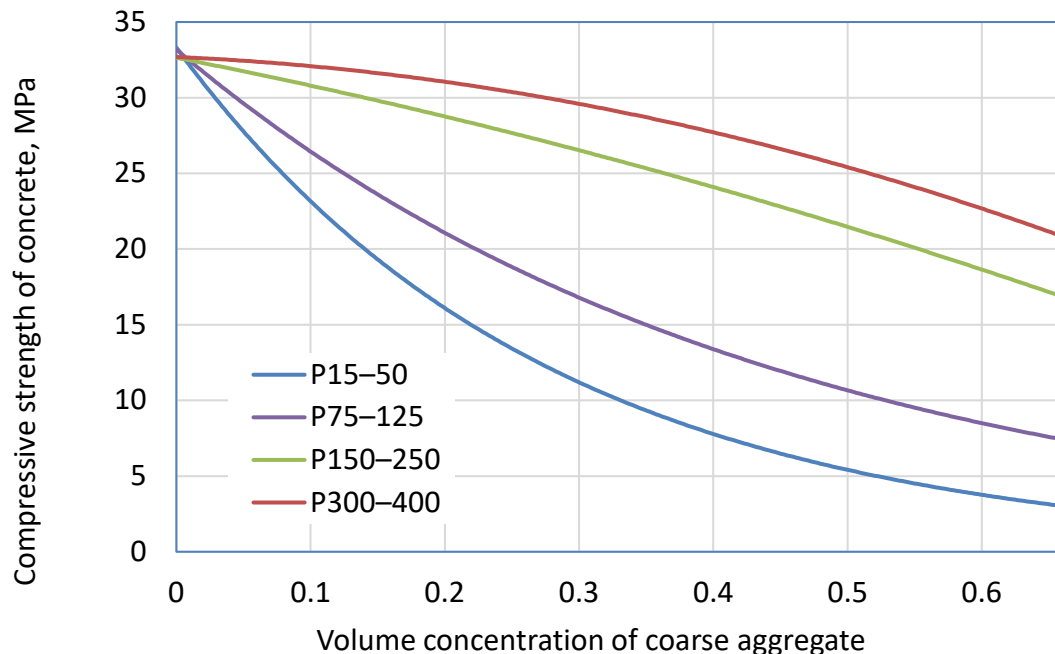


Figure 2. The dependence of the strength limit of concrete on the volume concentration of coarse aggregate of different grades of compressive strength in the cylinder.

From the formulas you can calculate the required volume concentration of aggregate to achieve a given strength, depending on the initial.

For aggregate grade P15-50:

$$\varphi = 1 - 0.28 \cdot \ln \left(\frac{R}{1.1 \cdot R_{ag.}} \right). \quad (16)$$

For aggregate grade P75-125:

$$\varphi = 1 - 0.44 \cdot \ln \left(\frac{R}{1.03 \cdot R_{ag.}} \right). \quad (17)$$

For aggregate grade P150-250:

$$\varphi = 1 - \left(\frac{R_{ag.}}{110} \right) \times (37 - 2.24 \cdot \sqrt{317 - 8 \cdot R}). \quad (18)$$

For aggregate grade P300-400:

$$\varphi = 1 - \left(\frac{R_{ag.}}{848} \right) \times (116 - \sqrt{17431 - 530 \cdot R}). \quad (19)$$

Further calculation of the composition of lightweight concrete can continue with the formulas 4–11.

A selection task was made to test the porous filler and the methodology (Table 6).

According to the methodology, the concrete compositions shown in Table 7 were calculated. The nominal composition (0) was obtained, according to the calculation, and was adjusted to obtain the density of concrete according to the selection card of the composition.

In additional compositions (1–3) varied the consumption of cement downward. According to the developed compositions of concrete mixtures cone slump and density of concrete mixtures were determined for compliance with the brand for workability and density control (Table 8). The actual consumption of concrete mixes was determined according to Interstate Standard 27006-2019 "Concretes. Rules for mix proposing". The average discrepancy between the components of the calculated composition and the actual – 9.1 %.

Table 6. Task for selection of lightweight concrete.

| Indicator | Defined properties and characteristics of starting materials |
|--|--|
| Compressive strength class | B15 |
| Density grade | D1500 |
| Grade of workability | P1 |
| Frost resistance grade | F ₁₅₀ |
| Terms of manufacture of products and structures: | |
| - molding | Vibrocompacting |
| - solidification | Steaming at 80° C |
| Raw materials: | |
| Binder | |
| Strength class | CEM I 32.5B Yakutcement, JSC PA |
| Fine aggregate | River sand from the Lena River floodplain |
| Grain modulus of sand, Mod. | 1.09 |
| Bulk density, kg/m ³ | 1444 |
| True density, g/cm ³ | 2.62 |
| Water consumption, % | 10 |
| Coarse aggregate | LLC Suntarzeolite |
| Foam-zeolite fractions 5-10 | |
| Bulk density grade | M700 (696 kg/m ³) |
| Strength grade | P100 (2.31 MPa) |

| Indicator | Defined properties and characteristics of starting materials |
|------------------------------|--|
| Water absorption, % | 15.04 |
| Foam-zeolite fractions 10-20 | |
| Bulk density grade | M800 (733 kg/m ³) |
| Strength grade | P125 (2.53 MPa) |
| Water absorption, % | 13.86 |
| Chemical additive | SP-1 |

Table 7. Concrete compositions.

| Component | Consumption per 1 m ³ , kg | | | | | | | | | | | |
|-----------|---------------------------------------|--------|--------------|-------|--------|--------------|-------|--------|--------------|-------|--------|--------------|
| | 0 | | | 1 | | | 2 | | | 3 | | |
| | Calc. | Actual | Δ , % | Calc. | Actual | Δ , % | Calc. | Actual | Δ , % | Calc. | Actual | Δ , % |
| PCG 10-20 | 375 | 413 | 9.2 | 254 | 279 | 9.0 | 254 | 279 | 9.0 | 254 | 279 | 9.0 |
| PCG 5-10 | 386 | 425 | 9.2 | 508 | 559 | 9.1 | 508 | 559 | 9.1 | 508 | 559 | 9.1 |
| Cement | 442 | 486 | 9.1 | 400 | 440 | 9.1 | 350 | 385 | 9.1 | 300 | 330 | 9.1 |
| Sand | 421 | 463 | 9.1 | 238 | 262 | 9.2 | 300 | 330 | 9.1 | 363 | 399 | 9.0 |
| Water | 195 | 215 | 9.3 | 197 | 217 | 9.2 | 204 | 224 | 8.9 | 213 | 234 | 9.0 |
| SP-1 0,5% | 2.21 | 2.4 | 7.9 | 2 | 2.2 | 9.1 | 1.75 | 1.9 | 7.9 | 1.5 | 1.7 | 11.8 |

Table 8. Properties of concrete mixes.

| Indicator, unit | Composition number | | | |
|----------------------------|--------------------|------|------|------|
| | 0 | 1 | 2 | 3 |
| Cone draft, cm | 0 | 0 | 1 | 0 |
| Density, kg/m ³ | 1730 | 1620 | 1510 | 1580 |

The results of checking the properties of light concretes are given in Table 9. The results obtained showed compliance of properties of zeolite concretes of the selected compositions with the requirements of Interstate Standard 25820, the task of selecting lightweight concrete composition with a large margin of safety factor and are comparable to the characteristics of lightweight concretes developed by various leading researches [24, 25] and accepted in structural calculations [26].

Table 9. Established grades of zeolite concretes in accordance with the requirements of Interstate Standard 25820-2121 "Lightweight concretes. Specifications".

| Number (marking) of composition | Mark of lightweight concrete by average density D | Compressive strength class of lightweight concrete B | Lightweight concrete frost resistance grade F ₁ | Heat-water coefficient, W/ (m ² °C) | Classification of concrete according to its main purpose |
|---------------------------------|---|--|--|--|--|
| Composition No. 0 of 05.09.2022 | D1700 | B27.5 | F ₁₅₀ | 0.52 | Structural |
| Composition No. 1 08.09.22 | D1600 | B25 | - | 0.52 | Structural and thermal insulation |
| Composition No. 2 08.09.22 | D1500 | B15 | - | 0.53 | Structural and thermal insulation |
| Composition No. 3 08.09.22 | D1550 | B20 | F ₁₅₀ | 0.50 | Structural and thermal insulation |

4. Conclusion

The research performed to establish the technology and peculiarities of selecting the composition of lightweight concrete using porous aggregate from modified zeolite-alkaline charge, which improves its properties, has determined the following:

1. The empirical equations for the dependence of lightweight concrete strength on concrete density and aggregate density and the dependence of lightweight concrete strength on the volumetric concentration of coarse aggregate and aggregate strength have an exponential trend.
2. In the derived dependencies, the average discrepancy between the components of the calculated composition of lightweight concrete with the actual is 9.1 %, but the margin of assured strength in the samples obtained suggests the need for further work to clarify the methods of calculation of lightweight concrete composition.
3. It is shown that the porous aggregate – M700-M800, P100-P125 foam-zeolite can produce structural lightweight concrete of strength classes from B15 to B27.5, with F₁₅₀ freeze-thaw-resistance grades. The developed compositions of concretes expand the scope of their use for load-bearing structures, including elements of the framework of buildings and structures.

Thus, the possibility of improving the characteristics of lightweight concrete by obtaining a more refined methodology for selecting the composition is shown. Further research should be aimed at obtaining the dependences of concrete characteristics on the quantitative and qualitative composition of components using numerical modeling methods and mutual verification with experimental data to obtain the most reliable method for selecting the composition of lightweight concrete on porous aggregate.

References

1. Ting, T.Z.H., Rahman, M.E., Lau, H.H., Ting, M.Z.Y. Recent development and perspective of lightweight aggregates based self-compacting concrete. *Construction and Building Materials*. 2019. 201. Pp. 763–777. DOI: 10.1016/J.CONBUILDMAT.2018.12.128
2. Hong, S.H., Choi, J.S., Yuan, T.F., Yoon, Y.S. A review on concrete creep characteristics and its evaluation on high-strength lightweight concrete. *Journal of Materials Research and Technology*. 2023. 22. Pp. 230–251. DOI: 10.1016/J.JMRT.2022.11.125
3. Tanyıldızı, M., Gökalp, İ. Utilization of pumice as aggregate in the concrete: A state of art. *Construction and Building Materials*. 2023. 377. 131102. DOI: 10.1016/J.CONBUILDMAT.2023.131102
4. Baishev, N., Matveeva, O., Popov, P., Semenov, K. Otsenka energoeffektivnosti zhilogo doma s razlichnymi variantami konstruktivnykh sten s primeneniem stenovykh blokov iz legkogo tseolitobetona [Assessment of the energy efficiency of a residential building with different variants of wall construction using wall blocks of lightweight zeolite concrete]. *Sovremennye problemy stroitel'stva i zhizneobespecheniia: bezopasnost', kachestvo, energo- i resursosberezhenie* [Modern problems of construction and life support: safety, quality, energy and resource saving]. 2022. Pp. 15–20.
5. Mestnikov, A.E., Pavlov, D.G. Vozmozhnosti proizvodstva granulirovannogo penostekliannogo materiala v usloviakh Iakutii. [Possibilities of production of granulated foam-glass material in the conditions of Yakutia]. *Sovremennye tendentsii razvitiia nauki i tekhnologii* [Modern trends in the development of science and technology]. 2016. 1–8. Pp. 32–35.
6. Jahami, A., Issa, C.A. Exploring the use of mixed waste materials (MWM) in concrete for sustainable Construction: A review. *Construction and Building Materials*, 2023. 398. 132476.
7. Jahami, A., Khatib, J., Raydan, R. Production of Low-Cost, High-Strength Concrete with Waste Glass as Fine Aggregates Replacement. *Buildings* 2022. 12. 2168.
8. Khatib, J., Jahami, A., El Kordi, A., Sonebi, M., Malek, Z., Elchamaa, R., Dakkour, S. Effect of municipal solid waste incineration bottom ash (MSWI-BA) on the structural performance of reinforced concrete (RC) beams. *Journal of Engineering, Design and Technology*. 2023. 21(3). Pp. 862–882.
9. Rekomendatsii po podboru sostavov tyazhelykh i melkozernistykh betonov [Recommendations for the selection of heavy and fine-grained concrete compositions]. Moscow: Minstroj Rossii, 2016.
10. Standard practice for selecting proportions for normal, heavyweight, and mass concrete. 211.1–91. Michigan, American Concrete Institute (ACI), 2009.
11. Rekomendatsii po podboru sostavov legkikh betonov (k GOST 27006-86) [Recommendations for the selection of heavy and fine-grained concrete compositions]. Moscow: Gosstroj SSSR, 1990.
12. Khatib, J., Jahami, A., Baalbaki, O. Flexural Characteristics of Reinforced Concrete Beams Containing Lightweight Aggregate in the Tensile Zone. *SSRN Electronic Journal*. 2019. DOI: 10.2139/ssrn.3523048
13. Nukah, P.D., Abbey, S.J., Booth, C.A., Nounu, G. Development of a Lytag-silica fume based lightweight concrete and corresponding design equation for pure bending. *Case Studies in Construction Materials*. 2023. 18. e01970. DOI: 10.1016/J.CSCM.2023.E01970
14. Dengke, W., Gaozhan, Z., Yang, L., Qingjun, D. Experimental investigation and reliability prediction of high performance concrete based on lightweight aggregate under 4-point bending loading. *Case Studies in Construction Materials*. 2023. 18. e01804. DOI: 10.1016/J.CSCM.2022.E01804
15. Chung, S.Y., Sikora, P., Kim, D.J., El Madawy, M.E., Abd Elrahman, M. Effect of different expanded aggregates on durability-related characteristics of lightweight aggregate concrete. *Materials Characterization*. 2021. 173. 110907. DOI: 10.1016/J.MATCHAR.2021.110907
16. Shaiksha Vali, K., Bala Murugan, S. Impact of manufactured fiber aggregate in the production of lightweight concrete. *Materials Today: Proceedings*. 2022. 65. Pp. 1690–1696. DOI: 10.1016/J.MATPR.2022.04.712
17. Tale Masoule, M.S., Bahrami, N., Karimzadeh, M., Mohasanati, B., Shoaie, P., Ameri, F., Ozbakkaloglu, T. Lightweight geopolymer concrete: A critical review on the feasibility, mixture design, durability properties, and microstructure. *Ceramics International*. 2022. 48(8). Pp. 10347–10371. DOI: 10.1016/J.CERAMINT.2022.01.298
18. Gorlov, Yu.P. Ed. *Iskusstvennye poristyie zapolniteli i legkie betony na ikh osnove. Spravochnoe posobie* [Artificial porous aggregates and light concretes based on them. Reference Guide]. Moscow: Stroizdat, 1987. 304 p.
19. Davidiuk, A.N. *Legkie betony na steklogranuliatakh* [Lightweight concretes on glass granulates]. *Stroitel'nye materialy*. 2007. 7. Pp. 6–7.

20. Davidiuk, A.N., Davidiuk, A.A. Prochnostnye svoistva legkikh betonov na steklovidnykh zapolnitiakh dlia mnogoslainnykh ograzhdaiushchikh konstruksii [Strength properties of light concretes on glassy aggregates for multilayer enclosing structures]. Beton i zhelezobeton. 2008. 6. Pp. 9–13.
21. Zimakova, G.A., Sharko, P.V., Rublev, D.S., Shestakova, S.S. Optimizatsiia granulometricheskogo sostava kak metod povysheniia strukturno-prochnostnykh kharakteristik betona [Optimization of granulometric composition as a method of increasing the structural-strength characteristics of concrete]. Arkhitekturno-stroitel'nyy i dorozhno-transportnyy kompleksy: problemy, perspektivy, innovatsii [Architectural and Construction and Road-Transport Complexes: Problems, Prospects, Innovations]. Omsk: SibADI, 2020. Pp. 655–660.
22. Belov, V.V., Obratsov, I.V. Optimizatsiia struktury melkozernistogo karbonatnogo betona s primeneniem komp'iuternogo modelirovaniia [Optimization of fine-grained carbonate concrete structure using computer modeling]. Vestnik Volgogradskogo gosudarstvennogo arkhitekturno-stroitel'nogo universiteta. Seriya: Stroitel'stvo i arkhitektura. 2013. 31–2 (50). Pp. 555–562.
23. Wu, Z., Zhang, J., Yu, H., Ma, H., Fang, Q. 3D mesoscopic analysis on the compressive behavior of coral aggregate concrete accounting for coarse aggregate volume and maximum aggregate size. Composite Structures. 2021. 273. Pp. 114271. DOI: 10.1016/J.COMPSTRUCT.2021.114271
24. Jia, Z., Aguiar, J., de Jesus, C., Castro, F., Cunha, S. Physical and mechanical properties of lightweight concrete with incorporation of ceramic mold casting waste. Materialia. 2023. 28. 101765. DOI: 10.1016/J.MTLA.2023.101765
25. Sujatha, A., Deepa Balakrishnan, S. Properties of high strength lightweight concrete incorporating crushed coconut shells as coarse aggregate. Materials Today: Proceedings. 2023. DOI: 10.1016/J.MATPR.2023.03.201
26. Im, C.R., Yang, K.H., Kim, S., Mun, J.H. Flexural performance of lightweight aggregate concrete columns. Engineering Structures. 2022. 251. 113545. DOI: 10.1016/J.ENGSTRUCT.2021.113545

Contacts:

Olga Matveeva, PhD in Technical Sciences

E-mail: matveeva_oi@mail.ru

Nikolay Baishev,

E-mail: nbaishev@gmail.com

Andrey Makarov,

ORCID: <https://orcid.org/0000-0001-7226-9859>

E-mail: andrmakarov16@mail.ru

Aleksandr Popov, PhD in Technical Sciences

ORCID: <https://orcid.org/0000-0002-7829-6839>

E-mail: surrukin@gmail.com

Irina Pavlyukova,

E-mail: pavlyukova-irina@mail.ru

Nikolay Grigoriev,

E-mail: matsugauser@mail.ru

Received 20.04.2023. Approved after reviewing 12.01.2024. Accepted 19.01.2024.



Research article

UDC 626.31

DOI: 10.34910/MCE.125.8



Determining parameters of high-velocity open water flow

O.A. Burtseva¹ , S.I. Evtushenko²  , V.N. Kokhanenko¹ 

¹ Platov South-Russian State Polytechnic University (NPI), Novocherkassk, Russian Federation

² Moscow State University of Civil Engineering (National Research University), Moscow, Russian Federation

✉ evtushenkosi@mgsu.ru

Keywords: mathematical model, 2D water flow, equations of motion, resistance forces, open-channel hydraulics, analytical solution, simple wave, characteristics method

Abstract. In the planar hydraulics, the problems with previously unknown boundaries are most difficult. The best adequacy in terms of flow parameters is provided by simplified analytical methods based on a potential flow model. A mathematical model of a stationary, potential, 2D planar high-velocity open water flow of an ideal fluid, freely spreading back from a non-pressure orifice is studied. The boundary problem of flow free spreading in plane were formulated. Studying the system of dimensionless equations of motion resulted in identification of the criteria influencing the process of flow spreading. A critical analysis was carried out and a description of various methods for solving the problem of free spreading of a high-velocity water flow was given. The problem in an analytical form was solved in the velocity hodograph plane. All flow parameters are determined in the physical plane. For the first time, the conjugating flow "simple wave" was applied. The proposed analytical method for solving the problem of flow free spreading is effective, unambiguous and has no singularities and discontinuities, particularly, at the outlet of a non-pressure pipe. The adequacy of the mathematical model was verified on a test example. The relative error of the flow parameters does not exceed 10 % compared to the experimental data.

Citation: Burtseva, O.A., Evtushenko, S.I., Kokhanenko, V.N. Determining parameters of high-velocity open water flow. Magazine of Civil Engineering. 2024. 17(1). Article no. 12508. DOI: 10.34910/MCE.125.8

1. Introduction

In modern hydraulic engineering construction, the hydraulic structures for passing water from elevated areas to lower ones are frequently used. These can be large hydro power plants, road drainage channels, spillways, junctions of various channels for changing flow parameters, small bridges that pass water flows during river floods or high water.

Due to inaccurate or irrational modeling in the construction of hydraulic structures, the operational reliability of a structure as a whole decreases; this causes collapses of fastenings of culverts under roads, small bridges under railways. Improper design of spillways leads to environmental disasters in Russia. There is a practical need for a reliable method for calculating the parameters of a water flow.

It was revealed that the methods of I.A. Sherenkov and G.A. Lilitky, referred to as the most famous, accessible and described in the reference literature ones, do not always give results with sufficient accuracy for practical calculations when we compared the experimental and calculated contours of the border streamlines of flow free spreading downstream of rectangular cross-section pipes according to these methods.

Among the many tasks in the hydraulics of planar flows, the tasks with previously unknown flow boundaries are the most difficult. At the outlet of the flow from the pipe, the best adequacy in terms of flow

parameters is represented by simplified analytical methods based on the model of the potential flow of the current. Further, the flow resistance forces increase and it is necessary to make a transition to numerical methods.

However, the fastening of the structure is carried out precisely at the culvert outlet for a flow, where an analytical solution may be enough. If the boundary value problem is immediately solved by numerical methods, then due to the characteristics of the problem (discontinuity of parameters in the pipe outlet area), the adequacy of the solution of the problem decreases. Therefore, first of all, it is necessary to use analytical methods as a basis for further use of numerical methods.

Therefore, there is a need for a simple analytical method for calculating the parameters of the water flow, which allows obtaining sufficient adequacy in terms of its parameters. Next, we consider a stationary, potential, high-velocity 2D planar open water flow of an ideal fluid freely spreading downstream of non-pressure culverts (hereinafter referred to as the water flow). Such a flow is characterized by local averaged velocities in depth and local depths at each point in the flow. The presence of velocities perpendicular to the planar flow plan distinguishes 3D flows from 2D planar flows. 2D water flows are studied and analyzed mathematically much easier than 3D spatial flows.

N. Bernadsky and V. Makkaveev were the first to set the problem of planar hydraulics. They also developed an approximate solving method for calm (precritical) flows. The theory of 2D planar flows was further developed in the works of Russian researchers N. Meleshchenko, G. Sukhomel, I. Levi, S. Numerov, F. Frankl, I. Sherenkov, B. Emtsev, A. Tursunov, N. Kartvelishvili, M. Mikhalev, V. Lyakhter, L. Vysotsky and foreign scientists A. Ippen, H. Rauz, D. Harleman, D. Dowson, R. Knapp, D. Liggett, T. Akatai, etc. The theory and methods for solving planar hydraulic problems are most fully described in monographs of G. Sukhomel, I. Levi, B. Yemtsev [1], I. Sherenkov [2], A. Yesin [3] and V. Kokhanenko [4].

There are two main types of engineering problems in the 2D planar hydrodynamics [2]. The first type, or the direct problems, includes the configuration of the planar channel, i.e. the shape of its banks, in addition to the bottom surface (topography). To supplement these data with known values of velocities and depths in one of the boundary cross-sections, it is necessary to find the form of the free surface and velocity distribution within the selected section of the channel. The second type of problems is the inverse problems, where the law of estimating certain hydraulic parameters is given and other flow parameters are found as well as geometric characteristics of the bed (relief of bottom) forming the indicated flow. At the same time, it is necessary to take into account the flow's dynamic features and properties. The authors of this paper consider the second type of problems.

The mathematical basis of the problems mentioned above are systems of quasi-linear partial differential equations. The analytical solution is difficult to obtain in most cases due to the complexity of the motion. Therefore, a numerically analytical approach to solving such problems is considered promising.

Furthermore, the use of approximate methods of solution is recommended. The most famous approximate solution method is the method of characteristics developed by S. Chaplygin and borrowed from gas dynamics [4].

Sherenkov's method based on using a universal graph [2] constructed by means of the characteristics method is considered to be one of the most known approaches to determining parameters of a high-velocity flow. However, this method was not adequate enough for practical use. The discrepancy between the calculated and experimental values reached 50 % [2]. The characteristic method was further developed in works of V. Kokhanenko and his students.

In 1997, V. Kokhanenko [4] proposed the idea of an analytical method for determining flow parameters using the velocity hodograph plane, where such natural coordinates were proposed: τ – flow kineticity (the square of the flow velocity coefficient) and θ – angle of direction of the velocity vector in relation to symmetry axis OX of the flow. As the unknown functions we considered the potential function $\varphi = \varphi(\tau, \theta)$ and the current function $\psi = \psi(\tau, \theta)$. The basic system of differential equations of motion for the flow in the plane of the variables τ, θ has become linear, allowing a wide set of solutions to be defined.

E. Duvanskaya [5] calculated hydraulic parameters considering the friction forces and the slope of the bottom of 2D stationary precritical flows for solving problems at designing melioration networks and road structures.

This idea was further developed in the works of N. Kosichenko [6]. She set the problem about free flow spreading, solved it and indicated the limits of applicability of the results of solving of the planar problem. She proposed an analytical method for calculating the geometry of the flow spreading area and its parameters inside and at the boundary of the flow area.

N. Papchenko has developed new mathematical methods for modeling 2D planar flows. He determined a set of previously unknown analytical solutions for systems of 2D planar flows in the plane of the velocity hodograph. He founded solutions of the boundary problem of a free flow spreading both in the plane of velocity hodograph, and in the physical plane of the flow by both analytical and numerical methods [7].

The main contribution of D. Kelekhsaev to theory of planar flows was the definition of the inertial front length formula at the pipe outlet [8].

Substantial development of an analytical method for determining flow parameters was presented in the works of O. Burtseva and M. Aleksandrova [9–10]. They have formulated a boundary problem of free spreading of a planar flow. The system of equations of motion of water flow in dimensionless form was obtained in two ways. Criteria influencing the process of flow spreading were revealed and their universality was proved. The problem has been solved in the analytical form in the velocity hodograph plane. The transition to the physical plane made it possible to determine all parameters of plane water flow.

Improvement of the accuracy of the analytical method by splitting the flow scheme into four main sections: uniform flow, "simple wave", section limited by the characteristics of the 1st family and the radial flow section. Conjugation the sections and obtaining an adequate mathematical model for determining the parameters of a high-velocity open water flow.

2. Methods

2.1. Motion equations of a 2D planar water flow in the physical region of a flow (OXY)

The initial physical assumptions for the 2D planar water flow model are [1]:

- a) vertical components of local averaged velocities and accelerations are small;
- b) velocity vectors of liquid particles located on the one vertical line are located in the same plane;
- c) velocity distribution on any vertical is almost uniform.

In practice, in most open water flows the assumptions a), b), c) are satisfied by the high-velocity flows, the transverse dimensions of which are several times greater than the flow depth and there are no return currents [11–13].

Background of the paragraph c). The uneven distribution of open flow velocities along the vertical is conditioned by the retarding effect of the channel bottom. Herewith, a boundary layer develops which spreads its influence up to the free surface. However, the velocity distribution in the boundary layer has an asymptotic character and its conditional thickness is decreased with an increase in the flow kineticity. Therefore, in high-velocity flows (Froude number $F > 1$), the longitudinal component of the velocity at some point becomes almost equal to the surface one at a small distance from the bottom. Hence, there appears an almost uniform distribution of velocities along the vertical [18].

To obtain the dynamic equations of motion of a 2D open planar flow N.M. Bernadsky [1] suggested to proceed from L. Euler's equations, supplemented by components considering the flow resistance forces. For the flows satisfying the assumptions (a-c), the form of the motion equations for the average values of parameters in terms of depth and time coincides with the L. Euler's equations for ideal liquid supplemented by the flow resistance force per mass unit of the liquid. This model has been obtained artificially but it has the right to both theoretical and practical use.

The system of dynamic equations of motion of a non-stationary open 2D planar flow has the form [1, 3]:

$$\begin{cases} u_x \frac{\partial u_x}{\partial x} + u_y \frac{\partial u_x}{\partial y} + g \frac{\partial}{\partial x} (z_g + h) + T_x = 0; \\ u_x \frac{\partial u_y}{\partial x} + u_y \frac{\partial u_y}{\partial y} + g \frac{\partial}{\partial y} (z_g + h) + T_y = 0, \end{cases} \quad (1)$$

where u_x, u_y are projections of the local velocity vector on the axes of a Cartesian coordinate system – OXY; z_g is the mark of the channel bottom; h is flow depth; g is acceleration of gravity; T_x, T_y are the projections of resistance forces to the flow, referred to the unit mass of the liquid.

In the case of a flat horizontal channel bottom $z_g = 0$, without taking into account the flow resistance forces $T_x = T_y = 0$, from (1) there follows the system of equations:

$$\begin{cases} u_x \frac{\partial u_x}{\partial x} + u_y \frac{\partial u_x}{\partial y} + g \frac{\partial}{\partial x}(h) = 0; \\ u_x \frac{\partial u_y}{\partial x} + u_y \frac{\partial u_y}{\partial y} + g \frac{\partial}{\partial y}(h) = 0. \end{cases} \quad (2)$$

Adding to the system (2) the flow continuity equation, which has a specific form (3) for 2D open water planar flows [1]:

$$\frac{\partial(u_x h)}{\partial x} + \frac{\partial(u_y h)}{\partial y} = 0 \quad (3)$$

and the flow potentiality equation

$$\Omega = \frac{\partial u_x}{\partial y} - \frac{\partial u_y}{\partial x} = 0 \quad (4)$$

we obtain a closed system of equations relatively to variables u_x, u_y, h .

2.2. Boundary value problem of flow free spreading in plane

The system of equations describing the flow is as follows:

$$\begin{cases} u_x \frac{\partial u_x}{\partial x} + u_y \frac{\partial u_x}{\partial y} + g \frac{\partial h}{\partial x} = 0; \\ u_x \frac{\partial u_y}{\partial x} + u_y \frac{\partial u_y}{\partial y} + g \frac{\partial h}{\partial y} = 0; \\ \frac{\partial(u_x h)}{\partial x} + \frac{\partial(u_y h)}{\partial y} = 0, \\ \frac{\partial u_x}{\partial y} - \frac{\partial u_y}{\partial x} = 0. \end{cases} \quad (5)$$

One can go from u_x, u_y to the local velocity vector V with modulus $V = \sqrt{u_x^2 + u_y^2}$ the angle θ characterizing the direction of the velocity vector to the longitudinal axis of flow symmetry [4, 18].

The boundary conditions for a flow:

1) at the outlet of a non-pressure rectangular pipe:

$$x = 0; \quad -\frac{b}{2} \leq y \leq \frac{b}{2}; \quad h = h_0; \quad V = V_0; \quad \theta = 0, \quad (6)$$

where b is the width of the culvert; h_0, V_0 are the depth of the flow and rate of its velocity at the outlet of the pipe into a diversion channel;

2) along the boundary streamline

$$y = f(x); \quad y'_x = tg\alpha; \quad \alpha = 0, \quad (7)$$

α is wave angle;

3) at

$$x \rightarrow \infty; \quad h \rightarrow 0; \quad V \rightarrow V_{\max}; \quad \theta \rightarrow \theta_{\max}, \quad (8)$$

where V_{\max} , θ_{\max} are maximum flow velocity and spreading angle.

2.3. Research of the boundary value problem without its complete solution

Reducing the system of motion equations of 2D planar water flow and boundary conditions to dimensionless form.

Obtaining a system of motion equations of a water flow in a dimensionless form is necessary to identify dimensionless criteria that influence the process of flow spreading, and to answer the question, whether the type of the system and the boundary value problem are universal in dimensionless coordinates as a whole.

As a basis, we take the system of equations (5). Let us consider various variants for bringing it to a dimensionless form.

Variant I. We introduce the following dimensionless coordinates and dimensionless flow parameters

$$\bar{x} = \frac{x}{b}; \quad \bar{y} = \frac{y}{b}; \quad \bar{h} = \frac{h}{h_0}; \quad \bar{V}_x = \frac{u_x}{V_0}; \quad \bar{V}_y = \frac{u_y}{V_0},$$

where x, y are coordinates of the flow.

After transition in the system (5) to the dimensionless quantities $\bar{x}, \bar{y}, \bar{h}, \bar{V}_x, \bar{V}_y$, we obtain the following system:

$$\left\{ \begin{array}{l} F_0 \left(\bar{V}_x \cdot \frac{\partial \bar{V}_x}{\partial \bar{x}} + \bar{V}_y \cdot \frac{\partial \bar{V}_x}{\partial \bar{y}} \right) + \frac{\partial \bar{h}}{\partial \bar{x}} = 0; \\ F_0 \left(\bar{V}_x \cdot \frac{\partial \bar{V}_y}{\partial \bar{x}} + \bar{V}_y \cdot \frac{\partial \bar{V}_y}{\partial \bar{y}} \right) + \frac{\partial \bar{h}}{\partial \bar{y}} = 0; \\ \frac{\partial (\bar{V}_x \cdot \bar{h})}{\partial \bar{x}} + \frac{\partial (\bar{V}_y \cdot \bar{h})}{\partial \bar{y}} = 0; \\ \frac{\partial \bar{V}_x}{\partial \bar{y}} - \frac{\partial \bar{V}_y}{\partial \bar{x}} = 0, \end{array} \right. \quad (9)$$

where $F_0 = \frac{V_0^2}{gh_0}$ is Froude criterion of a flow at the outlet from of a pipe.

Analyzing the system (9), we see that the first and the second equations are not reduced to a universal form as they contain the dimensionless parameter F_0 . The third and the fourth equations have a universal form. Therefore, without solving the boundary value problem, we can say that its solution will depend on the Froude criterion F_0 of a flow at the outlet of a pipe and is not reduced to a universal form¹.

In case of the boundary value problem is universal, it can be solved one time. For the different boundary conditions, we can use only recalculation of the parameters describing the problem in dimensionless parameters.

Variant II. Further we show that from I.A. Sherenkov's graph [2] in coordinates

$$\bar{y} = \frac{y}{b}; \quad \bar{x} = \frac{x}{b\sqrt{F_0}},$$

for the system (5) that he used, and for the boundary conditions (6), there follows a transformation:

¹ A universal form is a form of the boundary value problem in the dimensionless coordinates, which does not depend on any dimensionless criteria.

$$\bar{y} = \frac{y}{b}; \quad \bar{x} = \frac{x}{b\sqrt{F_{r0}}}; \quad \bar{h} = \frac{h}{h_0}; \quad \bar{V}_x = \frac{V_x}{V_0 K_x}; \quad \bar{V}_y = \frac{V_y}{V_0 K_y}.$$

The system of equations (5) is not reduced to the universal dimensionless form in this case:

the first three equations at $K_x = \frac{1}{\sqrt{F_{r0}}}$; $K_y = \frac{1}{F_0}$ are reduced to a universal form, except the fourth one.

$$\left\{ \begin{array}{l} \bar{V}_x \cdot \frac{\partial \bar{V}_x}{\partial \bar{x}} + \bar{V}_y \cdot \frac{\partial \bar{V}_x}{\partial \bar{y}} + \frac{\partial \bar{h}}{\partial \bar{x}} = 0; \\ \bar{V}_x \cdot \frac{\partial \bar{V}_y}{\partial \bar{x}} + \bar{V}_y \cdot \frac{\partial \bar{V}_y}{\partial \bar{y}} + \frac{\partial \bar{h}}{\partial \bar{y}} = 0; \\ \frac{\partial(\bar{V}_x \cdot \bar{h})}{\partial \bar{x}} + \frac{\partial(\bar{V}_y \cdot \bar{h})}{\partial \bar{y}} = 0; \\ \frac{\partial \bar{V}_x}{\partial \bar{y}} - \frac{1}{F_0} \frac{\partial \bar{V}_y}{\partial \bar{x}} = 0. \end{array} \right.$$

The boundary values (6-8) cannot be reduced to universal dimensionless form at the outlet of the pipe (6). That means that the problem of free spreading of the 2D flow cannot be reduced to the dimensionless form. Therefore, the universal graphic can be used only with the Froude criterion values close to 1 (see Fig. 1).

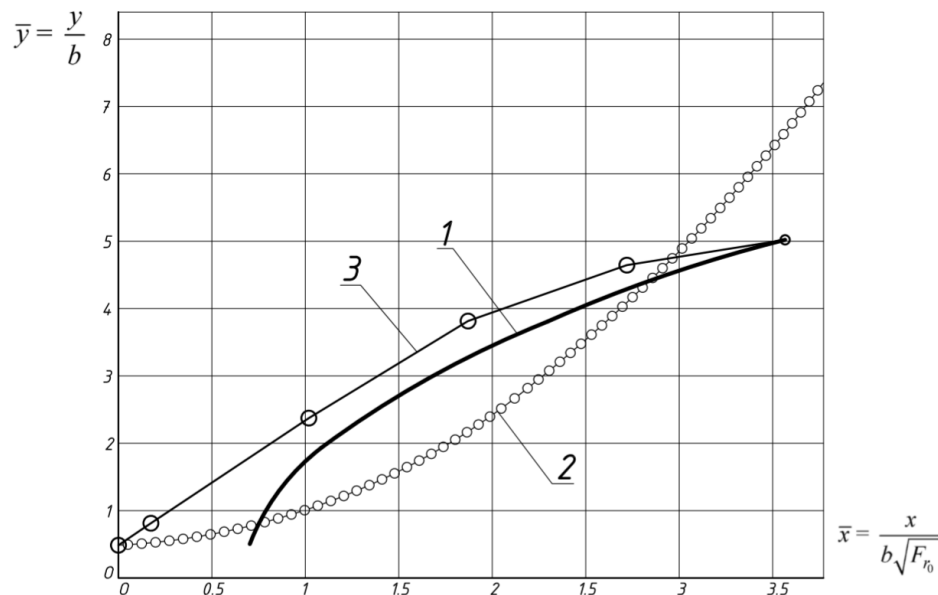


Figure 1. Graphs of boundary streamlines: 1 – according to the method of G.A. Lilitsky; 2 – according to the method of I.A. Sherenkov; 3 – according to the experimental data at $F_0 = 2.184$.

2.3.1. Methods for solving problem of free spreading of a water flow

I.A. Sherenkov's method. He developed a method based on the use of universal graphic with the additional D. Bernoulli equation for the total hydrodynamic pressure. The graphic was given in dimensionless coordinates, and at the first approximation, it allowed the design organizations to obtain the entire spectrum of flow parameters. However, the adequacy of this solution was rather low and it made the researchers of 2D planar water flows search for new ways to solve the problem. The development of numerical solution of the problem based on integral equation system has not been brought to possibility of practical use in hydraulic construction.

G.A. Lilitsky's method is not universal, it is based on the experimental data processing.

The most promising method of solving problems may be the analytical method using the velocity hodograph plane [4]. However, it has its own drawbacks.

2.4. Description of the analytical methods using the velocity hodograph plane

According to S.A. Chaplygin's method of [10], the system of equations (5) is converted to the variables τ and θ by using a complex differential connection between the physical plane $\Psi(XY)$ and the velocity hodograph plane $\Gamma(\tau, \theta)$:

$$d(x + iy) = \frac{1}{\tau^{1/2} \sqrt{2gH_0}} \left[d\varphi + i \frac{h_0}{H_0(1-\tau)} d\psi \right] \cdot e^{i\theta}, \quad (10)$$

where τ is flow kineticity; θ is angle characterizing the direction of the velocity vector to the longitudinal axis of symmetry of the flow; $i = \sqrt{-1}$ is the imaginary unit. We obtain a system of equations [1, 4]:

$$\begin{cases} \frac{\partial \varphi}{\partial \tau} = \frac{h_0}{2H_0} \cdot \frac{3\tau - 1}{\tau(1-\tau)^2} \cdot \frac{\partial \psi}{\partial \theta}; \\ \frac{\partial \varphi}{\partial \theta} = 2 \frac{h_0}{H_0} \cdot \frac{\tau}{1-\tau} \cdot \frac{\partial \psi}{\partial \tau}, \end{cases} \quad (11)$$

where $\varphi = \varphi(\tau, \theta)$ is the potential function; $\psi = \psi(\tau, \theta)$ is the current function; the hydro-dynamic pressure is

$$H_0 = \frac{V_0^2}{2g} + h_0 = \frac{V^2}{2g} + h = H;$$

the flow kineticity parameter is

$$\tau = \frac{V^2}{2gH_0}; \quad (12)$$

the local depth and velocity (average over the live section) is:

$$h = H_0(1-\tau); \quad V = \tau^{1/2} \sqrt{2gH_0}. \quad (13)$$

The system of equations (11) is already a linear system admitting to obtain analytical solutions. The authors in [4, 9, 18] chose from these solutions the following solution:

$$\psi = A \cdot \frac{\sin \theta}{\tau^{1/2}}; \quad \varphi = A \cdot \frac{h_0}{H_0} \cdot \frac{\cos \theta}{\tau^{1/2}(1-\tau)}, \quad (14)$$

where the constant A is determined according to the theory described in [4, 5]:

$$A = \frac{V_0 b}{2 \sin \theta_{\max}};$$

here b is the width of the culvert.

Therefore, by solving the problem in the plane of the velocity hodograph and using (11), we can define the solution over the entire spectrum of flow parameters in the flow plane.

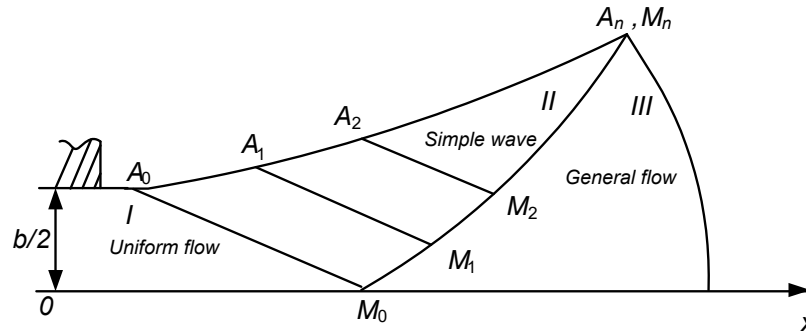
The main necessary requirements to perform boundary conditions of the problem of free flow spreading at $\tau \rightarrow 1$ are as follows:

$$h \rightarrow 0; \quad V \rightarrow V_{\max} = \sqrt{2gH_0}; \quad h = H_0(1-\tau). \quad (15)$$

There are two appropriate types of flows to fulfill conditions (15): radial spreading of the flow and flow of the type (14).

The additional condition is flow spreading with a free surface curved from the bottom towards the atmosphere along the channel (the axis of symmetry of the flow). This condition follows from experimental studies of flow spreading. The flow of type (14) also corresponds to this condition but the radial spreading of the flow does not. This is why the authors have chosen the scheme (Fig. 2) and the common type flow (14).

However, solution (14) satisfies the boundary conditions on infinity at $\tau \rightarrow 1$, but it does not satisfy the boundary conditions at the outlet of the pipe at $\theta = 0$, $\tau_0 = \frac{V_0^2}{2gH_0}$.



A_0M_0, A_1M_1 are characteristics of the 2nd family;

M_0, M_1, \dots, M_n are characteristic of the first family; OX –flow symmetry axis

Figure 2. Scheme of combining a uniform flow and the flow (14): I – steady-state flow in the pipe; II – simple wave; III – general flow.

The authors tried to eliminate this contradiction by searching for other types of solutions and by switching from a straight edge of the outlet pipe to a curvilinear shape as well. The authors obtained a sufficient adequacy to the real process in terms of the form of the border streamline (but not in all parameters) [5–7]. A detailed study of the theory of 2D planar water flows provided the following conclusion [10, 19]: a uniform flow in a pipe can be combined with a flow of the general type to which the flow belongs (14), only by a simple wave. This is why when using the scheme of free spreading of the flow (region 2, see Fig. 2) it satisfies the boundary conditions at the outlet of the pipe.

2.5. Determination of flow parameters in various areas

Let us consider the region of flow spreading in the plane of the velocity hodograph, see Fig. 3. Here are the following indications:

$M_0(\tau_0, 0)$ is the point corresponding to the region I of a uniform flow current (see Fig. 2) with parameters $\tau_0, \theta = 0$. On the velocity hodograph plane the point M_0 corresponds to the entire region I of the uniform flow current.

M_0M_n is the characteristic of the first family, the conjugation line of the flow of the general form (14) III and the simple wave flow (see Fig. 2).

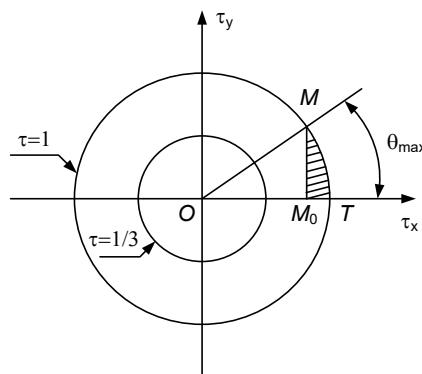


Figure 3. Flow spreading region in the velocity hodograph plane.

1. Determining the boundaries of the uniform flow area.

Point M_0 in the sector I (see Fig. 2) belongs to the characteristic of the 1st family with parameters τ_0 , $\theta = 0$. The wave angle at this point is

$$\alpha_0 = \arcsin \sqrt{\frac{1-\tau_0}{2\tau_0}}; \quad A_0 M_0 = \frac{b}{2 \operatorname{tg} \alpha_0}.$$

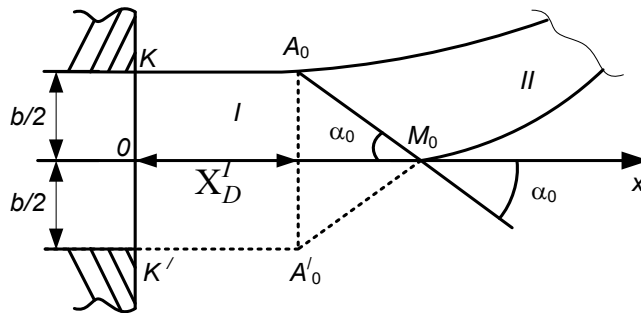


Figure 4. Boundaries of the of uniform flow area.

Since $M_0 A'_0$ and $M_0 A_0$ are straight lines, the pentagon is $K'OKA_0M_0A'_0$ in Fig. 4 is symmetrical about the OX axis. Its upper part is a rectangular trapezoid. Thus, with known distance X_D^I , the geometry and kinematics of sector I of the flow spreading are determined.

To determine the parameter X_D^I we use the formula given in [8]

$$X_D^I = \operatorname{trunc} \left[\frac{\sqrt{F_0 - 1}}{\sin \theta_{\max} (F_0 + 2)} h_0 \right] + 1, \quad (16)$$

where 1 is the depth measuring unit of h_0 . In calculations this is 1 cm, in natural experiments it is 1 m. Formula (16) was derived from the compilation of the structural formula and the determination of the coefficients by the regression analysis method. To derive this formula we used information from 70 experiments, some of which was published in [4].

The flow parameters V_0 , h_0 , τ_0 in the closed region I are constant and are defined by formulas (12) and (13).

2. Determining flow parameters in terms of the $M_0 M_n$ characteristic. The angle of inclination of the first family characteristics in the plane of the velocity hodograph has the following form [4, 18]:

$$\theta = \sqrt{3} \cdot \operatorname{arctg} \sqrt{\frac{3\tau - 1}{3(1-\tau)}} - \operatorname{arctg} \left(\sqrt{\frac{3\tau - 1}{1-\tau}} \right) + C', \quad (17)$$

where the constant C' is found from the condition of the characteristic's passing through the point M_0 :

$$C' = \operatorname{arctg} \sqrt{\frac{3\tau_0 - 1}{1-\tau_0}} - \sqrt{3} \cdot \operatorname{arctg} \left(\frac{1}{\sqrt{3}} \sqrt{\frac{3\tau_0 - 1}{1-\tau_0}} \right).$$

The angle θ takes the maximum value at the boundary condition

$$\tau \rightarrow 1; \quad h = H_0(1-\tau) \rightarrow 0; \quad V = \tau^{1/2} \sqrt{2gH_0} \rightarrow \sqrt{2gH_0}; \quad \theta \rightarrow \theta_{\max}$$

and is equal to

$$\theta_{\max} = C' + (\sqrt{3} - 1) \cdot \frac{\pi}{2}.$$

Note that at $\tau \rightarrow 1$ according to the scheme (Fig. 2), the boundary streamline (free boundary) tends to the characteristic M_0M_n and the points A_n and M_n approach each other, since the wave angle tends to zero:

$$\alpha_n = \arcsin \sqrt{\frac{1-\tau_n}{2\tau_n}} \rightarrow 0.$$

The parameters τ , θ on the characteristic of the 1st family are also parameters of the "simple wave" flow. In a simple wave the characteristics of the second family are straight lines [1].

Given the parameter $\tau_M \in [\tau_0, 1]$, we define the corresponding angle θ_M by formula (17) and calculate the depths and velocities by formulas (13).

2. Determining the coordinates of the points M_i along the characteristic of the first family, see Fig. 5.

The specific volumetric flow rate coefficient of an arbitrary streamline is equal to:

$$Q = K \frac{b}{2}, \quad 0 \leq K \leq 1,$$

where K is the flow rate coefficient.

To determine the kineticity τ_M along the characteristic of the 1st family we substitute function (17) into the streamline equation (14) and solve it [18]:

$$\frac{\sin \theta_M}{\tau_M^{1/2}} = K \sin \theta_{\max}. \quad (18)$$

We find τ_M and then θ_M .

To find the coordinates of points M_i , we use the relation equation (10) between the physical plane $\Psi(XY)$ and the plane of the velocity hodograph $\Gamma(\tau, \theta)$. Separating the imaginary and real parts in (10) and considering that $d\psi = 0$ along the streamline, we obtain

$$\begin{cases} dx = \frac{d\varphi}{\tau^{1/2} \sqrt{2gH_0}} \cdot \cos \theta; \\ dy = \frac{d\psi}{\tau^{1/2} \sqrt{2gH_0}} \cdot \sin \theta. \end{cases} \quad (19)$$

From the equation (18) we have

$$\sin \theta_M = K \cdot \tau_M^{1/2} \sin \theta_{\max}. \quad (20)$$

Then, by differentiating both parts of the expression (20) and omitting the index "M", we obtain:

$$\cos \theta d\theta = \frac{1}{2} K \cdot \frac{d\tau}{\sqrt{\tau}} \sin \theta_{\max} \quad (21)$$

or

$$d\theta = \frac{1}{2} K \cdot \frac{d\tau}{\sqrt{\tau}} \frac{\sin \theta_{\max}}{\cos \theta}. \quad (22)$$

To determine $d\varphi$ we use the expression for the potential function in equations (14)

$$\varphi = A \cdot \frac{h_0}{H_0} \cdot \frac{\cos \theta}{\tau^{1/2} (1-\tau)}. \quad (23)$$

Differentiating $\varphi = \varphi(\tau, \theta)$, we obtain

$$d\varphi = \frac{Ah_0}{H_0} \left[\frac{-\sin \theta d\theta}{\tau^{1/2} (1-\tau)} + \frac{\cos \theta (3\tau-1) d\tau}{2\tau^{3/2} (1-\tau)^2} \right]. \quad (24)$$

Considering expressions (20)–(24) we can transform the system (19) to:

$$\begin{cases} dx = f_1(\tau) d\tau; \\ dy = f_2(\tau) d\tau, \end{cases} \quad (25)$$

where $f_1(\tau)$, $f_2(\tau)$ are the functions of the flow kinetics parameter defined after transformations.

Integrating the system (25) at the initial values we obtain the values of the coordinates of the selected flow point:

$$X = X_{M_0} + \int_{\tau_0}^{\tau} f_1(\tau) d\tau; \quad Y = Y_{M_0} + \int_{\tau_0}^{\tau} f_2(\tau) d\tau.$$

Thus, we find the coordinates of the point M that is located of the intersection of the streamline with the flow rate coefficient K and the characteristics of the first family in the planar flow.

3. Determining flow parameters in the flow region III (see Fig. 2).

We have to solve the system of equations in the plane of the velocity hodograph to determine the parameters θ , τ at the point of intersection of an arbitrary streamline and an arbitrary equipotential:

$$\begin{cases} A \frac{\sin \theta}{\tau^{1/2}} = K \sin \theta_{\max}; \\ \frac{\cos \theta}{\tau^{1/2} (1-\tau)} = \frac{\cos \theta_x}{\tau_M^{1/2} (1-\tau_M)}, \end{cases} \quad (26)$$

where K is given; θ_M , τ_M are parameters at the point of intersection of the characteristics of the first family with the streamline determined by the flow rate coefficient K . The solution of the system (26) is reduced to the solution of the cubic equation [4].

4. Determining the parameters on the rectilinear characteristics of the second family, in a simple wave II and determining the coordinates of the points A_1, A_2, \dots, A_n (Fig. 2).

Parameters τ_M , θ_M change along the characteristic of the 1st family, but not in simple waves – section II (from the characteristic of the 1st family up to the flow boundary). In other words, the boundaries of the flow and characteristics of the 1st family have the same look in the velocity hodograph plane [1, 4].

Since the characteristics of the 2nd family are straight lines with constant parameters τ_M , θ_M , they will have the same values of the parameters $\tau_A = \tau_M$, $\theta_A = \theta_M$ in the points A_0, A_1, \dots, A_n of their intersection with the flow boundary. As soon as the value of the kinetic parameter τ_A is determined it is possible to find the velocity and depth of the flow at the point A_i using the formulas (13).

To construct the boundary streamline, we have parameters τ_A , θ_A , and the direction of the segments $A_i A_{i+1}$ should be taken along the corresponding streamline passing through these points on the characteristic, with the wave angle taken into account [4].

$$\alpha_i = \arcsin \left(\sqrt{\frac{1-\tau_i}{2\tau_i}} \right). \quad (27)$$

To determine the coordinates of the points of the boundary streamline, we write a system of equations in which the first equation determines a pencil of lines passing through the point M_i , and the second equation is the equation of a circle centered at the point M_i .

The coordinates of the boundary streamline point are the solution of this system of equations, i.e. intersection point of a pencil of lines and a circle.

Omitting the index " $i+1$ ", we have

$$\begin{cases} (Y_A - Y_M) = \operatorname{tg}(\theta - \alpha)(X_A - X_M); \\ (X_A - X_M)^2 + (Y_A - Y_M)^2 = \rho_{AM}^2. \end{cases} \quad (28)$$

Obviously, the following conditions must be met:

$$Y_A > Y_M > \frac{b}{2}; \quad Y_{A_{i+1}} > Y_{A_i}; \quad X_A > X_{A_0}; \quad X_{A_{i+1}} > X_{A_i}.$$

To determine the coordinates of points lying on the boundary streamline we solve the system of equations (28). As a result, we obtain:

$$\begin{cases} Y_A = Y_M + k|X_A - X_M|; \\ X_A = X_M - \frac{\rho_{AM}}{\sqrt{1+k^2}}, \end{cases} \quad (29)$$

where $k = |\operatorname{tg}(\theta - \alpha)|$.

Let us consider a model of a non-stationary potential 2D planar open high-velocity water flow of an ideal fluid with free spreading back of a culvert, as a test example. The validation of the model is performed on the basis of real experimental data published in [4]. Data on spreading coordinates, depth and flow velocity are given in Table 1.

Table 1. Experimental data on the coordinates of the water flow, its depth and velocity.

| | | | | | |
|------------|---------|---------|---------|---------|--------|
| X_E (cm) | 9 | 24 | 44 | 64 | 71 |
| Y_E (cm) | 9 | 38 | 59 | 76 | 80 |
| V (cm/s) | 151.928 | 186.461 | 191.243 | 192.714 | 194.49 |

The flow at the outlet of the pipe has the following initial parameters:

- initial flow velocity (at the outlet of a pipe) $V_0 = 147.654$ (cm/s);
- initial flow depth relative to the bottom $h_0 = 9.27$ (cm);
- acceleration of gravity $g = 981$ (cm/s²);
- pipe width $b = 16$ (cm);
- flow rate at the outlet of a culvert $Q = 2.19 \cdot 10^4$ (cm³/s);
- relative flow expansion $\beta = 5$.

3. Results and Discussion

3.1. Parameters in the area of uniform flow and on the characteristic of the 1st family

According to the above presented algorithm, we find:

- Froude criterion $F_0 = 2.397$ (see formula (16));
- hydrodynamic head $H_0 = 20.382$ (cm);

- initial flow kinetics $\tau_0 = 0.545$;
- length of the inertial front $X_D^I = 3$ (cm) [8];
- wave angle at the outlet of the pipe is $\alpha_0 = 0.702$ radian or $\alpha_0 = 40^\circ 23$;
- angle of inclination of the fluid flow velocity vector to the OX axis at infinity $\theta_{\max} = 0.981$ radian or $\theta_{\max} = 56^\circ 23$;
- distance along the flow symmetry axis from the end of the inertial section to the M_0 : $AM_0 = 9.457$ (cm);
- straight line length of a segment of the characteristic of the second family between the points A_0 and M_0 : $A_0M_0 = 12.387$ (cm).

We divide the width of the flow pipe $b/2$ into 40 parts with step length $\Delta Y = 0.2$. We find the flow parameters at the points of intersection of a particular streamline with the characteristic of the first family, see equation (18). Table 2 shows the calculated values of the flow coefficient K , kineticity τ_M , the angle of inclination of the velocity vector θ_M (radian), abscissa X_M (cm) and ordinate Y_M (cm) at the points on the characteristic of the 1st family.

Table 2. Values of the flow parameters on the characteristic of the 1st family.

| No. step | K_i | τ_{Mi} | θ_{Mi} | X_{Mi} | Y_{Mi} |
|----------|-------|-------------|---------------|----------|-----------------------|
| 0 | 0 | 0.545 | 0 | 0 | 0 |
| 1 | 0.25 | 0.559 | 0.016 | 12.633 | $4.162 \cdot 10^{-4}$ |
| 2 | 0.05 | 0.574 | 0.031 | 12.899 | $1.77 \cdot 10^{-3}$ |
| 3 | 0.075 | 0.588 | 0.048 | 13.185 | $4.234 \cdot 10^{-3}$ |
| ⋮ | ⋮ | ⋮ | ⋮ | ⋮ | ⋮ |
| 28 | 0.7 | 0.926 | 0.594 | 39.34 | 6.273 |
| 29 | 0.725 | 0.936 | 0.623 | 43.235 | 8.757 |
| ⋮ | ⋮ | ⋮ | ⋮ | ⋮ | ⋮ |
| 33 | 0.825 | 0.972 | 0.742 | 73.489 | 47.873 |
| 34 | 0.85 | 0.979 | 0.774 | 89.655 | 85.193 |
| ⋮ | ⋮ | ⋮ | ⋮ | ⋮ | ⋮ |

Next, we constructed a grid in the general flow region and the parameters are determined according to the equations (26). We do not present them here.

3.2. Determining the coordinates of points along the boundary streamline A_i

Since the parameters τ_M, θ_M do not change in simple waves, we assume that $A = \tau_M, \theta_A = \theta_M$.

We calculate the wave angle α (radian) (see expression (27)) for segments of the straight lines A_iM_i . From the system of equations (29) we find the radii of the circles ρ (cm) with centers at the points M_i and define the coordinates of the points A_i on the boundary streamline.

The adequacy of the model was evaluated in terms of the error of the abscissa, ordinate, and velocity compared to the experimental data. The calculation results are summarized in Table 3.

Table 3. Values of the flow parameters along the boundary streamline.

| No. step | α_i | ρ_i | X_{Ai} | X_E | $\delta X, \%$ | Y_{Ai} | Y_E | $\delta Y, \%$ | V_{Ai} | V_E | $\delta V, \%$ |
|----------|------------|----------|----------|-------|----------------|----------|-------|----------------|----------|---------|----------------|
| 0 | 0.702 | 12.387 | 0 | 0 | | 8 | 8 | 0 | 147.654 | | |
| 1 | 0.678 | 12.989 | 9.545 | 9 | | 9.457 | 9 | 0.455 | 149.561 | 151.928 | 1.558 |
| 2 | 0.656 | 13.303 | 10.643 | | | 10.324 | | | 151.45 | | |
| 3 | 0.634 | 13.64 | 11.75 | | | 11.458 | | | 153.321 | | |
| ⋮ | ⋮ | ⋮ | | | ⋮ | ⋮ | ⋮ | | | | |
| 28 | 0.201 | 61.37 | 23.337 | 24 | 2.761 | 35.771 | 38 | 6.233 | 192.435 | 186.461 | 3.204 |
| 29 | 0.185 | 70.962 | 25.767 | | 5.671 | 58.644 | | 0.607 | 193.504 | 191.243 | 3.067 |
| ⋮ | ⋮ | ⋮ | ⋮ | ⋮ | ⋮ | ⋮ | ⋮ | | | | |
| 33 | 0.121 | 158.398 | 46.495 | 44 | 8.654 | 73.13 | 59 | 3.924 | 197.109 | 192.714 | 2.649 |
| 34 | 0.105 | 212.027 | 58.462 | 64 | 9.855 | 89.332 | 76 | 10.446 | 197.82 | 194.49 | 2.034 |
| ⋮ | ⋮ | ⋮ | ⋮ | ⋮ | ⋮ | ⋮ | ⋮ | ⋮ | ⋮ | ⋮ | ⋮ |

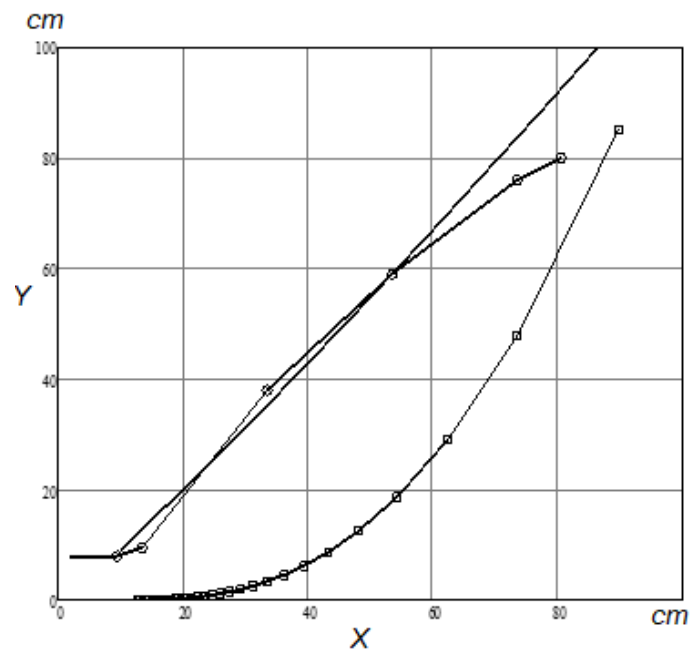


Figure 5. The graphs of the boundary streamlines obtained by the presented method (solid line) and experimental data (line labeled with circles), as well as the characteristic curves of the 1st family (line labeled with squares).

Fig. 5 shows the curves of the extreme streamline obtained by the presented algorithm (solid line) and experimental data (labeled with circles), as well as the characteristic curve of the 1st family (labeled with square markers).

Detailed development of programs was published by the authors in [22, 23].

This work develops the methods for the analytical study of problems of technical fluid and gas mechanics [1, 18–21], using a technique for solving nonlinear problems similar to those proposed in [24–27].

4. Conclusions

1. The article formulates a mathematical model of a 2D high-velocity planar flow with justification and consideration of some physical assumptions. The boundary problem of free spreading of the flow in terms of the flow has been set. A system of equations for the motion of a water flow in a dimensionless form has been obtained in two ways. The criteria influencing the process of flow spreading were revealed, their versatility was proved. The conclusion is drawn that the known methods based on Sherenkov's universal graph do not provide sufficient adequacy for the solution to the free spreading water flow problem.

2. The theory in the article agrees with the main points of the theory of conjugation of 2D potential flows. The proposed method for solving the problem includes both previously known and new points. The novelty is the division of the flow into three main sections: a uniform flow, a general flow and a conjugating flow of a simple wave. The use of simple waves to determine the coordinates of the extreme line of the water flow is also new.
3. Using Chaplygin's method made it possible to obtain an analytical method for solving the problem of flow free spreading in the plane of the velocity hodograph. The method is effective, unambiguous and has no singularities and discontinuities at the outlet of a pipe.
4. A test case was calculated. The parameters of the flow and its coordinates on the characteristic of the 1st family and the boundary streamline at the points coinciding with the natural experiment are given (Table 2 and Table 3). Relative errors are calculated. A more complete calculation is presented in the form of a graph in Fig. 5. The adequacy of the obtained flow model to the natural experiment was proved. The calculation error is less than 10 %, which is quite acceptable.

References

1. Yemtsev, B.T. Dvuhmernye burnye potoki [2D High-Velocities Flows]. Moscow, 1967. 212 p. (rus)
2. Sherenkov, I.A. O planovoj zadache rastekaniya strui burnogo potoka neszhimaemoj zhidkosti [On the Planned Problem of the Spreading of a Jet of a Rough Flow of an Incompressible Liquid]. Izv. Academy of Sciences of the USSR. REL. 1958. 1. Pp. 72–78. (rus)
3. Esin A. I. Hydrodynamics equation of two-dimensional open flows in natural coordinates. Fluid Mechanics. Soviet Research (Script a Technical, USA). 1984. 13(6).
4. Kokhanenko, V.N., Volosukhin, Ya.V., Lemeshko, M.A., Papchenko, N.G. Modelirovanie burnyh dvuhmernih v plane vodnyh potokov [Modeling of Stormy Two-Dimensional in Terms of Water Flows]. Rostov-on-Don: YuFU Publ., 2013. 180 p. (rus)
5. Duvanskaya, E.V. Obshchiy metod analiticheskogo resheniya zadach planovoy gidravliki spokojnykh potokov [Generalized method of analytical solution of precritical flows in problems of planned hydraulics]. Izv. VUZov. The North-Caucasus Region. Technical Sciences. 2011. 3. Pp. 91-93. (rus)
6. Kosichenko, N.V. Analiz izucheniya i utocneniya metodov svobodnogo rastekaniya potoka za beznapornymi vodopropusknyimi otverstiyami [The analysis of studying and specification of methods of free spreading of a stream behind free-flow water throughput openings]. Vestnik SGAU. 2011. 9. Pp. 27–33. (rus)
7. Papchenko, N.G. The general technology of solving practical problems of hydraulics of two-dimensional in terms of stationary turbulent water flows analytical method using the hodograph plane speed. Proceedings of Voronezh State University. Series: Physics. Mathematics. 2014. 2. Pp. 162–166. (rus)
8. Kelekhsaev, D.B. Calculation of the rapid flow of water at the outlet of the round pipe in the downstream of the culverts. Construction and Architecture. 2018. 3 (20). Pp. 29–34. DOI: 10.29039/article_5bee8ada6e3492.04272155
9. Burtseva, O.A., Alexandrova, M.S. Water flow parameters on the symmetry axis and extreme line of current. Vestnik MGSU [Monthly Journal on Construction and Architecture]. 2023. 18(8). Pp. 1262–1271. DOI: 10.22227/1997-0935.2023.8.1262-1271
10. Alexandrova, M.S. Method of analogies between hydraulics of two-dimensional water flows and gas dynamics. Construction and Architecture. 2020. 2(27). Pp. 49–52. DOI: 10.29039/2308-0191-2020-8-2-49-52
11. Nikora, V.I., Stoesser, T., Cameron, S.M., Stewart, M., Papadopoulos, K., Ouro, P., McSherry, R., Zampiron, A., Marusic, I., Falconer, R.A. Friction factor decomposition for rough-wall flows: theoretical background and application to open-channel flows. Journal of Fluid Mechanics. 2019. 872. Pp. 626–664. DOI: 10.1017/jfm.2019.344
12. Aranda, J., Beneyto, C., Sánchez-Juny, M., Bladé, E. Efficient design of road drainage systems. Water. 2021. 13. DOI: 10.3390/w13121661
13. Sanz-Ramos, M., Bladé, E., González-Escalona, F., Olivares, G., Aragón-Hernández, J.L. Interpreting the manning roughness coefficient in overland flow simulations with coupled hydrological-hydraulic distributed models. Water. 2021. 13. 3433. DOI: 10.3390/w13233433
14. Anees, M.T., Abdullah, K., Nordin, M.N.M., Rahman, N.N.N.A., Syakir, M.I., Kadir, Mohd.O.A. One- and two-dimensional hydrological modelling and their uncertainties. Flood Risk Management. InTech. 2017. DOI: 10.5772/intechopen.68924
15. Nematollahi, B., Abedini, M.J. Analytical solution of gradually varied flow equation in non-prismatic channels. Iranian Journal of Science and Technology – Transactions of Civil Engineering. 2020. 44. Pp. 251–258. DOI: 10.1007/s40996-019-00316-5
16. Castro-Orgaz, O., Cantero-Chinchilla, F.N. Non-linear shallow water flow modelling over topography with depth-averaged potential equations. Environmental Fluid Mechanics. 2020. 20. Pp. 261–291. DOI: 10.1007/s10652-019-09691-z
17. Li, J., Li, S.S. Near-bed velocity and shear stress of open-channel flow over surface roughness. Environmental Fluid Mechanics. 2020. 20. Pp. 293–320. DOI: 10.1007/s10652-019-09728-3
18. Evtushenko, S.I. A nonlinear system of differential equations in supercritical flow spread problem and its solution technique. Axioms. 2023. 12(1). 11. DOI: 10.3390/axioms12010011
19. Alexandrova, M.S. Simple waves in the theory of two-dimensional water flows and the scheme of their use for free flow spreading. Construction and Architecture. 2020. 3(28). Pp. 47–50. DOI: 10.29039/2308-0191-2020-8-3-47-50
20. Orlov, V., Gasanov, M. Analytic approximate solution in the neighborhood of a moving singular point of a class of nonlinear equations. Axioms. 2022. 11(11). 637. DOI: 10.3390/axioms11110637
21. Orlov, V., Gasanov, M. Technology for obtaining the approximate value of moving singular points for a class of nonlinear differential equations in a complex domain. Mathematics. 2022. 10 (21). 3984. DOI: 10.3390/math10213984
22. Papchenko, N.G. Certificate of state registration of computer programs No. 2014611308. 2014.
23. Aleksandrova, M.S. Determination of flow parameters along the border current line. Certificate of state registration of computer programs. No 2022666655. 2022.

24. Orlov, V., Chichurin, A. About analytical approximate solutions of the van der pol equation in the complex domain. *Fractal and Fractional* 2023. 7(3). 228. DOI: 10.3390/fractalfract7 030228
25. Orlov, V. Moving singular points and the van der pol equation, as well as the uniqueness of its solution. *Mathematics*. 2023. 11(4). 873. DOI: 10.3390/math11040873
26. Orlov, V., Chichurin, A. The influence of the perturbation of the initial data on the analytic approximate solution of the van der pol equation in the complex domain. *Symmetry*. 2023. 15(6). 1200. DOI: 10.3390/sym15061200
27. Orlov, V. Dependence of the Analytical Approximate Solution to the Van der Pol Equation on the Perturbation of a Moving Singular Point in the Complex Domain. *Axioms*. 2023. 12(5). 465. DOI: 10.3390/axioms12050465

Information about authors:

Olga Burtseva, PhD in Technical Sciences

ORCID: <https://orcid.org/0000-0003-4288-8709>

E-mail: kuzinaolga@yandex.ru

Sergej Evtushenko, Doctor of Technical Sciences

ORCID: <https://orcid.org/0000-0003-3708-380X>

E-mail: evtushenkosi@mgsu.ru

Viktor Kokhanenko, Doctor of Technical Sciences

ORCID: <https://orcid.org/0000-0002-9962-3966>

E-mail: kokhanenkovn@mail.ru

Received 18.05.2021. Approved after reviewing 18.12.2023. Accepted 10.01.2024.



Research article

UDC 631.6.03


DOI: 10.34910/MCE.125.9



Pilot installation of a biosorption facility on a rice irrigation system

V.A. Suprun, V.V. Ustinova 

Federal Scientific Centre of Agroecology, Complex Melioration and Protective Afforestation of the Russian Academy of Sciences, Volgograd, Russian Federation

 ustinova-v@vfanc.ru

Keywords: water quality, mineralization, water purification, drainage and waste water, bioengineering technology, sorbents, bioplateau

Abstract. The article presents the composition and design of the developed biosorption facility designed to purify drainage and waste water from rice irrigation systems. The object of the study is the Sarpin watering and irrigation rice System (SWIS) located in the semi-desert zone of the Republic of Kalmykia. The studies were conducted and tested in field and laboratory conditions. The composition of the biosorption facility should include at least four stages of purification. The main elements of the biosorption facility design are a settling tank (section 1), a filtration chamber filled with medium-sized crushed stone (20–40 mm) and NDP-600 diatomite powder (section 2), as well as a bioplateau complex (section 3) and a filter chamber with a mixture of sorbents (section 4). The parameters of the bioplateau were calculated and its design was improved by including dampers that provide the necessary contact time of the treated water with higher aquatic vegetation on a smaller area of the structure, increasing the efficiency of purification. A graphical model of the structure was created in the AutoCAD program. Also, the project of the biosorption facility module developed in AutoCAD made it possible to calculate the volume of earthworks and implement them on the SWIS in the Republic of Kalmykia.

Funding: The study was carried out within the framework of state assignment No. FNFE 2022-0004 “Reclamation complexes: assessment, condition monitoring and process management using digital technologies.”

Citation: Suprun, V.A., Ustinova, V.V. Pilot installation of a biosorption facility on a rice irrigation system. Magazine of Civil Engineering. 2024. 17(1). Article no. 12509. DOI: 10.34910/MCE.125.9

1. Introduction

To date, the Sarpin watering and irrigation rice system (SWIS) and part of the Kalmyk-Astrakhan irrigation rice system (KARIS) are major reclamation facilities. For this period of time, their total irrigation area is 50.9 thousand hectares, of which 14.9 thousand hectares (SWIS) and 8.5 thousand hectares (KARIS) are regular irrigation, and the rest of the area falls on estuaries [3]. The Sarpin (SWIS) and Kalmyk-Astrakhan (KARIS) systems are geographically located in the north-east of the Republic of Kalmykia. The soils are represented by light chestnut and brown semi-desert, in combination with salt pans. Water supply is carried out from the Volga River in the Volgograd and Astrakhan regions. On its shore there are two water intakes of machine water lifting – Raygorodsky (near the village of Raygorod, Volgograd region) and Ushakovsky (near the village of Ushakovka, Astrakhan region). Water supply is carried out through the channels P-1 with a length of 114.6 km, P-3 118.8 km, taking into account the channel BP-1 and the Connecting channel 9.7 km. The systems were designed for rice crop rotation.

In 2010, 14.8 thousand hectares of land were not regularly irrigated. On the KARIS, the area of reclaimed land is 8.5 thousand hectares, but today only 0.5 thousand hectares are irrigated. About 30 % of the lands on the studied systems initially already had an unsatisfactory condition in terms of land reclamation due to the increased proportion of salinity of the root zone and groundwater regime [2].

Over the past 10–15 years, there has been a decrease in part of the sown areas of rice, and the dynamics of grain and fodder cultures has increased, but their yield is not high. It is necessary to radically revise the model of cultivation of agricultural crops, their cultivation technologies in order to use irrigated land more efficiently on the studied systems, as well as to introduce water-saving technologies and purification methods for reuse of waste drainage waters [3].

Research and development of purification methods for mineralized drainage and waste water were done by S.Y. Bezdina, I.V. Glazunova, L.V. Kireicheva, E.V. Ovchinnikova, K.Yu. Rybka, L.I. Shelepova, N.M. Segalove and many others [4–11]. N.P. Andreeva's works are devoted to the research of sorption materials for wastewater and drainage water treatment [12–15] etc. The reuse of drainage and waste water from rice irrigation systems was carried out by J.V. Kizyun, V.V. Lysenko, N.V. Ostrovsky, A.N. Semenenko [16–18] etc. Based on the results of the conducted research, the possibility of using natural materials as sorbents for purification and desalination of drainage and waste water has been scientifically substantiated. Application of local salt-absorbing plants could also be useful.

It is also necessary to reduce the mineralization indicators to the standard values of irrigation water by reducing the content of the main ions, as well as to achieve a balance of the ratio of calcium and sodium. For this purpose, an additional design element of a bioengineered sorption facility is needed. The previous studies showed that for more effective purification and desalination, such sorbents as agroionite and diatomite can be used, together with local higher aquatic plants (HAP) such as common sedge (*Carex nigra*) and broad-leaved cattail (*Typha latifolia*). The above-mentioned sorbents in combination with HAP have shown the most effective results in the purification and desalination of drainage and waste water in a model experiment [23].

Thus, the purpose of the presented research is to develop the composition and design of a new biosorption facility for the purification and desalination of waste drainage waters from rice irrigation systems. A gabion open gravity filtration treatment facility, which provides the purification of stormwater from highways, was used as a prototype. In addition, a bioplateau and a special chamber with artificial sorption materials was added to the facility. Depending on the set of pollutants, higher aquatic plants and sorption materials were selected. In connection with the purpose of the research, the objectives of the study were: calculation of the parameters of the bioplateau using a computer program; calculation of the parameters of the sorption chamber and the irreducible volumes of sorbents in the biosorption facility; designing a biosorption facility module using the AutoCAD program.

2. Methods

2.1. The Sarpin irrigation system

In the Sarpin irrigation system (SWIS), water intake from the Volga River in 2022 amounted to 57538 million m³ per year, and the discharge of drainage and waste water from the rice irrigation system to the Sarpa Lake amounted to about 17 million m³ per year. The main place of accumulation of drainage and discharge waters is Sarpa Lake. The water in the Sarpa lake has an increased level of mineralization and is a water discharge of drainage and waste water (up to 200 million m³) from rice irrigation systems of the Sarpinsk lowland. Depending on the discharge volume from 10 to 30 million m³, the salinity ranges from 7.5 to 15 grams per liter, containing significant concentrations of sodium chloride and neutral activity (pH < 8.0) [19]. The dynamics of water intake, discharge of drainage and wastewater and the area of rice cultivation on SWISS are shown in Table 1.

Table 1. Dynamics of water intake, discharge of drainage and waste water into Sarpa Lake and the area of rice sowing (data from the October RMO RK).

| Year | 2011 | 2012 | 2013 | 2014 | 2015 | 2016 | 2017 | 2018 | 2019 | 2020 | 2021 | 2022 |
|--|-------|-------|-------|-------|-------|-------|-------|-------|--------|-------|--------|-------|
| Water intake, thousand m ³ | - | - | - | - | - | - | 78973 | 69246 | 101338 | 70319 | 105562 | 57538 |
| Discharge into Sarpa Lake, thousand m ³ | 30871 | 18904 | 26510 | 14523 | 12096 | 13968 | 14902 | 13871 | 17214 | 20732 | 18618 | 16859 |
| The area occupied by rice, thousand m ³ | 3560 | 4656 | 51456 | 4005 | 3251 | 3201 | 3270 | 3300 | 4290 | 2955 | 3626 | 2717 |

During rice irrigation by flooding, the mineralization of drainage and waste water increases almost twice (from 0.9 to 1.7 grams per liter). The type of water by chemical composition is sodium chloride. By the end of the growing season, as well as during non-vegetative periods, mineralization increases to 6.0–7.0 grams per liter with a significant predominance of chloride sulfate and sodium ions. Thus, such indicators can lead to deterioration of the condition of plants and salinization of the soil, and salinization processes can also occur due to the high pH (Table 2).

Table 2. Chemical analysis of water in the discharge channel near the pumping station (HC-9).

| Season | Ion concentration, grams per liter | | | | | | | Sum of salts, grams per liter | pH |
|--------|------------------------------------|-------------------------------|-----------------|------------------------------|------------------|------------------|-----------------|-------------------------------|-----|
| | CO ₂ ⁻ | HCO ₃ ⁻ | Cl ⁻ | SO ₄ ⁻ | Ca ⁺⁺ | Mg ⁺⁺ | Na ⁺ | | |
| Spring | 0.01 | 0.49 | 0.9 | 1.90 | 0.41 | 0.20 | 0.83 | 4.74 | 8.3 |
| Summer | - | 0.27 | 0.17 | 2.66 | 0.32 | 0.22 | 0.69 | 4.34 | 8.2 |
| Autumn | - | 0.19 | 0.80 | 2.46 | 0.36 | 0.32 | 1.13 | 5.10 | 8.3 |

The quality of drainage and waste water was assessed and found unsatisfactory (Class III-IV) for irrigation with an irrigation coefficient of 5.33. The use of such water can cause the processes of salinization and alkalinization of the soil, and an increase in pH, especially when growing crops on heavy soils, thus negatively affecting the crop yield [20]. The possibility of using this water for irrigation will partially solve the problem of lack of water resources and thus reduce the cost of rice [21]. A necessary condition is the removal of chloride and sodium ions from the water and an increase in the amount of calcium, which will improve the irrigation coefficient and prevent further deterioration of the quality of water resources. To do this, it is necessary to develop a bioengineering technology that could purify mineralized runoff contaminated with nutrients and partially desalinate water. The technology should be low-energy, as natural as possible, easy to maintain and should not require large financial investments in order to become economically viable.

2.2. The water treatment facility

As a prototype of the developed technology, an installation created by ECOLANDSCHAFT-XXI CENTURY LLC for the purification of stormwater, rainwater and meltwater from urban highways was chosen. According to their design features, these are gabion open gravity treatment filtration facilities, including a bioplateau and a special chamber with artificial sorption materials. Such structures aesthetically fit into the infrastructure of the city and have an attractive appearance [22].

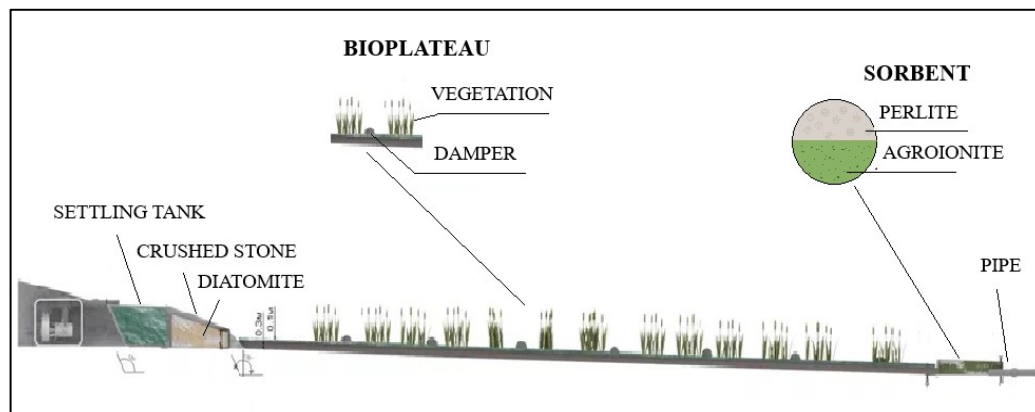


Figure 1. The main elements of the biosorption facility design (profile).

3. Results and Discussion

The composition of the biosorption facility should include at least four stages of purification. The main elements of the biosorption facility design are a settling tank (section 1), a filtration chamber filled with medium-sized crushed stone (20–40 mm) and NDP-600 diatomite powder (section 2), as well as a bioplateau complex (section 3) and a filter chamber with a mixture of sorbents (section 4) (Fig. 1).

The parameters of the section with a complex bioplateau were partially adjusted from the initial project of installation of ECOLANDSCHAFT-XXI CENTURY LLC after the choice of the construction site.

The construction site of the biosorption facility had to be chosen directly next to the 18xc3 discharge channel on the SWIS. In this section, the width of the structure had to be reduced. In order to reduce the width of the bioplateau and at the same time adjust the flow rate, special earthen zigzag mounds (dampers) were invented, thanks to which water moves longer on a smaller area of the bioplateau, thus the speed of movement is regulated and the flow time through the bioplateau increases. The calculated value of the bioplateau parameters was: length – 50 m, width – 3 m, water layer height – 0.3 m.

The modular installation for the SWIS was designed for a water consumption of 2.4 m³ per day.

The parameters of the biosorption facility were justified using existing techniques [22, 25] and preliminary results of field and laboratory studies. The parameters were calculated for the main structural elements of the biosorption facility.

The calculation of the settling tank is carried out based on its performance, that is, the volume of clarified water per unit of time. It is necessary that the water entering the sump should remain at rest for a certain period of time, in order to deposit the smallest suspended fraction to the bottom of the sump. Based on this, the depth was taken as 2.5 m, and the particle settling rate (1 m/hour) was calculated according to [27].

The settling time t can be expressed in terms of the path H of the particles and their velocity w :

$$t = \frac{H}{w} = \frac{2.5}{1} = 2.5 \text{ hours.} \quad (1)$$

The performance of the sump ($V_{lighten}$, m³ per s) of periodic action is calculated by the formula:

$$V_{lighten} = \frac{V}{t} = \frac{S * H}{t} = \frac{18.75}{2.5} = 7.5 \text{ m}^3/\text{hour}, \quad (2)$$

where $V_{lighten}$ is the volume of clarified liquid at the outlet of the settling tank, m³; H is the height of the clarified liquid layer, m; S is the surface area of settling, m²; t is the separation time (settling), h. Data according to [27].

Thus, the capacity of the sump for a modular installation in this case was 7.5 m³/h.

Calculations have shown that the performance of settling tanks depends only on the particle deposition rate and the deposition surface area.

Based on the calculations performed, the model installation of the biosorption facility has the following dimensions (Table 3).

Table 3. Parameters of the model installation of a biosorption facility.

| Cleaning stage | L (m) | B_1 (m) | B_2 (m) | H_1 (m) | H_2 (m) |
|---|---------|-----------|-----------|-----------|-----------|
| Accumulating sump | 5 | 2.5 | 3.3 | 2.5 | 1 |
| Chamber with sand and diatomite powder NDP-600 | 0.5 | 3 | 3.3 | 1 | 0.9 |
| Complex bioplateau | 50 | 3 | 3.3 | 0.5 | 0.3 |
| Chamber with a mixture of sorbents (agroionite + perlite agrotechnical) | 0.4 | 3 | 3.3 | 0.5 | 0.4 |
| Total, (max) | 55.9 | Max=3 | Max=3.3 | Max=2.5 | Max=1 |

Based on the table L is the length; B_1 is the width of the lower base; B_2 is the width of the upper base; H_1 is the height of the section at the water inlet; H_2 is the height of the section at the water outlet.

The functionality of a biosorption facility for water purification consists of the following stages. Drainage water is pumped from the discharge channel by a pump into a special settling tank. Suspended particles are deposited here, water is collected and accumulated. The flow rate of drainage and waste water in biosorption facility treatment can be from 1 l/s to 100 l/s and higher, depending on the size of the structure and, as necessary, is determined by the filtration flow rate through the filter elements. To determine the required sorbent loading mass, the dynamic exchange capacity (DEC) should be calculated. This is the amount of ionic particles absorbed by the sorbent at the moment when the solution is filtered through the sorbent layer until the so-called "breakthrough" moment. Thus, C_{exit} is the minimum permissible concentration in each specific case, or the minimum detectable concentration determined by the available

analyzer, or the required maximum permissible concentration (MPC) for a specific technological process. This level of concentration is called "breakthrough".

During laboratory studies, the moment of the "breakthrough" was recorded under dynamic conditions using such suitable sorbents as NDP-600 diatomite ("KVANT" production company) and a mixture of agrotechnical sorbents agroionite + perlite in three repetitions at the simulated salinity level of the solution (5 g/l). Certain samples of sorbents were placed in the filtration column and water was supplied until the value of the indicators of total mineralization began to grow. In total, 20 liters of the simulated solution were passed in each variant. The mass of the sorbent was selected based on the volume (100 ml) and was 7.5 g for NDP-600 diatomite, and 4.5 g for the agroionite + perlite mixture. The indicators of total mineralization were measured every 0.5 liters of the volume of the solution passed through the filtration column. The results of the study in the form of a graph of average indicators are presented in the figure (Fig. 2).

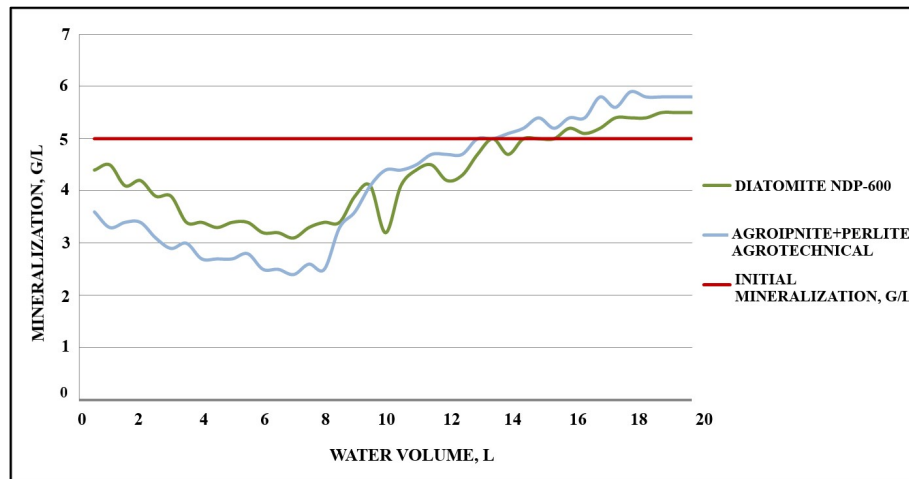


Figure 2. Output sorption curves.

The graph shows that NTP-600 diatomite in a volume of 100 ml is effective for cleaning 10 liters of saline solution with mineralization of 5 g/l, then the mineralization index of the filtrate begins to grow. After skipping 15.5 liters of solution, the mineralization index of the filtrate becomes higher than the initial one.

Based on the data obtained, the dynamic exchange capacity (DEC) of the studied sorbents before the breakthrough can be calculated according to the following formula (A.A. Komissarenkov) [24]:

$$DEC = \frac{1}{g} * \sum \left(\frac{C_{exit}}{C_0} \right) [(C_0 - C_{exit}) * V] \quad (3)$$

based on the formula, g is the mass of the sorbent; C_0 is the initial concentration of the ion, grams per liter; C_{exit} the concentration of the ion at the outlet of the column, grams per liter; V is the volume of filtrate with a concentration of C_{exit} , liter.

As a result of a laboratory experiment, C_{exit} and V were found for the sorbent diatomite NDP 600, for a mixture of sorbents agroionite + perlite, and $C_0 = 5$ g per l.

The DEC calculation for NDP-600 Diatomite is as follows:

$$DEC_D = \frac{1}{7.5g} * \sum \frac{C_{exit}}{C_0} [(5g/l - 3.2g/l) * 10l] = \frac{18}{7.5} = 2.4g/g. \quad (4)$$

3.2 grams per liter is the concentration of salt at the outlet of the filtration column obtained during laboratory tests.

Thus, it can be concluded that 1 g of the sorbent diatomite NDP-600 absorbs 2.4 g of salt.

Also, the calculation of DEC for a mixture of sorbents agroionite + perlite agrotechnical (DEC_{A+P}) is 4.4 g per 1 g of the mixture. This value is due to the porosity of the resulting sorbent mixture and different sorption mechanisms of the components of the mixture.

In order to calculate the required mass of the sorbent, it is necessary to know the period at which it is possible to return water to the irrigation channel and use it for irrigation in the future. It took 100–120 days to complete the processes of rice reproduction in the conditions of the desert zone of the Republic of

Kalmykia, provided that the average sum of active temperatures was 3400–3600 °C (according to the research data of E.B. Dedova, R.M. Shabanov) [22]. Thus, drainage and waste water can be returned to the irrigation canal for further use within 50–60 days.

The mass of the sorbent was calculated for 21 days. Based on the data obtained and the planned experimental installation with a flow rate of 2.4 m³/day, it is possible to calculate the mass of the sorbent for each section required for purification.

To substantiate the parameters of the sorption chamber, it is necessary to calculate the mass of sorbents. Based on the results of laboratory studies aimed at studying the static and dynamic capacity of sorbents. The mass of sorbents is calculated according to the following formulas. 10 % of the total mass was added to the resulting mass, as a margin of error (flushing, blowing, scattering).

Based on this, the mass of the sorbent for NDP-600 (m_d) diatomite powder in the second section will be equal to:

$$m_d = \frac{7.5g * 100l}{10l} * 24 * 21 = 37800g = 37.8 kg. \quad (5)$$

Similarly, for the fourth section with a complex sorbent (agroionite + perlite agrotechnical (m_{a+p})) the mass of the sorbent is 28.3 kg.

10 liters is the volume of saline solution that purification 7.5 grams of sorbent. The water consumption of the modular sorption plant, built in the field, is 100 liters per hour.

To develop a biosorption facility project, it was necessary to analyze the existing methods of calculating the bioplateau and sorption elements in order to calculate the necessary parameters of the sections of the biosorption facility module. The calculation was performed according to the standard method of V.G. Magomedov [25, 26].

Principles of bioplateau design. When designing a bioplateau, the main task of which is to remove biogenic bioplateau elements from the treated water, the contact time of water (t , day) with the HAP is calculated according to the dependencies (6) or (7):

$$t = \frac{27(\ln C_i - \ln C_e + \ln F)}{1.1^{T-20}} \quad (6)$$

or

$$t = \frac{\ln C_i - \ln C_e + \ln F}{65K_T}, \quad (7)$$

where C_i is the concentration of the biogenic substance at the entrance of the bioplateau, mg per l; C_e is the required concentration at the exit from the bioplateau, mg per l; F is the fraction of the substance attributable to water-soluble compounds, expressed as the ratio of the water-soluble substance to the total content, in fractions of one; T is the water temperature, °C; K_T is reaction rate constant (depends on the chemical composition of effluents and temperature), 1 per day; K_T is 0.0057 per day.

Then the area of the bioplateau (A) is calculated according to the dependence:

$$A = \frac{t}{d \frac{n}{Q}}, \quad (8)$$

where t is the contact time, day; d is the depth of water in the bioplateau, m; n is the ratio of the volume occupied by water to the total volume of water and plants, a fraction of one [22].

The dimensions of the biosorption facility model installation have the following indicators (Table 3):

After calculating the parameters of the structure, a graphical model of the structure was created in the AutoCAD program (Fig. 3).

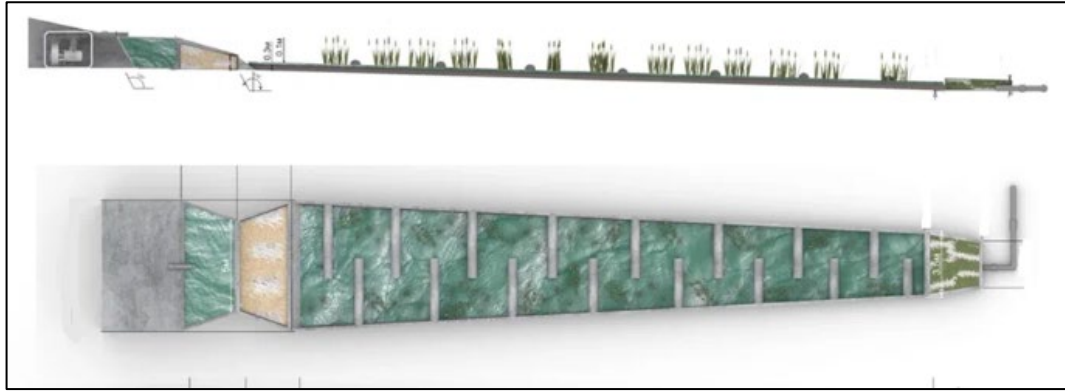


Figure 3. Visualization of the biosorption facility for the purification of drainage and waste water.

The project of the biosorption facility module developed in AutoCAD made it possible to calculate the scope of work and implement it on the SWIS in the Republic of Kalmykia.

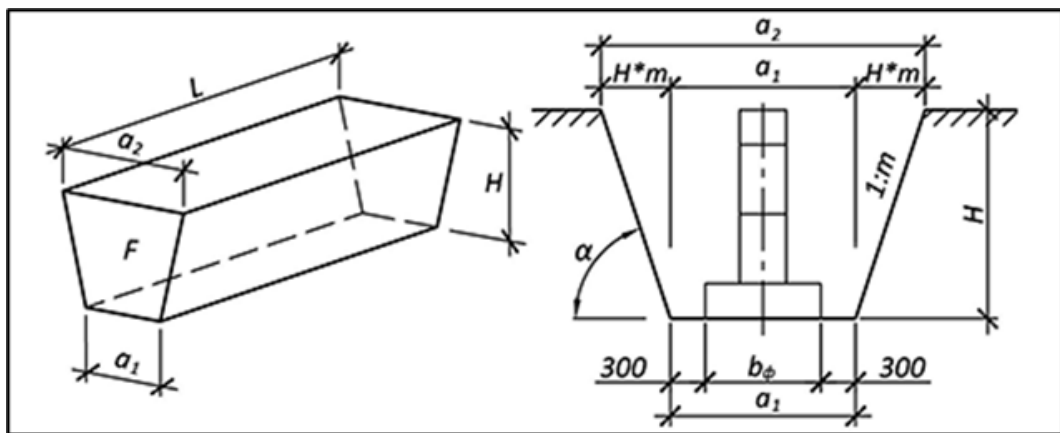


Figure 4. The scheme of the biosorption facility for calculating the volume of excavation of the trench.

To calculate earthworks, the following parameters are required: type of soil, width of the trench base ($a_1 = 3$), width of the trench top ($a_2 = 3.3$), trench height ($H_1 = 2$), trench height ($H_2 = 0.3$), trench length ($L = 55.9$) (Table 3).

The cross-sectional area of the recess (F_1) is 8 m^2 , the cross-sectional area (F_2) = 0.945 m^2 , then the volume of the recess (V) will be:

$$V = (F_1/2 + F_2/2 - m * (H_1 - H_2) 2/6) * L =$$

$$= (8/2 + 0.945/2 - m * (2 - 0.3) 2/6) * 55.9 = 236.55 \text{ m}^3. \quad (9)$$

The excavation work was carried out by a two-bucket excavator loader TEREX TLB 825-RM, with the assistance of the Sarpin branch of the Federal State Budgetary Institution "Kalmeliiovodkhoz Management". After that, the slopes were leveled and earthen ramparts were built at the bottom of the structure in a section designed to create bioplateau that act as dampers. Plastic pipes were laid on the earthen ramparts to strengthen the dampers and create the required height without expanding the base. 22 such dampers were built, alternately on the left and right sides of the base, 1 m long and 1.5 m wide.

The calculation of the settling tank (first section) was performed based on the required volume of clarified water. The second section, intended for the sorbent, was filled with a natural mineral sorbent – NDP-600 diatomite powder. Since this sorbent is used in powdered form and is washed out very quickly with water, a washed layer of crushed stone of medium fraction (20–40 mm) was placed over the sorbent so that 25–30 cm remained to the surface. A mixture of mineral sorbents (agroionite + agrotechnical perlite) was poured into the fourth section and thoroughly mixed to enhance the operation of various sorption mechanisms.

After the construction of the structure, plants were transplanted into the bioplateau section. The necessary plants were manually dug out in an irrigation canal, transferred to a bioplateau and planted. It was necessary to do this in a short time so that the aquatic plants would not lose their viability.

4. Conclusion

1. The composition and design of a new biosorption facility for the purification and desalination of drainage and waste water (DWW) from rice irrigation systems was developed. Its prototype was a gabion open gravity filtration treatment facility, which provides the purification of stormwater from highways. A feature of the developed biosorption facility distinguishing it from the prototype is the possibility, along with the removal of biogenic substances, to carry out partial desalination of mineralized DWW, which requires the inclusion of an additional chamber with a complex sorbent, justified in relation to the quality of the treated water. The main elements of the biosorption facility design are a settling tank (section 1), a filtration chamber filled with medium-sized crushed stone (20–40 mm) and NDP-600 diatomite powder (section 2), as well as a bioplateau complex (section 3) and a filter chamber with a mixture of sorbents (section 4).
2. The parameters of the bioplateau were calculated using a computer program [28] and its design was improved by including dampers that provide the necessary contact time of the treated water with the HAP to increase the cleaning efficiency. This allows reducing the area of the bioplateau without compromising its cleaning ability.
3. When calculating the parameters of the sorption chamber and the required volumes of sorbent in the biosorption facility, it was decided to calculate the mass of the sorbent according to the sorption capacity determined in laboratory and field studies.
4. The design of the biosorption facility module was carried out using the AutoCAD program, according to the previously calculated parameters, which made it possible to justify the amount of excavation work. A model of a biosorption structure in 3D space was compiled, which makes it possible to visually represent the type of the projected structure in full scale.

References

1. Dedova, E.B., Sazanov, M.A., Kovrigo, S.I. Kharakteristika vodnykh resursov Respubliki Kalmykiya i puti ikh ratsionalnogo ispolzovaniya dlya nuzhd agropromyshlennogo kompleksa. Materialy mezhdunarodnoi nauchnoi konferentsii «Ekologicheskoye sostoyaniye prirodnoy sredy i nauchno-prakticheskiye aspekty sovremennykh meliorativnykh tekhnologiy» [Characteristics of water resources of the Republic of Kalmykia and ways of their rational use for the needs of the agro-industrial complex. Mat. international scientific conference "Ecological state of the natural environment and scientific and practical aspects of modern reclamation technologies"]. Tom 6. Ryazan. 2014. Pp. 256–260. (rus)
2. Dedova, E.B., Sazanov, M.A. Problemy vodnogo khozyaystva Respubliki Kalmykiya v svyazi s razvitiyem melioratsii. Sovremennoye sostoyaniye i perspektivy razvitiya vodokhozyaystvennogo kompleksa Zapadno-Kaspiyskogo basseynovogo okruga: Vserossiyskaya nauchno-prakticheskaya konferentsiya [Problems of water management of the Republic of Kalmykia in connection with the development of land reclamation. Current state and prospects of development of the water management complex of the West Caspian Basin district: collection of articles of the All-Russian Scientific and Practical Conference]. Makhachkala: ALEF, 2013. Pp. 25–29. (rus)
3. Borodychev, V.V., Dedova, E.B., Chimidov, S.N. Rice cultivation under periodic surface irrigation in the Sarpinskaya Lowland. Plodorodie. 2013. 2. Pp. 35–37. (rus)
4. Bezdina, S.Ya. Ekologicheskie osnovy vodopolzovaniya [Ecological bases of water use]. Moskva. Vserossiyskiy nauchno-issledovatel'skiy institut agroximii imeni D.N. Pryanishnikova. 2005. 223 p. (rus)
5. Kireicheva, L.V., Glazunova, I.V. Environmentally friendly resources. Technical solutions for wastewater treatment. Voda Magazine. 2008. 4. Pp. 44–47. (rus)
6. Miroshin, M.A., Glazunova, I.V. Uchet predotvrashchennykh ushherbov pri raschete parametrov bioinzhenernykh sooruzhenij. Problemy kompleksnogo obustrojstva texnoprirodnnykh sistem. Materialy mezhdunarodnoj nauchno-prakticheskoy konferentsii [Taking into account the prevented damages when calculating the parameters of bioengineering structures. Problems of complex arrangement of technoprirodic systems: Materials of the International scientific and practical conference]. Moskva. 16–18 aprelya. 2013. Tom Chast' IV. Moskva. Moskovskij gosudarstvennyj universitet prirodoobustrojstva. 2013. Pp. 193–198. (rus)
7. Kontseptsiya razvitiya melioratsii sel'skokhozyaystvennykh zemel Respubliki Kalmykiya na period do 2020 goda [The concept of development of agricultural land reclamation in the Republic of Kalmykia for the period up to 2020]. Moskva. Rossiyskaya akademiya sel'skokhozyaystvennykh nauk. 2012. 64 p. (rus)
8. Kireicheva, L.V. Drainage flow as an alternative water resource for irrigation. Melioration and water management. 2018. 4. Pp. 13–18. (rus)
9. Rybka, K.Yu., Shchegol'kova, N.M. Features of functioning of constructed wetlands in arid regions. Arid Ecosystems. 2021. 27(3). Pp. 103–110. DOI: 10.24411/1993-3916-2021-10170
10. Shchegolkova, N. M., Kharitonov, S.L., Rybka, K.Y., Semenov, M.V. Taxonomic and Functional Diversity of Microbial Communities as an Indicator of the Effectiveness of Water Treatment in Constructed Wetlands. Water Resources. 2020. Vol. 47, No. 6. Pp. 1020–1030. DOI 10.1134/S0097807820060111
11. Ovchinnikov, A.S. Denisova, M.A., Bocharnikov. Water treatment of surface water using a ferrite reagent. IOP Conference Series: Earth and Environmental Science, Stavropol, 29–30 oktyabrya 2021 goda. Stavropol. 2022. Pp. 012002. DOI 10.1088/1755-1315/996/1/012002

12. Andreeva, N.P. Ochistka stochnykh vod s primeneniym sorbentov prirodnoho proiskhozhdeniya. Shestoy mezhdunarodnyy kongress "Voda: ekologiya i tekhnologiya" [Wastewater treatment with the use of sorbents of natural origin. Sat. tr. of the 6th International Congress of ECWATECH-2004]. Moscow. June 1-4. 2004. t 2. 697 p. (rus)
13. Glazunova, I.V., Martynenko, N.P. Kompleksnyy sorbent dlya ochistki stochnykh vod ot nefteproduktov i tyazhelykh metallov [Complex sorbent for wastewater treatment; from petroleum products and heavy metals]. Agrokhimicheskiy vestnik. № 4. 2001. Pp. 38-39. (rus)
14. Kireicheva, L.V. Yashin, V.M., Ilinsky, A.V., Nguen, S.H. Detoxification of heavy-metal contaminated leached chernozems and ancient alluvial soils with the use of sorption materials. Russian Agricultural Sciences. 2009. T. 35. № 3. Pp/ 182-184.
15. Kireicheva, L.V., Kuptsova, A.A. Improving the quality of drainage water using natural sorbents. Melioration and water management. 1998. 1. Pp. 6–8. (rus)
16. Kizyun, Zh.V., Shishkin, V.O., Ostrovsky, N.V. Estimation of economic efficiency of the method of cultivation of rice with the reuse of drainage waters. Scientific Journal of KubSAU. 2014. No. 97. Pp. 310–320. (rus)
17. Ostrovsky, N.V. Regulirovaniye vodno-vozdushnogo rezhima pochv v protsesse povtornogo ispolzovaniya sbrosnykh vod risovykh system. Nauchnyye dostizheniya molodezhi Kubani : sbornik tezisev dokladov nauchnykh konferentsiy studentov i aspirantov v 1998-2000 gg., Krasnodar, 01 yanvarya 1998 goda – 31 2000 goda [Regulation of the water-air regime of soils in the process of reuse of waste water of rice systems. Scientific achievements of youth – Kuban: collection of abstracts of scientific conferences of students and postgraduates in 1998–2000, Krasnodar]. Tom Vypusk 1. Krasnodar: Kubanskiy gosudarstvennyy agrarnyy universitet imeni I.T. Trubilina. 2001. 47 p. (rus)
18. Semenenko, A.N., Lysenko V.V. Vodooborotnaya risovaya orositelnaya sistema [Water-circulation rice irrigation system. The works of the Cubist]. Trudy Kub SKhI. Vyp. 224(252). Krasnodar. 1983. Pp. 127-132. (rus)
19. Tekhnicheskiye usloviya TU 2164-006-03029859-2009 "Agroionit - neorganicheskiy sorbent dlya rekultivatsii pochv i poglotitel soley tyazhelykh metallov" [Technical specifications TU 2164-006-03029859-2009 "Agroionite – inorganic sorbent for soil reclamation and a heavy metal salt absorber."]. (rus)
20. Ovchinnikov, A.S., Borodychev, V.V., Dedova, E.B., Sazonov, M.A. Monitoring of water resources in Republic of Kalmykia and water use ecosystem problems in agricultural industrial complex. Izvestia of the Lower Volga Agro-University Complex. 2015. 3(39). Pp. 9–19. (rus)
21. Dedova, E.B., Borodychev, V.V., Shuravilin, A.V. Economic and land-reclamation estimate of irrigation systems at the Kalmykia Republic. Melioration and water management. 2011. 4. Pp. 11–13. (rus)
22. Dedova, E.B., Shevchenko, A.A., Dedov, A.A., Shabanov, R.M. Technological regulations for improving the ecological state and increasing fodder production on estuary irrigation systems of the Caspian Lowland. IOP Conference Series. Earth and Environmental Science. II International scientific and practical conference "Ensuring sustainable development in the context of agriculture, green energy, ecology and earth science". Smolensk. Russian Federation. 2022. Vol. 1045. P. 012174. DOI 10.1088/1755-1315/1045/1/012174.
23. Ulrich, B. Natural and anthropogenic components of soil acidification. Zeitschrift für Pflanzenernahrung und Bodenkunde. 1986. 149.. Pp. 702–717. DOI: 10.1002/jpln.19861490607
24. Komissarenkov, A. A., Suslov, V.A. Nanokompleksy v tekhnologii vodopodgotovki [Nanocomplexes in water treatment technology]. Vodoochistka. 2011. № 6. Pp. 41-44. (rus)
25. Kulsy, L. A. Strokach, R.R. Tekhnologiya ochistki prirodnykh vod [Technology of natural water purification]. Kiev: Vishcha shk. 1981. Pp. 150–185. (rus)
26. Metodika (osnovnyye polozheniya) opredeleniya ekonomicheskoy effektivnosti ispolzovaniya v narodnom khozyaystve novoy tekhniki, izobreteniy i ratsionalizatorskikh predlozheniy [Methodology (basic provisions) for determining the economic efficiency of using new equipment, inventions and rationalization proposals in the national economy]. Izdatelstvo Ekonomika. Moskva. 1977. 48 p. (rus)
27. Rekomendatsii po raschetu sistem sbora, otvoda i ochistki poverkhnostnogo stoka s zhilykh massivov, ploshchadok predpriyatiy i opredeleniyu usloviy yego sbrosa v vodnyye obyekty [Recommendations on the calculation of systems for collecting, diverting and cleaning surface runoff from residential areas, enterprise sites and determining the conditions for its release into water bodies]. Moskva: AO "NII VODGEO", 2014. 88 p. (rus)
28. Glazunova, I.V., Romashchenko, A.K., Tishina, K.A. Bioengineering structures and storages of local flowing of watersheds for a more efficient usage of water resources of river basins. Environmental Engineering. 2018. 2. Pp. 46–54. (rus)

Information about authors:

Veronika Suprun, PhD of Technical Sciences

E-mail: suprun-v@vfanc.ru

Viktoriya Ustinova,

ORCID: <https://orcid.org/0000-0001-6490-7072>

E-mail: ustinova-v@vfanc.ru

Received 29.05.2023. Approved after reviewing 30.12.2023. Accepted 30.01.2024.



Research article

UDC 624.139

DOI: 10.34910/MCE.125.10



Buckling analysis of piles in solid frozen soils

V.S. Utkin, Zh.V. Kosheleva , O.V. Yarygina 

Vologda State University, Vologda, Russian Federation

✉ koshelevazhv@vogu35.ru

Keywords: soil bearing capacity, solid frozen soil, soil thawing, axial compression, longitudinal bending, critical force, critical pile length

Abstract. The object of the research is the behavior of axial compressed piles in the foundations on continuous permafrost soils under global warming. There is a degradation of permafrost soils at present. The permafrost layer is vertically divided into two parts: 1) the top, the active layer; 2) the bottom, the frozen mass. The active layer of soil thaws in summer and freezes in winter. Frozen soil behaves as a rock in winter and as a liquid mass on some soil thickness in summer. Accordingly, the surface forces acting on the pile surface in winter time disappear in the entire melted liquid soil layer in summer time. We considered the design of a pile by the condition of the first kind buckling (form) under axial compression. We took into account the conditions when the depth of the base thawing soil increases in the upper part of the pile at the stages of operation (in the summertime of the pile operation). In addition, we considered the calculation of the pile length under the same conditions at a given load on the pile at the stage of its design. To forecast the piles operating time in pile foundations or individual piles during global warming on the Earth, an algorithm for calculating pile length at the design stage is proposed. The paper provides a numerical example of calculating the pile operational life in the solid frozen soil of the foundation in an oil pipeline support.

Citation: Utkin, V.S., Kosheleva, Zh.V., Yarygina, O.V. Buckling analysis of piles in solid frozen soils. Magazine of Civil Engineering. 2024. Article no. 12510. DOI: 10.34910/MCE.125.10

1. Introduction

The object of the research is the behavior of axial compressed piles in the foundations of solid permafrost soil under the conditions of global warming on the Earth. Permafrost soils are also present in the northern regions of Russia. In the summer, there is a gradual transformation of the upper layer of permafrost into a fluid state (liquid soil). During winter periods, this layer of liquid soil remains at some increasing depth under the upper freezing layer. Therefore, it is required to develop a theory for calculating the piles bearing capacity in longitudinal bending with the time identification of buckling onset from compressive load in the operational stage. In addition, it is required to develop a method of determining the effective length of the pile at the design stage according to the same criterion of longitudinal stability at a design load.

The relevance of the study lies in the fact that the volumes of extraction, processing and use of mineral resources and energy sources are expanding in the northern regions of Russia. Pile foundations are used for the construction of buildings, gas and oil pipelines in these conditions of permafrost soils. Such pile foundations have been in operation for several decades. The development of infrastructure in the regions of the Arctic and Siberia (Russia) in the coming years was indicated by President Vladimir V. Putin in a Message on February 21, 2023. There is no information on the design of piles in the normative regulations SP 25.13330.2020 "Soil bases and foundations on permafrost soils", SP 410.1325800.2018 "Main and field pipelines for oil and gas, construction in permafrost conditions and control of works" and

other sources, in the conditions noted above. All the above increases the importance of the presented article.

The design, construction and operation of foundations in areas of permafrost are very difficult tasks. The correct solution of this problem is possible only if the processes taking place in the active layer and the permafrost layer are taken into account. The active layer is the layer in which the soil freezes and thaws. If the nature of these processes is taken into account incorrectly in the design, then unacceptable deformations often occur in buildings and structures. Sometimes this fact is the reason for accidents and emergencies. Examples are the disasters during the construction of the railway to Vorkuta (Russia) and the recent failure of buildings in the city [1–14].

Permafrost is located at least 25 % of the entire land area of the globe. Huge massifs of permafrost are located in the northern part of the Eurasian continent, in the northern territories of Canada, Alaska, Greenland, on the islands of the Arctic Ocean, in Antarctica. The thickness of the frozen soil layer varies from a few tens of centimeters to a kilometer and more. For example, the largest recorded depth according to information sources is about 1500 m, and it is located in Yakutia (Russia) [11].

There is a degradation of permafrost soils at present. It is caused by global warming and anthropogenic influences (heat loss of buildings, waterlogging and flooding of areas, errors in the construction and maintenance of urban infrastructure, salinization of soils). As a result, there is a reduction in the area of permafrost soils, an increase in their temperature and a deepening of the active layer of soil. All the above leads to decrease of soil bearing capacity and loss of stability of buildings and structures with possible catastrophic and other consequences. One such disaster occurred in Norilsk (Russia) at CHP-3 in May 2020. A massive diesel fuel leakage and subsequent catastrophic contamination of nearby rivers and lakes occurred due to sagging foundations and oil tank supports. In the Taimyr Telegraph online publication, Mikhail Korolev, deputy director of the Institute of Applied Mechanics of the Russian Academy of Sciences, head of the geomechanics laboratory and head of the applied geomechanics department at National Research Moscow State University of Civil Engineering, noted that the permafrost area is rapidly shrinking, the depth of seasonal thawing and freezing is changing, the temperature of frozen ground has risen from $-6\text{ }^{\circ}\text{C}$ to $-2.5\text{ }^{\circ}\text{C}$, and temperature changes of even one degree often lead to a 50 percent loss in bearing capacity of piles [15].

More than 300 buildings in Yakutsk (Russia) have been seriously damaged due to subsidence of frozen soil in the last 30 years according to the studies given in [16–23]. In 1992, the percentage of damaged buildings was 10 % in Norilsk (Russia), 22 % in Tiksi (Russia), 35 % in Dudinka (Russia), 50 % in Pevek (Russia) and Amderma (Russia), 55 % in Magadan (Russia), 60 % in Chita (Russia) and 80 % in Vorkuta (Russia). Unfortunately, by 1999, the number of structures damaged due to uneven foundation subsidence increased in Norilsk by 42 %, in Yakutsk by 61 %, and in Amderma by 90 % compared to the previous decade. The Taimyr Telegraph online publication notes that in 2009 in Norilsk a quarter of the housing stock is under special control for the condition of soils and supporting structures, and every year one or two houses are declared uninhabitable due to foundation deformation [15].

The need to develop the method for calculating piles under the above-described conditions is due to the lack of calculation methods in the normative regulations SP 25.13330.2020 "Soil bases and foundations on permafrost soils" and in other documents. In addition, the reason for the study is the presence of areas with solid frozen soils in the Russian Federation and the inevitable global warming of the Earth.

The purpose of the research is to develop methods for calculating the safe operating time of piles in the foundations of existing buildings and the length of piles in pile foundations during the design phase under conditions of global warming on Earth. The piles are under axial compression conditions in solid-frozen soil bases. The criterion of pile stability (form) under longitudinal bending is considered.

2. Methods

Permafrost in Russia occupies large areas in the European territory and especially in Siberia. The permafrost layer is vertically divided into two parts: 1) the top, the active layer; 2) the bottom, the frozen mass. The active layer of soil thaws in summer and freezes in winter. The thickness of this layer varies in Russia and varies from a fraction of a meter up to four or more meters [24]. It is possible to say that the thickness of thawing layer of soil can reach significant dimensions after 50–100 years of building exploitation in permafrost conditions, according to existing forecasts. The thickness of the layer is not known in advance. Thus, in order to avoid accidents, it is necessary to study and develop preventive measures nowadays. For example, it is necessary to measure the thickness of thawed ground at different time intervals. Then extrapolate the thickness limit to the planned lifetime of the pile from the data obtained. The pile length and its bending stability must be taken into account. It is also necessary to determine the pile length in the design phase with regard to the pile's service life.

There are two types of active layer of soil: merging and nonmerging. In the first case, the active layer freezes completely in winter and joins the permafrost. In the second case, a layer of thawed ground (suprapermafrost groundwater) remains between the upper permafrost layer and the permafrost strata in winter time. In the second case, in summer time, the top soil layer thaws and a common active thawed layer is formed with the suprapermafrost groundwater. This layer affects the lower frozen ground, partially transforming it into a fluid state. Over time, with global warming on Earth, the active thawing layer increases. For example, as noted above, it reaches considerable depth in some areas of Russia. Thus, the active layer contains groundwater, which is deposited (located) on the permafrost soil. In the permafrost state, soils are divided into rocky, semi-frozen and dispersed soils. The temperature gradient ranges from $-36\text{ }^{\circ}\text{C}$ in winter to $+34\text{ }^{\circ}\text{C}$ in summer [24].

The proposed article deals with the behavior and calculation of piles under a building or structure according to their bearing capacity in solid frozen soils. Frozen soil behaves as a rock in winter and as a liquid mass on some soil thickness in summer. Accordingly, the surface forces acting on the pile surface in winter time disappear in the entire melted liquid soil layer in summer time. In this case, the pile load is completely transferred to the underlying frozen soil layer. Although soils of the rock class (type) occupy a minor place in Russia, they are of interest in construction practice during the design, construction and operation phases of buildings and structures. This is due to the complete absence of information about the operation and calculation of piles in the SP 25.13330.2020 "Soil bases and foundations on permafrost soils" and in other existing and previously existing normative regulations.

It is known [25] that the bearing capacity for a long rod of a constant specified length in compression is limited by the value of critical force, and for a rod with a constant specified load is limited by the value of its critical length. These criteria will be used in the proposed compression pile calculations in permafrost conditions of frozen ground at the base of foundations. Individual calculation examples will be demonstrated.

The pile design peculiarity in solid frozen soils is that the pile bearing capacity under compressive load can be additionally limited by the buckling (form) of the pile. This occurs when the thawed soil layer thickness reaches the critical pile length according to the condition of its stability with its ends restrained in the foundation pile cap and in the underlying frozen soil, as shown in Fig. 1. This does not correspond to the design diagram of SP 25.13330.2020 "Soil bases and foundations on permafrost soils" shown in Fig. 2 for thawed soil with the friction forces on pile surface $R_{af} A_{af}$ given in equation (1) below.

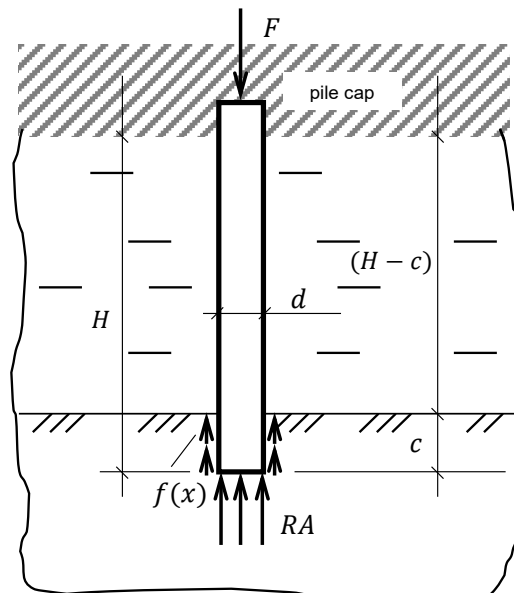


Figure 1. Design diagram of a pile in solid-frozen soil at permissible thawing depth, d – cross-sectional diameter of the pile (borehole).

The limit design diagram of a pile with the top part restrained in the foundation pile cap and the bottom part restrained in the frozen soil at length c is shown in Fig. 1. The value of length c must be at least 0.5 m according to SP 410.1325800.2018 "Main and field pipelines for oil and gas. Construction in permafrost conditions and control of works".

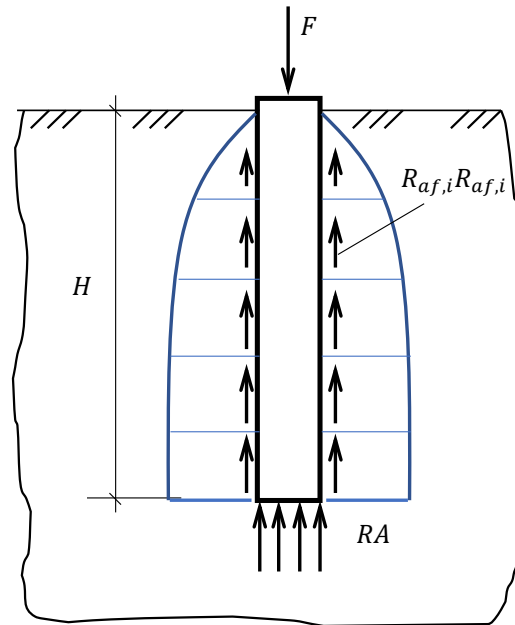


Figure 2. Design diagram of the limit state of a pile under load according to SP 25.13330.2020.

The information from the SP 25.13330.2020 is given in Fig. 2 as a design diagram of a pile in axial compression in permafrost soil bases. The soils go into a fluid state during thawing but retain the effect on the pile surface in the form of friction forces $R_{af} A_{af}$ and on the pile tip in the form of force RA . The pile bearing capacity in Fig. 2 is determined according to the equation

$$F = \gamma_t \gamma_c \left(RA + \sum R_{af,i} A_{af,i} \right). \quad (1)$$

The description and values of the term in equation (1) can be found in SP 25.13330.2020, so they are not given in the text of the article.

The design diagram of the pile (Fig. 2) is given to show that it and equation (1) are not applicable to the design of piles in foundations with solid frozen soil and a liquid soil layer above it, as shown in Fig. 3. In the pile limit state, the reaction at the pile tip is equal to $R_{soil} A$, where R_{soil} is the design resistance of the base soil and A is the pile cross-sectional area. The forces $f(x)$ according to Fig. 1 on the length of the pile section c are not taken into account, which gives a reliability reserve for pile operation.

Let us consider the calculation equation for the design diagram in Fig. 3 as applied to the calculations of existing individual piles in solid frozen base soils. The pile ultimate depth in the solid frozen soil in the limiting state is denoted by c . As the solid frozen soil thaws, the values of the members $R_{af,i}$ of equation (1) decrease and at full thawing to the depth $(H - c)$ they are equal to zero. Then, the pile design diagram has a form as shown in Fig. 3. In this case the pile will keep its operating state under the condition $F \leq \gamma_t \gamma_c RA$ in solid frozen soils. Hereafter we will replace R in (1) with R_{soil} .

To prevent lateral offset of the pile tip in the limit state, the pile must enter the permafrost to a depth equal to or greater than 0.5 m, as shown in Fig. 3, as well as according to SP 410.1325800.2018. The friction forces $R_{af,i}$ on the pile length c , as shown in Fig. 1, are neglected, given the low height of the pile penetration into the soil, to the reliability reserve. According to our investigations, the solid frozen soil under the pile tip does not fracture when the load F increases, but the fracture occurs in the pile material. In this case, pile operational safety in bearing capacity depends not on soil strength but on pile material strength R . The calculation equation is $F \leq R \cdot A$. The pile operating time is equal to the time it takes for the foundation soil to thaw to a depth $(H - c)$. For this purpose, the soil thawing depth h must be measured periodically during operation and compared with the permissible pile length $(H - c)$ determined from the condition $F = F_{cr}$. The pile's serviceability in terms of material strength is retained at $F \leq R \cdot A$, where R is the design resistance of the pile material. The problem, however, is to determine the value of H

(taking into account c) at which the pile stability is retained in its longitudinal bending from the operational load on the pile F .

For a building foundation (foundation pile cap) with pile group, the individual piles with more intensive thawing must be monitored. The remaining service life of the structure must then be determined from the condition of the piles according to the pile bearing capacity and the condition of their stability in axial compression. To determine the maximum depth h of the thawed soil layer at time t , the simplest methods that do not need to be described in the article are used. If the pile length H in the existing structure is not known, the value of H can be determined, for example, by the method described in [26, etc.].

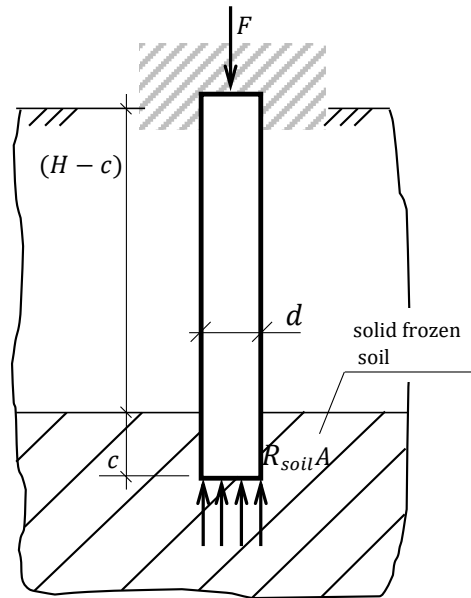


Figure 3. Design diagram of the pile limit state during thawing of the top soil layer to depth $(H - c)$.

3. Results and Discussion

Let us consider the design of a pile by the condition of the first kind buckling (form) under axial compression. We take into account the conditions when $F \leq F_{cr}$ and the depth of the base thawing soil increases in the upper part of the pile at the stages of operation (in the summertime of the pile operation). Also consider the calculation of the pile length under the same conditions at a given load on the pile at the stage of its design.

The main task of calculation for operational piles in load-bearing structures is to determine their life remaining. When designing the pile, its cross-sectional dimensions and length must be determined according to the design life of the pile. In both cases, the operation of the pile under the described conditions will be limited to the pile buckling in compression, according to the design diagram shown in Fig. 4. The following notations are used: h is the thawed layer height of solid frozen soil, l_0 is the pile design length according to the first kind stability criterion in the longitudinal bending of the pile with the restrained ends [25]. The design diagram of the pile in the buckling analysis (form) takes into account the full restraint of the upper end of the pile in the foundation pile cap. The pile tip is assumed to be elastically restrained (at the level of its length measurement) as a safety margin because the soil is in an intermediate state between liquid thawed soil and permafrost foundation soil. Under such conditions, the soil is exposed to water for a long period of time and its hardness and compressive effect on the pile may be reduced.

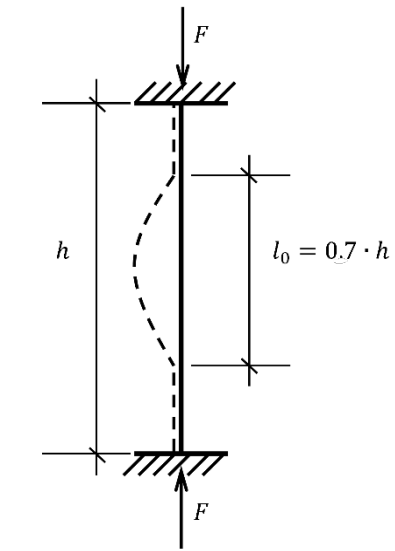


Figure 4. Design diagram of a pile in longitudinal bending operation, h is thawed layer height of the base soil.

Consider the calculation of a pile at the operational stage under axial compression according to the design diagram in Fig. 4. The pile serviceability is determined by the condition $F \leq F_{cr}$, where F is the load on the pile and F_{cr} is the critical load in the longitudinal bending of the rod (pile). For example, for reinforced concrete columns (piles) according to [27] we have

$$F_{cr} = \varphi(R_b A_b + R_{sc} A_s), \quad (2)$$

where R_b , R_{sc} are design compressive resistance of concrete and reinforcement of reinforced concrete pile, A_b , A_s are cross-section areas of concrete and reinforcement, φ is the buckling coefficient of the rod in axial compression. The values of φ for reinforced concrete rod (pile) with restrained ends (Fig. 4) can be determined, for example, according to Table 1 from [27] by the values $l_0 = 0.7h$. The length l_0 is sometimes called the “unbraced length” or “buckling length” of the unrestrained rod [25].

Table 1. Values of coefficients φ for reinforced concrete columns (piles) of circular or square cross-section in compression*.

| l_0/d | l_0/b | φ |
|---------|---------|-----------|
| 7 | 8 | 1 |
| 8.5 | 10 | 0.98 |
| 10.5 | 12 | 0.96 |
| 12 | 14 | 0.93 |
| 14 | 16 | 0.89 |
| 15.5 | 18 | 0.85 |
| 17 | 20 | 0.81 |
| 19 | 22 | 0.77 |
| 21 | 24 | 0.73 |
| 22.5 | 25 | 0.68 |
| 24 | 28 | 0.64 |
| 26 | 30 | 0.59 |
| 28 | 32 | 0.54 |
| 29.5 | 34 | 0.49 |
| 31 | 36 | 0.44 |
| 33 | 38 | 0.40 |
| 34.5 | 40 | 0.35 |

l_0 is design length of the pile, see Fig. 4, d is pile diameter, b is the size of the pile cross-sectional side.

* the effect of sustained load on the bearing capacity due to concrete creep is not taken into account

The design resistance of the pile concrete in axial compression R_b and the design resistance to compression of the pile reinforcement R_{sc} are determined by non-destructive methods at the pile operation stage [28, 29]. At the design stage these characteristics of the materials are determined by SP 63.13330.2018 "Concrete and reinforced concrete structures. General provisions".

It is possible to plot the dependence of φ on l_0/d or l_0/b from the data in Table 1, or a calculation program can be created.

For the time moment t , let us represent equation (2) as

$$F_{cr}(t) = \varphi(t)(R_b A_b + R_{sc} A_s). \quad (2')$$

By measuring the depth of thawed solid frozen soil in summertime and revealing the maximal depth of the upper liquid soil layer, we find the value of $h(t)$ at the time t of measurement and, respectively, $l_0(t) = 0.7 \cdot h(t)$ and the value of $F_{cr}(t)$. The number of measurements h_i during the summertime is anything. It depends on the liability of the pile's operating condition in the structure. The same applies to measurements by years. In all cases, the highest value $h(t)$ from the series of measurements is taken into account.

Using the value of $l_0(t)/d$ from Table 1, find the value of $\varphi(t)$. Using the formula (2') find $F_{cr}(t)$ and compare it with the load F on the pile. At $F \leq F_{cr}$, the pile retains its serviceability. Based on the values of $F_{cr}(t)$ at different time values t , a graph is plotted and extrapolated by time (by year). Then the pile operating life to failure at $F = F_{cr}$ is approximated. The value obtained with the passage of short time intervals (years) and measurements $h(t)$ can be refined. The calculation algorithm will be discussed below using a numerical example.

Table 1 shows that the greater l_0 , the smaller φ and, consequently, the smaller the value of the critical force $F_{cr} = \varphi(R_b A_b + R_{sc} A_s)$ by (2). In our problem, l_0 is the height of the thawed layer h of solid frozen soil. We can find $\varphi_{cr} = F / (R_b A_b + R_{sc} A_s)$ from the condition $F \leq F_{cr}$. And we can find the value of the thawing soil limit depth l_0 or h_{max} from Table 1. If, at the operation stage of pile (or building), to measure $h(t)$ values during the first years of operation and to identify $h(t)$ function, it is possible to find the limiting value h_{cr} and correspondingly the value $l_0 = 0.7 \cdot h_{cr}$ by extrapolation of the function for a longer time t . Then use h_{cr} to determine the limit time of the pile or building, thereby preventing an accident or failure of the pile or structure.

The pile stability is high in the first years of operation with small values of h . Further, with increasing values of h it decreases to the point of losing stability. Thus, with an effective pile length, the residual operating time of buildings or structures in terms of the bearing capacity of piles will be determined by the time of reaching the limit pile length according to the calculation scheme of Fig. 3 under the conditions of global warming and the condition of pile stability in the thawed foundation soil layer according to Fig. 4.

Let us show by example the pile calculation method by the stability criterion at the stage of operation. Conditionally consider the pile calculation by the example of an oil pipeline pile in the conditions of the north of the Russian Federation (numerical values in the example are taken conditionally). Let us know the values of the pile diameter $d = 0.2$ m with the cross-section area $A_b = 0.0314$ m², diameter and reinforcement area of the reinforced concrete pile are respectively equal to $d_s = 0.02$ m and $A_s = 18.8 \cdot 10^{-4}$ m². Concrete and reinforcement compressive resistance characteristics according to SP 63.13330.2018 $R_b = 14.5$ MPa, $R_{sc} = 210$ MPa. The load on the pile $F = 0.42 \cdot 10^6$ N. If the load F on the pile is not known, and it is impossible to determine it theoretically by calculation, then for reinforced concrete piles of buildings and structures it can be identified by the method described in the invention patent [28].

The oil pipeline section under consideration is located in the permafrost zone. The foundation soils are classified as solid frozen. The length of the pile below the ground surface $H = 8.5$ m, and its lower part should be in the unfrozen soil by at least $c = 0.5$ m. It is required to determine the residual pile operating life.

If the pile length under a building or structure is not known from the design documentation, it can be determined using various radar-type devices [24], devices "Spektr-4", "PDS-MG4" [30], the acoustic method [31], etc.

Let us assume that after $t_1 = 20$ years of operation the soil thawed to a depth of $h_1 = 2$ m, which corresponds to the value of the calculated length of $l_0(20) = 0.7 \cdot 2 = 1.4$ m and $l_0/d = 1.4/0.2 = 7$. This value of Table 1 corresponds to $\varphi(20) = 1$ and the critical load on the pile

$$F_{cr} = 1 \cdot (14.5 \cdot 10^6 \cdot 0.0314 + 210 \cdot 10^6 \cdot 18.8 \cdot 10^{-4}) = 0.851 \cdot 10^6 N,$$

which is greater than the load on the pile $F = 0.42 \cdot 10^6 N$. The pile is in operational condition.

For full $t_2 = 40$ years of pipeline operation the soil has thawed to a depth of $h_2 = 5$ m at $l_0(40) = 0.7 \cdot 5 = 3.5$ m and $l_0/d = 3.5/0.2 = 17.5$. According to Table 1 we have $\varphi(40) = 0.79$ and

$$F_{cr} = 0.79 \cdot 0.851 \cdot 10^6 = 0.673 \cdot 10^6 N.$$

In this case $F_{cr} > F = 0.42 \cdot 10^6 N$, the pile is serviceable.

At operation of the pile during $t_3 = 60$ years we have $h_3 = 7$ m at $l_0(60) = 0.7 \cdot 7 = 4.9$ m. At the value of $l_0/d = 4.9/0.2 = 24.5$ according to Table 1 $\varphi(60) = 0.62$, then we obtain

$$F_{cr} = 0.53 \cdot 10^6 N > F = 0.42 \cdot 10^6 N,$$

the pile is serviceable.

During the pile's operation over the next 70 years, when interpolating the graph $(\varphi(t)h(t))$ constructed from several measurements of soil thawing depth $h(t) - F_{cr}(t)$ over the last 60 years, we would have a value of $h_4 = 8$ m and $l_0(70) = 5.6$ m. Then $l_0/d = 5.6/0.2 = 28$ and $\varphi(70) = 0.54$ and $F_{cr} = 0.46 \cdot 10^6 N$.

Taking into account the fact that $F = 0.42 \cdot 10^6 N$ slightly differs from $F_{cr} = 0.46 \cdot 10^6 N$, and the diagram $h(t) - F_{cr}(t)$ has been built at $t_3 > 60$ years by interpolation, it is unacceptable to operate the pile after 70 years at the soil thawing depth of $h_4 = 8$ m. Thus, according to the condition of oil pipeline support safety, it is necessary to limit the time of its operation by the pile bearing capacity to 60 years.

The above example of a pile calculation according to the stability criterion during the operational phase can be implemented for piles with a square cross-section with side b in a similar way using Table 1.

Consider the pile calculation in compression at the design stage in solid frozen soils in conditions of increasing thawing depth. The dimensions of the cross-section of the pile and its length for a given operation life of an individual pile or of the building (structure) as a whole are sought. The dimensions of the pile cross section are determined by the values of the load on it, the strength of the pile materials and the design requirements for it in accordance with the Codes.

The basis for calculating the length of a pile in the foundation or an individual pile at the design stage under conditions of annual increase in the height h of the upper water layer during thawing of the ground above the solid frozen (rocky) foundation soil is a graph of the growth of $h(t)$ values over time (years). For

this purpose, it is necessary to organize observations of the growth of $h(t)$ values over time (in summer periods) in conditions of the construction site or close to them. It is possible to use the available information about the results of observations $h(t)$ in the corresponding control organizations. Let us denote the current increasing height of the liquid soil layer for the time t of observation $h_i(t)$, where i is the number of the year of observation (measurement). Using the set of values $h_i(t)$ and time (years) t , a graph $H(h_i)$ is plotted, for example, using the method of least squares. A function $H(h)$ is selected to describe the graph, by which H values are predicted for the planned lifetime (time) of the pile or structure $H(h)$ according to the project. At this value of the pile length (denote H_{cr}) the critical load F_{cr} must be equal to or greater than the pile load F . For this purpose, the dimensions of the pile cross-section d or b according to the designations in Table 1 are specified.

From the content of Fig. 4, we find $l_0 = 0.7H_{cr}$ and set the value of d (or b). According to Table 1, find the value of φ , corresponding to the value of l_0/d , and then by (2) determine the value of F_{cr} . If F_{cr} turns out to be less than the pile load F , it is necessary to increase the values of A_b and A_s in (2). Thus, we increase the value of $(R_b A_b + R_{sc} A_s)$ and consequently the diameter d of the pile. This leads to a decrease in φ , but more to an increase in $(R_b A_b + R_{sc} A_s)$ and hence an increase in F_{cr} . So, if we use the initial data to calculate the pile according to the first example in the article, then with $d = 0.2$ m, $l_0 = 8 \cdot 0.7 = 5.6$ m and $\varphi = 0.54$, we have $F_{cr} = 0.46 \cdot 10^6$ N, which is a little more than $F = 0.42 \cdot 10^6$ N found in the first example for the reinforced concrete pile and, therefore, can be taken for the project.

Thus, for example, according to the values of t and $h(t)$ in the previous example of calculation of the existing pile in the axis "time – layer height" a graph of dependence $h(t)$ is plotted, which is approximated by some function $H(t)$. The design length of the pile H , taking into account the depth of its lower end into the ground to a depth of $c \geq 0.5$ m, is determined according to the project operating time t_{cr} and the graph of the increasing value of $h(t)$.

4. Conclusions

1. The pile behavior under axial compression in the solid frozen foundation soil at various stages of operation at partial and full layer height thawing of the base soil at different depths $h(t)$ is considered.
2. The design diagrams of the pile in the base soil at various stages of its operation in summertime during thawing of the upper base soil layer are presented.
3. A pile design diagram and calculation algorithm are given, using the pile bearing capacity estimation at the operation stage in the longitudinal bending in the solid frozen soil in summertime as an example.
4. To forecast the piles operating time in pile foundations or individual piles during global warming on the Earth, an algorithm for calculating pile length at the design stage is proposed.
5. A numerical example of calculating the pile operational life in the solid frozen soil of the foundation in an oil pipeline support is given.

References

1. Trofimenko, Y.V., Yakubovich, A.N., Yakubovich, I.A., Shashina, E.V. Modeling of influence of climate change character on the territory of the cryolithozone on the value of risks for the road network. International journal of online and biomedical engineering. 2020. 16 (7). Pp. 65–74. DOI: 10.3991/ijoe.v16i07.14557
2. Vasiliev, A., Drozdov, D., Gravis, A., Malkova, G.V., Nyland, K.E., Streletskiy, D.A. Permafrost degradation in the Western Russian Arctic. Environmental Research Letters. 2020. 15. 045001. DOI: 10.1088/1748-9326/ab6f12

3. Hong, E., Perkins, R., Trainor, S. Thaw settlement hazard of permafrost related to climate warming in Alaska. *ARCTIC*. 2014. 67(1). Pp. 93–103. DOI: 10.14430/arctic4368
4. Hjort, J., Streletskiy, D., Guy Doré, G., Wu, Q, Bjella, K., Luoto, M. Impacts of permafrost degradation on infrastructure. *Nature Reviews Earth & Environment*. 2022. 3(1). Pp. 24–38. DOI: 10.1038/s43017-021-00247-8
5. Suter, L., Streletskiy, D., Shiklomanov, N. Assessment of the costs of climate change impacts on critical infrastructure in the Circumpolar Arctic. *Polar Geography*. 2019. 42(4). Pp. 267–286. DOI: 10.1080/1088937X.2019.1686082
6. Vasiliev, A.A, Gravis, A.G., Gubarkov, A.A., Drozdov, D.S., Korostelev, YU.V., Malkova, G.V., Oblogov, G.E., Ponomareva, O.E., Sadurtdinov, M.R., Streleckaya, I.D., Streleckij D.A., Ustinova, E.V., Shirokov, R.S. Degradaciya merzloty: rezultaty mnogoletnego geokriologicheskogo monitoringa v zapadnom sektore rossijskoj arktiki [Permafrost degradation: results of the long term geocryological monitoring in the western sector of russian arctic]. *Kriosfera Zemli*. 2020. XXIV(2). Pp. 15–30. (rus)
7. Yakubovich, A.N., Trofimenko, Y.V., Yakubovich, I.A., Shashina, E.V. Assessment of the road transport infrastructure facility functionality loss risk resulting from climate change. 2021. *IOP Conf. Ser.: Mater. Sci. Eng.* 1159. 012040. DOI: 10.1088/1757-899X/1159/1/012040
8. Glasser, R. The Climate change imperative to transform disaster risk management. *International Journal of Disaster Risk Science*. 2020. 11. Pp. 152–154. doi.org/10.1007/s13753-020-00248-z
9. Li, M.V., Glyzin, A.V., Bilyushova, T.P. Ideal housing for the north. *Architecture and Design: History, Theory, Innovation*. 2023. 7. Pp. 166–171. (rus)
10. Wang, G.-S., Yu, Q.-H., You, Y.-H., Zhang, Z., Guo, L., Wang, S.-J., Yu, Y. Problems and countermeasures in construction of transmission line projects in permafrost regions. *Sciences in Cold and Arid Regions*. 2014. 6(5). Pp. 432–439.
11. Alekseeva, O.I., Balobaev, V.T., Grigoryev, M.N., Makarov, V.N., Chzhan, R.V., Shats, M.M., Shepelev, V.V. 2007. O problemakh gradostroitel'stva v kriolitozone (na primere Yakutsk) [On the problems of urban planning in cryolithozone (on the example of Yakutsk)]. *Kriosfera Zemli*. 2007. 2. Pp. 76–83. (rus)
12. Anisimov, O.A., Belolutskaya, M.A. Otsenka vliyaniya izmeneniya klimata i degradatsii vechnoi merzloty na infrastrukturu v severnykh regionakh Rossii [Assessment of the climate impact change and permafrost degradation on infrastructure in the northern regions of Russia]. *Meteorologiya i gidrologiya*. 2002. 6. Pp. 15–22. (rus)
13. Anisimov, O.A., Lavrov, S.A. Globalnoe poteplenie i tyanie vechnoi merzloty: otsenka riskov dlya proizvodstvennykh ob'ektov TEHK [Global warming and permafrost melting: risk assessment for fuel and energy facilities]. *Tekhnologii TEHK*. 2004. 3. Pp. 78–83. (rus)
14. Solovyev, S.A., Sushev, L.A., Kochkin, A.A., Solovyeva, A.A. Problem of piles structural reliability analysis on the stability criterion in permafrost regions. *Building and Reconstruction*. 2021. 4. Pp. 3–15. (rus) DOI: 10.33979/2073-7416-2021-96-4-3-16
15. Taimyrskiy telegraf [Taimyr telegraph] [Online]. URL: <https://www.ttelegraf.ru>. (reference date: 08.01.2023)
16. Wu, Q., Zhang, T. Changes in active layer thickness over the Qinghai- Tibetan Plateau from 1995 to 2007. *Journal of Geophysical Research: Atmospheres*. 2010. 115. Pp. 1–12.
17. Streletskiy, D., Anisimov, O., Vasiliev, A. Permafrost degradation. Snow and ice-related hazards, risks and disasters. 2015. Pp. 303–344. DOI: 10.1016/B978-0-12-394849-6.00010-X
18. Oberman, N.G. Contemporary permafrost degradation of the European north of Russia. In D. L. Kane, & K. M. Hinkel (Eds.), *Proceedings of the Ninth International Conference on Permafrost*. Institute of Northern Engineering, University of Alaska Fairbanks. 2008. Pp. 1305–1310.
19. Malkova, G.V. Mean-annual ground temperature monitoring on the steady-state-station "Bolvansky". *Earth's Cryosphere*. 2010. 14(3). Pp. 3–14.
20. Wang, F., Li, G., Ma, W., Mu, Y., Zhou, Z., Mao, Y. Permafrost thawing along the China-Russia Crude Oil Pipeline and countermeasures: a case study in Jiagedaqi, Northeast China. *Cold Regions Science and Technology*. 2018. 155. Pp. 308–313. DOI: 10.1016/J.COLDREGIONS.2018.08.018
21. Streletskiy, D.A., Shiklomanov, N.I., Hatleberg, E. Infrastructure and a changing climate in the Russian Arctic: a geographic impact assessment. *Proceedings of the 10th International Conference on Permafrost*. 2012. 1. Pp. 407–412.
22. Connon, R., Devoie, E., Hayashi, M., Veness, T., Quinton, W. The influence of shallow taliks on permafrost thaw and active layer dynamics in subarctic Canada. *Journal of Geophysical Research: Earth Surface*. 2018. 123(2). Pp. 281–297. DOI: 10.1002/2017JF004469
23. Hou, X., Chen, J., Sheng, Y., Rui, P.-F., Liu, Y.-Q., Zhang, S.-H., Dong, T.-C., Gao, J.-W. Field observations of the thermal stability of permafrost under buildings with an underfloor open ventilation space and pile foundations in warm permafrost at high altitudes. *Advances in Climate Change Research*. 2023. 14 (2). Pp. 267–275. DOI: 10.1016/j.accre.2023.03.004
24. Orlov, V.A., Nechitaeva, V.A., Peterburgskij, D.A. Construction and reconstruction of pipelines in permafrost conditions. *Plumbing, Heating and Air Conditioning*. 2021. 5(233). Pp. 18-23. – EDN BSILUM. (rus)
25. Smirnov, A.F., Aleksandrov, A.V., Lashchenikov, B. YA., Shaposhnikov, N. N. *Stroitel'naya mekhanika. Dinamika i ustoychivost sooruzheniy* [Construction mechanics. Dynamics and stability of structures]. Moskva: Stroizdat, 1984. 415 p. (rus)
26. Skvortsov, D.S., Zhaisambaev, E.A., Derevnin, D.V., Parenkina, O.A. Determination of the length of piles immersed in the soil by the method of an acoustic wave excited in a pile by impact. *Russian Journal of Transport Engineering*. 2020. 2(7). DOI: 10.15862/13SATS220 (rus)
27. Linovich, L.E. *Raschet i konstruirovaniye chastej grazhdanskix zdaniy* [Calculation and design of civil building parts]. Kiev: Budivel'nik, 1972. 664 p. (rus)
28. Utkin, V.S., Sushev, L. A., Solov'ev, S.A. Sposob opredeleniya znacheniya e'kspluatatsionnoj nagruzki na zhelezobetonnyy svayu v sostave zdaniy ili sooruzheniy [Method of determining the value of operational load on reinforced concrete pile in buildings or structures]. Patent Russia no 2765358, 2021.
29. Utkin, V.S., Solov'ev, S.A. Sposob izmereniya deformatsij, napryazhenij i usilij v armature e'kspluatiruemy'x zhelezobetonny'x konstrukcij [Method of measurement of deformations, stresses and forces in reinforcement of operated reinforced concrete structures]. Patent Russia no 2721892, 2020.
30. Ulybin, A.V., Korenev, V.V. The method of length measurement for hollow steel piles. *Construction of Unique Buildings and Structures*. 2013. 6(1). Pp. 28-35. (rus). DOI: 10.18720/CUBS.6.5
31. Snezhkov, D. Yu., Leonovich, S.N., Budrevich, N.A. Methodology of testing bored piles by seismo-acoustic and ultrasonic methods. *Concrete and Reinforced Concrete*. 2022. 2(610). Pp. 20–24. DOI: 10.31659/0005-9889-2022-610-2-20-24

Information about authors:

Vladimir Utkin, Doctor of Technical Sciences
E-mail: UtkinVoGTU@mail.ru

Zhanna Kosheleva, PhD in Technical Sciences
ORCID: <https://orcid.org/0000-0003-2076-4377>
E-mail: koshelevazhv@voqu35.ru

Olga Yarygina, PhD in Technical Sciences
ORCID: <https://orcid.org/0000-0002-2497-5609>
E-mail: ola_yarigina@mail.ru

Received 05.09.2023. Approved after reviewing 18.01.2024. Accepted 30.01.2024.

